Assembly of Highly Asymmetric Genetically-Encoded Amphiphiles for Thermally Targeted Delivery of Therapeutics

by

Jonathan Roger McDaniel

Department of Biomedical Engineering
Duke University

Date:_____

Approved:

_____
Ashutosh Chilkoti, Supervisor

_____
Mark Dewhirst

_____
Gabriel Lopez

_____
Kam Leong

_____
Sidney Simon

Dissertation submitted in partial fulfillment of the requirements for the degree of Doctor of Philosophy in the Department of Biomedical Engineering in the Graduate School of Duke University

2013

ABSTRACT

Assembly of Highly Asymmetric Genetically-Encoded Amphiphiles for Thermally Targeted Delivery of Therapeutics

by

Jonathan Roger McDaniel

Department of Biomedical Engineering
Duke University

Date:_____

Approved:

_____
Ashutosh Chilkoti, Supervisor

_____
Mark Dewhirst

_____
Gabriel Lopez

_____
Kam Leong

_____
Sidney Simon

An abstract of a dissertation submitted in partial fulfillment of the requirements for the degree of Doctor of Philosophy in the Department of Biomedical Engineering in the Graduate School of Duke University

2013

Copyright by
Jonathan Roger McDaniel
2013

Abstract

Traditional small molecule chemotherapeutics show limited effectiveness in the clinic as their poor pharmacokinetics lead to rapid clearance from circulation and their exposure to off-target tissues results in dose-limiting toxicity. The objective of this dissertation is to exploit a class of recombinant chimeric polypeptides (CPs) to actively target drugs to tumors as conjugation to macromolecular carriers has demonstrated improved efficacy by increasing plasma retention time, reducing uptake by healthy tissues, and enhancing tumor accumulation by exploiting the leaky vasculature and impaired lymphatic drainage characteristic of solid tumors. CPs consist of two principal components: (1) a thermally responsive elastin-like polypeptide (ELP) that displays a soluble-to-aggregate phase transition above a characteristic transition temperature (T_t); and (2) a cysteine-rich peptide fused to one end of the ELP to which small molecule therapeutics can be covalently attached (the conjugation domain). This work describes the development of CP drug-loaded nanoparticles that can be targeted to solid tumors by the external application of mild regional hyperthermia (39-43°C).

Highly repetitive ELP polymers were assembled by Plasmid Reconstruction Recursive Directional Ligation (PRe-RDL), in which two halves of a parent plasmid, each containing a copy of an oligomer, were ligated together to dimerize the oligomer and reconstitute the functional plasmid. Chimeric polypeptides were constructed by

fusing the ELP sequence to a $(CGG)_8$ conjugation domain, expressed in *Escherichia coli*, and loaded with small molecule hydrophobes through site specific attachment to the conjugation domain. Drug attachment induced the assembly of nanoparticles that retained the thermal responsiveness of the parent ELP in that they experienced a phase transition from soluble nanoparticles to an aggregated phase above their T_t. Importantly, the T_t of these nanoparticles was near-independent of the CP concentration and the structure of the conjugated molecule as long as it displayed an octanol-water distribution coefficient (LogD) > 1.5.

A series of CP nanoparticles with varying ratios of alanine and valine in the guest residue position was used to develop a quantitative model that described the CP transition temperature in terms of three variables – sequence, chain length, and concentration - and the model was used to identify CPs of varying molecular weights that displayed transition temperatures between 39°C and 43°C. A murine dorsal skin fold window chamber model using a human tumor xenograft was used to validate that only the thermoresponsive CP nanoparticles (and not the controls) exhibited a micelle-to-aggregate phase transition between 39-43°C *in vivo*. Furthermore, quantitative analysis of the biodistribution profile demonstrated that accumulation of these thermoresponsive CP nanoparticles was significantly enhanced by applying heat in a cyclical manner. It is hoped that this work will provide a helpful resource for the use of thermoresponsive CP nanoparticles in a variety of biomedical applications.

I dedicate this dissertation to the memory of my father,

Dr. Roger L. McDaniel

for inspiring my fascination with science and engineering.

Contents

List of Tables

List of Figures

Acknowledgements

This work was supported through grants to Dr. Ashutosh Chilkoti from the National Institutes of Health. I thank the Center for Biomolecular and Tissue Engineering for supporting me with a graduate student training grant from the National Institutes of Health, as well as the Triangle Materials Research Science and Engineering Center for their support with a graduate student fellowship from the National Science Foundation.

I am extremely grateful to all of the members of my dissertation committee for their time and effort in guiding me throughout the course of this project. My advisor, Dr. Ashutosh Chilkoti has been a constant source of ideas and encouragement over the past six years, and has provided the intellectual and financial freedom to pursue fascinating projects. I also must thank Dr. Dewhirst for providing both scientific advice and laboratory resources in performing *in vivo* hyperthermia experiments.

There are a number of people who have directly aided me in this work. Drs. Xinghai Li and Wenge Liu were critical assets in performing all of my *in vivo* studies – these studies simply could not have been done without their help. The CP-drug conjugations described in Chapter 3 (Oxycodon, Gemcitabine, and Paclitaxel) were performed by Dr. Jayanta Bhattacharyya, a postdoc who has provided me with a significant amount of scientific and moral support. Kevin Vargo, a graduate student in

Dr. Daniel Hammer's lab at the University of Pennsylvania, made a heroic effort in providing all of the cryo-TEM data presented in Chapters 3 and 6. I am also particularly grateful to my office and bench mate, Sarah MacEwan, for assistance with window chamber studies, fluorescent microscopy, and simply tolerating me every day for six years; Wafa Hassouneh, who was kind enough to train and lead me in the everlasting war against dust particles (static and dynamic light scattering); Isaac Weitzhandler, who has been a huge help in the past year as many aspects of this project are transferred to his portfolio; Chris Radford, an undergraduate researcher, for his monumental effort in cloning and measuring transition temperatures for days on end; Drs. Felipe García-Quiroz and Mira Amiram, for while we rarely worked on the same project, I can't count the number of hours we spent discussing elastin-like polypeptides; and Dr. Andrew MacKay, who spent a tremendous amount of time and effort training me to be meticulous in designing experiments. Finally I would like to thank the rest of the Chilkoti lab for contributing to and sustaining such a great academic culture.

Most of all, I am greatly indebted to my mother, my sister, my family, my girlfriend Sarah, and my long-time roommates Alex, Chris, Andy, and Shasta for keeping me sane for as long as they did.

1. Introduction to Cancer and Drug Delivery

1.1 Cancer as a Disease

Since the war on cancer began in the early 1970's, an estimated $300 billion has been spent on R&D to develop new therapeutics and treatments, increase the sensitivity and efficiency of detection and screening methods, and elucidate the genetic factors that cause cancer [1]. Despite this massive effort, the total incidence and mortality of those suffering from cancer clearly illustrate that cancer treatment and prevention remain critical issues for improving the quality of healthcare for an aging U.S. population. Cancer will kill over a half million Americans in 2013 – accounting for nearly 23% of all deaths – and an additional 1.7 million new patients will be diagnosed with the disease, resulting in an estimated cost to the U.S. economy of over $202 billion annually from direct healthcare costs and loss of productivity [2].

Cancer is a collection of diseases typically caused by several genetic mutations that can arise from environmental factors, internal processes, and inherited defects [3]. Although all cancers can display vast phenotypic and genotypic differences – even between cells within the same tumor - all contain a series of hallmark characteristics essential to the survival and proliferation of these abnormal cells [4, 5]. These acquired characteristics, outlined in a theory put forth by Hanahan and Weinberg, include the following: (1) the ability to sustain proliferative signaling while (2) circumventing pathways that suppress growth; (3) the ability to divide an unlimited number of times

and (4) evade apoptotic pathways; (5) the ability to induce the formation and growth of neovasculature that can provide tumor cells with essential nutrients and oxygen in a process known as angiogenesis; and (6) the ability to invade neighboring tissues, extravasate into the blood stream, and form distant metastases [6]. An increasing body of evidence suggests that many cancers are also able to evade recognition by the immune system (in particular, B and T lymphocytes, macrophages and natural killer cells) as well as modify and reprogram their cellular metabolism to more effectively support their state of rapid proliferation, although it is still unknown whether these characteristics are universal to all cancers [6].

1.2 Treatment

Despite the vast degree of heterogeneity between tumors, the standard of care is a combination of three primary strategies: surgery, radiation, and chemotherapy, as well as the emerging fields of molecularly targeted therapeutics and hormone therapies [7]. This section will focus on the first three strategies with an emphasis on chemotherapy.

Surgical intervention remains the oldest and most common form of treatment; complete removal of the diseased tissue is a highly effective strategy when performed prior to local invasion and metastasis [7]. Surgery is also commonly used to remove nonmalignant tissue surrounding the tumor site to prevent recurrence, diagnose the malignant potential of a tumor through biopsy, determine the stage and type of a tumor

to facilitate diagnosis and assess treatment options, and debulk unresectable tumors to relieve pain or increase the effectiveness of radiotherapy or chemotherapy [7]. However, surgery is limited to providing control over the primary tumor; once a tumor has metastasized, surgery must be supplemented with a more systemic approach such as chemotherapy to significantly prolong survival.

Subjecting solid tumors to high doses of radiation has also become a standard treatment for primary tumor control [7]. Ionizing radiation produces free radical capable of inducing single and double stranded DNA breaks and covalent crosslinks between DNA strands [8]. Although this activity preferentially destroys rapidly dividing cells (*i.e.*, tumor cells), high radiation levels are also toxic to healthy cells. To address this issue, radiation treatments are commonly fractionated into multiple smaller doses spread over the course of weeks to allow healthy tissue time to recover and repopulate between treatments [9]. Radiation treatments can be applied via external beam radiation, which uses an acute concentrated exposure at multiple angles to maximize the dose at the beams' focal point while minimizing the dose to the surrounding tissues, or brachytherapy, which involves precise spatial implantation of several small radioactive capsules throughout the tumor mass to provide a uniform and sustained level of radiation within the tumor for days to weeks [10]. Radiotherapy can also be enhanced by combining treatments with specific chemotherapeutics [11]. As radiation is least

effective in hypoxic cells, treatment is often combined with chemotherapeutic regimens that increase cellular oxygenation and provide independent toxicity modalities [12].

1.2.1 Chemotherapy

The third treatment modality is the systemic application of chemotherapeutic drugs. These molecules tend to prohibit or interrupt cell division, and thus prove most fatal to rapidly dividing cells, although their nonspecific activity can be toxic to healthy tissues as well. This section will briefly discuss the main classes of chemotherapeutics and their respective mechanisms in terms of which phase of the cell cycle they are most effective. Alkylating agents (chlorambucil, cyclophosphamide, and melphalan) and platinates (cisplatin, carboplatin, oxaliplatin) are an exception to this classification, as they are cell cycle nonspecific chemotherapeutics that indiscriminately induce covalent DNA-DNA and DNA-protein crosslinks that inhibit DNA repair and synthesis [7]. As this class is cell cycle nonspecific, they are commonly included in multidrug combination regimens to complement their cycle-specific counterparts [13, 14].

As the S-phase or synthesis phase is characterized by extensive DNA replication prior to cell division, it provides a popular target for a variety of chemotherapeutics that interfere with DNA processes. Many drugs in this family are particularly toxic because even a few genetic abnormalities can lead to cell death. Antimetabolites, one class of S-phase specific drugs, are comprised primarily of nucleotide analogs (Figure 1). These

molecules typically resemble purines (fludarabine, 6-thioguanine) and pyrimidines (gemcitabine, 5-fluorouracil) that prematurely terminate growing DNA chains upon incorporation [7]. They have also shown the ability to inhibit enzymes necessary for DNA synthesis, such as dyhydrofolate reductase (methotrexate), phosophoribosyl pyrophosphate amidotransferase (mercaptopurine), and ribonucleotide reductase (hydroxyurea). Anthracyclines are another class that include many S-phase specific drugs, including doxorubicin (the primary chemotherapeutic used throughout this dissertation), daunorubicin, epirubicin, and idarubicin. These drugs exhibit a variety of toxic mechanisms: DNA intercalation, which prevents the synthesis of DNA and RNA; generation of toxic free radicals; and inhibition of topoisomerases and helicases [15].

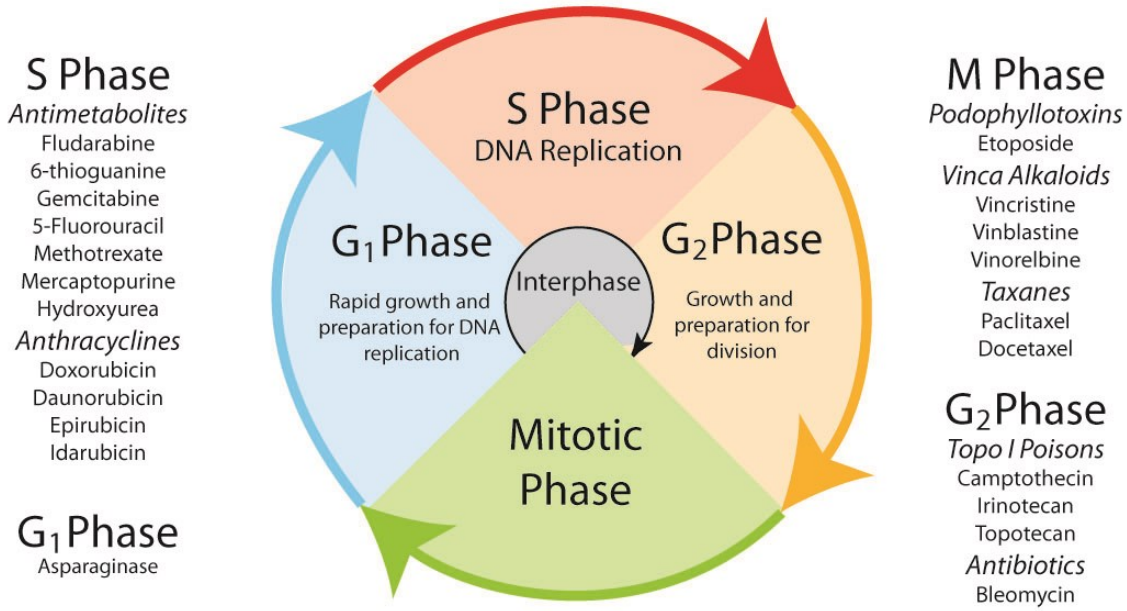

Figure 1: Diagram of the cell cycle and a list of common chemotherapeutics grouped according to their phase toxicity.

Chemotherapeutics that are most effective during M (Mitosis) phase are typically cytoskeletal drugs that arrest the cell in metaphase by affecting microtubule formation, a dynamic process that is necessary for proper chromosome alignment and cell division. Podophyllotoxins (etoposide) and vinca alkaloids (vincristine, vinblastine, and vinorelbine) block the assembly of tubulins, whereas taxanes (paclitaxel and docetaxel) stabilize microtubules and prevent microtubule detachment from the centromere [16]. By inhibiting microtubule dynamics, these drugs cause the cell to trigger apoptosis or to revert back to the G_2-phase without dividing.

The G_1-phase is characterized by protein synthesis; drugs that inhibit the formation of amino acids, proteins, and enzymes can cause G_1-phase arrest. One interesting example of a G_1 specific chemotherapeutic is the enzyme asparaginase. Acute lymphoblastic leukemia (ALL) cells are unable to produce the nonessential amino acid asparagine, and thus must harvest asparagine from extracellular sources. Asparaginase, an enzyme that catalyzes the reduction of extracellular asparagine to aspartic acid and ammonia, selectively starves the leukemia cells because healthy cells are capable of generating asparagine [17, 18].

There are a few drugs that result in cell cycle arrest in the late S-phase or G_2 (Gap-2) phase. Topoisomerase I poisons, such as camptothecin and its analogs (irinotecan and topotecan) bind and stabilize the Topoisomerase I – DNA complex. These drugs induce the formation of double stranded DNA breaks when the advancing replication fork collides with the stabilized complex [19]. Bleomycin, a glycopeptide antibiotic, also results in the arrest of cells in the early G_2 phase by inducing DNA strand breaks, although the exact mechanism remains unknown [20]. Importantly, as the camptothecins and bleomycin exhibit unique mechanisms of action and display non-overlapping toxicities with other common chemotherapeutics, they are frequently included in combination chemotherapy regimens.

1.2.2 Hyperthermia

While not commonly recognized as a primary treatment modality in the United States (except for superficial tumors), the local application of mild hyperthermia (temperatures ranging from 39-43°C) is used as a powerful adjunctive therapy in Europe for the local control of a variety of cancers when used in combination with radiotherapy and chemotherapy [21-24]. The primary objective of this dissertation is to use externally applied hyperthermia to trigger the accumulation of a chemotherapeutic carrier within a tumor, and thus exploit hyperthermia as an externally applied stimulus. However, hyperthermia also induces a therapeutic response in tumor tissue, which is addressed in this section.

Heating tumors to supraphysiological temperatures is not only cytotoxic, but it also activates several mechanisms by which tumor cells are potentiated to the primary treatment. The degree of cytotoxicity caused by hyperthermia is a complex function of the temperature, the duration of treatment, and the cell type. Generally, the rate of cell killing increases exponentially for every 1°C increase in temperature above 39°C; hence, it is possible to achieve similar cytotoxic profiles in much shorter time periods by slightly increasing the temperature [25]. This toxicity is primarily caused by the thermal denaturation or destabilization of cellular proteins. In fact, mammalian cells tend to develop a resistance to this effect (*i.e.*, thermotolerance) when heated to temperatures below ~43.5°C by upregulating heat shock proteins that assist in protein folding [26].

Fortunately, thermotolerance is a transient effect and can be avoided in the clinic by limiting treatment times to 1 hour and increasing the interval between treatments to 2-3 days.

Hyperthermia also affects the physiology of tissues by increasing blood flow and vascular permeability. Interestingly, while elevated temperatures substantially increase the blood flow in healthy tissues, this effect is suppressed in tumor tissues [27]. This phenomenon leads to effective thermoregulation in healthy tissues: as the temperature increases, the rate at which the heat is removed also increases. Tumor tissues, however, experience an increase in temperature without a corequisite increase in blood flow. This lack of thermoregulation drives tumors to higher temperatures than the surrounding tissues, thereby causing a higher degree of tissue and vascular damage. Mild hyperthermia has also been shown to promote the extravasation and deposition of therapeutics into the tumor interstitium. Whereas the accumulation of macromolecular carriers, such as monoclonal antibodies, shows a slight enhancement (2-4 fold) in the presence of hyperthermia [28], the penetration of nanoparticles can be greatly enhanced. For example, vasculature in human ovarian carcinoma xenografts (SKOV-3) that was impermeable to 100-nm liposomes under normothermic conditions (< 39°C) exhibited an exponential increase in liposome deposition for every 1°C the tumor was heated between 39 and 42°C [29].

Several phase III clinical trials spanning multiple tumor types (cancers of the breast, head and neck, esophagus, and cervix, as well as melanomas and glioblastomas) indicate that hyperthermia in combination with radiotherapy provides substantial benefits over radiotherapy alone without significantly increasing toxicity or tissue damage to the surrounding region [30]. This combined effect can be attributed to the fact that hyperthermia inhibits DNA repair pathways [31, 32], reduces the severity of radio-resistant hypoxic regions throughout the tumor by enhancing tumor oxygenation [33-35], and is particularly cytotoxic to cells in S-phase [36, 37], which display the highest resistance to radiation.

Similarly, the efficacy of many chemotherapeutics is also improved at elevated temperatures. The degree of enhancement varies widely between different classes of drugs. Whereas antimetabolites such as methotrexate remain unaffected by hyperthermia, the effectiveness of alkylating agents and anthracyclines (doxorubicin) exhibit an additive increase in efficacy when heated [38, 39]. The drug classes nitrosoureas, platinates (cisplatin and carboplatin), and bleomycin display a synergistic increase in efficacy and hence represent promising candidates for delivery by thermoresponsive carriers.

1.3 Drug Delivery to Solid Tumors

1.3.1 Overview

One of the primary goals of drug delivery for cancer therapy is to improve the therapeutic index of anticancer drugs by increasing the amount of drug delivered to the tumor site and decreasing its exposure to healthy tissues; the therapeutic index is defined as the ratio of LD_{50} to ED_{50}, where the median lethal dose (LD_{50}) is defined as the dose necessary to cause death in 50% of a population, and the minimum effective dose (ED_{50}) is defined as the smallest dose able to induce the desired effect in 50% of a population. A large therapeutic index is preferable as it describes a situation in which the efficacious dose is far below the lethal dose. Unfortunately, many cancer chemotherapeutics are hydrophobic compounds with a MW of less than 500 Da that have suboptimal pharmacokinetics, significant systemic toxicity and a small therapeutic index. This low therapeutic index has two main causes: first, upon injection into the systemic blood circulation, only a small fraction of these low MW compounds accumulate in the body, while the bulk of the drug is rapidly cleared through the kidneys, taken up by the liver, or excreted through the digestive tract. Second, because the cellular toxicity of these molecules is correlated with drug concentration and length of exposure, both healthy cells and tumor tissue are subjected to the same distribution profile, resulting in similar toxicities. Although increasing the injected dose increases the amount of drug that reaches the tumor site, it also exacerbates undesirable side effects,

whereas reducing the dose to minimize side effects makes the drug less effective. Furthermore, because many of these drugs are hydrophobic they are poorly soluble in water, which also limits the maximum solubility of the drug and hence the amount of therapeutically active drug able to reach the desired site of action. Finally, many small molecule chemotherapeutics have been shown to display incomplete tumor coverage due to a variety of factors, including increased distances between blood vessels in tumors and poor tissue penetration of small molecule drugs, interactions between the drug and the extracellular matrix and cellular organelles, drug metabolism, and a high interstitial fluid pressure gradient combined with a lack of convection [40].

Engineered drug carriers provide a means to circumvent many of these issues, and thus improve the therapeutic index of anticancer drugs through conjugation of the drug to macromolecular carriers such as polymers [41, 42], proteins [43], and polysaccharides [44], or by encapsulation within liposomes [45], polymer micelles [46], and nanoscale polymer emulsions [47]. While these carriers also provide the opportunity for a range of delivery strategies, release mechanisms, targeting modalities, and pharmacokinetic profiles, the most important rationale for their use stems from the observation that these high molecular weight carriers improve accumulation within solid tumors compared to free drug via the enhanced permeability and retention (EPR) effect and reduce accumulation in healthy tissues [48, 49]. The EPR effect arises from the rapid pathological development of the tumor vasculature, which results in highly

porous vessel walls lacking the tight junctions found in healthy tissue [50]. These pores can range from 100 to 800 nm, depending on the tumor and organ environment [51], thereby permitting extravasation of both small and macromolecules. Thus, many macromolecular drug carriers that are excluded from healthy tissues are able to extravasate across the leaky tumor vasculature, while the lack of lymphatic drainage in tumor tissue leads to enhanced retention of these delivery vehicles.

1.3.2 Macromolecular Carriers

Macromolecular polymers provide a wide array of advantages for drug delivery. First, they can extend the circulation half-life of the drug by simply increasing the apparent molecular weight of the drug [52]. This decreases the rate of clearance of the drug and its nonspecific absorption into systemic tissues. Extending the plasma half-life also increases tumor exposure and can hence increase the amount of drug that accumulates in the tumor by the EPR effect. Second, these carriers can specifically target tumor tissue, passively through the EPR effect [53, 54], or actively via targeting ligands [55] or application of focused mild hyperthermia to tumors [56], thereby increasing the efficacy and reducing the systemic toxicity of the drug. Third, for drugs that are covalently conjugated to a polymer, the presence of a covalent link between the drug and polymer provides a cleavable tether that can be tailored to release the drug in response to an active trigger (e.g., low pH in endo-lysosomal compartments). In the case

of low MW, hydrophobic drugs, conjugation to a soluble carrier can also increase the solubility of the drug in plasma by many orders of magnitude, enabling administration of higher doses [41]. In some cases, covalent conjugation of the drug to the carrier can also stabilize the metabolically active drug, thereby further increasing efficacy. Fourth, the presence of a hydrophilic corona can impart "stealth" characteristics by preventing opsonization by immune tissues and degradation by proteases. Some polymeric carriers also enhance the cytotoxicity of a drug by overcoming the cellular multidrug resistance exhibited by many solid tumors [57-59].

1.3.3 Active and Passive Targeting Strategies

Macromolecular drug carriers commonly exploit both passive and active targeting strategies to increase the bioavailability of the drug within the tumor. Passive targeting utilizes the size of the carrier to passively accumulate in the tumor via the enhanced permeability and retention (EPR) effect [60], which results in the extravasation of sub-100 nm nanoparticles into the tumor and prevents their clearance. In healthy tissues, this passive transvascular transport of therapeutics occurs through two primary pathways: diffusion, in which a concentration gradient drives the molecules from an area of high concentration (intravascular space) to an area of low concentration (intratumoral environment); and convection, in which molecules move with the bulk solution current [61]. However, the rapid proliferation of cells within the tumoral matrix

combined with an impaired lymphatic drainage system results in a high interstitial fluid pressure (IFP) within most tumors that severely reduces convection currents from the vasculature into the tumor space [62]. Consequently, many treatment modalities attempt to generate high transvascular concentration gradients in order to best enhance diffusion across the vessel wall [63-65].

Active targeting approaches, on the other hand, typically involve decorating the outer surface of the nanoparticle carrier with tumor-specific ligands such as antibodies [66] and aptamers [67] that tightly bind receptors overexpressed by the tumor. While active affinity targeting remains the focus of many delivery strategies, it is limited by the heterogeneity of receptor expression between tumors [68] and even between patients diagnosed with the same cancer [69].

1.3.4 Thermoresponsive Carriers

1.3.4.1 Overview

Thermoresponsive drug delivery systems are capable of exploiting an alternative active targeting approach that relies on the regional application of mild hyperthermia to spatially and temporally control the accumulation of a chemotherapeutic agent within a solid tumor. Despite their distinct features, most of these systems are designed to respond to hyperthermia in one of two ways: (1) carriers that physically encapsulate drugs, such as thermally sensitive liposomes [70, 71], polymer micelles [72], and

hydrogels [73, 74] typically release their therapeutic payload upon heating. These carriers are subdivided into fast release vehicles (release in seconds to minutes) that exhibit complete drug release within the first pass through the tumor vasculature, and slow release vehicles (minutes to hours) that exploit the EPR effect to accumulate within the tumor over a period of 24 hours and then release the drug within the tumor extravascular space upon heating. (2) Carriers that are physically conjugated to a drug, such as polypeptide-drug conjugates [63] and polypeptide micelles [75, 76], undergo a morphological or physicochemical change in response to heat to induce the accumulation of the carrier in the tumor extravascular space. These carriers typically rely on conventional cleavage mechanisms such as hydrolysis or pH to release the drug upon cellular uptake [76, 77]. Both targeted accumulation and triggered release are capable of increasing the bioavailability of the chemotherapeutic within the tumor, potentially reducing the tumor burden prior to resection, or even abolishing the tumor entirely.

1.3.4.2 Elastin-like Polypeptides

Elastin-like polypeptides (ELPs) are a class of temperature sensitive biopolymers based on the structural motif found in mammalian tropoelastin [78, 79]. ELPs consist of a repeated pentapeptide sequence $(VPGXG)_n$, where X is any amino acid except proline. ELPs exhibit a thermodynamic inverse phase transition in aqueous solution at a specific

temperature (T_t), below which ELPs are soluble and above which ELPs become insoluble and phase separate into a polymer-rich coacervate. This phase transition is completely reversible.

ELPs retain all the advantages of polymeric drug delivery systems, but also provide a number of additional benefits that are unique to genetically engineered biopolymers. First, because ELPs are composed of amino acids, they are non-toxic [80] and biodegradable [81]. Second, ELPs have a favorable pharmacokinetic profile [82]. Third, because ELPs are designed and synthesized using genetic engineering techniques [83], the molecular weights of ELPs can be precisely specified resulting in monodisperse polymers, parameters that are critical to tune the pharmacokinetics of polymers. In contrast, the MW and polydispersity of synthetic polymers is difficult to control with the same level of precision as recombinant peptide polymers. Fourth, their composition can also be precisely encoded at the gene level. This has the consequence that the degree of hydrophobicity and the degree of ionization of an ELP can be precisely tuned, both of which impact its tissue distribution and sub-cellular uptake. Control over the ELP sequence also allows the numbers and locations of reactive sites for drug conjugation to be precisely specified, which allows the architecture of an ELP-drug conjugate to be controlled at the sequence level. Fifth, ELPs can be easily expressed at high yield (100-200 mg/L) from *Escherichia coli* and rapidly purified by exploiting their phase transition behavior [84, 85].

As elastin-like polypeptides retain their thermal responsiveness following chemical conjugation, ELP-drug conjugates have been rationally designed by optimizing their sequence and molecular weight to exhibit a phase transition between 39°C and 42°C, a range that is achievable through the application of mild clinical hyperthermia. Triggering the phase transition through the application of mild hyperthermia increased cellular uptake of an ELP conjugated to a fluorescent reporter in three different human carcinoma lines *in vitro* (ovarian carcinoma SKOV-3, squamous cell carcinoma FaDu, and cervical adenocarcinoma HeLa) compared to a soluble ELP control [86], an effect likely mediated by enhanced interactions between the phase-separated ELPs and the phospholipid membrane of the cells. Meyer *et al*. observed that the ELP transition could increase total uptake in human ovarian tumors (SKOV-3) implanted within a dorsal skin-fold tumor window chamber model. The window chamber allows real-time fluorescent measurements of the vasculature and extravascular space of an implanted tumor. By heating the window chamber to 42°C, they observed a 2-fold increase in the intratumoral accumulation of a thermoresponsive ELP conjugate over the course of one hour when compared to a non-heated control [87].

To further increase the accumulation of ELP-drug conjugates within solid tumors, Dreher *et al*. proposed a cyclical heating regimen [63]. Applying localized mild hyperthermia to a window chamber tumor model induced the formation of small ELP aggregates that adhered to the vascular walls, increasing in number and size over time

(Figure 2). Upon cessation of hyperthermia, the rapid solubilization of the ELP aggregates created a steep transvascular gradient that "pumped" the ELP into the tumor across the interstitial fluid pressure gradient. By measuring the fluorescence as a function of time, the authors observed that the thermally sensitive ELP displayed a 2.8-fold concentration increase over a non-heated control and a 1.6-fold increase over a heated control that lacked the phase transition.

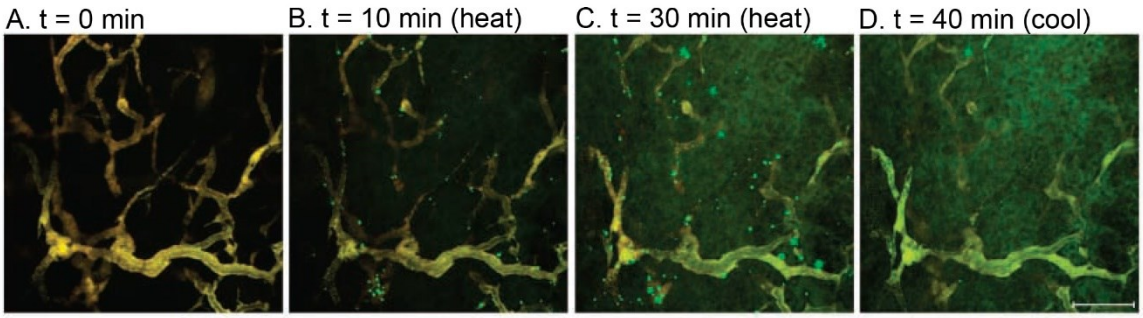

Figure 2: ELP response to clinical hyperthermia visualized with a dorsal skin-fold tumor window chamber. A thermally sensitive (green) and a thermally insensitive (red) ELP in a solid tumor before, during, and following hyperthermia treatment. (A) Prior to heating, the green and red levels were normalized to produce a uniform yellow throughout the vasculature. Between (B) 10 minutes and (C) 30 minutes of heating, the thermally sensitive ELPs began to adhere to the vasculature walls, indicated by the green punctate fluorescence. (D) Upon return to normothermia, the aggregates rapidly resolubilized and dissipated, demonstrating the reversibility of the ELP transition. The scale bar represents 100 μm in all images [63].

This technique was also used *in vivo* to induce tumor regression in a murine E0771 breast cancer model. Thermally sensitive ELP-doxorubicin (DOX) conjugates were fused to the terminal cell penetrating peptide (CPP) SynB1 to enhance cellular uptake in

both tumor and vasculature cells. The DOX moiety was attached through a pH-sensitive hydrazone linker that rapidly cleaves in the low pH environment of the late endosome [88, 89]. The authors observed that thermally cycling (20 min heat; 10 min cool; 4 cycles) the tumor following each of the four SynB1-ELP-DOX administrations (2 day intervals) resulted in a statistically significant four-fold reduction in tumor volume by day 14 over normothermia treatment [90].

While the delivery strategies described above rely solely on the application of mild hyperthermia to the tumor site, the diversity in structure and composition available to polypeptide carriers enables elastin-like polypeptide conjugates to utilize a vast array of "smart" triggers in conjunction with heat, including pH-sensitivity [91], ligand binding [92], metal ion concentration [93], and light [94].

1.3.4.3 Micelles

Diblock polymers exhibiting a large solubility difference between the two blocks form core-shell micelles above their characteristic critical micelle concentration (CMC) to reduce the unfavorable interactions between the hydrophobic block and the aqueous environment. The spontaneous self-assembly of micelles creates a hydrophobic, water-excluding core stabilized by a soluble corona. First popularized by Kataoka and coworkers in 1990 [95], drug-encapsulating micelles remain a common therapeutic delivery vehicle because they exhibit many desirable characteristics for treating solid

tumors. The micellar core provides a high loading capacity for small and lipophilic molecules (*i.e.*, most of the chemotherapeutic drugs on the market), while the hydrophilic corona –when comprised of specific polymers - can extend the plasma half-life of the vehicle by evading uptake by the RES [96]. The sub-100 nm size and narrow size distribution is ideal for accumulating within the tumor interstitium by the EPR effect and avoiding renal filtration. Actively targeted micelles – whether through the addition of targeting ligands or the localized application of hyperthermia or magnetic fields – represent a new class of drug delivery vehicles that can increase the therapeutic payload reaching the tumor while decreasing nonspecific uptake in healthy tissues. To this end, micelles have been modified through the incorporation of thermally sensitive polymers, resulting in two basic classes of thermosensitive micelles that can be actively targeted to a solid tumor: micelles with thermoresponsive coronas and micelles with thermoresponsive cores.

1.3.4.3.1 Micelles with thermosensitive coronas

The most commonly used polymer in the design of thermosensitive coronas is poly(N-isopropylacrylamide) (*i.e.*, pNIPAAm). This synthetic polymer displays a distinct lower critical solution temperature (LCST) at 32°C; pNIPAAm is a soluble polymer below this temperature but undergoes a coil-to-globule phase transition above 32°C that makes it insoluble. The LCST phase transition is thermally reversible. The LCST is frequently tuned by copolymerizing pNIPAAm with a hydrophilic polymer to increase the LCST or a hydrophobic polymer to decrease the LCST [97]. Despite the large

compositional diversity of thermally sensitive micelles in the literature, there are only a few examples that are responsive within the physiological range of 39-43°C (Table 1) [72, 98-104].

Table 1: Thermosensitive therapeutic micelles that respond to clinical hyperthermia

Thermosensitive Corona	Core Block	LCST (°C)	Size (nm)	Therapeutic	Ref
p(NIPAAm-co-AAm)	PDLLA	41	80	Docetaxel	[98]
p(NIPAAm-co-AAm)	PDLLA	39.8	80	Docetaxel	[72, 99]
p(NIPAAm-co-AAm)	PDLLA	39.7	80	Paclitaxel	[72]
p(NIPAAm-co-DMAAm)	PDLLA	40	65	Adriamycin	[100]
p(NIPAAm-co-DMAAm)	PDLLA	39	170	Adriamycin	[101]
p(NIPAAm-co-DMAAm)	PCL	40.5	87	Adriamycin	[101]
p(NIPAAm-co-DMAAm)	PLGA	39	75-243	Doxorubicin	[102]
p(NIPAAm-co-DMAAm)	PDLLA	39.4	20	None	[103, 104]

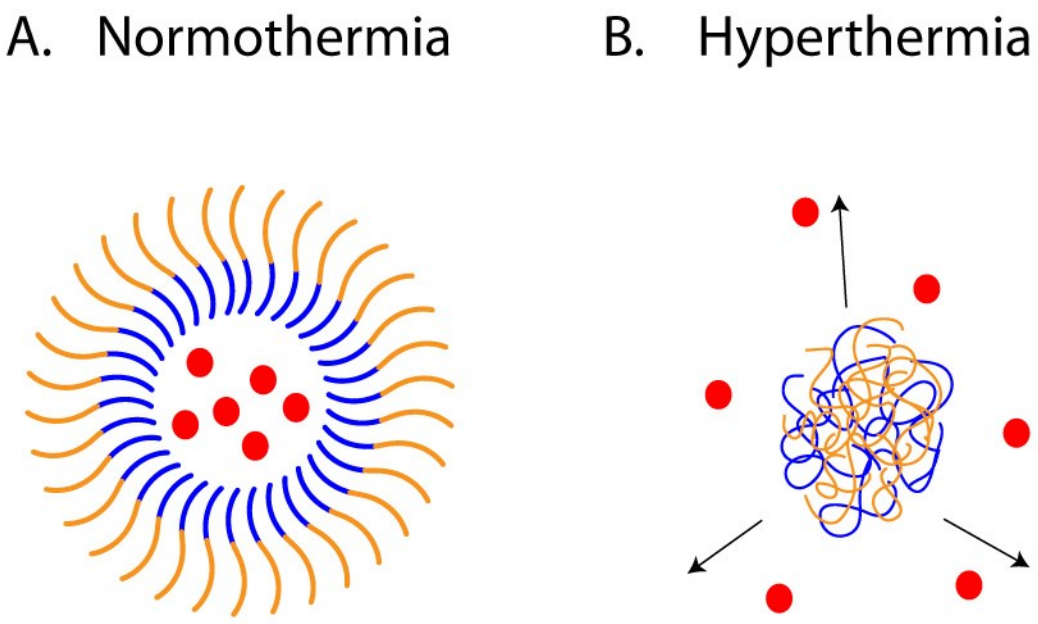

Figure 3: Diblock micelles with thermosensitive coronas. (A) At temperatures below the transition temperature of the thermosensitive polymer (orange; pNIPAAm), the hydrophilic

thermosensitive corona and the hydrophobic core (blue; poly(ε -caprolactone)) spontaneously assemble into micelles that can encapsulate drugs. (B) At temperatures above the LCST of pNIPAAm, the corona collapses into a hydrophobic coacervate, thereby destabilizing the structure and releasing the drugs [105].

In general, these micelles encapsulate their payload at physiological temperatures (37°C) and accumulate within the tumor via the EPR effect (Figure 3A). The subsequent application of hyperthermia to the tumor tissue induces the collapse of the thermoresponsive corona into a hydrophobic aggregate, which both enhances intracellular uptake by increasing hydrophobic interactions with the cellular membrane and drastically increases the rate of drug release within the tumor interstitium by destabilizing the micelle structure (Figure 3B). The micelles listed in Table 1 release DOX slowly and incompletely at 37°C, a temperature below the transition temperature, but rapidly release DOX at and above their respective transition temperature (39-43°C). The release of free drug from the micelles typically increases therapeutic efficacy by allowing the therapeutic molecule to penetrate deeply into the tumor due to its lower molecular weight and higher diffusivity.

1.2.4.3.2 Micelles with thermally sensitive cores

Thermally sensitive micelles can also be designed with the thermoresponsive polymer in the core. In contrast to micelles that disassemble and release their payload in response to hyperthermia, micelles that contain thermoresponsive cores spontaneously assemble when heated. This triggered assembly is uniquely suited to allow the

locoregional modulation of ligand density in response to heat [75, 106, 107]. In a recent example of the utility of this approach, MacEwan and Chilkoti synthesized diblock ELPs that self-assemble into monodisperse micelles in response to a thermal trigger, wherein self-assembly in the narrow temperature range between 37°C (normal body temperature) and 42°C (highest temperature approved for mild clinical hyperthermia) results in the presentation of a functional cell penetrating peptide (CPP) motif on a ELP nanoparticle [75]. In this system, nanoparticles were assembled by fusing two ELPs: one with a hydrophilic composition and one with a hydrophobic composition, resulting in a diblock ELP (ELP_{BC}) that exhibited two independent LCST transitions (T_{t1} = 39°C and T_{t2} = 56°C). At systemic physiological temperatures (37°C) the ELP_{BC} was in a unimer state – soluble polymer chains– that display five Arg residues on one end of the polymer chain (Figure 4A). Five Arg residues were selected because previous studies have shown that there is minimum threshold of six consecutive Arg residues required to create a functional CPP [108], so at 37°C where the ELP_{BC} is in a unimer state, cell uptake should be low. When heated to the range of clinical hyperthermia (42°C) the hydrophobic ELP (T_{t1} = 39°C) collapsed into a hydrophobic core whereas the hydrophilic ELP formed a soluble corona decorated with a high local density of Arg (Figure 4B). This high-density presentation of arginine in the heated Arg_5-ELP_{BC} resulted in an 8-fold increase in cellular uptake *in vitro* compared to the 37°C control. Uptake was negligible for ELP_{BC}s without fused CPPs and CPP-ELPs that did not self-assemble [75]. The presentation of a

functional CPP only at 42°C, but not at 37°C opens the way to convert CPPs which are powerful yet promiscuous agents to promote the uptake of drugs into cells into an exquisitely targeted system for cancer drug delivery via the application of focused external hyperthermia to solid tumors. While it remains to be seen whether this strong enhancement of cellular uptake *in vitro* translates *in vivo*, it represents a potentially powerful strategy to overcome the problem of nonspecific targeting of CPPs and promotes the tissue specific delivery of therapeutics.

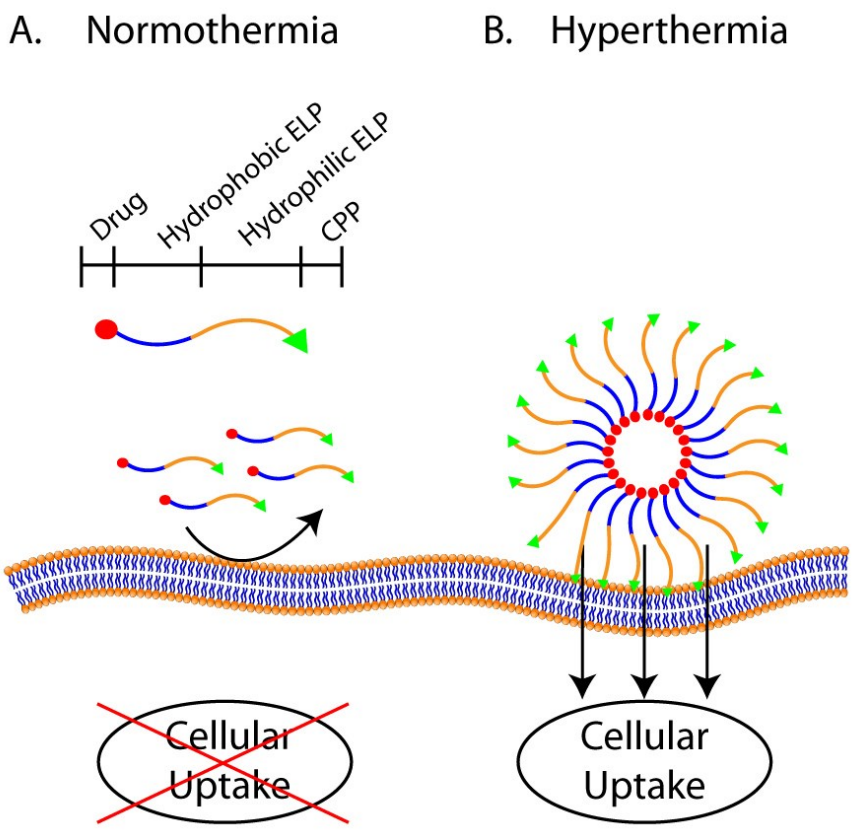

Figure 4: Diblock micelles with thermosensitive cores. (A) A diblock ELP construct that consists of a conjugated drug (red circle), a hydrophobic block with a low T_t (blue), a

hydrophilic block with a high T_t (orange), and a dysfunctional cell penetrating peptide (CPP; green triangle). At physiological temperatures, the diblock is a soluble chain and the low Arg density on the terminus of the ELP_{BC} does not promote cellular uptake. (B) At ~40°C, desolvation of the hydrophobic block results in the assembly of spherical micelles that display a high density of Arg restudies, thus creating a functional CPP motif on the surface of the nanoparticle. This results in the enhanced uptake of the nanoparticles by cells heated to the clinically relevant mild hyperthermia temperature of 42°C [105].

1.3.4.4 Vesicles

Since their debut in 1965 [109], liposomes have comprised a substantial fraction of known drug delivery vehicles and currently represent one of the most extensively studied systems in the literature. Liposomes consist of a stable phospholipid bilayer encompassing an aqueous core. The aqueous compartment is capable of encapsulating water soluble therapeutics whereas the phospholipid membrane can solubilize lipophilic molecules. Incorporation of small molecule therapeutics into liposomes improves drug performance by extending the plasma half-life [110], increasing the solubility of the drug, enhancing accumulation in solid tumors via the enhanced permeability and retention (EPR) effect [111, 112], and shielding the drug from deactivating plasma proteases [113]. These benefits are also reflected in the clinic where there are currently multiple systems in clinical trials and on the market, including the chemotherapeutics Doxil® and Caelyx® (pegylated liposomal doxorubicin) and Daunoxome® (liposomal daunarubicin) [114]. Despite the significant increase in tumor accumulation, these formulations continue to display poor drug bioavailability because they suffer from slow and incomplete drug release. Furthermore, the extended plasma half-life of the drug combined with nonspecific targeting can result in a number of systemic side effects

such as hand and foot syndrome [115]. Using clinical hyperthermia to trigger thermoresponsive liposomal drug release has emerged as a viable strategy to address these issues and allow the rapid release of the entire drug payload within the tumor vasculature.

In sharp contrast to using hyperthermia to *target* the drug delivery vehicle to a diseased site, as is the case with ELP-conjugates, thermosensitive liposomes typically use hyperthermia to facilitate the *release* of their encapsulated payload. Yatvin *et al.* first developed temperature sensitive liposomes (TSLs) by selecting phosopholipids that provided an acyl chain gel-to-liquid crystalline phase transition at temperatures slightly above body temperature (42-45°C) [116]. The melting temperature (T_m) was tuned by mixing dipalmitoyl phosphatidylcholine (DPPC; T_c = 41°C) with small amounts of distearoyl phosphatidylcholine (DSPC; T_c = 54°C). The resultant vesicles displayed a single transition between 42.5 and 44.5°C that was accompanied by enhanced drug release.

This basic design served as a foundation for further improvements in thermosensitive liposomal delivery. Based on several studies demonstrating that grafting short polyethylene glycol (PEG) chains to the surface of liposomes enhanced the plasma half-life, increased liposomal stability in serum, and reduced immune system recognition [110, 117], Li *et al.* showed that these "stealth" properties could be imparted to TSLs without affecting the stability of the liposome or the gel-to-liquid crystalline

phase transition [118]. The first few generations of thermoresponsive liposomes also suffered from a relatively slow release rate in response to hyperthermia (15-60 min). This slow release prevented the drug from releasing exclusively within the tumor vasculature, so these liposomes were allowed to accumulate in the tumor prior to hyperthermia exposure. To address this limitation, lipid components such as lysolipids and phosphatidyloligoglycerols were incorporated into the membrane to enhance the degree and speed of the thermal response [64, 119].

Needham and Dewhirst have amassed a large body of work detailing the effect of incorporating the micelle-forming lysolipid, monostearoyl phosphatidylcholine (MSPC) into a stealth DPPC membrane (Figure 5A) [64, 65, 120-124]. At the melting temperature (T_m) of these liposomes, the membrane coexists in two states: solid crystalline regions separated by liquid grain boundaries. Upon heating, the incorporated lysolipids migrate to the grain boundaries in high concentrations where they form highly curved, semispherical pores that rapidly release the encapsulated drug (Figure 5B) [125]. In fact, these self-assembled pores enable the encapsulated doxorubicin to be completely released in 10-20 seconds at mild hyperthermic temperatures, essentially allowing the drug to be released within the transit time through the tumor vasculature [64]. This rapid release has shown the ability to both flood a tumor with free drug and to shut down the tumor vasculature [65, 121, 124]. This technology, now owned by Celsion and marketed as ThermoDox®, is currently undergoing a phase II clinical trial for

recurrent chest wall disease for breast cancer patients and phase II and III clinical trials for metastatic and primary liver cancers (www.celsion.com).

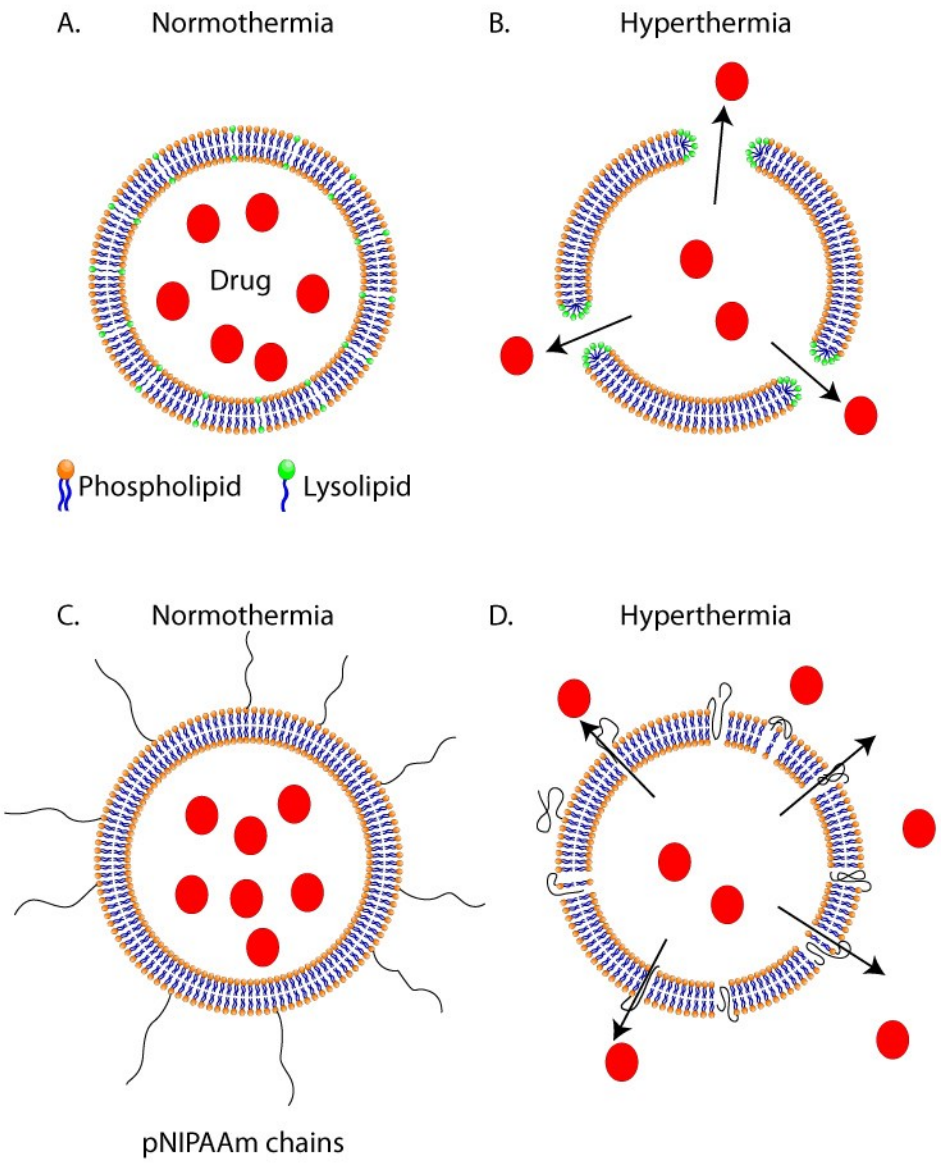

Figure 5: Temperature sensitive liposomes. (A) Under normothermia, micelle-forming lysolipids are uniformly dispersed throughout the phospholipid bilayer, forming a

barrier that is impenetrable to encapsulated drugs. (B) Upon exposure to hyperthermia, the lysolipids congregate and form large pores that enable rapid drug release. (C) Liposomes conjugated to soluble pNIPAAm chains. (D) When heated above the pNIPAAm LCST, the chains become hydrophobic and destabilize the membrane, promoting the release of encapsulated drugs.

Although micelle-forming lysolipids display a remarkable ability to rapidly migrate to grain boundaries and form pores, they have also shown the tendency to desorb from the bilayer when diluted or when in the presence of acceptor lipid pools. This process, which is likely to occur upon *in vivo* administration, destabilizes the membrane and significantly reduces the thermal sensitivity of the liposome. As an alternative, Kono *et al.* proposed a design in which the thermosensitive polymer poly(N-isopropylacrylamide) (*i.e.,* pNIPAAm) was used to decorate the outer membrane of the liposomes Figure 5C) [126, 127]. Upon reaching the pNIPAAm LCST, the grafted polymer experiences a hydrophilic coil to hydrophobic globule phase transition that disrupts the liposomal membrane, releasing the contents (Figure 5D). These formulations have shown high stability in serum and minimal leakage over time [71].

Thermally sensitive liposomes have proven capable of capturing many of the passive benefits associated with the co-application of hyperthermia, including increased tumor accumulation and enhanced drug activity, as well as the active benefits of a rapid drug release in a site-specific manner. The safety and efficacy of this approach in human trials suggests that it will be a strong challenger in the upcoming decade to many of the passive strategies currently used in the clinic.

1.3.4.5 Dendrimers

Dendrimers are a specialized class of synthetic polymers that consist of a spherical topology with a well-defined tree-like architecture. Polymer branches grow outward from a central core in a stepwise fashion such that each new branch represents a new generation. Thus, dendrimers are commonly described according to the number of generations, or branches, that they contain, which also correspond to their macromolecular size. In contrast to polymeric micelles, dendrimers are single molecules. Their interior contains numerous nanoscopic cavities that are capable of hosting guest molecules [128]. The specific environment of these cavities can be tuned to favor certain molecules by modifying the terminal end groups of the central polymer [129]. Dendrimers also offer a small size distribution relative to multimolecular micelles, can be easily functionalized, and are stable at very high dilutions. As they do not display a critical aggregation concentration (CAC), they do not suffer from structure destabilization and premature drug release upon systemic administration as can multimolecular micelles.

Stratified dendrimers are generated by growing different polymer layers off of the terminal end groups. Thermally sensitive dendrimers have been created in this manner by decorating the outer layer with pNIPAAm. Increasing the temperature above the LCST of the dendrimer has been shown to increase the release rate of hydrophobic molecules encapsulated in the core [130, 131]. These dendrimers theoretically operate in

a manner similar to thermosensitive micelles: the dendrimers accumulate in a solid tumor via the EPR effect and are then triggered to release the encapsulated drug by hyperthermia. One example of this mechanism is the hyperbranched block copolymer of H40-poly(ε-caprolactone) and poly(N-isopropylacrylamide-co-acrylamide) that encapsulates paclitaxel [132]. Upon the administration of hyperthermia, the release rate of paclitaxel doubled and the hydrophobicity of the outer layer increased cellular uptake of the polymer.

Surprisingly, it is also possible to design dendrimers that release their payload in response to hyperthermia without triggering an LCST phase change. Chandra *et al*. demonstrate that an oligo(ethylene glycol)-grafted amidoamine can encapsulate doxorubicin through a series of hydrogen bond interactions [133]. While these bonds result in a stable encapsulation at 37°C with only a basal 10% release over 24 hours, they rapidly break and release doxorubicin when heated to 43°C leading to 90% release in 2-3 hours *in vitro*. With the continued development of stimuli-responsive branched structures, this thermally triggered release mechanism will undoubtedly become more prominent.

1.3.4.6 Hydrogels

Polymers can be crosslinked into three-dimensional hydrogel networks that can absorb large quantities of water, ranging from ~ten percent to thousands of times their

own weight. Hydrogels have become a popular material for drug delivery for several reasons: (1) the crosslinks between polymers vastly increase the physiological stability of the gel; (2) hydrogels can be loaded with aqueous drugs or vehicles that are released in a sustained manner via diffusion or matrix degradation; (3) their environmental sensitivity can be precisely controlled through the choice of polymer; and (4) many of the physical properties such as elasticity, degradation rate, swelling ratio, and hydrophilicity can be tailored by altering polymer parameters such as block length, polymer, crosslinker ratio, etc.

Recently, nanohydrogels – hydrogels that range in size from tens to hundreds of nanometers – have begun to receive attention in the field of drug delivery. Similar to many polymer micelles, they are made through common self-assembly techniques such as solvent emulsion, diffusion, and precipitation [134]. Nanohydrogels retain the material benefits of a hydrogel and gain access to the broad range of applications available to nanoparticles: their small size promotes cellular uptake and tumor accumulation while avoiding renal filtration, and the outer shell can be decorated with ligands to target specific tissues and stealth polymers to extend the plasma half-life by evading the RES.

Thermally sensitive nanohydrogels are formed by crosslinking polymers that display LCST behavior, most commonly p(NIPAAm) copolymers. Nanohydrogels that have been tuned to respond to mild hyperthermia maintain a swelled state below the

characteristic transition temperature (37°C) but experience a volume phase transition when heated above physiological temperatures (42°C). The hydrophobic collapse of the polymer chains results in a rapid shrinking of the nanoparticle, aggregation, and deposition within the heated tissue. The reduced volume may result in the expulsion of the entrapped water and/or molecules within the plasma during the transit through the tumor and following nanoparticle deposition within the heated tissue.

Two different p(NIPAAm) copolymers have been used in the synthesis of thermally sensitive nanohydrogels. Zhang *et al*. showed that p(NIPAAm-co-AAm) nanohydrogel particles with a 50 nm diameter and a volume phase transition between 37 and 43°C were able to deliver a near-infrared fluorophore (NIRF) to a heated tumor [135]. No tumor accumulation was observed for the dye by itself (with hyperthermia) or for the nanohydrogels without hyperthermia. The same group later showed that this methodology could also be used to deliver the chemotherapeutics docetaxel and 5-fluorouracil [74]. In this study, nanohydrogels loaded with docetaxel displayed significant tumor inhibition against the S180 murine sarcoma line (78%) when coupled with mild hyperthermia, compared to nanohydrogels without hyperthermia (49%) and free docetaxel (40%). Peng *et al.* synthesized p(NIPAAm)-co-poly(2-(dimethylamino)ethyl methacrylate) (PDMAEMA) hydrogel nanoparticles that experienced a volume phase transition that caused the 140 nm diameter hydrogel particles to shrink to 100 nm at 41°C *in vivo* [73]. Loaded with the highly active SN-38

metabolite of the chemotherapeutic, irinotecan, these nanoparticles were used to treat the C26 murine colon carcinoma by spacing five treatments (20 mg/kg) over 15 days. In combination with hyperthermia, these nanoparticles induced a significant decrease in the tumor burden after 30 days post-treatment compared to the nanoparticles without hyperthermia (2.5-fold decrease) and free irinotecan (2.5-fold decrease). The extensive crosslinking found throughout these hydrogel systems provides a high degree of stability against the large mechanical and biological stresses of circulation that simply cannot be matched by classical polymer micelles. This unique characteristic of nanoscale hydrogels, which significantly reduces premature and off-target drug release, will likely become a commonly adopted motif in thermally targeted systems.

1.4 Conclusions and Future Perspectives

Many active-targeting strategies rely on the unique characteristics of tumors, such as drug release in response to tumor pH or ligands that bind upregulated receptors or enzymes. While these strategies can be effective, these features dramatically vary between tumors and even between patients diagnosed with the same cancer. In contrast, thermoresponsive chemotherapeutic delivery systems in combination with focused mild hyperthermia have the potential to circumvent the limitations of other active targeting approaches. Hyperthermia mediated targeting can remotely trigger the rapid release of

therapeutics, induce drug accumulation, and/or enhance cellular uptake in a site-specific manner.

The thermally sensitive delivery systems that have been optimized to exploit this strategy typically display two common traits: (1) at the physiological temperature of 37°C, the carrier protects the therapeutic from clearance, inactivation, and harmful interactions with healthy tissue; and (2) at temperatures above 39°C but below 43°C, the carrier undergoes a significant morphological change that results in rapid drug release or accumulation at the target site. Both of these effects result in increased drug bioavailability at the site of the tumor, thereby addressing the principle limitation of many chemotherapeutic regimens. Although the current state of the art exclusively utilizes polymers displaying LCST type behavior to release drugs in response to hyperthermia, we anticipate that the use of UCST (upper critical solution temperature) polymers that are insoluble at low temperatures and soluble at high temperatures will soon be integrated into these smart systems. This will open up new applications such as micelles that simply dissociate at high temperatures to release a payload and micelles that invert (the hydrophobic block becomes hydrophilic and the hydrophilic block becomes hydrophobic) past a specific transition temperature to outwardly present a ligand or CPP that was previously protected in the core.

One of the challenges in the field at the synthesis level is the fact that most thermally sensitive systems are not designed to display a morphological transition in the

clinically relevant temperature range of 39-43°C in blood where the many cosolutes present can influence their phase transition behavior in unanticipated ways. Hence, while many such systems have been reported, very few have been shown to explicitly exhibit their thermal phase transition in plasma or blood. Ideally, an engineered carrier that responds to mild hyperthermia would experience a highly cooperative phase transition (1-2°C range) in blood and hence have the ability to fully release its payload during its transit through the tumor vasculature. The cooperativity of this transition can be enhanced by minimizing the polydispersity of the polymer either by recombinant synthesis of peptide polymers that are completely monodisperse or alternatively using precision polymerization techniques for the chemical synthesis of polymers with low polydispersity [136-139]. The continued development of thermosensitive polymers and approaches to thermally trigger the targeted *in vivo* assembly and disassembly of drug delivery systems promises to provide exciting new tools for cancer chemotherapy.

2. Seamless Cloning of Elastin-like Polypeptide Genes

2.1 Objective and Motivation

The purpose of this chapter is to describe a strategy that enables the rapid construction of highly repetitive elastin-like polypeptide genes for use in drug delivery applications. The ease with which synthetic genes that encode these biopolymers can be assembled has greatly improved over the past decade, primarily due to advances in molecular biology for the synthesis and assembly of genes that encode multiple repeats of peptide "monomers." These advances have been motivated by the utility of biopolymers for a variety of applications including biomaterials [140, 141], tissue engineering scaffolds [142, 143], as materials for surface modification [144] and as drug delivery vehicles [56, 89, 145]. The driving force for the use of artificial repetitive polypeptides in these applications stems from the ability of genetically encoded synthesis to control the polypeptide sequence, architecture, molecular weight (MW), and polydispersity with a precision that is, as yet, unmatched by chemical polymerization.

As a result, a number of strategies to rapidly assemble synthetic genes that encode repetitive polypeptides have been developed, which include PCR cloning [146, 147], concatemerization [148], overlap extension rolling circle amplification [149], and seamless cloning [150-152]. Our lab previously developed a method known as Recursive Directional Ligation (RDL) that utilizes stepwise, recursive addition of an oligomer with itself, or with another compatible DNA sequence by ligation of an insert with a

linearized parent vector containing a copy of the same or compatible insert [83]. RDL has proven to be very useful for the deterministic synthesis of genes that encode large biopolymers with a precisely specified molecular weight. It is also a useful method for the synthesis of genes that encode block copolymers when the orientation, sequence, and molecular weight of the two blocks are critical to their function. Although this method for the assembly of synthetic genes for repetitive polypeptides has proven to be extraordinarily useful, its limitations have also became apparent to us over the last decade of extensive use. These limitations are: first, it is not generalizable, *a priori,* to biopolymers of any arbitrary sequence. Although our implementation of RDL exploited codon degeneracy to select endonucleases that would enable seamless cloning of elastin-like polypeptides (ELPs), the endonuclease recognition sequence in RDL overlaps the coding region. The type II restriction enzymes used in RDL place restrictions on the codons (and therefore the biopolymer sequence) that can be used in the gene (Figure 6B). Second, RDL results in a significant number of clones lacking the insert due to self-ligation of a vector or incomplete digestion of the vector, thereby increasing the number of colonies that must be screened in every round of cloning. Third, the insert itself can self-ligate and circularize, which reduces cloning efficiency at each oligomerization step. Fourth, RDL requires many time-consuming cloning steps. For example, our implementation of RDL was designed in a pUC vector that was unsuitable for

expression, such that the final product –the gene oligomer of interest– had to be cloned into an expression plasmid following gene construction.

To address these limitations of RDL, this chapter introduces a significantly improved cloning methodology – Recursive Directional Ligation by Plasmid Reconstruction (PRe-RDL) – to rapidly clone repetitive polypeptides of any sequence and length. PRe-RDL is a modified form of Recursive Directional Ligation (RDL) that has new features that overcome the limitations of RDL [83]. In PRe-RDL, two halves of a parent plasmid, each containing the desired oligomer, are ligated together, thereby dimerizing the oligomer and reconstituting a functional plasmid. Unlike RDL, PRe-RDL is applicable to any arbitrary DNA sequence (and hence any peptide sequence) and produces peptide oligomers with no extraneous peptides at the junction between repeats, because it uses type IIs endonucleases (Figure 6C). Unlike most other classes of endonucleases, type IIs restriction enzymes cut at a defined number of nucleotides away from their recognition sequence. Because the cleavage site is degenerate, it allows the selection of any single amino acid to join two repeats. When this amino acid is selected as the leading or trailing peptide of the repeated segment, the junctions become seamless. This feature of PRe-RDL hence addresses the inability to oligomerize any arbitrary peptide sequence using type II restriction endonucleases, which was a serious limitation of RDL. The reconstitution of a functional plasmid only upon successful ligation in PRe-RDL also addresses two the other limitations of RDL: the significant

background from self-ligation of the vector and the decreased efficiency due to circularization of the insert. The modular design of PRe-RDL is suitable for the rapid generation of any repetitive peptide sequence of a specified length, and can also be used to join blocks of different lengths and sequences in a predetermined order.

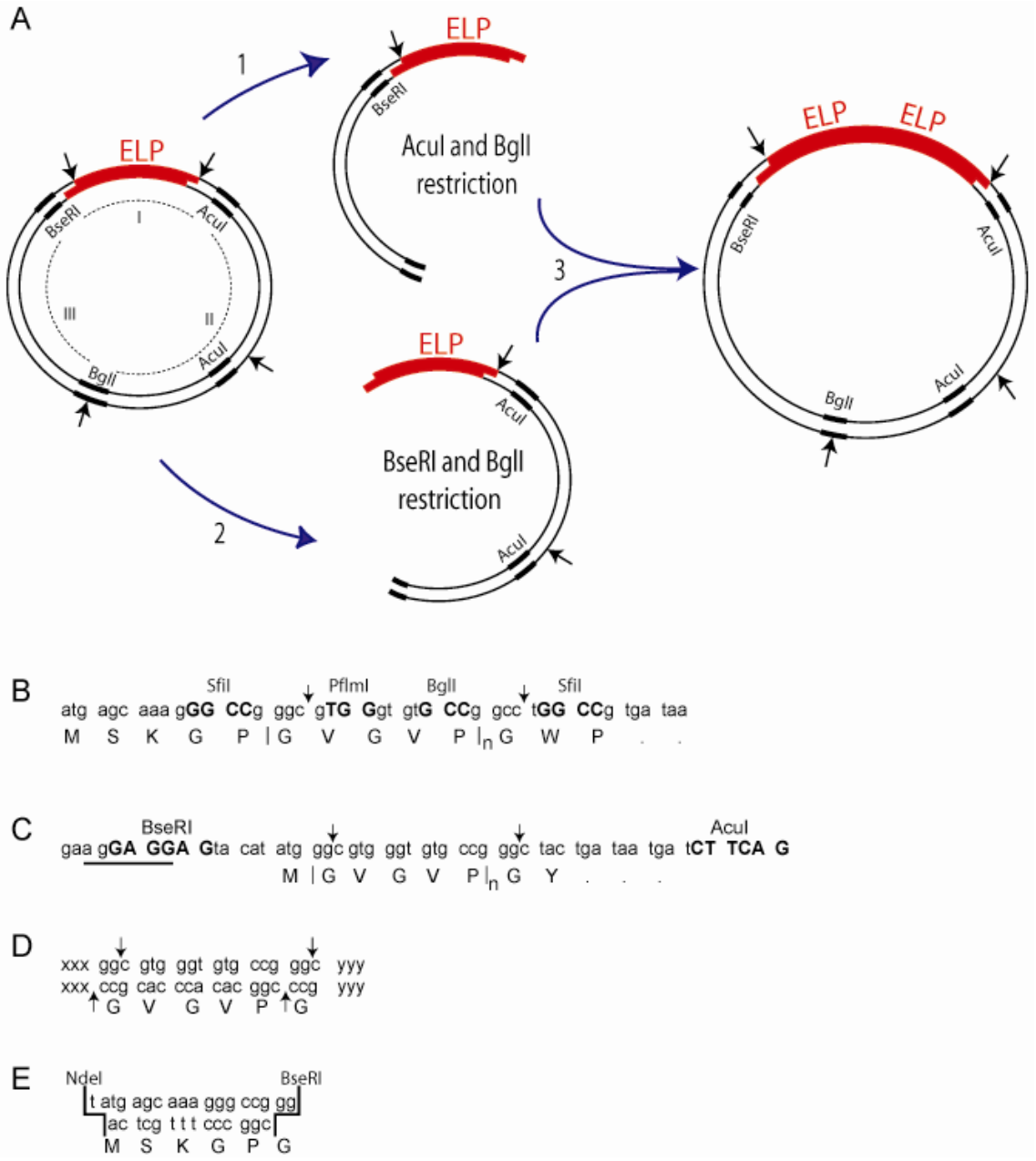

Figure 6: (A) Recursive directional ligation by plasmid reconstruction (PRe-RDL) [153]. One round in PRe-RDL involves: (1) purifying the ELP-containing DNA fragment from the parent vector that is digested with AcuI and BglI; and (2) purifying the ELP-containing fragment from the parent vector that is digested with BseRI and BglI; and then (3) ligating the two compatible halves to reconstitute the original vector, and thereby doubling the length of the insert. (B) Original RDL vector design reported by Meyer [83], with a representative pentamer sequence. The identity of the

capitalized base pairs are specified by the recognition site of the restriction enzyme listed above those nucleotides. Note that the sequence of the restriction endonucleases required for RDL are contained within the DNA sequence that is oligomerized. The vertical arrows indicate the endonuclease restriction sites. (C) PRe-RDL vector, which utilizes the type IIs restriction enzymes, BseRI and AcuI, to eliminate sequence dependence upon the recognition sites. The recognition sequence for BseRI has been designed directly into the Shine-Delgarno ribosomal binding sequence (RBS; underlined), AGGAGGAG, which is required to initiate translation. The BseRI cleavage site ('CC' in this vector) is 8-bases downstream of its recognition site. The recognition site for AcuI, CTGAAG, is 14-bases downstream of its degenerate cleavage site, which is 'GG' in this vector. The vertical arrows indicate the endonuclease cleavage site on the sense strand. (D) BseRI and AcuI have 2-bp overhangs, which reduces intra-sequence dependence within the repeating unit to a single amino acid. (E) Basic design for a leader sequence to be inserted into a vector restricted with NdeI and BseRI [153].

2.2 Recursive Directional Ligation by Plasmid Reconstruction

2.2.1 Selection of Restriction Enzymes

PRe-RDL is a methodology in which two halves of a parent plasmid, each containing a copy of a DNA insert, are ligated together, thereby dimerizing the insert and reconstituting the full plasmid (Figure 6A). To implement PRe-RDL to oligomerize a gene directionally (*i.e.*, head-to-tail) and with no extraneous nucleotides introduced at the ligation junctions, six criteria must be fulfilled in the selection of the restriction enzymes: (1) one restriction enzyme (RE) must be unique (RE_1), *i.e.*, only present once in the cloning plasmid, and is needed to linearize the vector in preparation for ligation of the insert. (2) The second RE is preferably unique (RE_2) to the cloning vector, but if it is present in the plasmid, it should be present only in Region II of the plasmid, which is

defined as the region between RE_2 and RE_3, excluding the insert (see Figure 6A). (3) RE_1 and RE_2 must have different recognition sequences so that their sites can be cut independently of each other. This last feature is essential to implement PRe-RDL, as it allows the isolation of the A and B fragments that together constitute an entire functional plasmid. (4) The two enzymes must result in compatible overhangs, with at least a 2 bp overhang on their 3′-end so that the 3′-cohesive "sticky" end of the A fragment is compatible with the 5′-sticky end of the B fragment. (5) Palindromic overhangs at the ends of the repeat unit must be avoided to allow for directional and seamless ligation. (6) The plasmid must also contain a unique restriction site (RE_3) elsewhere on the plasmid, with overhangs that are incompatible with RE_1 and RE_2. This restriction site is the point at which the plasmid is cut into two halves, both of which must be unable to circularize. Although the exact location of RE_3 is not critical, it would ideally be within the antibiotic resistance gene to further decrease viability of each half of the plasmid.

We first examined all three classes of restriction endonucleases, particularly those that were asymmetric, to identify enzymes that are capable of fulfilling these requirements. Although the cleavage sites of type I restriction endonucleases are asymmetrically displaced from their recognition sequence, this distance is highly variable, reducing their usefulness for cloning. Type II enzymes cut symmetrically within a palindromic or interrupted palindromic sequence, either of which places local

sequence constraints on the biopolymer. Type IIs and type III enzymes both cut asymmetrically at a defined distance from their recognition sequence, thereby eliminating any constraints on the sequence to be oligomerized. The only difference between the type IIs and type III endonucleases is structural, and either class of enzymes is suitable for PRe-RDL [154, 155].

Having identified type IIs or type III restriction endonucleases as the two classes of enzymes with the necessary attributes to implement PRe-RDL, we narrowed the choice of the enzymes by examining which of the many commercially available enzymes would be compatible with the commercial vectors. We chose to carry out oligomerization directly in low-copy number expression vectors, as working with high-copy number cloning plasmids such as the pUC series – used for RDL – proved to be unnecessary, thereby eliminating one cloning step. Of the various expression vectors that are commercially available, we solely focused on the pET system (Novagen Inc.), given the high expression yield of diverse ELPs and their fusion proteins in this expression system [84, 85, 156].

These six requirements were met with BseRI, AcuI, and BglI as the three restriction endonucleases, and pET-24a(+) as the vector. BseRI is a type IIs restriction enzyme, whose recognition sequence is not present in the unmodified pET-24a(+), and AcuI is a type IIs enzyme, whose recognition sequence of CTGAAG only occurs once in the unmodified vector. BseRI cuts at a degenerate site 8 bps downstream of its

recognition site (GAGGAG) on the coding strand, which allows any two amino acids to be encoded between the recognition site and the beginning of the oligomer. AcuI cuts 14 bps downstream of its recognition site, and permits any four amino acids to be encoded between its recognition and cleavage site. A dsDNA cassette was designed to incorporate both of these restriction endonucleases and include a short, default leader sequence (Met) and trailer (Tyr – Stop – Stop) that would encompass the oligomer until the desired length was obtained (Figure 6C). BseRI was chosen as RE_1 for the 5'-end of the ELP because the minimal default leader sequence (Met) was shorter than the two amino acid limit imposed by the choice of this enzyme. In addition, the BseRI recognition site could be easily incorporated into the Shine-Delgarno ribosomal binding site proximal to the start codon. Similarly, AcuI was selected as RE_2, because the default peptide trailer of Tyr-Stop-Stop was shorter than the four amino acid limit imposed by Acu I. This dsDNA cassette consisting of two chemically synthesized oligonucleotides with XbaI and BamHI compatible sticky ends was then inserted into the multiple cloning region of pET 24a(+) by cleaving pET 24a(+) with XbaI and BamHI and ligation of this insert into the linearized plasmid. AcuI also only occurs once in pET 24a(+) vector, within Region II (Figure 6A). Both AcuI and BseRI have different recognition sequences (Figure 6C), so that the first three requirements were met by this pair of REs.

The fourth and fifth requirements were considered simultaneously. If the enzymes resulted in overhangs of 3 bp or less, the overhangs would be contained within

the sequence of a single amino acid to maintain a seamless union. Because any repetitive gene can be designed to repeat seamlessly by partitioning the first amino acid into two complementary overhangs encompassing the monomer, RE's yielding an overhang of 3 bp or less are generalizable to any polypeptide sequence (Figure 6D). In systems that are even more sensitive to overhang length, RE's with only one bp overhangs can be selected, such as AlwI, BceAI and BspPI. The sixth requirement was met by the selection of BglI as RE_3 because its recognition site occurs only once on pET 24a(+), which is on the opposite side of the plasmid as the site of gene oligomerization. In addition, BglI has incompatible overhangs with AcuI and BseRI.

2.2.2 Concatemerization Provides the Initial Oligomer Reactants

In order to decrease the number of rounds in PRe-RDL, we exploited the fact that the inserts in PRe-RDL can be forced to concatamerize to create larger inserts that can serve as the starting point for PRe-RDL. The compatibility of PRe-RDL with concatemerization is especially useful to minimize the number of recursive steps required to arrive at genes with a high degree of oligomerization. We therefore concatemerized the monomer ELP_4 genes that encoded $(GVGVP)_5$ to obtain a hexamer that encodes $(GVGVP)_{30}$ (see Figure 38 in Appendix 8.1 for precise sequence). Similarly, the ELP_2 monomer $(GXGVP)_{10}$ – a 10 pentamer ELP monomer where X alternates between A and G in a 1:1 ratio – was concatemerized to obtain the dimer, $(GXGVP)_{20}$.

One of the limitations of concatemerization is that it is difficult to reliably obtain a large number of higher order oligomers. While concatemerization of the ELP_4 monomer provided a hexamer with no trouble, ELP_2, despite several attempts only yielded a dimer.

2.2.3 Repetitive Gene Synthesis by Recursive Directional Ligation by Plasmid Reconstruction

With the products of concatemerization (ELP_4-30 and ELP_2-20) in hand, we next proceeded to recursively dimerize these sequences by PRe-RDL. The gene for ELP_4-30 was doubled in each round to create the -60, -120, and -240 mers (Figure 7A). The ELP_2 library was similarly recursively oligomerized starting with the gene encoding $(GXGVP)_{20}$ (ELP_2-20) to obtain the -40, -80, -160, and -320 mers after each round of PRe-RDL (Figure 7C). After the ELP_2 gene library was generated, an 'A' fragment of ELP_2-60 and a 'B' fragment of ELP_2-80 were then combined to generate ELP_2-240 to demonstrate how PRe-RDL can be used to generate intermediate length ELPs (lane 7, Figure 7C). The same approach can also be used to join together two different sequences to create more complex block copolymers. Following the synthesis of the ELP_2 gene library, the ELP_2 constructs selected for expression (ELP_2-80, -160, -240, and -320) were all modified with a leader sequence to demonstrate that PRe-RDL also enables attachment of a leader L_1, or a trailer, in a single round of cloning in order to increase yield.

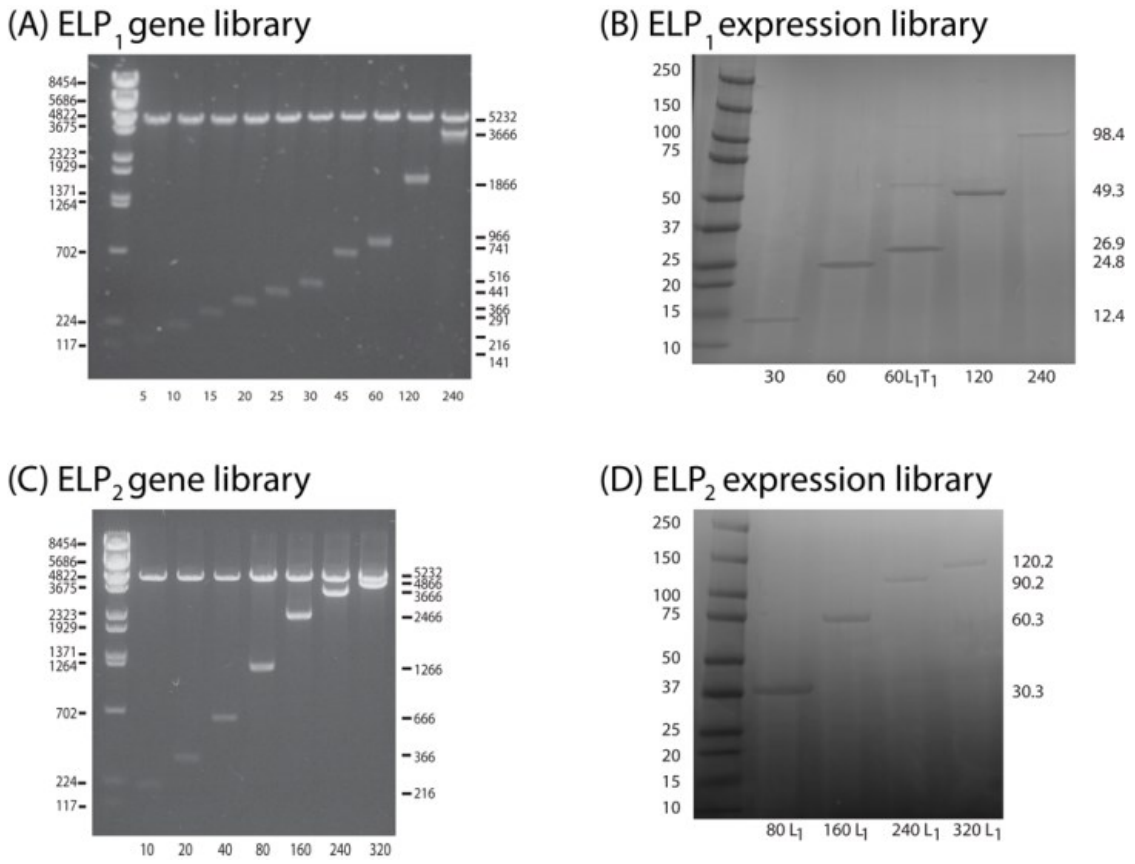

Figure 7: ELP_4 and ELP_2 libraries produced by PRe-RDL [153]. (A) ELP_4 gene library run on an agarose gel (1%). The left lane represents a size standard ladder, with sizes in base pairs shown on the left. Lanes 2-11 are diagnostic digests of each construct (restricted with XbaI and BamHI, which flank the ELP sequence with 66 bp), with the length shown on the right (in base pairs) and bottom (in pentapeptides). Lanes 2-8 were generated using concatemerization, while 9-11 were created using PRe-RDL. (B) ELP_4 expression library run on an SDS-PAGE gel. The left lane is the Bio-Rad Kaleidoscope™ Ladder, with lengths in kDa on the left. Lanes 2-6 show the expressed ELPs with the lengths shown on the right (in kDa) and bottom (in pentapeptides). The dimer in lane 4 (ELP_4-60 L_1T_1) is indicative of disulfide bonds formed between the cysteine residues present in T_1. (C) ELP_2 gene library run on an agarose gel. Lanes 2-3 were generated using concatemerization, whereas lanes 4-8 were formed via PRe-RDL. (D) ELP_2 expression library run on an SDS-PAGE gel. To increase expression yields, the ELP_2 library was modified with L_1 (MSKGPG) on the amino terminus [153].

2.2.4 Plasmid Reconstruction Enables the Facile Modular Addition of Leading and Trailing Peptides

In the modified PRe-RDL cloning plasmid, the default DNA leader and trailer sequences are restricted in length by RE_1 and RE_2 to 2 and 3 amino acid residues, respectively. While this length of leader and trailer peptide may be adequate for some applications, in many instances having the flexibility to append other, longer leader or trailer peptides with any arbitrary sequence of interest is desirable, as they can provide peptide sequences for targeting, encode other purification tags (*e.g.*, an oligohistidine tag) or provide unique reactive groups for site-specific conjugation of the polypeptide with drugs or imaging agents as is described in detail in the following chapters. To demonstrate the feasibility of appending an arbitrary leader and trailer peptide sequence (Figure 8), a leader plasmid (L_1) consisting of MSKGPG and a trailer plasmid (T_1) consisting of $G(CGG)_8WP$ were generated in separate cloning vectors, identical to the vector used in the ELP_4 library. DNA encoding these leader and trailer peptides were added to ELP_4-60 in a two-step process: (1) The 'A' fragment of L_1 was ligated to the 'B' fragment of the ELP_4-60, and (2) The 'A' fragment of the L_1 ELP_4-60 was ligated to the 'B' fragment of T_1, generating L_1ELP_4-60T_1. Once a desired length is reached, PRe-RDL can be used to add leaders and trailers of unrestricted length, although the addition of a leader or trailer prevents further seamless dimerization of the original monomer. However, this procedure enables the rapid generation of a library of leaders and a

library of trailers that can be used to systematically modify the 5′-and 3′-ends of the gene encoding a repetitive polypeptide once it has been assembled. For example, the ELP_2 constructs described in the following section (ELP_2 - 80, -160, -240, and -320) were modified with L_1 in a single round of cloning. While these modified constructs cannot be further dimerized with themselves in a seamless manner, each could be modified at its 3′-end, either with a library of trailers, or other compatible sequences lacking the 5′-modification.

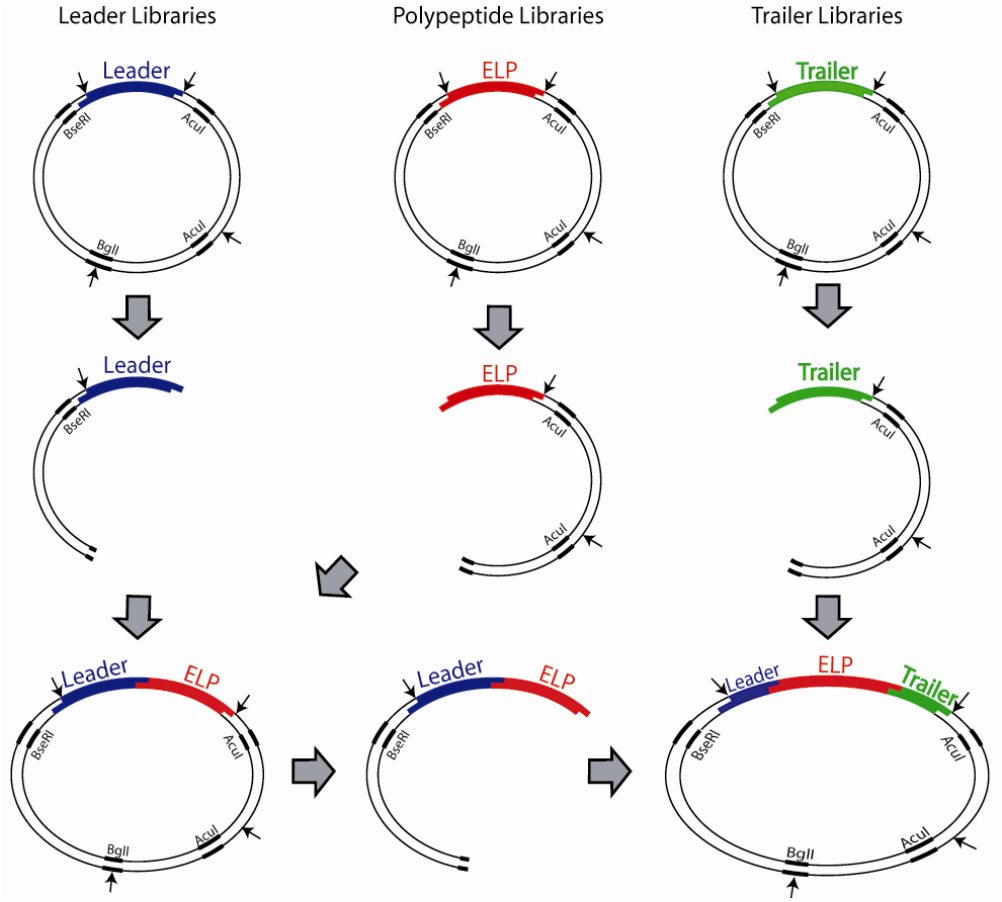

Figure 8: PRe-RDL is a modular design that allows for the combination of multiple libraries. This figure demonstrates the stepwise ligation of a leader to an ELP, and then the ligation of a trailer to the Leader-ELP fragment. The ligation order shown here is not essential; leaders were appended to the ELPs before incorporating the trailers, though the order could be reversed if needed [153].

2.3 Validation of the Elastin-like Polypeptide Library

To demonstrate that this method was capable of producing ELPs similar in both composition and physicochemical characteristics as previous recombinant strategies such as Recursive Directional Ligation, we designed two ELP libraries – one that has

been characterized extensively (ELP_4) and one new library (ELP_2) – and measured their molecular weight and thermal properties as follows. After validating the genes by DNA sequencing, each of the higher molecular weight ELPs from each library were transformed into BL21™ cells and expressed in 4 – 6 L of media each. The ELP was then purified by 3-5 rounds of inverse transition cycling (ITC), followed by overnight dialysis into distilled, deionized water and subsequent lyophilization. Each of the ELPs produced between 30 – 70 mg purified protein/L media, which was gravimetrically quantified. The size and purity of each of the expressed ELP_4 and ELP_2 specimens was visualized by SDS-PAGE (Figure 7B, 4D). Each of the ELPs ran approximately 20% higher than expected, which matches previously published data [83, 157]. To further verify the molecular weight of each of the constructs, ELPs < 240 pentapeptides in length were characterized by MALDI-MS (Table 11 in Appendix 8.4). The MWs of all ELPs determined by MALDI-MS were close to their calculated MWs, indicating that the gene oligomerization in PRe-RDL proceeded as expected.

The thermal behavior of both ELP libraries was then assessed by monitoring the turbidity of a solution of each ELP as a function of temperature. The linear dependence of the T_t on the log of concentration can be seen for ELP_4 in Figure 9A. The measured T_t's for the ELP_4 library were then compared with the fit generated for the same ELP sequence by Meyer and Chilkoti [158]. This fit (Equation 1) describes the T_t dependence of ELP in terms of the critical T_t (T_{tc}; °C), the critical concentration (C_c; μM), the length (L;

pentapeptides) of the sequence, the concentration of the ELP (Conc; μM), and k (°C), a proportionality constant (this equation will be discussed in more detail in the following chapter.)

(1) $$T_t = T_{tc} + \frac{k}{Length} \ln \frac{C_c}{Conc}$$

Despite the small sequence variation at the C-terminus (the ELP_4 library contains a Tyr trailer instead of the Trp-Pro trailer used in Meyer's work) the model very accurately predicts the measured transition temperatures (Figure 9A). The ELP_2 constructs were also characterized in PBS, but their T_t's were above 80°C, the highest measurable temperature on the temperature-controlled UV-vis spectrophotometer available for these studies. Their inverse transition behavior was hence analyzed in PBS + 1 M NaCl, which significantly depresses the T_t, allowing the thermally triggered transition behavior to be quantified in a temperature range that is experimentally accessible (Figure 9B). The T_t of ELP_2 in 1 M NaCl were not fit to Meyer's model as this model does not compensate for the depression in the T_t due to the addition of salt. Figure 9C also shows the T_t dependence on chain length at the given concentration of 25 μM for both ELP_4 in PBS, which also closely matches the data obtained by Meyer, and ELP_2 in 1 M NaCl.

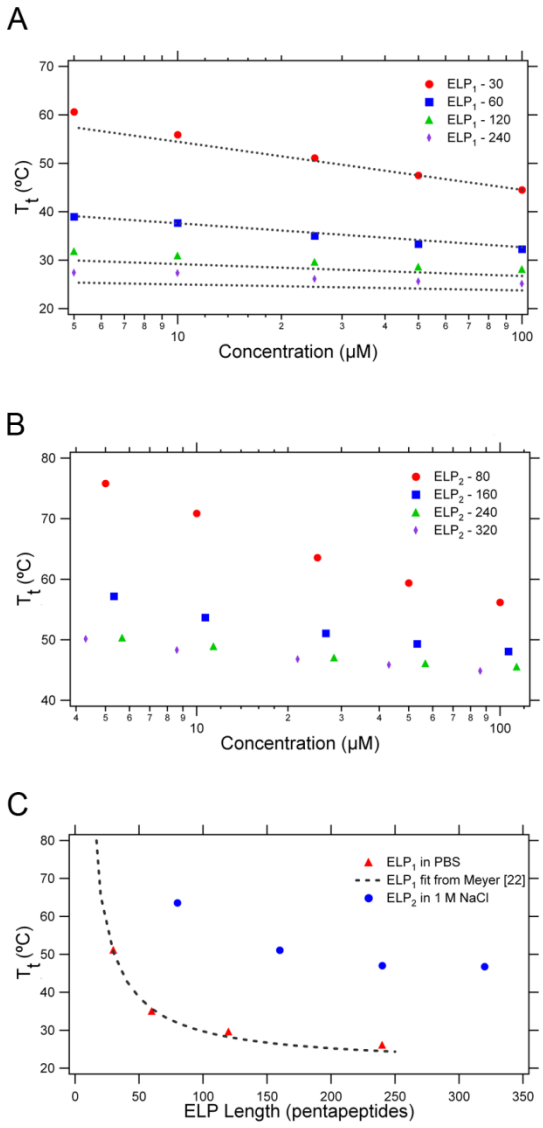

Figure 9: Thermal properties of the ELP$_4$ and ELP$_2$ series [153]. (A) ELP$_4$ T_t as a function of concentration and chain length. The dashed line represents the predicted T_t for each ELP$_4$ length based on Meyer and Chilkoti's model [158]. (B) ELP$_2$ T_t as a function of concentration and chain length in 1 M NaCl. The ELP$_2$ T_t was > 80˚C at these concentrations. 1 M NaCl was added to depress the T_t to demonstrate the presence of the thermal transition. (C) The ELP T_t as a function of chain length at a constant 25 μM ELP. ELP$_4$ is in a PBS solution, whereas ELP$_2$ is in 1 M NaCl in PBS. The dashed line represents the expected T_t for ELP$_4$ based on the model developed by Meyer and Chilkoti [158].

2.4 Advantages of Recursive Directional Ligation by Plasmid Reconstruction

The use of three restriction enzymes in PRe-RDL has the intrinsic benefit of reducing background by eliminating the possibility of self-ligation of the vector. This is possible because BglI (RE_3) is incompatible with both BseRI and AcuI, so that each half of the vector can only ligate to its complement, rather than itself. PRe-RDL also increases cloning efficiency by eliminating the possibility of circularization of the insert. It has been our experience that RDL [83] has a high yield (up to 80%) when dimerizing small inserts < 1000 bp. However, the efficiency rapidly drops to 5-30% when working with inserts over 1000 bp. An added inconvenience of RDL is that the cloning is performed in a high copy number plasmid that is not designed for expression, so that the insert must be transferred to an expression vector once it reaches the desired length. Because this final length is commonly 1500 - 2400 bp, this step can be tremendously rate limiting. In contrast, this issue is eliminated in PRe-RDL, because cloning is carried out in an expression vector. PRe-RDL has shown efficiencies of 80-100% for dimerizing inserts less than 1500 bp, which gradually drops to 20-50% as the insert length approaches 2400 bp. However, even with the longest oligomer (ELP_2-320, 4800 bp, 120 kDa), the final step of adding a leader was near 100%, suggesting that the reduced efficiency is limited to joining two large moieties.

PRe-RDL was motivated by the utility –and limitations– of RDL, and it also borrows from the work of Kempe *et al.* who used Type II palindromic endonucleases

[159] to recursively clone up to 64 repeats of the 11-mer peptide substance P, and Lewis *et al*. [160] who also used Type II palindromic endonucleases to recursively synthesize genes consisting up to 32 repeats of spider silk protein [147]. Both Kempe and Lewis used the similar strategy of compatible but nonregenerating restriction sites to ligate two halves of a parent vector, each containing the oligomer, to reconstitute the plasmid and thereby double the oligomer length. This method allowed for recursion because as the oligomers were ligated together, the restriction site internal to the oligomer was abolished. Although these methods displayed the low background inherent in PRe-RDL, each was also restricted to sequences compatible with the selected palindromic endonuclease restriction sites, making each not generalizable to any arbitrary peptide repeat. Lee *et. al* used the unique asymmetric cutting characteristics of type IIs endonucleases to eliminate sequence constraints to oligomerize a gene encoding the antimicrobial peptide, magainin, in an iterative strategy based upon multiple concatemerization reactions, although the use of 4 bp overhangs resulted in a 4 bp seam between each monomer [148]. Ståhl *et al*. also capitalized on the asymmetry of type IIs endonucleases to build a polypeptide comprised of two different concatemerized sequences, each derived from malaria blood-stage antigen [150]. In a design similar to our own plasmid, they eliminate extraneous amino acid residues from the N- and C-terminus as well as the junction between inserts. Our work combines the advantages of these methodologies by using type IIs endonucleases to allow for directional head-to-tail

oligomerization of the gene encoding any peptide of interest, with no extraneous peptides encoded at the junction between two repeats, while maintaining the ability to encode a biopolymer of a predetermined length. The plasmid reconstruction strategy also greatly increases cloning efficiency, significantly decreases background, and limits self-ligation of the insert, thereby increasing the efficiency of cloning by reducing the loss of the insert in an unproductive side-reaction.

2.5 Conclusions

This chapter presents a straightforward and general method to rapidly produce repetitive polypeptides of any desired sequence and length over a wide range of molecular weights, which proved valuable in the generation of new ELP libraries described in later chapters. The key to this approach is to use type IIs restriction enzymes to produce seamless, head-to-tail repeats of any arbitrary DNA sequence by a process that requires reconstitution of the plasmid in every oligomerization step, while avoiding the problems of poor ligation efficiency and high background that limit RDL. Carrying out PRe-RDL with an initial concatemerization step in an expression vector permitted the gene assembly of two ELP libraries up to 4800 bp in length with 3-4 fewer steps than required by conventional RDL. With a dimerization efficiency of 80-100%, PRe-RDL is also enormously efficient compared to RDL, thereby largely simplifying the screening process at each cloning step. This system is also flexible in that the genes for

other, non-repetitive peptide sequences can be appended at the two ends of the gene, which allows leader and trailer peptide sequences with unique functional groups to be incorporated at the two ends of a repetitive polypeptide. This modular strategy is used in later chapters to generate new CP libraries by the C-terminal fusion of short $(CGG)_8$ peptides.

2.6 Materials and Methods

2.6.1 Materials

Restriction enzymes and calf intestinal phosphatase (CIP) were purchased from New England Biolabs (Ipswich, MA). T4 DNA ligase was purchased from Invitrogen (Carlsbad, CA). The pET-24a+ cloning vector was obtained from Novagen Inc. (Madison, WI), and all custom oligonucleotides were synthesized by Integrated DNA Technologies Inc. (Coralville, IA). Top10™ cells were purchased from Invitrogen (Carlsbad, CA) and BL21™ *E. coli* cells were purchased from Novagen (Madison, WI). All *E. coli* cultures were grown in TBDry™ media purchased from MO BIO Laboratories, Inc (Carlsbad, CA). The DNA miniprep, gel purification, and PCR purification kits were purchased from Qiagen Inc. (Germantown, MD).

2.6.2 Methods

2.6.2.1 Modification of pET-24(+) for PRe-RDL

1.5 μg of the pET-24a(+) vector was digested with 20 U of XbaI and 20 U of BamHI in NEB buffer 3 for 4 h at 37°C. The 5′ ends were dephosphorylated with 1 U CIP for 1 h at 37°C, and the vector was then purified using the Qiagen PCR purification kit. The linearized vector was eluted in 30 μL of distilled, deionized water. Two oligonucleotides were designed: 5′ctagaaataattttgtttaactttaagaagGAGGAGtacatatgg gctactgataatgatCTTCAG -3 ′ and 5′- gatcCTGAAGatcattatcagtagcccatatgtaCTCCTC cttcttaaagttaaacaaaattattt – 3′. This DNA sequence was designed to encode two new endonuclease restriction sites for BseRI and AcuI (shown in capitalized letters), as well as a short leader sequence (Met) and trailer sequence (Tyr – Stop – Stop). The BseRI site was incorporated into the Shine-Delgarno ribosomal binding site adjacent to the start codon (underlined). The two oligonucleotides were annealed by heating each oligonucleotide (50 μL at 2 μM concentration) in T4 DNA ligase buffer to 95°C for 2 min, then slowly cooling the solution to room temperature over 3 h. This resulted in a double stranded (ds) DNA with XbaI and BamHI compatible sticky ends. Ligation of the modified cloning insert into the multiple cloning site within pET 24a(+) was carried out by incubating 20 pmol of the annealed dsDNA with 0.1 pmol of the linearized vector with 400 U of T4 DNA ligase at 20°C for 1 h in T4 DNA ligase buffer. The product was transformed into Top10™ chemically competent cells, which were allowed to recover for 1 h at 37°C in Luria broth. The cells were then plated on TBdry™ plates that were

supplemented with 45 μg/mL of kanamycin. The sequence was then confirmed by DNA sequencing.

2.6.2.2 Monomer Gene Synthesis

A synthetic gene that encodes the $(GVGVP)_5$ peptide sequence for ELP_4 was synthesized as two 75 nt long single stranded oligonucleotides that encoded for the sense and antisense strands of the gene. The two oligonucleotides were annealed by heating each oligonucleotide (50 μL at 2 μM concentration) in T4 DNA ligase buffer to 95°C for 2 min, then slowly cooling the solution to room temperature over 3 h. This resulted in a double stranded (ds) DNA with nonpalindromic, 2 bp, 3′ overhangs. The same procedure was used to anneal the two 150 nt long, single stranded oligonucleotides that encoded the $(GXGVP)_{10}$ peptide sequence for ELP_2, where X alternates between the amino acids A and G in a 1:1 ratio.

2.6.2.3 Concatemerization

1.5 μg of the pET 24a(+) modified cloning vector was digested with 2 U of BseRI for 16 h at 37°C. The 5′ ends were dephosphorylated with 1 U CIP for 1 h at 37°C, and the vector was then purified using the Qiagen PCR purification kit. The linearized vector was eluted in 30 μL of distilled, deionized water. Ligation of concatemers was carried out by incubating 20 pmol of the annealed dsDNA with 0.1 pmol of the linearized vector with 400 U of T4 DNA ligase at 20°C for 1 h in T4 DNA ligase buffer. The product was transformed into Top10™ chemically competent cells, which were allowed to recover for

1 h at 37°C in Luria broth. The cells were then plated on TBdry™ plates that were supplemented with 45 μg/mL of kanamycin. A detailed procedure is shown in Appendix 8.9.1.

2.6.2.4 Gene Oligomerization by PRe-RDL

PRe-RDL was used to recursively double the ELP_4 gene that encodes $(GVGVP)_{30}$ and the ELP_2 gene that encodes $(GXGVP)_{20}$ where X = A and G in a 1:1 ratio, which were obtained after a single round of concatemerization. Using the dimerization of the 30 repeat fragment of ELP_4 in the second round of PRe-RDL as an example, the designated 'A' fragment was obtained by digestion of 4 μg of ELP_4-30 with 10 U AcuI and 40 U BglI for 3 h at 37°C (see Figure 6A) in NEB Buffer 2 (New England Biolabs; Ipswich, MA). The 'B' fragment was obtained by digestion of 4 μg of ELP_4-30 with 8 U BseRI and 40 U BglI for 3 h at 37°C in NEB Buffer 2. Both DNA digests were run on a low melting point agarose gel. The 'A' digestion resulted in 3 bands: 1586 bp, 1821 bp, and a 2341 bp (1891 + ELP) fragment. The 2341 bp band was excised from the gel and purified with Qiagen's gel purification kit. The 'B' digestion resulted in 2 bands: 1891 bp, and a 3857 (3407 + ELP) fragment, and the 3857 bp band was excised from the gel, purified, and eluted in 30 μL of distilled, deionized water. Equimolar amounts of the A and B fragments at a total DNA concentration of 5 ng/μL in a volume of 20 μL were ligated by incubation with T4 DNA ligase at 20°C for 1 h. Top10™ chemically competent cells were transformed with the ligation product, as described previously. *Escherichia coli*

transformants were screened by colony PCR and by diagnostic restriction digests on an agarose gel. Each sequence was then confirmed by DNA sequencing. A detailed procedure is included in Appendix 8.9.1.

2.6.2.5 Cloning of Leader and Trailer Sequences

A plasmid containing a leader sequence and a plasmid containing a trailer sequence were also constructed. The gene segment encoding a $(CGG)_8$WP trailer (T_1) was created by annealing two chemically synthesized oligonucleotides that encode this peptide sequence, as described previously (Monomer gene synthesis). The annealed oligonucleotides were inserted into the linearized pET 24a(+) expression vector using the same preparation protocol and insert to vector ratios as provided in the Concatemerization section. The DNA segment encoding a MSKGPG leader (L_1) was similarly synthesized by annealing two oligonucleotides, which provide the 'TA' and 'CC' overhangs that are compatible with NdeI and BseRI (Figure 6E). Because the NdeI restriction site is between the BseRI recognition sequence and BseRI cleavage site, 1.5 μg vector was first digested with 8 U BseRI for 2 h at 37°C in NEB Buffer 2. 60 U NdeI was then added, and the sample was incubated at 37°C for an additional 1 h. The linearized vector was purified using a Qiagen PCR purification kit, and eluted in 30 μL distilled, deionized water. Annealing of the oligonucleotides encoding L_1 to yield a dsDNA cassette, the insertion of the cassette into the linearized vector, and transformation of the plasmid into *Escherichia coli*, proceeded as described above. Colonies were screened by a

diagnostic restriction endonuclease digestion using XbaI and BamHI and agarose gel electrophoresis, and the sequence of positive clones were confirmed by DNA sequencing.

The ligation of the plasmid encoding L_1 to the ELP proceeded in a manner similar to a typical dimerization step in PRe-RDL. The construction of the ELP_4-60 L_1T_1 oligomer is shown in Figure 8 to illustrate the modular process by which a leader or trailer gene sequence can be appended to the 5′- and 3′-end of the oligomerized gene that encode for peptide sequences that are distinct from the repetitive polypeptide. The plasmid containing the gene encoding L_1 was subjected to an 'A' digestion (AcuI and BglI), resulting in 3 bands: 1586 bp, 1821 bp, and 1903 bp (1891 + leader), and the 1903 bp band was excised and purified, as previously described. The ELP_4-60 construct was subjected to a 'B' digestion (BseRI and BglI), resulting in the 2 bands: 1891 bp and a 4307 bp (3407 + ELP_4-60) fragment. These two fragments were ligated together under the previously described conditions, thereby joining the leader fragment to the N-terminus of ELP_4-60 and reforming the parent plasmid. The colonies were then screened via diagnostic digest and sequenced. The plasmid containing the gene for T_1 was then subjected to a 'B' digestion, resulting in 2 bands: 1891 bp and 3476 bp (3407 + trailer), and the 3476 band was excised and purified. The L_1 ELP_4-60 construct from the previous step was then subjected to an 'A' digestion, resulting in three bands: 1586 bp, 1821 bp, and 2803 bp (1891 + L_1 ELP_4-60), of which the 2803 band was excised and purified. The

two purified fragments were ligated together, which ligated the T_1 encoding DNA fragment at the 3'-end of the gene encoding L_1 ELP_4-60, forming L_1 ELP_4-60 T_1. *E. coli* transformants were screened by colony PCR, followed by a diagnostic restriction digest, and positive clones were confirmed by DNA sequencing.

2.6.2.6 Expression of Elastin-like Polypeptides

100 ng of plasmid DNA was transformed into chemically competent *Escherichia coli* BL21™ cells (Novagen; Carlsbad, CA), and used to inoculate a 250 mL flask containing 50 mL TBdry™ media supplemented with 45 μg/mL kanamycin. The cultures were incubated on a shaker at 200 rpm overnight at 37°C. This starter culture was then used to inoculate 4 L flasks containing 1 L of TBdry media with 45 μg/mL kanamycin. The flasks were incubated on a shaker at 200 rpm for 24 h at 37°C. This "hyperexpression" expression protocol relies upon the leakiness of the T7 promoter to express the ELP [161].

2.6.2.7 Purification of Elastin-like Polypeptides

After a 24 h incubation period, the cells were centrifuged at 3000 g for 15 min in 1 L bottles. The cell pellet was resuspended in 10 mL of PBS, and the cells were lysed by 54 cycles of sonication for 10 s separated by 20 s intervals (Sonicator 3000, Misonix, Farmingdale, NY) on ice. 0.7% w/v polyethyleneamine (PEI) was added to the cell lysate to precipitate nucleic acid contaminants. The ELP was then purified by inverse transition cycling (ITC) as follows: the cell lysate was centrifuged in a 30 mL round bottom tube at

11,000 g for 10 min at 4°C to precipitate the insoluble fraction of cell lysate. The supernatant, containing soluble ELP, was then transferred to a new 30 mL round bottom tube and heated to 37°C. For ELP_2, which has a higher transition temperature, up to 3 M salt was added to trigger the phase transition at 37°C. Once the solution became turbid, it was centrifuged at 11,000 g for 10 min at 37°C to precipitate aggregated, insoluble ELP. The supernatant was decanted and the pellet was resuspended in 10 mL of cold, low ionic strength buffer (PBS). Typically, 3-5 rounds of ITC were enough to attain > 95% purity, as assessed by SDS-PAGE.

2.6.2.8 Physicochemical Characterization of Elastin-like Polypeptides

The purified ELP constructs were characterized with SDS-PAGE, matrix-assisted laser desorption/ionization mass spectrometry (MALDI-MS) and UV-vis spectrophotometry. The ELP concentration was determined by UV-vis spectrophotometry (Nanodrop, Thermo Scientific, Waltham, MA) using the extinction coefficient of tyrosine at 280 nm (1285 $M^{-1}cm^{-1}$) or tryptophan at 280 nm (5630 $M^{-1}cm^{-1}$). The purity of the ELPs was determined by SDS-PAGE, using 4-20% Tris-HCl Ready Gels™ (Bio-Rad, Hercules, CA), which were stained with copper chloride. MALDI-MS was performed on a PE Biosystems Voyager-DE instrument equipped with a nitrogen laser (337 nm). The MALDI-MS samples were prepared in a 50% (v/v) aqueous – acetonitrile solution, containing 0.1% trifluoroacetic acid, using a sinapinic acid matrix. To characterize the inverse transition temperature (T_t) of the ELPs, the optical density at

350 nm (OD_{350}) of ELP solutions were measured as a function of temperature on a UV-visible spectrophotometer equipped with a multicell thermoelectric temperature controller (Cary 300, Varian Instruments, Walnut Creek, CA) as follows: an ELP solution in PBS, at concentrations between 1 – 100 μM, was heated from 20°C to 80°C at a rate of 1°C/min. The T_t was defined as the temperature that corresponds to the maximum of the first derivative of its turbidity profile with respect to temperature, which is indicative of the onset of the phase transition.

3. Self-Assembly of Thermoresponsive Elastin-like Polypeptide Nanoparticles by Drug Conjugation

3.1 Objectives and Motivation

Most small molecule therapeutics utilized in the clinic have poor bioavailability and suboptimal pharmacokinetics because of their hydrophobicity and low molecular weight. Engineered drug delivery vehicles seek to improve the efficacy of these therapeutics by increasing their solubility, extending their plasma half-life, increasing the amount of drug deposited in the desired tissue, and decreasing their exposure to healthy tissues [41]. Repackaging hydrophobic drugs by sequestering them within the core of soluble polymeric nanoparticles can overcome these limitations by increasing drug solubility; the appropriate choice of polymer can also lead to long *in vivo* circulation and improved tissue distribution as compared to the free drug [41, 88, 162, 163]. Furthermore, the choice of stimulus responsive polymers as the carrier suggests the intriguing possibility of endowing these nanoparticles with thermal responsiveness in the clinically relevant temperature range of 37-43°C that would allow them to be targeted *in vivo* to a site of disease by externally applied, focused mild hyperthermia.

The launching point of our attempt to rationally design drug-loaded, thermally targeted nanoparticles was our recent observation that the site-specific (C-terminal), covalent attachment of multiple copies of doxorubicin –a small molecule chemotherapeutic– to a chimeric polypeptide (CP) resulted in the formation of near-monodisperse micelles [88]. Chimeric polypeptides are comprised of two components: a

high molecular weight elastin-like polypeptide which imparts solubility and thermosensitivity to the system and a short cysteine-rich motif appended to the C-terminus of the ELP that provides eight unique drug attachment sites. The observation that the attachment of doxorubicin to the CP initiated micelle assembly prompted three questions that provided the roadmap for this chapter: (1) is the conjugation triggered self-assembly of a CP observed in the previous study restricted to a small set of compounds or does it reflect a more general propensity of CPs to undergo self-assembly upon conjugation to small molecules? (2) If this is indeed a general phenomenon, what is the mechanism that drives their self-assembly? (3) If we can uncover the rules that drive self-assembly, can we use this information to rationally design drug-loaded nanoparticles that also exhibit thermal responsiveness in the clinically relevant temperature range of 37-42°C under physiologically relevant conditions?

3.2 Formation of Chimeric Polypeptide Amphiphiles by Chemical Conjugation

To explore these questions, 14 different maleimide derivatives of small molecules spanning a large range of hydrophobicity were covalently attached to a CP (Figure 10A). These model compounds were chosen with two considerations in mind: first, they display a range of hydrophobicity, as reflected by their octanol-water distribution coefficient, Log(D) [164]. Log(D) is a common measure in the pharmaceutical industry to describe the solubility of a compound, and is defined as the ratio of the concentration of

the therapeutic in octanol to the concentration in an aqueous buffer (pH 7.4) following extensive mixing. Second, they all contain a reactive maleimide moiety so that they could be covalently coupled to the CP. The CP used in this study consists of two segments: a hydrophilic, biodegradable elastin-like polypeptide (ELP) segment with a MW of 62 kDa, and a short, 1.6 kDa cysteine-rich Cys(Gly-Gly-Cys)$_7$ segment that provides eight thiol groups for conjugation of the maleimide derivatives (Figure 10A).

The CP was overexpressed from a plasmid-borne gene in *Escherichia coli* and was purified by a nonchromatographic method, inverse transition cycling [84, 85]. The model compounds with Log(D) values ranging from -1 to 4 were selectively conjugated to the Cys residues in the CP by a Michael addition reaction. Figure 10B displays the structure of the model compounds, as defined by their Log(D) at pH 7.4, where higher

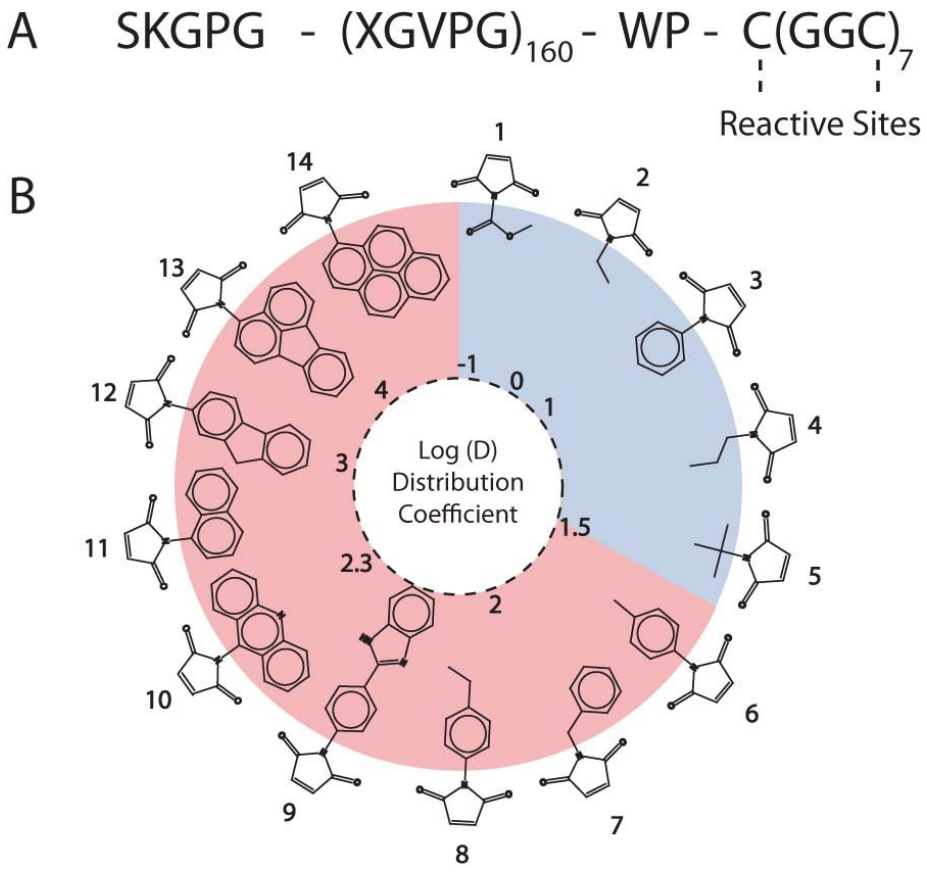

Figure 10: (A) Sequence of the chimeric polypeptide. The 62 kDa ELP segment of the CP consists of 160 repeats of VPGXG with the guest residue X having the composition $Val_1Gly_7Ala_8$. The 1.6 kDa cysteine-rich sequence at the C-terminus provides sites for covalent conjugation of maleimide derivatives of model compounds. (B) Structure of the model compounds. The circle represents a visual map of the model compounds and their hydrophobicity as measured by the distribution coefficient at pH 7.4. The attachment of compounds with a Log(D) ≤ 1.5 (shown in blue) did not trigger self-assembly of the CP, whereas compounds with a Log(D) > 1.5 (shown in pink) triggered the CP to self-assemble into nanoparticles [77].

values indicate greater hydrophobicity. The Log(D) was calculated with the ACD Labs/PhysChem Suite [50], which fragments a molecule into non-overlapping structures. The Log(D) value is then calculated through a summation of the hydrophobicities of the

individual components and their correction factors [164, 165]. Following attachment, the degree of conjugation was assessed by measuring the ratio of free, residual cysteine residues, quantified with Ellman's reagent, and the polypeptide concentration, measured by the bicinchoninic acid assay, and ranged from 3.3 – 6.4 for all of the molecules, as listed in Table 15 in Appendix 8.7.

3.3 Physicochemical Characterization of the Formed Amphiphiles

Next, the spontaneous self-assembly of the conjugates were investigated by dynamic and static light scattering (DLS, SLS), temperature-programmed turbidimetry, and fluorescence spectroscopy.

3.3.1 Dynamic and Static Light Scattering

The attachment of 3-6 copies of compounds with a Log (D) < 1.5 (shown in blue in Figure 10B) did not trigger self-assembly of the CP, whereas compounds with a Log(D) > 1.5 (shown in pink) imparted sufficient amphiphilicity to the CP to trigger their self-assembly into nanoparticles with the conjugated molecules presumably comprising the hydrophobic core. The conjugates that did not trigger self-assembly had an average hydrodynamic radius (R_h) of 5.9 ± 0.7 nm, which was similar to the R_h of the unmodified, control CP. In contrast, the conjugates that formed nanoparticles had an R_h ranging from 30 nm to 58 nm, with an average standard deviation of ~15% within each population

(Figure 11B). There was no correlation between the hydrodynamic size of the nanoparticles and the number of molecules conjugated per CP ($r^2 = 0.0009$).

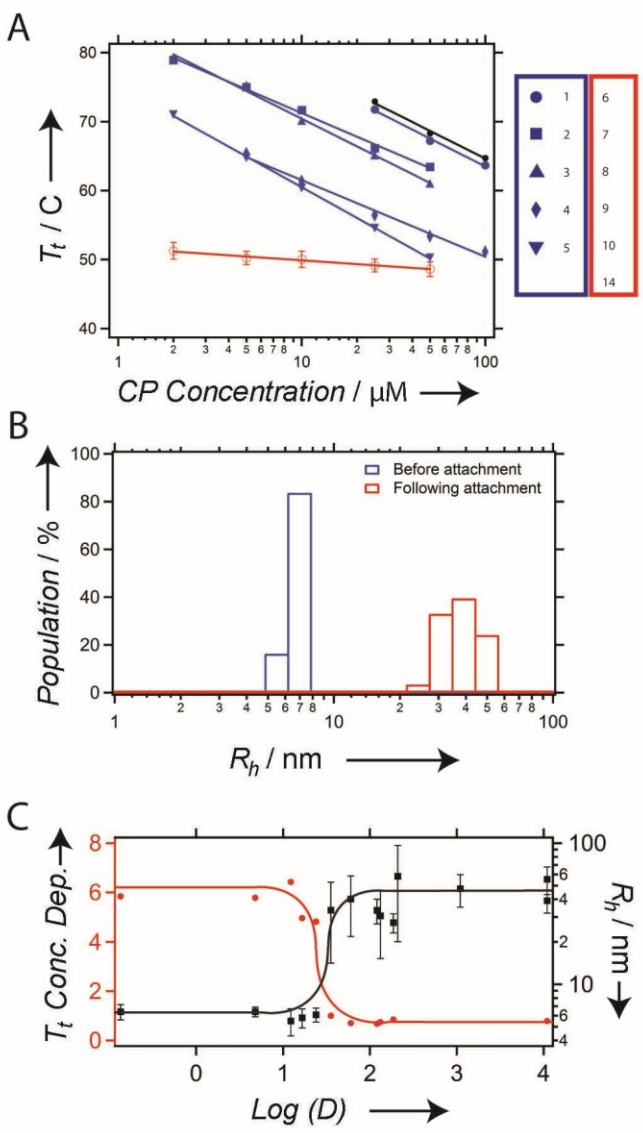

Figure 11: Physical properties of CP nanoparticles. (A) CP thermal characterization. Transition temperature (T_t) as a function of CP concentration of CPs conjugated to hydrophilic compounds (blue; unimer; compounds 1-5), and hydrophobic compounds (red; nanoparticle; compounds 6-10, 14) compared with an unconjugated control (black; unimer). The thermal behavior of all 6 CP-small molecule conjugates that formed nanoparticles was identical, and is hence plotted together as the mean of the

T_t of each of the CP-small molecule conjugate, and the error bars are the standard deviation. The lines are linear fits to the data. (B) DLS results of the CP-conjugate of compound 8 with a Log(D) of 2.1, which shows the increase in R_h from ~6 nm corresponding to unimers prior to conjugation to the formation of nanoparticles with a R_h of ~33 nm after conjugation. (C) Relationship between the T_t (left Y-axis, data in red) and R_h (right Y-axis, data in black) as a function of Log(D) for all 14 conjugates. As the Log(D) increases to greater than 1.5, the particle R_h increases from the unimer size of 6 nm to nanoparticles with an R_h of 30 – 55 nm for different conjugates. The concentration dependence of the T_t (slope from A) decreases from an average value of -5.5 to -1.0°C/Log(concentration). The curves in (C) are solely a guide to the eye [77].

Each nanoparticle-forming conjugate was next analyzed by SLS to determine the number of CPs per nanoparticle and the shape factor ($\rho = R_g/R_h$) that describes the distribution of mass within the nanoparticle. The shape factors ranged from 0.69 to 1, indicating that there is likely a significant difference in the morphology of some of these nanoparticles. The precise attribution of the morphology of nanoparticles by light scattering is subject to some ambiguity, as the shape factor is subject to deviations arising from polydispersity and shape diversity within the ensemble of nanoparticles. Shape factors of 0.775 are indicative of spherical micelles, which is likely to be the case for nanoparticles with ρ values in the 0.69 to 0.8 range, while nanoparticles with shape factors of ~1.0 could instead be vesicles, as spherical shells have a ρ of 1.0, or polydisperse rods with relatively low aspect ratios [166]. The apparent coordination number (Z) also varied significantly, ranging from ~10-60 for the different conjugates. We note that the apparent coordination numbers were not corrected for the critical aggregation concentration (CAC) of the nanoparticles, which suggests that the numbers

shown in Figure 15 are the minimum coordination numbers for each nanoparticle. There was a trend toward larger apparent coordination numbers as the hydrophobicity of the conjugated molecules increased (Figure 15).

3.3.2 Cryogenic Transmission Electron Microscopy

To directly visualize the morphology and shape diversity of the nanoparticles, selected conjugates were imaged via cryogenic transmission electron microscopy (cryo-TEM). The samples were imaged at 80 keV to increase the contrast between the environment and the nanoparticle core, which exhibited a relatively high aqueous content. Figure 12 shows that the conjugates with a Log(D) > 1.5 formed nanoparticle cores distributed throughout the ice at regular intervals (Figure 12B-F) whereas the one hydrophilic conjugate displayed a film devoid of any structures (Figure 12A). In agreement with the light scattering data, the selected conjugates primarily consisted of spherical nanoparticles, though there were subpopulations of worm-like micelles and stiff rods present in a few of the samples (Figure 13) that may explain the variability of the shape factor measured by light scattering.

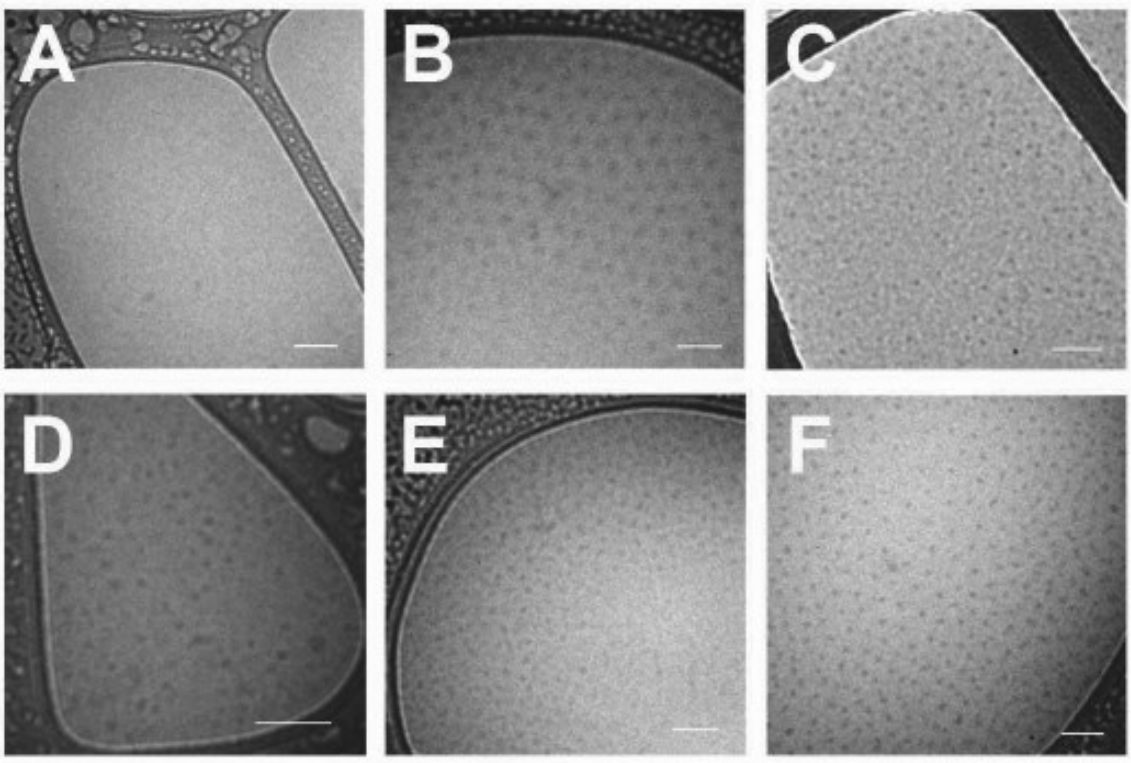

Figure 12: Cryo-TEM. CP conjugates were imaged via cryo-TEM in phosphate buffered saline. (A) N-methoxycarbonylmaleimide (Compound 1) did not form nanoparticles and is displayed as a negative control. The remaining conjugates spontaneously formed nanoparticles: (B) n-benzylmaleimide (Compound 7); (C) n-[4-(2-benzimidazolyl)phenyl]maleimide (Compound 9); (D) 2-maleimido fluorene (Compound 12); (E) n-(1-pyrenyl)maleimide (Compound 14); and (F) paclitaxel. Scale bars represent 100 nm [77].

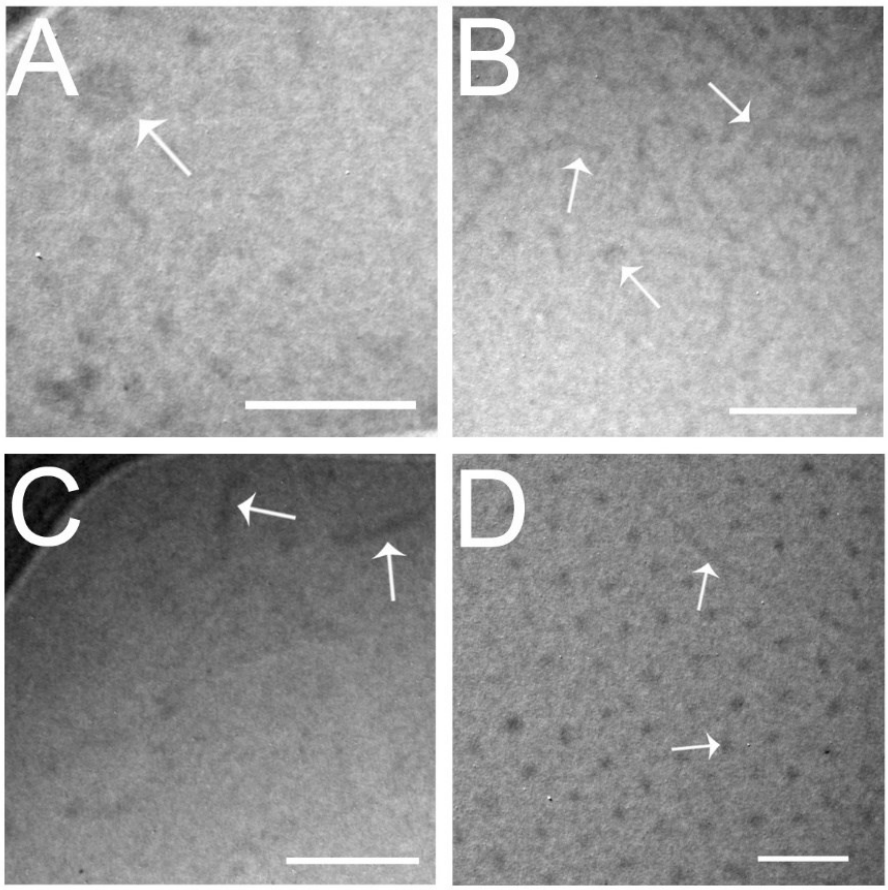

Figure 13: Cryo-TEM of trace amounts of non-spherical morphologies. (A-B) Arrows indicate both spherical (large and small) and worm-like nanoparticles present within the n-acridinylmaleimide sample. (C) The 2-maleimidofluorene sample contained rod-like morphologies. (D) CP-Paclitaxel included both spherical and worm-like micelles. The scale bars represent 100 nm [77].

3.3.3 Fluorescence Spectrophotometry

Four of the conjugates that formed nanoparticles were further characterized by fluorescence spectroscopy using pyrene as a probe of the local hydrophobicity, which enables measurement of the critical aggregation concentration (CAC) of self-assembled

nanoparticles [167]. For each conjugate, the ratio of the first fluorescence emission peak ($I_{370-373}$) and the third peak ($I_{381-384}$) were plotted over a range of CP concentrations (Figure 14). The ratio smoothly transitioned from a low value indicating a lipophilic environment into which the pyrene can partition (I_1/I_3 = 1.35 – 1.45) at higher polymer concentrations to ~1.87 at lower polymer concentrations, a ratio indicative of disassembly and the release of pyrene into water (Figure 14B). This two-state transition indicates the disassembly of the nanoparticle upon reducing the concentration below the CAC. The sigmoid of best fit was used to calculate the CAC, defined as the inflection point of the curve. For an unmodified CP, the ratio remained independent of polymer concentration consistent with the absence of a lipophilic compartment, indicating the lack of self-assembly even at higher concentrations of the CP (Figure 14C). The CAC ranged from ~1-30 μM for the different nanoparticles, and higher Log(D) values were associated with a lower CAC (Figure 14D), and thus higher stability, which qualitatively scales with their hydrophobicity.

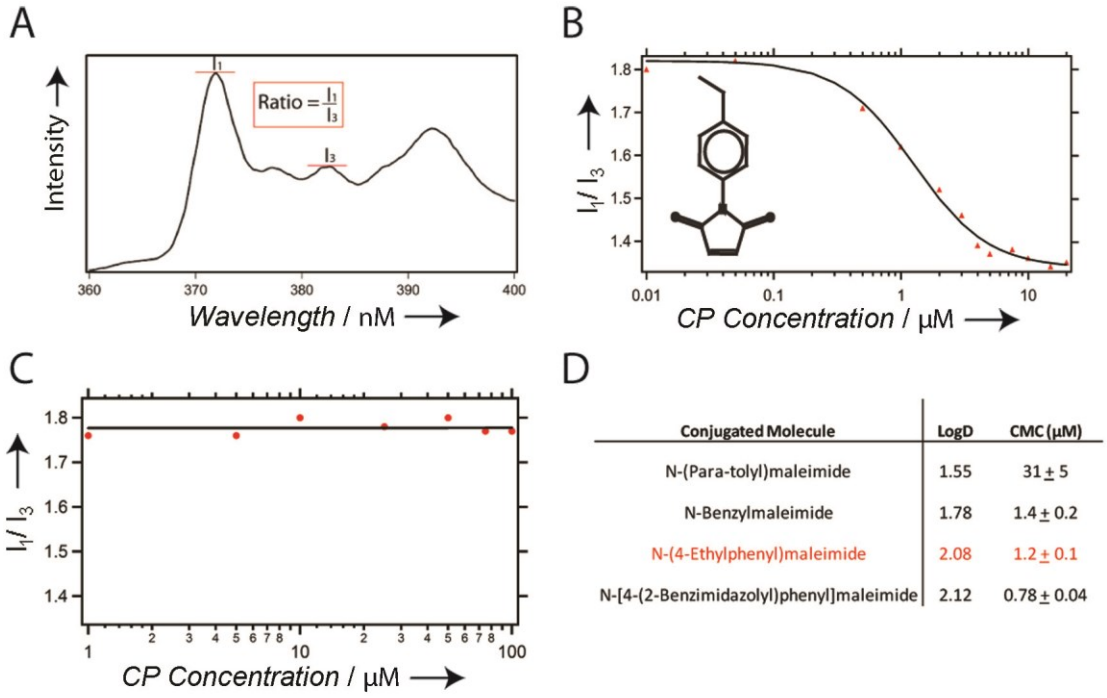

Conjugated Molecule	LogD	CMC (µM)
N-(Para-tolyl)maleimide	1.55	31 ± 5
N-Benzylmaleimide	1.78	1.4 ± 0.2
N-(4-Ethylphenyl)maleimide	2.08	1.2 ± 0.1
N-[4-(2-Benzimidazolyl)phenyl]maleimide	2.12	0.78 ± 0.04

Figure 14: Fluorescence spectroscopy. (A) Pyrene fluorescence in water. (B) Pyrene fluorescence of a CP conjugate of N-(4-ethylphenyl)maleimide (compound 8) as a function of CP concentration in water. (C) Pyrene fluorescence as a function of concentration of unconjugated CP (control) in water. (D) Table showing the Log(D) of the conjugated molecule and the critical micelle concentration (CMC) of the CP nanoparticle conjugates calculated from the pyrene fluorescence assay for each conjugate [77].

3.4 Self-Assembly Alters the Phase Transition Temperature

These data clearly demonstrate that CPs can be driven to assemble by conjugation to a diverse range of hydrophobic small molecules. These results are also notable because they clearly reveal a simple predictive rule that governs the self-assembly of CPs based on a threshold hydrophobicity of the conjugated small molecule.

Although the threshold of Log(D) > 1.5 predicts whether self-assembly will occur, the Log(D) of the conjugated molecule does not predict the size or shape of the nanoparticle that is formed, as we observed significant differences in both parameters based on the light scattering results that are likely related to structural differences between these molecules.

We also found that the phase transition behavior of the CP was altered following conjugation of the model compounds (Figure 11A). CPs, similar to the ELPs from which they are derived, display a characteristic transition temperature (T_t), below which they are soluble in aqueous solutions, and above which they form polydisperse micron-sized aggregates. This T_t is typically modulated by varying the hydrophobicity of the guest residue (X), with hydrophobic guest residues depressing the T_t, and hydrophilic residues elevating the T_t [168]. In a similar manner, as the hydrophobicity of the conjugated molecules increased to the assembly threshold as defined by Log(D) = 1.5, the T_t shifted downward, though the dependence upon concentration (the slope) remained uniform (Figure 11A). Upon reaching this threshold, however, the T_t was immediately reduced to a temperature that was near-independent of concentration, though we note that this transition occurs from a nanoparticle to micron-sized aggregates in contrast to unmodified CPs, which undergo a transition from soluble unimers to micron-sized aggregates. Notably, all conjugates that form nanoparticles display the same thermal behavior that is described by the same quantitative

relationship between the T_t and unimer CP concentration. The fact that all self-assembled CP nanoparticles display the same functional relationship between their T_t and their solution concentration (on a unimer basis) strongly suggests that their phase behavior is controlled by the high and invariant local CP concentration within the nanoparticles and not by the total concentration of the CP in solution.

This finding is significant because this near-independence of T_t from CP concentration enables the nanoparticles to maintain a very stable T_t (within 2°C) over a 100-fold decrease in concentration that would arise from physiological effects such as clearance from circulation. In contrast, the CP conjugates and the unmodified CP that exist as unimers show a T_t shift of over 20°C within the same concentration range (Figure 11A). The ability of these thermoresponsive nanoparticles to maintain a constant thermal response over a range of concentration eliminates the need to compensate for the effect of dilution and clearance that would occur upon their injection into systemic circulation and is hence likely to be an extraordinarily useful feature in future attempts to thermally target these CP nanoparticles to specific tissues *in vivo* by the application of external focused hyperthermia to disease sites.

3.5 Hydrophobicity as a Predictor of Assembly

These experiments with model compounds provide a simple physical model for self-assembly, in that molecules with a Log(D) > 1.5 will drive self-assembly of the

conjugate into nanoparticles. To further investigate the predictive validity of this model, three small molecule therapeutics were selected for conjugation to the CP through heterobifunctional linkers, where one end of the linker was attached to the CP and the other end to a reactive moiety on the drug. We chose three drugs that spanned a range of LogD at pH 7.4, estimated by ACD Labs/PhysChem Suite [50]: gemcitabine (-2.2), oxycodone (1.2), and paclitaxel (4.0). Conjugation of gemcitabine and oxycodone did not trigger self-assembly of the CP, while paclitaxel conjugation led to the spontaneous formation of nanoparticles that were similar in size to the nanoparticles that self-assembled by the attachment of hydrophobic small molecules to the CP (Table 2 and Figure 15). Conjugation of paclitaxel to the hydrophilic CP also significantly increased the solubility of paclitaxel in excess of 2 mM paclitaxel equivalents in PBS, which was ultimately limited by the viscosity of the CP solution. Cryo-TEM of the CP-paclitaxel nanoparticles displayed close-packed spherical nanoparticles with a dense electron core, whose size (measured by the core-to-core distance) was smaller than the R_h determined by dynamic light scattering (R_{TEM} = 22 ± 4 nm; n = 50) (Figure 12F). This discrepancy is likely due to the fact that the soft CP nanoparticle corona can become significantly compressed under the conditions necessary to visualize the particles with cryo-TEM (high shear stress may be induced by blotting and the high polymer concentration) when compared to the very dilute conditions necessary for light scattering measurements. The CP-paclitaxel nanoparticles were also highly stable with a CAC ≤ 10

μM (Figure 16). These results are consistent with the model: gemcitabine and oxycodone, as predicted by the model, were too hydrophilic to drive the assembly of nanoparticles at pH 7.4, whereas paclitaxel, with a Log(D) of 4.0, is above the threshold of hydrophobicity needed to trigger self-assembly.

Table 2: CP nanoparticles assembled through drug conjugation

Drug	Log(D)[a]	R_h (nm)	Drug/CP	#CPs/NP
Gemcitabine	-2.2	5.7	5	0.9
Oxycodone	1.2	9.7	4	1.3
Paclitaxel	4.0	53.3	2	72.0

[a] Log(D) was estimated using ACD Labs/PhysChem Suite.

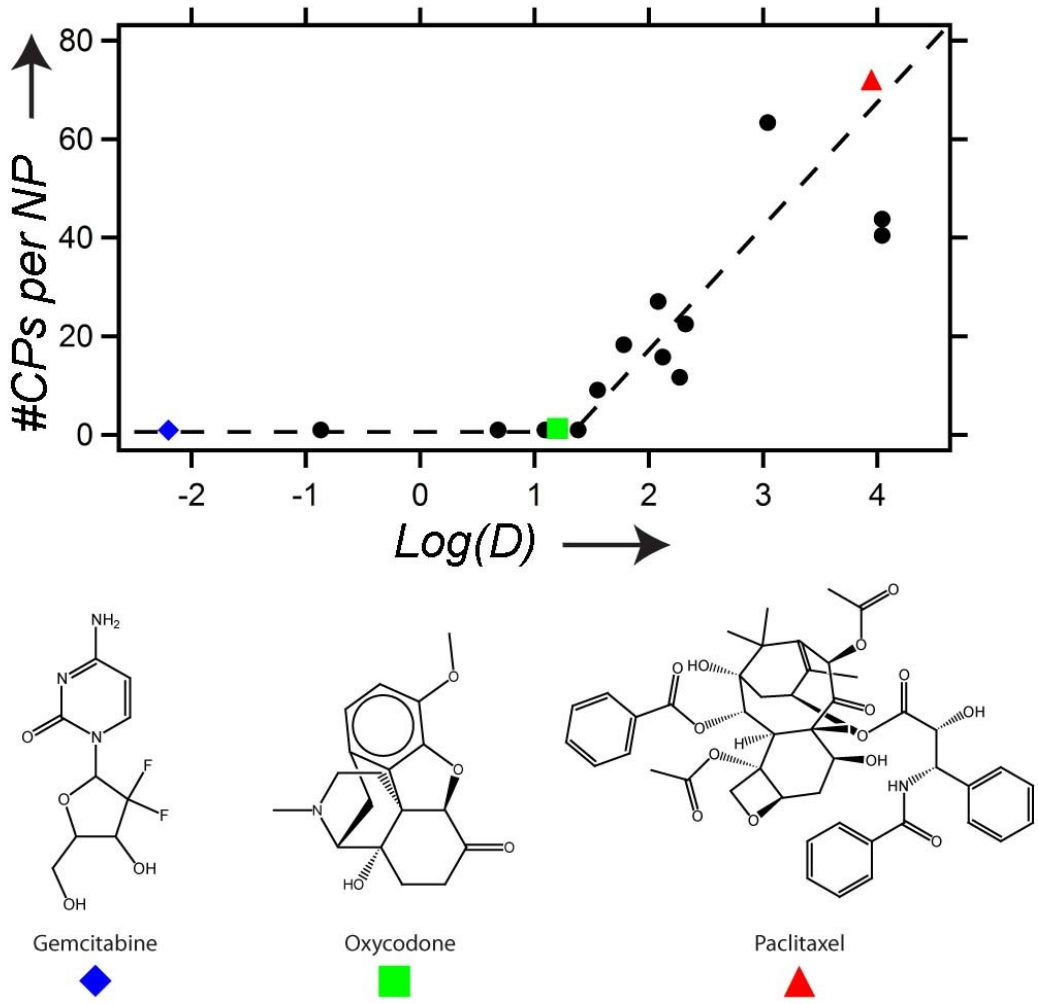

Figure 15: The apparent coordination number of the 14 small molecule conjugates (●) (#CPs per NP) versus the Log(D) of each molecule. Above the threshold of Log(D) = ~1.5, the number of CPs per nanoparticle (#CPs/NP) increases with hydrophobicity of the conjugated small molecule [Log(D)]. The blue diamond, green square, and red triangle markers indicate gemcitabine, oxycodone, and paclitaxel, respectively. The lines are drawn solely as a guide to the eye [77].

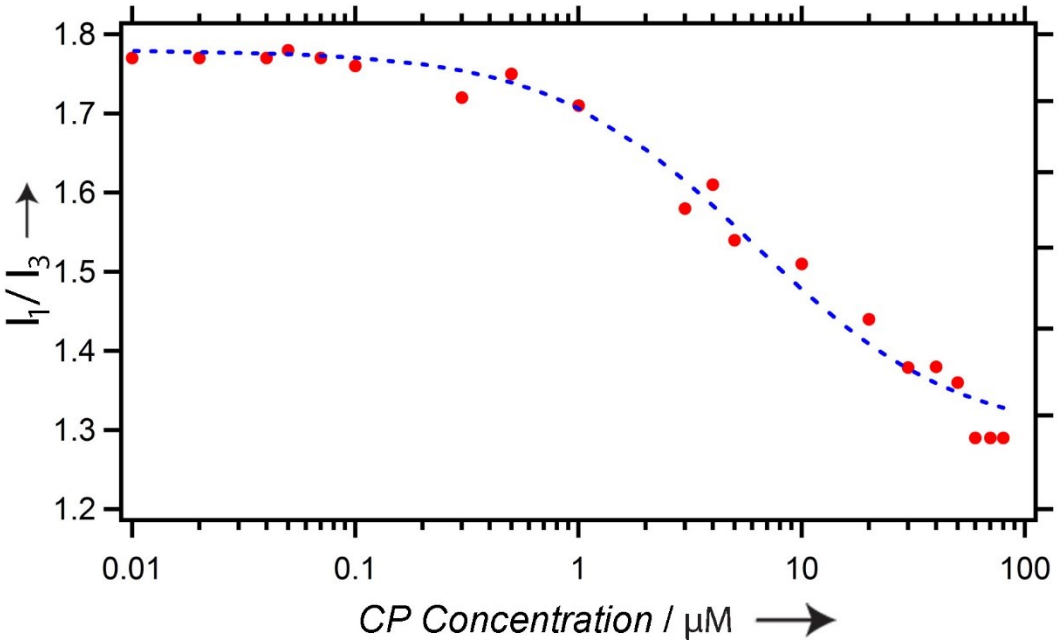

Figure 16: CAC of CP-Paclitaxel. The pyrene fluorescence was measured for CP-PTX as a function of CP concentration in PBS. The CAC was defined as the inflection point of the curve; CAC = 6.1 ± 0.6 μM. The dashed line represents the sigmoid of best fit [77].

3.6 Conclusions

Our results are notable for several reasons. Although attachment of drugs to polymers has been used to develop self-assembling therapeutic formulations, this work departs significantly both in its conceptual novelty and scope from these previous studies: adriamycin was covalently conjugated to the aspartate groups in PEG_{4300}-b-polyaspartate (NK911), thereby assembling into 50 nm micelles [95]; the biologically active metabolite of irinotecan, SN-38, was attached to the glutamate chain in PEG_{5000}-b-polyglutamate (NK012) to form micelles [169]; and the polyaspartate chain of PEG_{12000}-

b-polyaspartate was modified with 4-phenyl-1-butanol, which induced assembly and facilitated the noncovalent incorporation of paclitaxel into (NK105) [170]. In these studies, a general route to the conjugation triggered self-assembly of the polymer by a range of molecules was not shown, nor did these and related studies provide a model that enabled a priori prediction of the propensity –or lack thereof– of a molecule to trigger the self-assembly of the polymer [95, 171-173]. Furthermore, none of these systems exhibit the thermal responsiveness observed with these CPs over a range of concentrations relevant for drug delivery, a feature that can be exploited for *in vivo* thermal targeting of CP-drug nanoparticles

In conclusion, this chapter illustrates a roadmap for the rational design of highly soluble, thermally responsive drug-loaded nanoparticles whose properties can be tailored at the molecular level. We show that attachment of small molecules above a critical threshold of hydrophobicity trigger self-assembly of the CP into soluble nanoparticles ranging from 60 nm to ~100 nm in diameter. These nanoparticles are soluble at concentrations greater than 100 μM of CP and ~3-6 fold higher for the small molecules, and are stable upon dilution up to low micromolar concentrations of the CP, a concentration regime that is of great utility for drug delivery. These results provide a simple predictive model for nanoparticle formation that permits *a priori* screening of the propensity of drugs to be sequestered into the nanoparticle core solely based on their

Log(D) value and demonstrate that conjugation-triggered self-assembly can package a hydrophobic drug into soluble nanoparticles.

3.7 Materials and Methods

3.7.1 Materials

BL21™ *Escherichia coli* cells were obtained from Edge BioSystems (Gaithersburg, MD) and were grown in TBDry™ media (MO BIO Laboratories, Inc; Carlsbad, CA). Chemicals used for the purification of ELPs include: IPTG (Gold Biotechnology; St. Louis, MO), TCEP (Thermo Scientific; Waltham, MA), and ampicillin (CalBioChem; San Diego, CA). Maleimide derivatives were obtained from Sigma Aldrich (St. Louis, MO).

3.7.2 Methods

3.7.2.1 Synthesis of Chimeric Polypeptides

The ELP segment of the CP selected for conjugation to the series of small molecule maleimide derivatives and the therapeutics gemcitabine, oxycodone, and paclitaxel– was comprised of the sequence SKGPG-$(XGVPG)_{160}$-WPC$(GGC)_7$, where the guest residue X = Val_1, Gly_7, Ala_8, and is hereafter referred to as ELP_2*. This specific guest residue composition of $V_1A_8G_7$ and 160 VPGXG pentapeptide repeats was chosen to ensure that the CP has a T_t above body temperature in the concentration range of 1-100

μM, a concentration range that is useful for systemic delivery of drugs. This construct was synthesized using recursive directional ligation, as described elsewhere [83, 88].

3.7.2.2 Expression and Purification of Chimeric Polypeptides

The ELP was expressed using a previously published hyperexpression protocol, which relies on the leakiness of the T7 promoter [161]. 50 mL cultures grown for 16 h were used to inoculate six 1 L flasks of TBDry supplemented with 100 μg/mL ampicillin. Each 1 L flask was then incubated at 37°C for 24 h and 210 rpm, after which the cell suspension was centrifuged at 3,000 rpm for 10 min at 4°C. Each ELP was purified using Inverse Transition Cycling, which has been described elsewhere [84]. Briefly, the cell pellet was resuspended in PBS and lysed via sonication on ice for 3 min (10 s on, 40 s off) (Masonix S-4000; Farmingdale, NY). Polyethyleneimine (PEI) 0.7% w/v was added to the lysate to precipitate nucleic acid contaminants. The supernatant was then subjected to multiple rounds of ITC as follows. The solution was heated to 37°C in the presence of 3 M NaCl. The coacervate was centrifuged for 10 min at 14,000 g and 20°C, and resuspended in 20 mM TCEP in water, pH 7. This suspension was cooled to 4°C, and then centrifuged for 10 min at 14,000 and 4°C to remove any insoluble contaminants. Typically, 3-5 rounds of ITC generated a sufficiently pure product (>95% by SDS-PAGE).

3.7.2.3 Purity Analysis

Following CP purification, SDS-PAGE was performed on Biorad ReadyGels with a 4-20% Tris gradient. The gels were visualized by copper staining (0.5 M $CuCl_2$).

3.7.2.4 Dynamic and Static Light Scattering

Dynamic and static light scattering measurements were performed using the ALV/CGS-3 goniometer system (Germany). Samples for the ALV/CGS-3 goniometer system were prepared in PBS at 20 μM CP and filtered through 0.22 μm Millex-GV filters into a 10 mm disposable borosilicate glass tube (Fischer). The tube was precleaned by washing three times with filtered ethanol (0.2 μM cellulose acetate filter). Simultaneous SLS/DLS measurements were obtained at 25°C for angles between 30°-150° at 5° increments, with each angle consisting of 3 runs for 10 s. Results were analyzed by partial Zimm plot analysis using ALV/Dynamic and Static FIT and PLOT software.

3.7.2.5 Cryogenic Transmission Electron Microscopy

Cryogenic Transmission Electron Microscopy was performed at the University of Pennsylvania in the Penn Regional Nanotechnology Facility (Philadelphia, PA). Lacey formvar/carbon grids (Ted Pella) were washed in chloroform to remove the formvar template and carbon coated with a Quorum Q150T ES carbon coater (Quorum Technologies, United Kingdom). Grids were cleaned with hydrogen/oxygen plasma for 15 s using the Solarus Advanced Plasma System 950 (Gatan, Pleasanton, CA). A sample in the form of a 2 μl drop was deposited onto the grid and added to a Gatan Cp3 cryoplunger (Gatan, Pleasanton, CA). The samples were blotted by hand and plunged into liquid ethane. Grids were transferred to a Gatan CT3500TR cryoholder (Gatan,

Pleasanton, CA) and immediately inserted into a JEOL 2010 TEM (JEOL, Tokyo, Japan) operating at 80 keV. Micrographs were imaged with an Orius SC200 digital camera.

3.7.2.6 Absorbance Spectroscopy

The transition temperature (T_t) of each sample was calculated by recording the optical density at 350 nm as a function of temperature (1°C/min ramp) on a temperature controlled UV-Vis spectrophotometer (Cary 300 Bio; Varian Instruments, Palo Alto, CA). The T_t was defined as the inflection point of the turbidity plot, or the maximum of the first derivative. All samples were analyzed in PBS, and 3-5 different concentrations ranging from 1 μM to 100 μM were used for each sample.

3.7.2.7 Fluorescence Spectroscopy

An assay to determine the critical aggregation concentration (CAC) using pyrene as a probe was performed using a Cary Eclipse spectrophotometer equipped with a Xenon flash lamp (Varian Instruments; Palo Alto, CA). 1 μL of a stock solution of 12 mM pyrene (Fluka/Sigma-Aldrich; St. Louis, MO) in ethanol was diluted into 20 mL of PBS. Both the stock solution and the PBS mixture were sonicated for 10 min prior to use. This solution was used to resuspend 1-5 mg of lyophilized sample, which was then used to create a dilution series. Each sample was placed in a reduced volume cuvette, and scanned (Ex: 334; Em: 360-380, Ex slit 10 nm; Em slit 2.5 nm). Pyrene fluorescence displays four peaks; the intensity at the first (I_1; 370-373 nm) and third peak (I_3; 381-384

nm) were recorded. The ratio I_1/I_3 was plotted as a function of CP concentration. The CAC was defined as the inflection point of the sigmoid of best fit.

3.7.2.8 Conjugation of the Maleimide Derivatives

15 mg of lyophilized CP was resuspended in 800 μL of 100 mM phosphate buffer, pH 7.4, and spiked with an additional 100 μL of 100 mM TCEP in water, pH 7.4. Finally 100 μL of a 50 mM solution of each maleimide derivative in DMSO was added to the CP solution dropwise, and allowed to mix for 3 h (additional DMSO was added for compounds that were not soluble in 10% DMSO). Following conjugation, the CP was purified by passage through a PD10 column (SEC) and dialysis in ddH_2O overnight. The solution was centrifuged at 13,000 g and 4°C for 10 min, lyophilized, and stored at 20°C for future use.

3.7.2.9 Conjugation of Drugs to the Elastin-like Polypeptide

The specific chemical reaction schemes and characterization protocols (NMR, MALDI-MS, and ESI-MS) are included Appendix 8.9.2.1 (Gemcitabine), 8.9.2.2 (Oxycodon), and 8.9.2.3 (Paclitaxel).

3.7.2.10 Calculation of Conjugation Ratio

Following purification, 2-3 mg of lyophilized ELP was dissolved in 1 mL ddH_2O. In order to break any pre-existing disulfide bonds between unconjugated cysteine residues, 100 μL of the conjugate was incubated with 100 μL of Immobilized TCEP Reducing Gel (Thermo Fisher Scientific; Rockford, IL) for 1 h at 25°C. Included spin

columns were utilized to separate the TCEP beads from the CP conjugates. The solution was then split for use in two parallel assays. To determine the CP concentration, a 96-well bicinchoninic acid assay (Thermo Fisher Scientific) was used on a Victor^{3TM} microplate reader (Perkin Elmer; Waltham, MA) at an absorbance of 560 nm. 10 μL of CP solution was mixed with 200 μL of BCA working reagent, incubated for 30 min at 37°C, and was compared to an ELP standard curve (100, 75, 50, 40, 33, 30, 25, 20, 16.7, 15, 13.3, 10, 6.7, 5, 3.3, 1.7, 0 μM) fit to a 2nd order polynomial in order to estimate the CP concentration. Each conjugate was measured in triplicate. To determine the concentration of free thiols, a 96-well Ellman's assay was developed for use on the Victor^{3TM} microplate reader at an absorbance of 405 nm. 40 μL of an ELP solution was mixed with 200 μL of a working reagent (25 μM Ellman's reagent in 100 mM phosphate buffer, 1 mM EDTA, pH 8.0), incubated for 2 h at 25°C, and was compared to a standard curve of the ELP prior to conjugation (33, 30, 25, 20, 16.7, 15, 13.3, 10, 6.7, 5, 3.3, μM). The available cysteines in each sample could then be calculated by determining the ratio between the Ellman's assay standard curve (assumed to have 8 free cysteines / CP) and the Ellman's assay sample measurement at the concentration determined by the BCA assay. The conjugation ratio was the difference between the number of cysteines (8 / CP) and the calculated number of free cysteines.

3.7.2.11 Determination of Nanoparticle Assembly

The determination of whether a construct assembled into a nanoparticle or remained in its unimer form was based on a combination of the R_h and the transition behavior (Figure 11). A few samples showed a combination of unimer and nanoparticle at 25 μM by DLS. This could be due to the following factors: (1) micelle theory indicates that nanoparticles assemble above a specific threshold concentration of unimer (CMC). As the bulk concentration increases past this threshold, the concentration of nanoparticles increases while the unimer concentration remains constant. If the concentration (25 μM) is near the CMC, then the unimer population will be visible via light scattering. (2) Since assembly is induced through the conjugation of chemicals, a polydisperse conjugation may result in some chains that are unconjugated or below the hydrophobicity threshold for assembly (*i.e.*, only 1 molecule/chain), resulting in a substantial unimer population in addition to a nanoparticle population (3-4 molecules/chain). All samples reported as unimer were >80% unimer by mass, displayed a T_t concentration dependence of approximately -5°C/Log(concentration), and had an average T_t of 65°C ± 8 (over all concentrations). Samples considered nanoparticles were >50% nanoparticle by mass, displayed a T_t concentration dependence of approximately -1°C/Log(concentration), and had an average T_t of 50°C ± 1.

4. An Empirical Model for De Novo Design of Elastin-like Polypeptide Transition Temperatures

4.1 Overview

The previous chapter describes a method to assemble chimeric polypeptide nanoparticles whose transition behavior is near independent from the concentration of the polypeptide and the properties of the attached molecules (as long as the Log(D) > 1.5). However, because Figure 11A clearly illustrates that the transition temperature resides outside of the desired 39-43°C range, it was necessary to devise a strategy to re-engineer the CP transition behavior. In fact, many applications of ELPs require the T_t to occupy a narrow temperature window [56, 63, 76, 174-177]. Theoretically, an ELP or CP can be "forced" to exhibit a T_t within a given window by using highly concentrated or very dilute polymer solutions, by adding kosmotropic or chaotropic salts [178], or by using high or low molecular weight ELPs. From a practical perspective, however, this strategy is not typically feasible because the MW or concentration is often set by the application, while the addition of other cosolutes may be impractical in many applications or simply impossible if the intended application of the ELP is *in vivo*. These constraints on modulating the T_t of an ELP require an alternative strategy to tune the transition temperature for most applications.

Clearly, what is needed is an algorithm that quantitatively relates the T_t to ELP or CP composition, MW, and concentration. A unified model that does so would allow users to design ELPs and CP nanoparticles *de novo* for a range of applications by

constraining one or more of the operating parameters for a given application (MW or concentration) to yield one or more sequences that will exhibit the desired T_t. In response to this need, we first developed a quantitative model that predicts the T_t of ELP unimers from their sequence, MW, and concentration in phosphate buffered saline (PBS). We term this a unified model because it "unifies" the effect of ELP composition, MW and concentration on the T_t of the ELP within a single analytical equation. In the following chapter this model is used as the basis for a second model that describes the transition behavior of CP nanoparticles.

This model describing the transition behavior of ELP unimers builds upon, but departs significantly from previous studies that quantified the ELP phase transition behavior as a function of guest residue composition. Urry used chemically synthesized ELPs to demonstrate that their T_t correlated with the mean hydrophobicity of the guest residue [168, 179, 180]. That study did not, however, examine the effect of ELP MW and concentration on its T_t, two variables that we know have a large impact on the experimentally observed T_t in solution. In response to this limitation, Meyer and Chilkoti developed a quantitative model describing the effects of ELP chain length and concentration on the T_t of three different ELP libraries comprised of a mixture of Val, Ala, and Gly residues at the 4^{th} guest residue position for a range of ELP chain lengths [158]. MacKay then modified that model to incorporate the effects of pH on the T_t for ELPs that contain ionizable residues at the guest residue position [91]. These models,

though valuable, only predict the T_t as a function of MW and concentration within a single ELP sequence, and only once at least three members of that sequence with different MWs have been synthesized and characterized with respect to their T_t. Because these models did not explicitly include a term that accounts for the effect of composition on the T_t, their utility as a design tool is limited because the composition is the most useful experimental parameter to modulate the T_t. In contrast, by incorporating ELP composition, MW, and concentration within a single equation that predicts the T_t, the model developed herein will enable *de novo* selection of ELP sequence and molecular weight combinations that will display a T_t of interest within a specific range of concentration.

4.2 Elastin-like Polypeptide Sequence Design Considerations

To develop this model, we first limited the sequence space, as the number of unique ELP sequences that will exhibit a desired T_t are enormous, even if one of two parameters such as MW or solution concentration are fixed. This is given by the fact that 19 natural amino acids (and many more unnatural amino acids) are available to tune the T_t by incorporation at the guest residue position 'X' in the VPGXG repeat unit. The number of such sequences expands enormously when using a combination of three or more guest residues. We also restricted the choice of guest residues to a binary combination of amino acids to minimize the sequence order related complexity in phase

behavior because the complexity that sequence order creates can unpredictably alter the T_t [158]. Choosing a binary composition also has the benefit that it can be easily numerically encoded for modeling purposes.

We hence narrowed the composition of the two guest residues to alanine (Ala) or valine (Val) at the guest residue position. We selected Ala and Val as the specific guest residues for two reasons: (1) because a major focus of our efforts is to design ELPs that would exhibit T_t's in the physiological temperature range, we surmised that copolymer ELPs ranging from 100% Ala to 100% Val at the guest residue position would yield multiple copolymers that exhibit T_t's between 30-45°C for a range of MWs and ELP concentrations, given that the T_t of their homopolymers span this range [180]; and (2) the side chains of Ala and Val are aliphatic and thus will not display a sensitivity to pH. Although the ability to tune the T_t by pH is potentially valuable [93], it adds an unnecessary degree of complexity to model development at this stage.

With these parameters fixed, we recombinantly synthesized eight ELP libraries in *Escherichia coli* (the gene sequences are shown in Figure 38 in Appendix 8.1 and the gene libraries are shown in Figure 41 in Appendix 8.2). Each ELP library consists of a set of ELPs of constant composition as defined by the fraction of Ala at the guest residue (reminder is Val) with members in that library only differing in their MW, consisting of 15, 30, or 60 kDa (40, 80, and 160 pentapeptides, respectively; Figure 44 in Appendix 8.3). The guest residue composition defined by the fraction of Ala steps across from 0 (solely

Val guest residue) to 1 (solely Ala guest residue) in increments of 0.1 or 0.2 across the eight ELP libraries. After expression in *Escherichia coli*, the 24 unique ELPs were purified to homogeneity; details of their physical characterization (SDS-PAGE and MALDI-MS) are contained in Appendices 8.3 and 8.4, respectively.

We next fixed the solution conditions that the model was developed for by choosing phosphate buffered saline (PBS) as the solvent, as most applications of ELP are likely to be in biotechnology or medicine wherein PBS is the buffer of choice. We then measured the T_t of all 24 members of these 8 ELP libraries in PBS for a range of ELP concentrations (Figure 46 in Appendix 8.5). The experimentally measured T_t's of these ELPs were used to develop a quantitative model that incorporates the effects of ELP MW, ELP concentration, and guest residue composition within a single equation.

4.3 Development of a Mathematical Model to Describe the Elastin-like Polypeptide Transition Temperatures

The first step in building the model was to quantify the effect of composition on the T_t of ELPs. Each ELP composition library followed the relationship previously developed by Meyer and Chilkoti [158] to describe the transition behavior of ELPs (average $r^2 = 0.987 \pm 0.018$):

(1) $$T_t = T_{tc} + \frac{k}{Length} \ln \frac{C_c}{Conc}$$

where the T_t depends on the chain length (Length, number of pentapeptide repeats) and polymer concentration (Conc, μM), as well as three parameters specific to each ELP composition: the critical transition temperature T_{tc} (°C), the proportionality constant k (°C·pentapeptides), and the critical concentration C_c (μM) (Equation 1). The T_{tc} represents the transition temperature for a given composition at a critical limit –high ELP concentration and chain length – at which point these two parameters no longer affect the T_t, and thus likely represents the lowest critical solution temperature of the system. The parameter C_c is the corresponding theoretical polypeptide concentration that would be required to achieve T_{tc}. Finally, the parameter k indicates the concentration and length dependence of the T_t: larger values signify that the transition temperature is more sensitive to concentration fluctuations or changes in chain length.

Table 3: Summary of multivariate fits to Equation 1 for eight ELP compositions[a]

f **Alanine**	T_{tc} **(°C)**	**k (°C·pentapeptides)**	C_c **(μM)**	r^2	**n**
1	54.3 (1.4)	623.0 (36.1)	844 (209)	0.98	30
0.9	44.7 (2.0)	507.0 (53.1)	2412 (1311)	0.95	30
0.8	39.3 (0.8)	484.7 (21.3)	2005 (442)	1.00	15
0.7	33.8 (0.6)	433.7 (16.3)	2748 (547)	1.00	15
0.6	29.9 (0.6)	387.0 (16.1)	3684 (851)	1.00	15
0.5	27.7 (0.6)	316.9 (15.3)	6219 (1822)	0.99	30
0.2	22.9 (0.2)	201.2 (5.0)	13573 (2307)	1.00	30
0	20.2 (0.1)	144.1 (3.4)	22130 (3786)	1.00	30

[a]Data fit to Equation 1 and reported as estimate (standard error).
'n' represents the number of measurements per fit.

These three parameters were simultaneously determined for each compositional library using a multivariate regression fit to Equation 1. The fits, summarized in Table 3, were based on a range of MWs (40, 80, and 160 pentapeptide repeats) and five ELP concentrations (100 to 5 μM). The ELP libraries are labeled according to their composition, which is defined by the fractional alanine content (fAlanine). For example, a value of 1.0 indicates that the guest residue composition consists exclusively of alanine, and a value of 0.2 indicates that the compositional ratio is 2 alanine to 8 valine. We found that the parameters could be calculated with reasonable certainty with the exception of C_c, which showed a high level of variation that is likely due to its derivation from a logarithmic ratio.

To elucidate the relationship between the ELP composition and the three parameters (T_{tc}, k, and C_c), each parameter was plotted as a function of fAlanine (Figure 17). These plots revealed that the empirical relationship between the composition and T_{tc} ($r^2 = 0.947$), k ($r^2 = 0.989$), and C_c ($r^2 = 0.959$) fit the exponential form $Ae^{b \cdot f\text{Alanine}}$, where A and b are constants.

It is not entirely surprising that these parameters show a quantitative correlation with the ELP composition. Urry demonstrated that the critical transition temperature (T_{tc}) was influenced by the mean hydrophobicity of the guest residue composition [181]. We have also observed that the T_t's of hydrophobic ELPs are less dependent on the concentration (hence smaller k values) than the T_t's of hydrophilic ELPs. Meyer and

Chilkoti consolidated these observations by demonstrating that the parameters were related across three ELP libraries; they observed that k varied linearly with T_{tc}, whereas C_c varied as a power function with T_{tc} [158]. Although only three compositions were sampled and the ELP hydrophobicity was approximated by the T_{tc} (instead of the sequence, as demonstrated here), the postulated relationships are supported by this data set. As T_{tc} and k follow the form $e^{fAlanine}$, k as a function of T_{tc} generates a near-linear correlation (Figure 18; r^2=0.929). C_c, on the other hand, is approximated by $e^{-fAlanine}$, which signifies that C_c as a function of T_{tc} ($e^{fAlanine}$) yields a power function ($C_c \approx T_{tc}^{-1}$) (r^2=0.938).

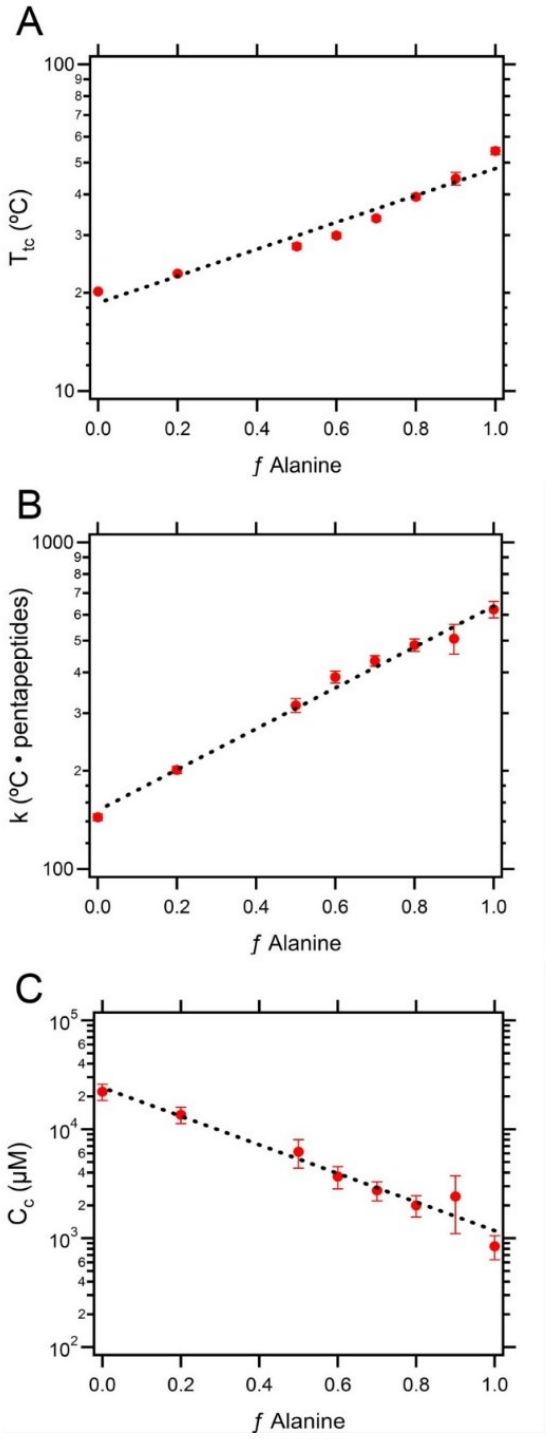

Figure 17: Relationship between the composition and the three parameters defined in Eq. 1. (A) T_{tc}, (B) k, and (C) C_c as a function of *f*Alanine. Data are reported as mean ± standard error. The dashed lines represent the best fit of the form $Ae^{b \cdot f\text{Alanine}}$ [182].

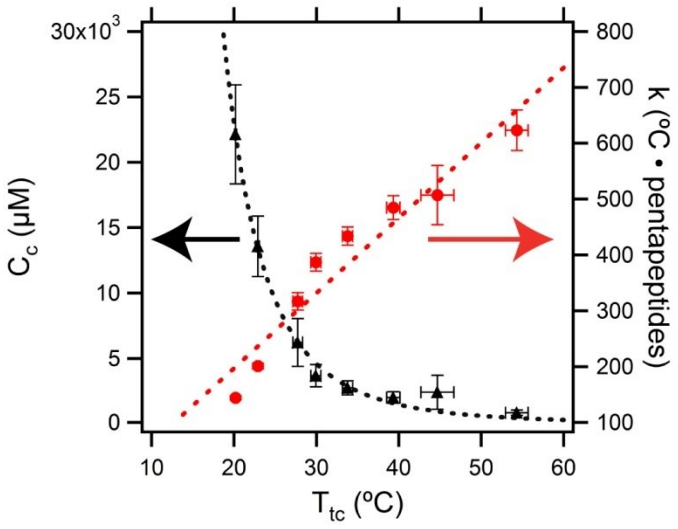

Figure 18: Parameters k (red; right axis; $r^2 = 0.929$) and C_c (black, left axis; $r^2 = 0.938$) as a function of T_{tc}. Data reported as estimates ± standard error. The dashed lines represent curves of best fit for k (linear) and C_c (power function) [182].

With these relationships validated, this exponential form was substituted for each parameter in Eq. 1 to yield Eq. 2:

$$(2) \qquad T_t = Ae^{b*fAlanine} + \frac{Ce^{D*fAlanine}}{Length}\ln\left(\frac{Ee^{F*fAlanine}}{Conc}\right)$$

where A-F are non-zero constants and fAlanine represents the ratio of alanines to the total number of guest residue positions. For fitting purposes, Eq. 2 was then simplified with logarithmic identities to yield Eq. 3:

$$(3) \qquad T_t = Ae^{b*fAlanine} + \frac{Ce^{D*fAlanine}}{Length}[\ln(E) + F * fAlanine - \ln(Conc)]$$

Eq. 3 was used to perform a global multivariate regression analysis (n = 120) on the data to yield the empirical relationship between the T_t, chain length, concentration,

and composition for all synthesized guest residue combinations of Ala and Val (Equation 4):

$$T_t = 16.8e^{1.1*fAlanine} + \frac{181.5e^{1.2*fAlanine}}{Length}[\ln(12881.2) - 2.3 * fAlanine - \ln(Conc)] \quad (4)$$

A 3-dimensional surface plot of this model, holding the ELP concentration constant (Figure 19A) illustrates the wide range of T_t's available to ELPs of varying length and composition. This model describes 99.4% of the observed variability in the T_t over all 24 unique ELP constructs (Figure 19B) in PBS. Also evident from these data is the inverse relationship of T_t with chain length (Eq. 4); higher molecular weight ELPs exhibit lower T_t's than smaller ELPs at the same composition and concentration. This graph indicates that there are several ELPs with a T_t above 100°C. Each T_t > 80°C in PBS (the temperature limit of our UV-Vis spectrophotometer) was linearly extrapolated from the T_t of the ELP at three different NaCl concentrations, which is known to quantitatively depress the T_t of ELPs as a function of NaCl concentration [178]. Finally, while this relationship holds true in PBS, the model does not apply to transition temperatures in different solvents, such as FBS. If this model was desired, the data points would have to be collected in FBS and fit to equation 3, as the transition temperatures of longer hydrophobic ELPs are affected less by the presence of cosolutes and salt than shorter hydrophilic ELPs.

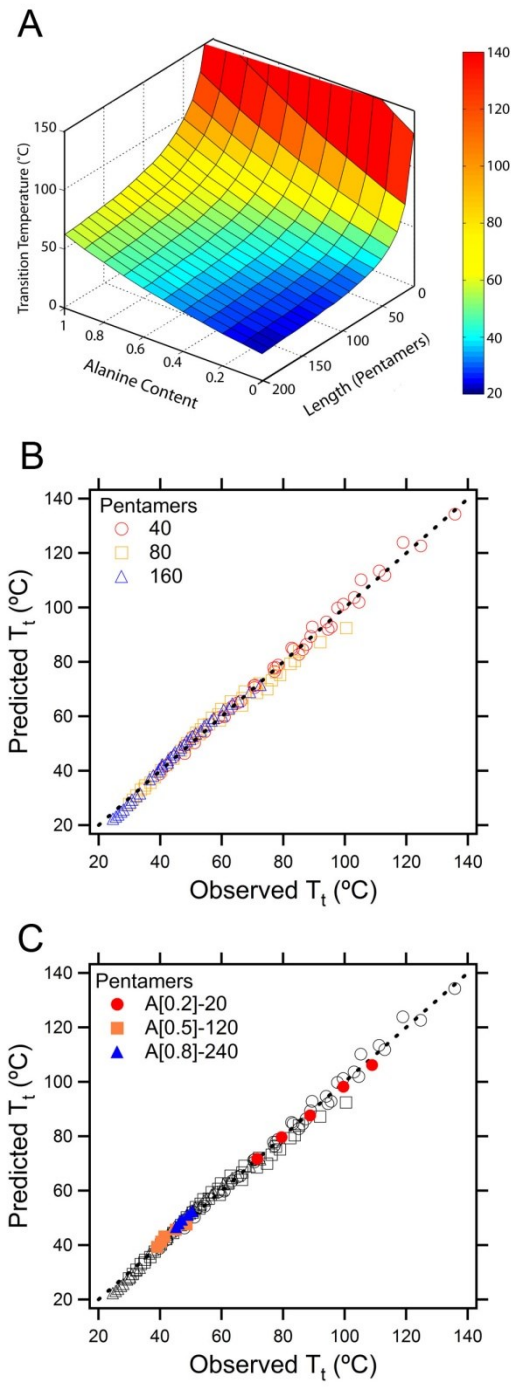

Figure 19: (A) A 3-dimensional plot of the predicted T_t landscape for the Ala and Val superfamily of ELPs at 25 μM in PBS. (B) Predicted versus observed T_t for a global fit of eight ELP sequences across 3 molecular weights and 5 concentrations in PBS

(r^2=0.993; n=120). (C) Predicted versus observed T_t for 3 additional sequences (A[0.2]-20, A[0.5]-140, and A[0.8]-240) not included in the original data set. These three ELPs showed a high fidelity to the model (r^2=0.999, slope = 0.95) [182].

4.4 Validation of the Model against Elastin-like Polypeptide Size Variants

To test the robustness of the model, three ELPs were synthesized with molecular weights that were not included in the original data set (shown in Table 12 in Appendix 8.4). Figure 19C shows that the model accurately predicts (r^2=0.999; n=15) the transition temperatures for ELPs with MWs that are larger (240 pentamers), smaller (20 pentamers), and in-between (120 pentamers) the molecular weights used to construct the model. Finally, this model was used to develop Appendix 8.6 (Table 14), which provides possible combinations of sequence (*f* Alanine = 0 to 1 with a 10% Ala step size) and length (pentamers = 20 to 200 with a 10 pentamer step size) to achieve a specific T_t at a specified concentrations (1 to 1000 μM) in PBS. This resource provides a clear starting point for designing ELPs for specific thermoresponsive applications.

4.5 Advantages of a Predictive Model for Elastin-like Polypeptide Transition Temperatures

The selection of ELPs that exhibit a T_t within a specific temperature window has historically relied upon trial-and-error. The Meyer and Chilkoti model [158] was the first to quantitatively model the T_t of ELPs as a function of ELP chain length and

concentration. However, the model incorporated 3 parameters that could only be determined once the ELP was synthesized and its inverse transition behavior characterized. While the resulting relationship proved very useful in predicting the transition behavior of ELPs with different MWs within the same family, the absence of a defined "sequence" variable did not allow the *a priori* prediction of the T_t of new ELP sequences. The MacKay and Chilkoti model [91] expanded upon the Meyer and Chilkoti model by incorporating the Henderson-Hasselbalch equation to predict the relative quantities of protonated and nonprotonated residues. By splitting each of the 3 parameters into protonated and nonprotonated parameters (for a total of 6 parameters), the MacKay model is able to predict the T_t of ELPs within a specific sequence family at a specific pH. While the third design parameter is useful in exploiting the pH behavior of charged ELPs, like the Meyer model it remains limited to a single ELP family at a time.

The Meyer model can be applied in situations where the ELP library has already been generated and the user wants to know how changing the length or concentration will influence the T_t of a construct within that particular ELP library. The MacKay model also requires that the ELP library be constructed and characterized, and can be used to predict how length, concentration, or pH will influence the transition temperature of new constructs within that library. Because the model presented here is constructed from multiple separate ELP libraries, the user is able to predict how the length, concentration, and sequence will influence the transition temperature of entirely new

libraries as long as the sequence is contained within that ELP superfamily (X=Ala and/or Val). This greatly increases the sequence space that can be screened for ELPs with the desired thermal behavior.

The most important finding of this study is that each of the three parameters defined in the Meyer model can be described as an analytical function of the sequence, represented by the fraction of alanines in the guest residue position. This new feature of the model eliminates the need to express and characterize ELPs prior to predicting their T_t and thereby provides an *a priori* predictive tool for the design of ELPs in the superfamily of constructs containing Val or Ala guest residues. While this compositional limitation restricts the compositions available for designing new ELPs, we purposely selected Ala and Val because they exhibit transition temperatures that are far removed from each other, maximizing the coverage over the physiologically relevant temperature range that is of greatest interest to us. This is evident when observing the predicted range of T_t for ELPs of different MW at a specific concentration (100 μM): 40 pentamers (38.8 – 89.4°C); 80 pentamers (27.8 – 69.9°C); and 160 pentamers (22.3 – 60.2°C).

This study also sheds light on the limitations of previous models that investigated whether the T_t's of heterogeneous ELPs (heteropolymers composed of two or more different guest residues with a pseudorandom distribution of guest residues across the ELP's primary amino acid sequence) could be calculated by linearly interpolating between the T_t of two or more homogeneous ELPs (homopolymers), and

then weighing each homopolymer ELP T_t by the mole fraction of the guest residue composition in the heteropolymer. The implementation of this method, however, has been met with conflicting results [158, 181]. This study conclusively demonstrates that the T_t of heteropolymer ELPs cannot be calculated in this manner. Figure 20 illustrates that the T_t for any combination of Ala and Val is clearly depressed from the linear interpolation between the T_t of the two homopolymer ELPs. While this particular set of conditions (80 pentamers at 25 μM) yields a maximum departure of ~5°C from the linear interpolation, the departure is inversely proportional to concentration and length. This study only examined the combination of two specific amino acids; it remains unknown to what degree other guest residue combinations will be affected, although it is our opinion that this error will be greatest when mixing guest residues of vastly different hydrophobicities. We hypothesize that the T_t is not simply dependent upon the mean hydrophobicity of the guest residue composition as previously proposed [181], but is actually determined by the specific sequence of the guest residues [183] and the difference in hydrophobicity between the guest residues. This hypothesis is currently under investigation.

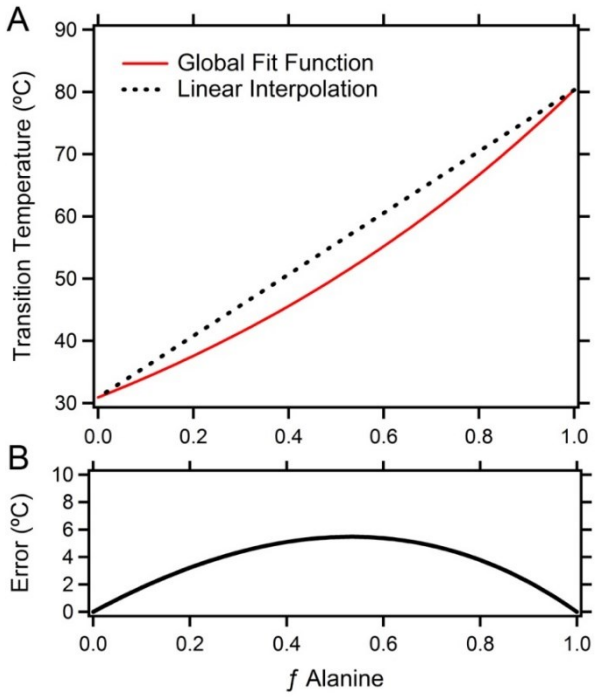

Figure 20: (A) The global fit of the ELP T_t's for ELP constructs with a chain length of 80 pentapeptides and at 25 μM ELP concentration (red line) as a function of composition. The black dashed line represents a linear interpolation between the T_t's of two homopolymer ELPs composed with 100% Ala or Val as their guest residue. (B) Error, defined as the departure of the linear interpolation from the global curve of best fit in degrees Celsius as a function of the fractional Ala content of the ELP [182].

4.6 Potential Improvements to the Model

Although this model is a useful step forward in the design of ELPs, more remains to be done. Examination of Appendix 8.6 shows that although regions of the matrix of T_t as a function of ELP concentration is populated by ELPs with a range of MWs, there are regions in that matrix that are sparse in terms of available ELPs. In particular, constructs that display low T_t's at small MW and dilute conditions and

constructs that display high T_t's at large MW and concentrated conditions are absent from the matrix. This is because at the extremes of MW and ELP concentration, this model is fundamentally limited by the properties of the Val (low T_t's) and Ala (high T_t's) homopolymers. Future studies will address this limitation by expanding this model by the synthesis and characterization of ELPs with other combinations of hydrophobic (Leu, Ile) and hydrophilic amino acids (Ser, Gly) that will provide additional ELPs to populate these regions of the matrix.

This model could also be combined with the MacKay model to explore the pH sensitivity (in the physiological range) of the superfamily of ELPs constructed with glycine and histidine, for example. Finally, it should be noted that a similar model developed for other binary systems would not require 8 families of ELPs prior to constructing the T_t landscape of the superfamily. In fact, this model can be recreated with little to no loss of information with only 3 ELP families (the two endpoints and the midpoint: 0%, 50%, and 100% Ala) across 3 molecular weights and 5 concentrations (n=45). The resultant model predicts the T_t's of all eight families with high accuracy (r^2 = 0.992; slope of predicted T_t versus observed T_t = 1.002; n=120).

4.7 Conclusions

The model presented in this chapter is the first to quantitatively correlate the T_t of a set of Ala and Val containing ELPs with an explicit compositional variable, its MW,

and concentration. This allows the *a priori* prediction of the T_t of any ELP consisting of a combination of Ala and Val at the guest residue position across a range of ELP MWs and concentrations in PBS. This simple analytical model provides researchers with an easy tool that can be implemented as an Excel™ (Microsoft Inc.) macro for the design of ELPs. The model will enable *de novo* design of ELPs wherein given a desired T_t in physiological buffer, the model will provide a set of ELPs (sequence and length combinations) that will exhibit that T_t across a specific concentration regime, thereby greatly facilitating the design of new ELPs. One of its most useful applications is likely to be in the design of ELPs that exhibit a T_t in aqueous solution under physiologically relevant conditions, thereby greatly facilitating their use in medicine and biotechnology.

4.8 Materials and Methods

4.8.1 Materials

Restriction enzymes, calf intestinal phosphatase (CIP), and T4 DNA ligase were purchased from New England Biolabs (Ipswich, MA). The pET 24a(+) cloning vector was purchased from Novagen Inc. (Madison, WI), and all custom oligonucleotides were synthesized by Integrated DNA Technologies Inc. (Coralville, IA). The DNA miniprep, gel purification, and PCR purification kits were purchased from Qiagen Inc. (Germantown, MD). EB5α™ and BL21™ *Escherichia coli* cells were obtained from Edge BioSystems (Gaithersburg, MD) and were grown in TBDry™ media (MO BIO

Laboratories, Inc; Carlsbad, CA). Chemicals used for the purification of ELPs include: IPTG (Gold Biotechnology; St. Louis, MO) and kanamycin (CalBioChem; San Diego, CA).

4.8.2 Methods

4.8.2.1 Elastin-like Polypeptide Synthesis and Nomenclature.

The synthetic genes for ELPs were assembled from chemically synthesized oligomers (IDT Inc.) by plasmid reconstruction recursive directional ligation (PRe-RDL) as described in Chapter 2 [153]. The oligomers used to construct each compositional library are described in Appendix 8.1. The ELP nomenclature used throughout this chapter is A[55]-Y, where X represents the fraction of alanine (A) in the guest residue composition (rest, valine (V)), and Y represents the length of the ELP in pentamers.

4.8.2.2 Expression of Elastin-like Polypeptides

BL21(DE3) cells transformed with an ELP-containing plasmid were used to inoculate a 250 mL flask containing 50 mL TBDry media supplemented with 45 μg/mL kanamycin. This flask was incubated on a shaker overnight at 200 RPM and 37°C before being used to inoculate six 4-L flasks containing 1 L of TBDry media, supplemented with 45 μg/mL kanamycin. These cultures were incubated on a shaker at 200 RPM at 37°C for 6 h, treated with 0.2 mM IPTG, and grown overnight.

4.8.2.3 Purification of Elastin-like Polypeptides

Escherichia coli expression cultures were centrifuged in 1 L bottles at 4°C for 10 min and 3,000 g to concentrate the cells. The supernatant was discarded and the cell pellet was resuspended in 10 mL PBS. The cells were placed on ice and were lysed via sonication for 3 min (10 s on, 40 s off) (S-4000 Misonix Sonicator; Farmingdale, NY). Polyethyleneamine (PEI; 0.7% w/v) was added to the lysate to precipitate nucleic acid contaminants, and the remaining cell debris was removed from the solution following centrifugation at 14,000 g for 10 min at 4°C. The ELP was then purified by two cycles of inverse transition cycling with minor modifications. The supernatant was heated to 60°C for 10 min, thereby inducing the ELP phase transition and precipitation of contaminant proteins, then immediately placed on ice to redissolve the ELP. Protein debris was removed by another centrifugation step (14,000 g, 10 min, 4°C). The supernatant (containing soluble ELP) was heated to 37°C, and NaCl crystals were added to a final concentration of 1-3 M to induce the ELP phase transition. ELP aggregates were precipitated by centrifugation (14,000 g, 10 min, 25°C), and the supernatant was discarded. The ELP was then resuspended in PBS, cooled, and centrifuged (14,000 g, 10 min, 4°C) to remove any remaining insoluble contaminants. This cycle (starting at the 60°C incubation) was repeated once more to yield the final product. The product was then dialyzed overnight in ddH_2O and lyophilized.

4.8.2.4 Analysis of Elastin-like Polypeptides

The purity of the ELPs was visually determined by SDS-PAGE, using 4-20% Tris-HCl Ready Gels (Bio-Rad, Hercules, CA) stained with $CuCl_2$ (0.5 M) (Appendix 8.3). MALDI-MS was performed with a PE Biosystems Voyager-DE instrument, equipped with a nitrogen laser (337 nm). Samples were prepared in a 50% (v/v) aqueous acetonitrile solution that contained 0.1% trifluoroacetic acid. The samples were analyzed in a sinapinic acid matrix, and all measured ELP masses were within a 0.5% margin of error (Appendix 8.4).

4.8.2.5 Thermal Turbidimetry

The optical density at 350 nm (OD_{350}) of each ELP was measured as a function of temperature on a UV-vis spectrophotometer equipped with a multicell thermoelectric temperature controller (Cary 300, Varian Instruments; Walnut Creek, CA). ELP solutions in PBS ranging in concentration from 2 to 100 μM were heated at a rate of 1°C/min. The T_t was defined as the inflection point of the turbidity plot. To measure transition temperatures above 80°C, the ELPs were diluted into known quantities of NaCl in PBS (0.25, 0.5, 0.75, 1.0, 1.5, 2.0, or 2.5 M NaCl) to lower the T_t. A linear extrapolation of the T_t as a function of NaCl concentration for each ELP concentration was then used to estimate the transition temperatures in PBS [184, 185].

4.8.2.6 Data Analysis

Non-linear regression analysis was performed with IBM SPSS Statistics 19.0 (SPSS, Chicago, IL). MATLAB (MathWorks; Natick, MA) was used to generate the 3-dimensional plot of the predicted T_t as a function of composition and chain length.

5. Development of Drug-Loaded Chimeric Polypeptides Micelles that Respond to Clinical Mild Hyperthermia

5.1 Motivation

Previous publications from our lab show that intravenously injected, thermally responsive ELP unimers allow thermal targeting of solid tumors by the application of mild hyperthermia to a solid tumor. This was achieved by tuning the ELP transition temperature between 39°C (slightly above physiological temperature) and 42°C (the temperature achieved with mild clinical hyperthermia) [186]. Because the physiological temperature is below the T_t, the ELP circulates systemically as a soluble unimer; upon reaching a heated tumor in which the temperature is above the T_t, the ELP undergoes its inverse phase transition and forms micron-sized aggregates that adhere to the tumor vasculature [187]. The localized aggregation of ELP in a tumor has been shown to increase uptake through two separate mechanisms. First, upon cessation of hyperthermia, the resolubilization of the ELP aggregates creates a steep transvascular concentration gradient that drives ELP extravasation into the tumor by diffusion. This effect was amplified by thermally cycling tumors in a two-step process: (1) inducing the accumulation of ELP aggregates by the application of mild hyperthermia to the implanted tumors; and (2) redissolving the ELP aggregates by turning off hyperthermia, which leads to an increase in drug accumulation within the tumor compared to passive diffusion under normothermic conditions or to a single cycle of hyperthermia [188]. Second, by complementary cell culture studies, we have previously shown that the

combination of hyperthermia and thermally triggered aggregation of ELP unimers increases cellular uptake by 2-fold *in vitro*, mediated through the interactions of the hydrophobic microscopic ELP aggregates with the cell membrane [189].

While these results were encouraging, two limitations needed to be solved to move this system into relevant preclinical animal models. First, the *in vivo* demonstration of thermal targeting with ELPs was performed with polypeptides that lacked a relevant therapeutic cargo (typically fluorophores or radionuclides were used in these studies) and these markers were attached at low conjugation ratios (< 1 wt%) to a single reactive site on the ELP [57, 187-190]. We solved this problem by converting the ELP into a chimeric polypeptide by appending a drug conjugation peptide segment that provides a tunable number of reactive sites (typically 8 per CP, though this number can be increased at will) so as to increase the number of drug molecules conjugated per polypeptide chain.

The second problem –that of the steep dependence of the ELP transition temperature on ELP concentration– was more critical, as it only provides a narrow temporal window in which focused mild hyperthermia of tumors could be applied, especially if repeated cycles of hyperthermia were required to increase the accumulation of the ELP within a tumor. This is because the temperature required to trigger aggregation of the ELP steeply increases as the ELP concentration within the blood is reduced through renal clearance, degradation, and normal tissue or tumor uptake. Once

the transition temperature increases above the hyperthermic tumor temperature (42°C) because of dilution effects, the ELP loses its thermal targeting capability. The self-assembly of a CP into nanoparticles upon the attachment of drugs provides a solution to this problem, as these drug-loaded nanoparticles display almost no dependence on concentration in their thermal phase behavior and enable a useful amount of drug (~5 wt%) to be loaded into the nanoparticle via chemical conjugation, a strategy that we have previously shown provides a nanoparticle formulation of Dox that is highly potent *in vivo* [191]. However, in that study, the CP-Dox nanoparticle was not designed for thermal targeting and consequently had a T_t that was far too high to be useful for tumor targeting by mild hyperthermia. To address this limitation, this chapter demonstrates that the CP can be redesigned to display a thermally triggered phase transition from nanoparticles to microscopic aggregates *in vivo* in response to mild hyperthermia, without compromising drug loading, stability, cytotoxicity, or *in vivo* pharmacokinetics and biodistribution. These attributes will finally allow us to exploit thermal targeting for the *in vivo* delivery of chemotherapeutics to solid tumors in relevant preclinical animal models.

5.2 Development of a Mathematical Model to Describe the Phase Transition of Chimeric Polypeptide Nanoparticles

Because the CP conjugates analyzed in Chapter 3 displayed an *in vivo* transition temperature (T_t) of ~50°C, we had to design new CPs that would be responsive within

the desired physiological range of 39-42°C. To this end, we created a series of CPs by appending the drug attachment domain $(Cys\text{-}Gly\text{-}Gly)_8$ to the C-terminus of each ELP listed in the Chapter 4. The drug attachment domain consists of eight cysteines that provide unique reactive thiols for site-specific conjugation and seven digylcine spacers that reduce steric hindrance between the conjugated molecules. We selected the maleimide derivative n-benzylmaleimide for conjugation to the drug attachment sites because it displays sufficient hydrophobicity to drive assembly of CP nanoparticles, and the reaction is rapid, low cost, and can be performed in a single step. The thermal properties of the 24 unique CP nanoparticles formed by n-benzylmaleimide attachment were then measured with respect to CP concentration and fit to Eq. 3 via multivariate analysis to determine the values of T_{tc}, k, and C_c (Table 4).

Table 4: Summary of multivariate fits to Equation 1 for CP nanoparticles[a]

*f*Alanine	T_{tc} (°C)	k (°C·pentapeptides)	C_c (μM)	r^2	n
1	45.7 (0.3)	63.6 (7.6)	4.0E+05 (5.2E+05)	0.99	15
0.9	40.4 (0.5)	49.3 (13.3)	2.7E+06 (9.3E+06)	0.97	15
0.8	37.6 (0.2)	35.0 (6.2)	4.4E+07 (1.2E+08)	0.99	15
0.7	33.7 (0.2)	37.8 (4.7)	9.9E+06 (1.6E+07)	0.99	15
0.6	31.0 (0.2)	36.4 (4.1)	1.4E+07 (2.1E+07)	0.99	15
0.5	28.7 (0.2)	23.4 (4.7)	1.5E+09 (5.5E+09)	0.99	15
0.2	23.4 (0.2)	16.5 (4.6)	7.8E+08 (3.9E+09)	0.98	15
0	20.8 (0.2)	22.6 (3.9)	1.8E+05 (3.1E+05)	0.98	15

[a]Data fit to Equation 1 and reported as estimate (standard error).

Because the baseline transition temperature T_{tc} represents the lowest attainable transition temperature for a given composition once length and concentration effects are saturated (the lowest critical solution temperature), the value for a given CP nanoparticle should not significantly deviate from that of the parent ELP. As expected, we observed that the T_{tc} values for the nanoparticles remained statistically indistinguishable from those of the unimer sequences ($p > 0.25$; pair-wise t-test, 7 DOF). We have also shown that CP-drug nanoparticles are highly insensitive to changes in the bulk polymer concentration because the local polymer concentration within the nanoparticle is high and invariant, suggesting that the nanoparticles should display a lower k value [76]. In fact, when compared with the unimer values, the nanoparticles exhibited an average 11-fold reduction in k. This reduction provides a distinct advantage when designing CPs to display a specific T_t. For example, the ELP unimers examined in Chapter 4 exhibit an average ΔT_t of 17.0 ± 12.4°C upon a 20-fold change in concentration, whereas the complement CP nanoparticles exhibit an average ΔT_t of 2.0 ± 0.9°C upon a 25-fold change in concentration. This demonstrates that while ELP unimers can be designed to display a specific thermal behavior within a defined concentration window, CP nanoparticles can be designed to transition in response to a specific temperature over a large range of concentrations. Finally, the parameter C_c, the theoretical concentration corresponding to the T_{tc}, was again highly variable due to its derivation from a

logarithmic ratio. The exceptionally large values were a byproduct of reducing the parameter k while maintaining the T_{tc}.

The global dataset for the CP-drug nanoparticles was fit to Eq. 3, which yielded the following empirical model:

(5) $$T_t = 20.0e^{0.8*fAlanine} + \frac{17.1e^{1.2*fAlanine}}{Length}[\ln 6.4x10^6 - 0.4 * fAlanine - \ln(Conc)]$$

where *f*Alanine represents the guest residue composition of the ELP domain in terms of alanine (rest valine), Length represents the chain length of the polypeptide in pentapeptide units, and Conc represents the solution concentration of the CP.

Similar to the model developed for ELP unimers, the CP nanoparticle model also described 99% of the variability in the data (Figure 21A; r^2=0.994; n=120). While the distribution of the constructs follows a similar pattern to the global unimer fit (Figure 19A), the CP nanoparticle range is much smaller (64.8 - 21.2°C) than the ELP unimer range (135.8 - 23.1°C). This model demonstrates that CP-nanoparticles display a thermal behavior that is not only predictable and tunable, but also much less susceptible to concentration fluctuations than ELP unimers. This model enables the selection of specific molecular weight and composition pairs that display sharp phase transitions in response to specific temperatures in PBS (Figure 21B).

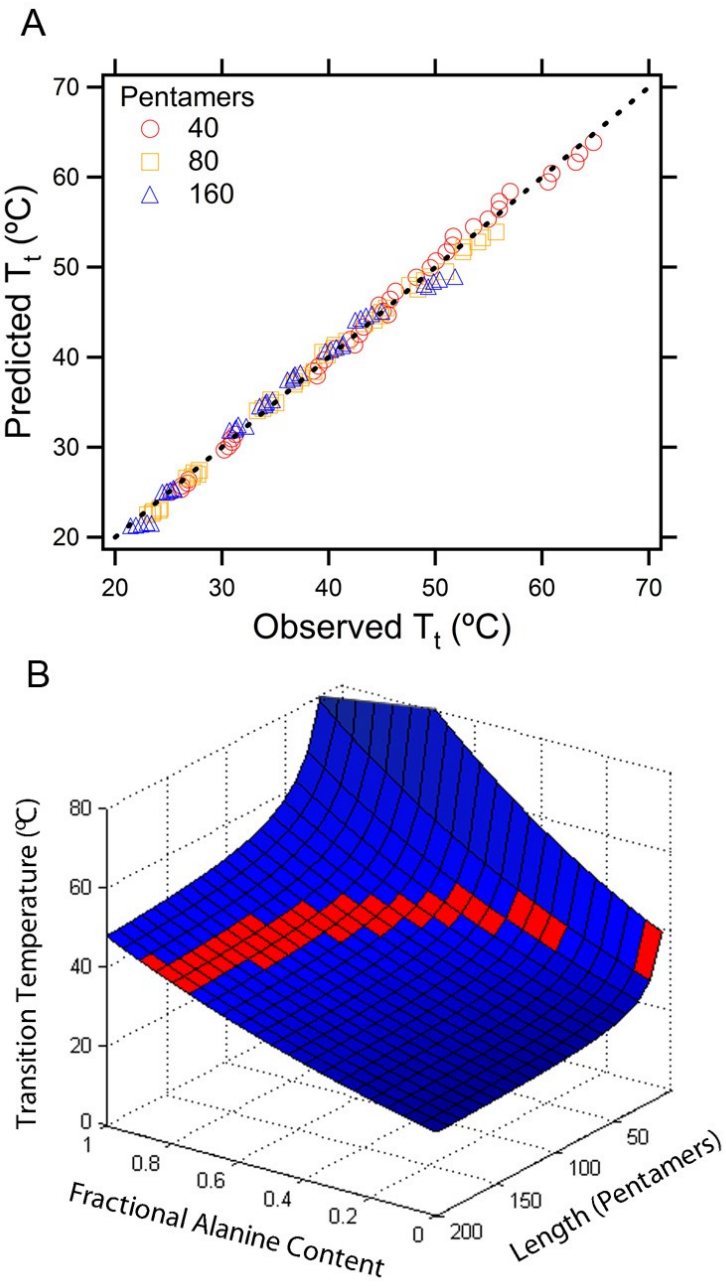

Figure 21: (A) Predicted versus observed transition temperatures for a global fit of CP nanoparticles in PBS (r^2=0.994; n=120). The CP nanoparticles were generated through the conjugation of n-benzylmaleimide to the C-terminal cysteine residues. (B) The model was used to predict the composition and length of a family of thermally responsive (39-42°C) CP nanoparticles (shown in red) at a concentration regime typical of CP drug delivery applications (25 μM).

Despite the utility of this model for the prediction of transition temperatures in phosphate buffered saline, it was essential to examine the thermal behavior of the CP nanoparticles in a relevant medium. This is necessary because the ions and proteins in serum lower the transition temperature from the values measured in PBS [187]. In order to mimic the vascular environment, we measured each of the CP nanoparticles in 90% fetal bovine serum (FBS) at a fixed concentration of 50 μM (Figure 22). We were able to screen the phase transition behavior of nanoparticles generated by attaching the model compound n-benzylmaleimide because the transition profiles between these nanoparticles and those generated through the attachment of other compounds such as n-pyrenylmaleimide and doxorubicin remained nearly indistinguishable (less than 1°C) in 90% FBS (Table 5), which suggests that the curves in Figure 22 can be used to predict transition temperatures for a variety of CP conjugates *in vivo*. It can also be seen that the three CP-drug nanoparticles selected for doxorubicin attachment (indicated by arrows in Figure 22) represent potential compositions at each length (40, 80, and 160 pentamers) that can be used to induce a nanoparticle-to-aggregate transition in conditions of mild hyperthermia.

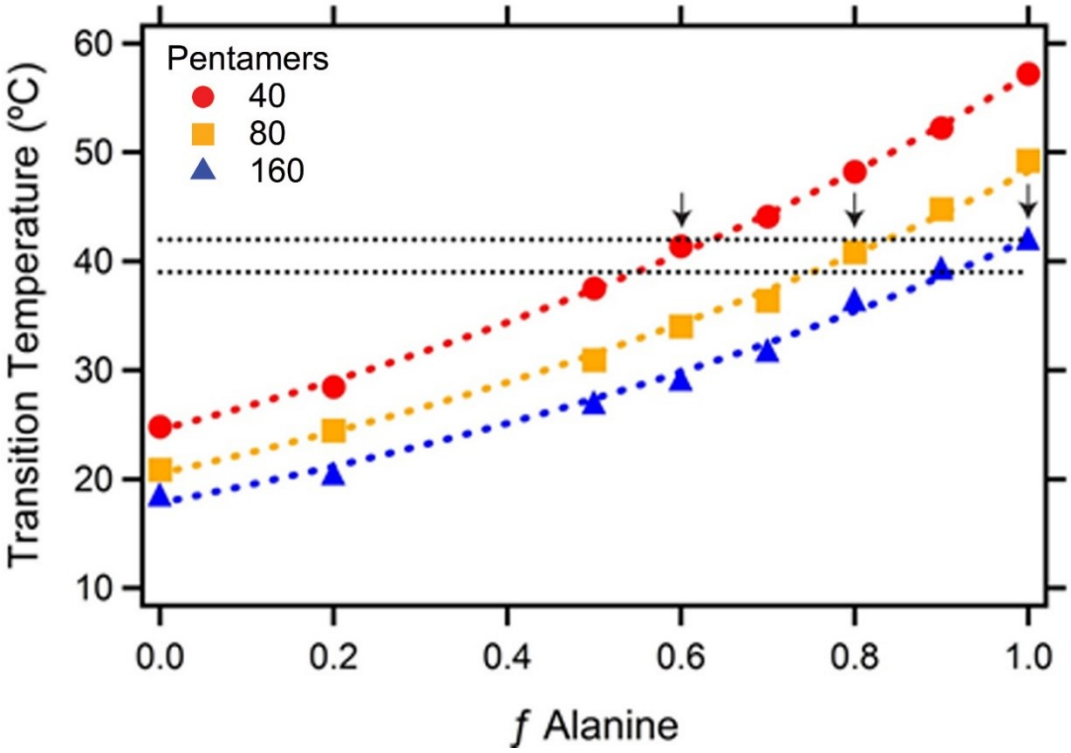

Figure 22: Observed (markers) transition temperatures for CP nanoparticles (conjugated to n-benzylmaleimide) in 90% FBS. Dashed lines represent the best exponential fit. Black dashed lines demarcate the targeted range of hyperthermia (39 to 42°C). Indicated constructs (↓) represent those selected for additional *in vivo* thermal targeting studies.

Table 5: Phase transition temperature of three CP nanoparticles of varying molecular weight in 90% FBS in response to conjugation to three compounds

		Observed T_t (°C, 50 μM) [a]		
***f*Alanine**	**Length**	**N-Benzylmaleimide**	**N-Pyrenylmaleimide**	**Doxorubicin**
1	160	42.7 (0.6)	43.2 (0.1)	42.9 (1.1)
0.8	80	40.5 (0.2)	40.7 (0.1)	39.8 (0.4)
0.6	40	40.5 (0.7)	40.8 (0.2)	39.8 (0.3)

[a]Data reported as estimate (standard error)

5.3 Screening Physicochemical Properties of Chimeric Polypeptide Nanoparticles as a Function of Chain Length

The model presented in Figure 21 (transition temperatures in PBS) and Figure 22 (transition temperatures in 90% FBS) indicates that there are numerous combinations of chain length and sequence capable of transitioning within the narrow temperature window of 39-43°C. To narrow the field of candidates, we selected chimeric polypeptides of three different molecular weights (15, 30, and 60 kDa) from within this thermal window for three reasons: first, these specific chain lengths were generated in the recursive cloning process and required no further processing prior to expression and purification. Second, these sizes span the range of the chimeric polypeptides used to construct the mathematical model. Lastly, this size range also supplies polypeptides that are both above (60 kDa) and below (30 and 15 kDa) the estimated renal filtration cutoff, which has consistently played a strong role in the plasma clearance of macromolecular carriers [192, 193].

5.3.1 Light Scattering Analysis

To examine how chain length influences the physicochemical properties of the nanoparticles, each of these constructs were separately conjugated to the chemotherapeutic doxorubicin via an acid labile heterobifunctional linker to drive self-assembly into nanoparticles and enable the rapid intracellular release of the drug once

exposed to the low pH of the late endosome [88]. Upon conjugation, the CPs spontaneously assembled into micelles with a hydrodynamic size that linearly correlated with chain length (Figure 23). Static light scattering analysis indicated that the average number of chains per micelle (calculated by dividing the absolute molecular weight of the assembled structure by the polypeptide molecular weight) was inversely proportional to the chain length, with the micelles comprised of 160 pentamer units displaying 13 chains per structure, the 80 pentamer units 18 chains per structure, and the 40 pentamer units 45 chains per structure.

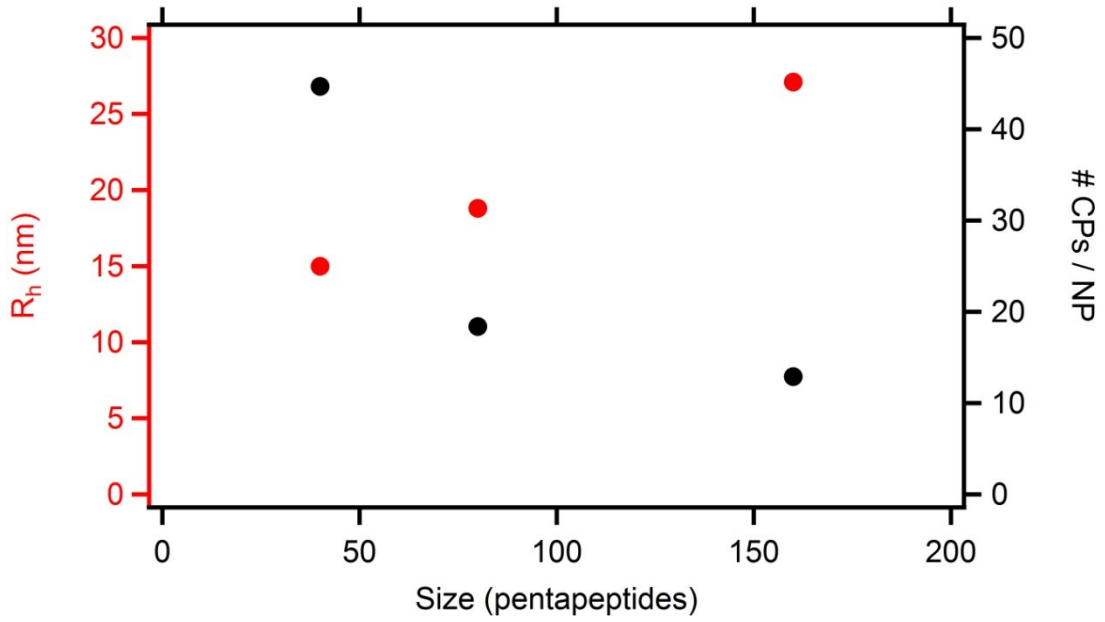

Figure 23: Light scattering analysis of CP-Dox nanoparticles. Points in red represent the hydrodynamic radius, and the points in black represent the average number of CPs per nanoparticle as calculated by dividing the absolute molecular weight of the micelle by the molecular weight of the CP.

5.3.2 In Vitro Cytotoxicity

After verifying that doxorubicin conjugation initiated the formation of micelle structures, we next examined how chain length affected cytotoxicity *in vitro*. C26 cells isolated from a murine colon adenocarcinoma were exposed to CP-Dox nanoparticles over a wide range of concentrations (0.001 to 60 μM Dox equivalents) for a period of 72 hours. Following this incubation period, a 3-(4,5-dimethylthiazol-2-yl)-5-(3-carboxymethoxyphenyl)-2-(4-sulfophenyl)-2H-tetrazolium (MTS) assay was performed to measure the metabolic viability of the cells as measured by the IC_{50}, or the concentration of drug necessary to inhibit cellular proliferation by 50%. We observed that chain length did not significantly alter the measured IC_{50} (Free Dox: 0.2 ± 0.1 μM; 40 pentamer construct: 2.6 ± 0.8 μM; 80 pentamer construct: 1.7 ± 0.5 μM; and 160 pentamer construct: 1.5 ± 0.2 μM). However, similar to other systems that rely on chemical conjugation (rather than physical encapsulation), conjugation to the CPs resulted in an approximately 11-fold reduction in activity compared to free doxorubicin [88, 194, 195].

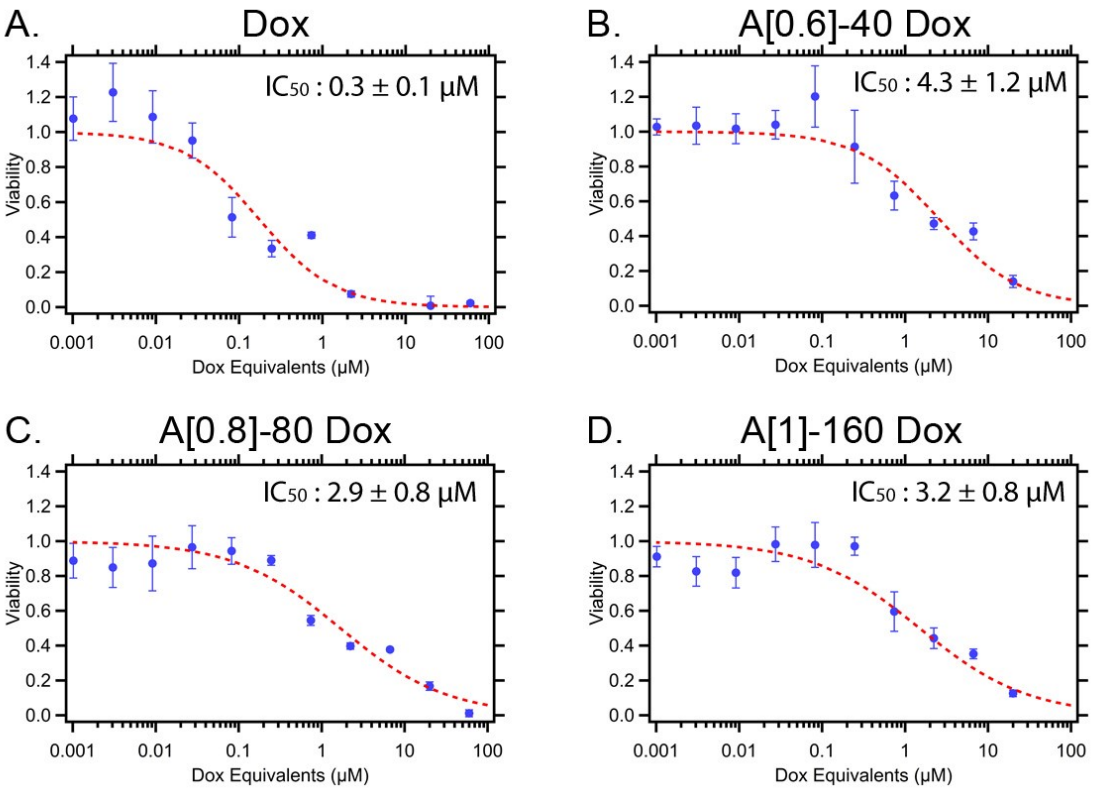

Figure 24: ***In vitro*** **toxicity against a C26 murine colon carcinoma line for (A) free doxorubicin, (B) A[0.6]-40-Dox, (C) A[0.8]-80-Dox, and (D) A[1]-160-Dox. Data shown as mean ± SD averaged over three independent experiments. The dashed line represents the best fit of the equation Viability = 1 / (1 +** $(C_{Dox}/IC_{50})^{p}$**), where** C_{Dox} **is the effective Dox concentration in the well, the** IC_{50} **measures the necessary dose to inhibit cell proliferation by 50%, and** p **represents the slope of the sigmoidal curve.**

5.3.3 Pharmacokinetic Analysis

To determine the pharmacokinetic parameters of the CP-Dox nanoparticles, the plasma doxorubicin concentration was longitudinally tracked over a period of 48 hours following systemic administration to mice via tail vein injection (Figure 25A). We found that these nanoparticles followed a two compartmental model (Figure 25B), signifying

that plasma drug concentration declined biexponentially as two first order processes: distribution and elimination [196]. Immediately following injection into the central compartment (comprised of the blood, extracellular fluid, and highly perfused tissues such as the liver and kidneys) the drug is considered homogeneously distributed. In the α-phase (distribution phase), the drug concentration in the central compartment rapidly diminishes by partitioning into the surrounding tissue (the peripheral compartment). While excretion does occur in the distribution phase, this effect is generally negligible in comparison to the net transfer of drug to the peripheral tissues. In the β or elimination phase, the drug concentration in the peripheral compartment has already reached equilibrium with the central compartment, and the amount of drug in both tissues declines as a first order process due to elimination. In the model shown in Figure 25B, drug elimination is assumed to occur from the central compartment because the kidneys, responsible for renal excretion, and the liver, responsible for metabolic degradation of the drug, are both highly perfused organs.

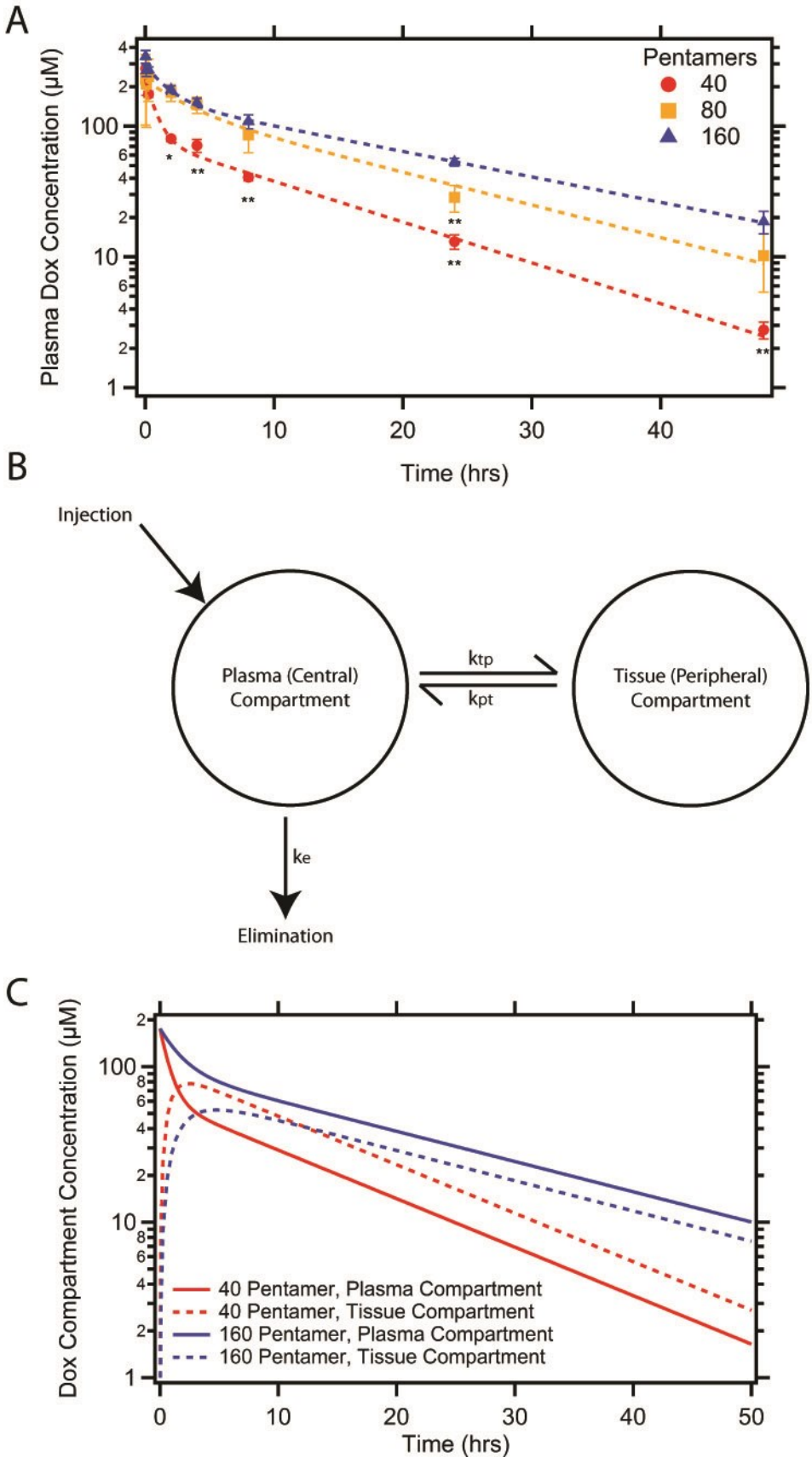
A
Plasma Dox Concentration (μM)
Pentamers
40
80
160
Time (hrs)
B
Injection
Plasma (Central) Compartment
ktp
kpt
Tissue (Peripheral) Compartment
ke
Elimination
C
Dox Compartment Concentration (μM)
40 Pentamer, Plasma Compartment
40 Pentamer, Tissue Compartment
160 Pentamer, Plasma Compartment
160 Pentamer, Tissue Compartment
Time (hrs)

Figure 25: Pharmacokinetic parameters of CP-Dox micelles. (A) Plasma concentration of doxorubicin-loaded chimeric polypeptide nanoparticles following systemic administration into mice. The data points represent mean ± SD (n=3) and the dashed lines represent the curves of best fit to the two compartment model by SAAM II. Significance (one-way ANOVA, Tukey post-hoc) was calculated for A[0.6]-40-Dox and A[0.8]-80-Dox against the A[1]-160-Dox for all time points. *p<0.05 and **p<0.005 (B) Diagram of a two compartmental model. (C) Compartmental analysis of CP-Dox. The theoretical drug concentration in the plasma and tissue compartments for A[0.6]-40-Dox and A[1]-160-Dox as a function of time.

Table 6: Half-life and area under the curve of CP-Dox micelles of varying size[a]

Parameter		A[0.6]-40	A[0.8]-80	A[1]-160
elimination half-life	β $t_{1/2}$ [hr]	9.6 (0.4)	12.1 (1.0)	15.5 (0.9)
area under the curve	AUC [μM hr]	1202.9 (42.8)	2690.5 (119.6)	3734.6 (112.3)

[a]Data represent the mean (SD) of the best fit parameters determined by SAAM II.

Table 6 indicates that chain length does play a significant role in the pharmacokinetics of CP-Dox micelles, with the 160 pentamer construct exhibiting a β elimination half-life of 15.5 hours, followed by the 80 pentamer construct at 12.1 hours, and the 40 pentamer construct at 9.6 hours (see Table 16 in Appendix 8.8 for the complete list of parameters). However, the most descriptive parameter for determining the efficacy of a given treatment is the area under this curve (AUC), as it describes the total drug exposure of an area over the time course of the experiment. Similar to the half-life, the AUC was the greatest for the longest chain length (160 pentamers) and decreased to 72% for the 80 pentamer construct, and 32% for the 40 pentamer construct.

Figure 25C illustrates the theoretical distribution of the 160 pentamer and 40 pentamer construct in the plasma and tissue compartments as a function of time. Interestingly, the theoretical doxorubicin concentration in the peripheral tissues rises to a maximum of 53 μM over a period of approximately 4.7 hours for the 160 pentamer construct, but rapidly peaks to 78 μM in only 2.4 hours for the 40 pentamer construct. In fact, the 40 pentamer construct preferentially partitions into the peripheral compartment to such a degree that within the first 1.5 hours following administration, the majority of the delivered doxorubicin exists within the peripheral compartment. This is in contrast to the 160 and 80 pentamer constructs, which establish a two compartmental equilibrium in which the plasma concentration is consistently higher than the tissue concentration.

5.3.4 Biodistribution Analysis

Following pharmacokinetic analysis, it was necessary to validate the biodistribution of the three conjugates with the intent to select the conjugate with the lowest instance of accumulation within the heart and general off-target toxicity. Reduction of the doxorubicin levels in the heart is particularly critical as cardiomyopathy is the primary dose-limiting factor for doxorubicin treatment in the clinic. As it was unknown whether inducing the phase transition within the tumor would influence the biodistribution of the drug, the mice were administered CP-Dox via tail vein injection, and the tumor, which was inoculated on the right flank of the mouse,

was immediately heated to 42°C via water bath for 1 hour. The mice were sacrificed 24 hours following administration and the doxorubicin concentration within the tissue was quantified via a fluorescent plate assay.

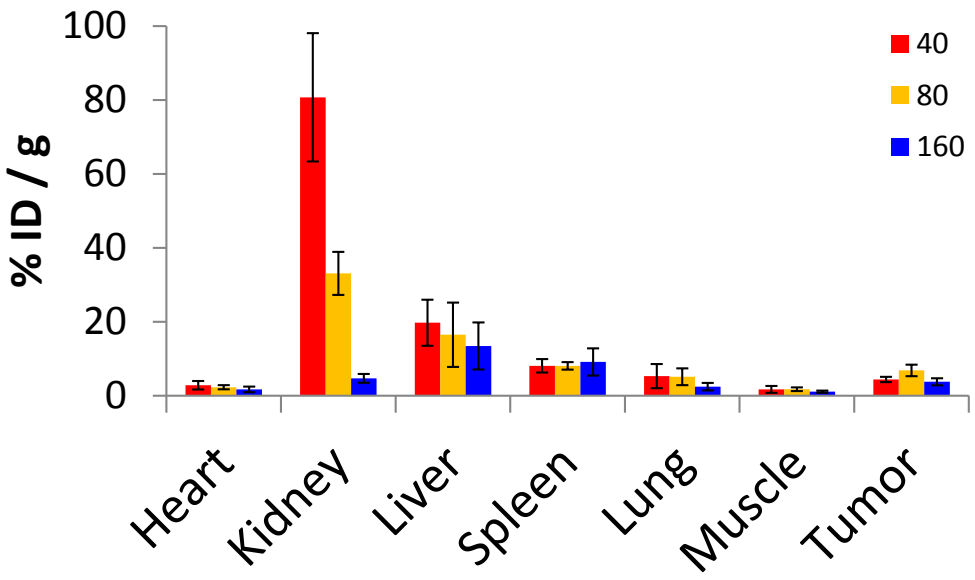

Figure 26: Doxorubicin concentration in select tissues 24 h following tail vein administration of doxorubicin loaded micelles assembled from 40, 80, and 160 pentamer chain lengths. Immediately following injection, the tumor-bearing leg was heated to 42°C for 1 h. The data represent the mean ± SD.

Figure 26 illustrates the doxorubicin load in each of the seven primary tissues examined 24 hours following administration. In general, accumulation was correlated with chain length, with higher molecular weight constructs showing a decrease in accumulation. This effect was most notable in the kidneys, which exhibited a marked decrease in accumulation when comparing the 40 pentamer construct (81 ± 17 %ID/g) to

the 80 (33 ± 6 %ID/g) and the 160 (5 ± 1 %ID/g). Compared to the 40 pentamer construct, the 160 pentamer conjugate also demonstrated a 33% reduction in liver accumulation and a 40% reduction in heart accumulation, supporting the results observed in the two compartmental pharmacokinetic model. Future studies would benefit from performing bone marrow analysis, as this also represents a primary target of doxorubicin toxicity [197].

The finding that micelles assembled from chains of varying molecular weight exhibit an altered pharmacokinetic and biodistribution profile suggests that the molecular weight of the individual chains comprising the higher order structure is a critical design parameter. This observation is likely a result of continual renal filtration of the single chain polymer, whose molecular weight is below the estimated renal filtration cutoff of 50 kDa for both the 40 (15 kDa) and 80 (30 kDa) pentamer constructs, as noncovalently assembled higher order systems exist in dynamic equilibrium with their single chain components. In fact, this phenomena has been observed in a variety of systems including diblock micelles [198] and multisubunit enzymes [199].

These data, in combination with the pharmacokinetic profile indicate that micelles constructed with higher molecular weight chains retain doxorubicin in the plasma for a longer period of time (longer half-life), thereby increasing the overall exposure of the tumor vasculature to the drug (higher AUC). Furthermore, they also exhibit a lower concentration of drug within the tissue compartment, thus reducing

systemic toxicity. In particular, the high overall toxicity associated with significant drug accumulation in the kidneys suggest that the 160 pentamer construct will provide both an enhanced anti-tumor effect over shorter chain lengths and a significant reduction in off-target toxicities. Hence, we selected the 160 pentamer chain length for use in all following studies.

5.4 Validation of the In Vivo Micelle Phase Transition

Following selection of the 160 pentamer construct for further examination, it was necessary to confirm that the micelles would reversibility phase separate *in vivo* within the thermal window of 39-43°C. To accomplish this, we utilized a dorsal skin fold tumor window chamber model, which allows the visualization of the tumor vasculature in real time using an epifluorescent confocal microscope. We examined three chimeric polypeptide micelles: (1) a hydrophilic control with a chain length of 160 pentamers and a guest residue composition of X=Ala_1Gly_1. This micelle phase separates at 50°C in physiological media, and hence should not display thermal sensitivity within the range of 39-43°C. (2) A thermally responsive formulation of 160 pentamers and a guest residue ratio of X=Ala_9Val_1 that phase separates at 39°C in physiological media, and (3) a thermally responsive formulation of 160 pentamers and a guest residue of Ala that displays a phase transition at 42°C. Each of the CPs were labeled on the amino-terminus with a rhodamine dye derivative, which supplies red fluorescence and did not perturb

assembly or the transition temperature. The CPs were assembled into spherical micelles through the attachment of n-pyrenylmalemide to the unique cysteines localized to the carboxy-terminus. Pyrenylmalemide was selected over doxorubicin for two reasons. First, doxorubicin supplied the presence of a second, albeit weak, fluorophore that quenched rhodamine fluorescence (data not shown). Second, as the CP formulation extravasated into the tumor extracellular matrix, doxorubicin was released from the micelle, leading to an increase in background signal that further reduced image quality.

A large molecular weight (2 MDa) dextran conjugated to fluorescein was co-injected with the CP micelles to provide a distinct green vascular mask. The color balance was then adjusted to provide a yellow overlay in the presence of both soluble green dextran and soluble red CP micelles. As the control CP has a transition temperature higher than 42°C, it is homogenously distributed throughout the vasculature at both 37 and 42°C (Figure 27A, B). In contrast, the thermally responsive CP micelle formulation, which phase separates at 39°C, is soluble at 37°C, as observed by the homogenous yellow overlay. However, as the tumor is heated to 42°C, the CP demonstrates a rapid and robust phase separation into micron-sized hydrophobic spheroids seen throughout the vasculature (Figure 27C, D). We also observed that the degree of phase separation could also be controlled through the transition temperature. Figure 27E shows the rhodamine-labeled CP micelle channel for A[1]-160, which displays a transition temperature at 42°C. While this thermal stimulus was sufficient to

induce a response (image taken after 30 minutes of heating), it was not nearly as robust a response as seen by A[0.9]-160 (image taken after 10 minutes of heating), which displays a transition temperature of 39°C.

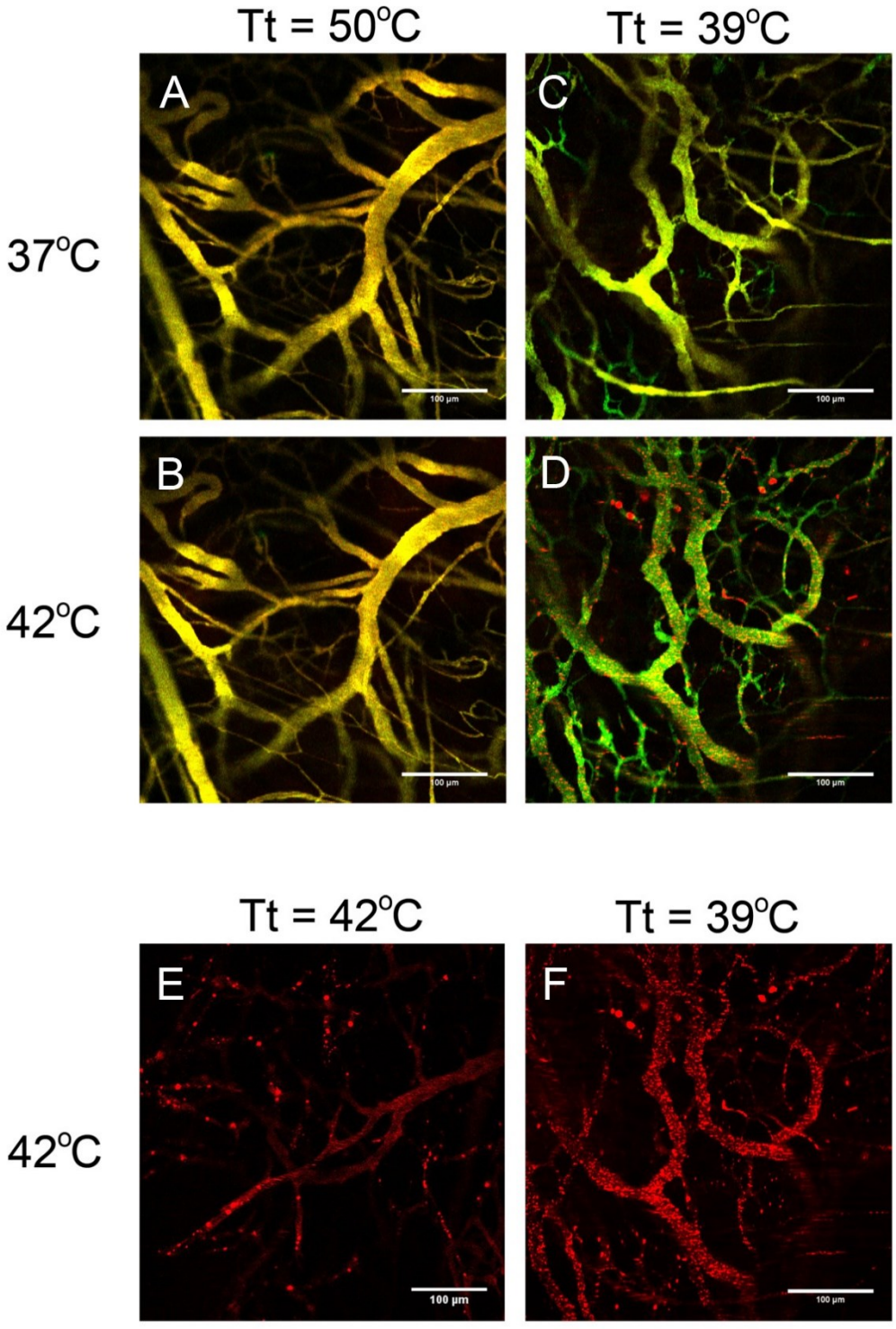
Tt = 50°C
Tt = 39°C
37°C
42°C
A
B
C
D
100 µm
Tt = 42°C
Tt = 39°C
42°C
E
F
100 µm

Figure 27: *In vivo* visualization of the phase transition in response to heat. A control CP micelle formation with a transition temperature of 50°C remained soluble when heated to (A) 37°C and (B) 42°C for 10 min each. A thermally responsive micelle formulation that transitions at 39°C remains soluble at (C) 37°C for 10 min but phase separates at (D) 42°C (image taken after 10 min). The red CP-rhodamine channel for (E) A[1]-160 (T_t = 42°C) held at 42°C for 30 min and (F) A[0.9]-160 (T_t = 39°C) held at 42°C for 10 min. Scale bars represent 100 nm.

With a clear phase separation occurring selectively between 39 and 42°C, we next examined whether the phase transition was reversible under physiological conditions. Figure 28 shows images of the green (fluorescein-dextran) and red (CP-rhodamine) channels as the temperature is slowly ramped from 37 to 42 to 37°C. At 37°C, the CP micelles are homogeneously distributed throughout the vasculature. As the temperature approaches 42°C, the micelles coalesce into discreet hydrophobic aggregates (visualized by the punctate red fluorescence) that fully dissipate upon cooling.

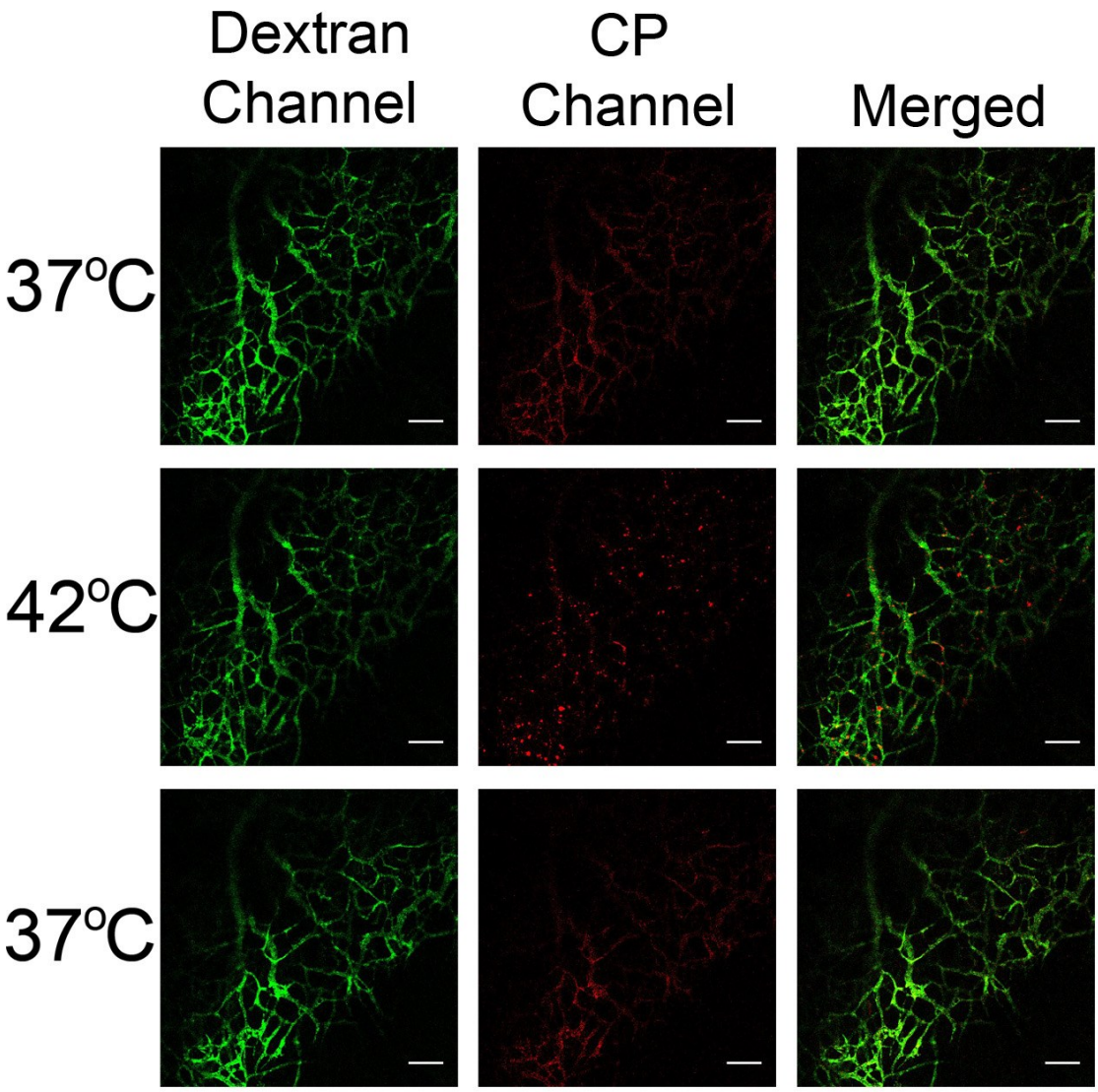

Figure 28: Confocal images of tumor vasculature containing 2 MDa dextran (green) and CP-Rhodamine (red) as the vasculature is heated from 37 to 42°C and then cooled back to 37°C. The scale bars represent 100 nm.

5.5 Triggering the Phase Transition to Induce Drug Accumulation within a Solid Tumor

Finally, it was necessary to examine whether triggering the phase transition increased drug accumulation within the tumor. To test this hypothesis, we administered the same control (T_t=50°C) and thermoresponsive (39°C) CP-Dox formulations as described above to Balb/c mice bearing a murine C26 colon carcinoma in their hind leg. Each treatment was then subdivided into three experimental cohorts: mice receiving (1) no thermal therapy; (2) one hour of hyperthermia applied by submerging the hind leg of the mouse in a water bath heated to 42°C; and (3) one hour of hyperthermia divided into six intervals of 10 minutes of heat followed by 10 minutes without heat (Figure 29). The mice were sacrificed 2 hours following administration of the drug, and the Dox concentration in the tumor was measured via a fluorescent plate assay. Surprisingly, one hour of hyperthermia increased the accumulation of Dox within the tumor by 50% for both CP-Dox constructs, signifying that the effects of hyperthermia - and not the phase transition - dominated the biodistribution of the CP carrier under these conditions. However, when the same one hour of hyperthermia was divided into six separate heating and cooling cycles, the control CP showed the same ~50% increase in accumulation while the thermoresponsive CP exhibited a 160% increase ($p<0.001$).

We hypothesize that because the physiological temperature is below the T_t in systemic circulation, the CP circulates as a soluble nanoparticle; upon reaching a heated tumor in which the temperature is above the T_t, the CP undergoes its inverse phase

transition and forms micron-sized aggregates that adhere to the tumor vasculature. Upon cessation of hyperthermia, the rapid resolubilization of the CP aggregates creates a steep transvascular concentration gradient that drives CP extravasation into the tumor by diffusion. This hypothesis suggests that the accumulation of drug positively correlates with the number of heating and cooling cycles, and thus it may be possible to further augment the efficacy of this strategy by simply increasing the number of cycles. This is currently under investigation.

In addition to doxorubicin taken up by tumor cells upon CP-Dox extravasation across the vasculature, it is also possible that the tumor endothelial cells will experience vascular damage and perfusion shut down following such high levels of exposure to doxorubicin. Although the thermally sensitive liposome formulations that typically observe this effect are capable of achieving much higher vascular concentrations of doxorubicin [124], the phase separated CP-doxorubicin is in direct contact with sections of the vasculature for the length of the hyperthermia treatment (Figure 27D, E). Future studies may use window chamber analysis to quantitatively determine whether phase transitioned CP-Dox similarly alters vasculature health and perfusion.

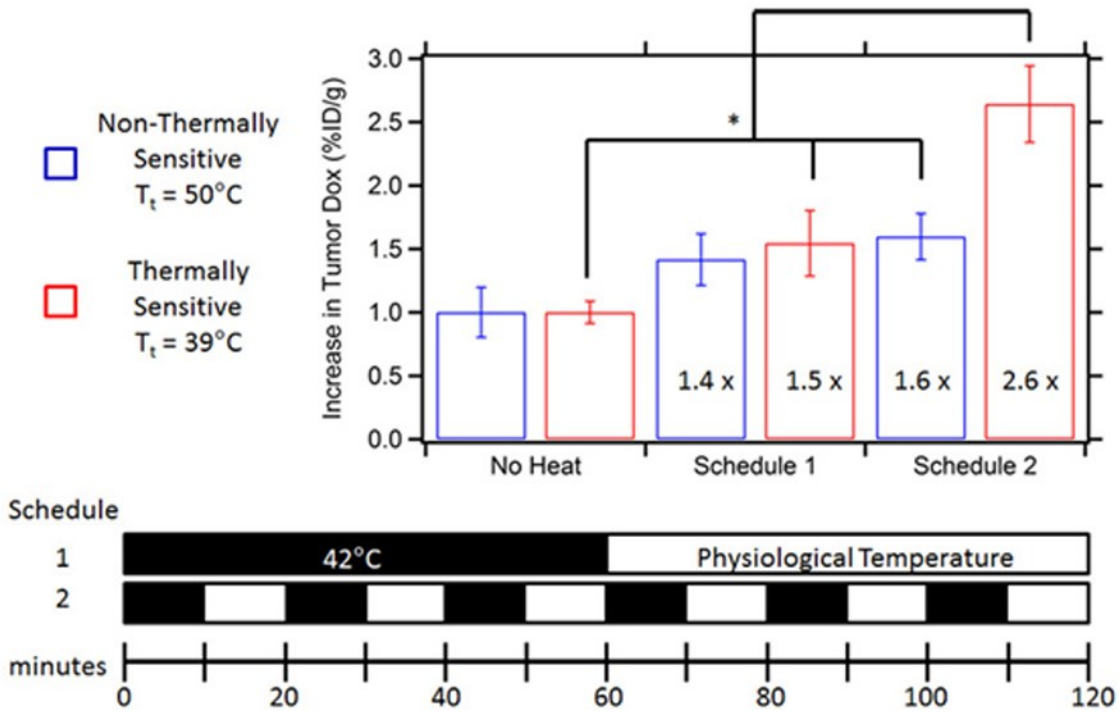

Figure 29: Tumor biodistribution of a thermally responsive and a control CP-Dox nanoparticle formulation following two heating schedules. Mice were sacrificed 120 min following drug administration. * $p < 0.05$.

5.6 Conclusions

In this chapter, we demonstrate that the micelle-to-aggregate transition temperature of CP nanoparticles can be predicted by their sequence, chain length, and concentration, and visually confirm that the phase separation is reversible and occurs within the narrow temperature range of 39-43°C *in vivo*. Cyclically heating the tumors following injection of the thermoresponsive CP-Dox formulation resulted in significantly enhanced drug accumulation over non-thermally responsive formulations and over thermally responsive and non-responsive controls subjected to hyperthermia

without cycling. We hypothesize that this increase is due to the creation of a steep transvascular CP-Dox concentration gradient upon cooling that is capable of pumping the soluble conjugate across the vascular and interstitial fluid pressure barrier. These results suggest that thermally cycling tumors will provide a significant boost in efficacy for thermally responsive CP nanoparticles. This hypothesis is currently under investigation.

5.7 Materials and Methods

5.7.1 Materials

Restriction enzymes, calf intestinal phosphatase (CIP), and T4 DNA ligase were purchased from New England Biolabs (Ipswich, MA). The pET 24a(+) cloning vector was purchased from Novagen Inc. (Madison, WI), and all custom oligonucleotides were synthesized by Integrated DNA Technologies Inc. (Coralville, IA). The DNA miniprep, gel purification, and PCR purification kits were purchased from Qiagen Inc. (Germantown, MD). EB5α™ and BL21™ *Escherichia coli* cells were obtained from Edge BioSystems (Gaithersburg, MD) and were grown in TBDry™ media (MO BIO Laboratories, Inc; Carlsbad, CA). Chemicals used for the purification of ELPs include: IPTG (Gold Biotechnology; St. Louis, MO), TCEP (Thermo Scientific; Waltham, MA), and kanamycin (CalBioChem; San Diego, CA).

5.7.2 Methods

5.7.2.1 Chimeric Polypeptide Synthesis and Nomenclature

The synthetic genes for CPs were assembled from chemically synthesized oligomers (IDT Inc.) by plasmid reconstruction recursive directional ligation (PRe-RDL) as described in Chapter 2. The oligomers used to construct each compositional library are described in Appendix 8.1. The CP nomenclature used throughout this chapter is A[X]-Y, where X represents the fraction of alanine (A) in the guest residue composition (rest, valine (V)), and Y represents the length of the CP in pentamers. Each CP contains an N-terminal $(CGG)_8$ domain that can be covalently conjugated to drugs (*e.g.*, A[X]-Y Dox indicates the covalent conjugation of Dox to the unique Cys residues in the $(CGG)_8$ domain).

5.7.2.2 Expression of Chimeric Polypeptides

BL21(DE3) cells were transformed with an CP-containing plasmid and were used to inoculate a 250 mL flask containing 50 mL TBDry media supplemented with 45 μg/mL kanamycin. This flask was incubated on a shaker overnight at 200 RPM and 37°C before being used to inoculate six 4-L flasks containing 1 L of TBDry media, supplemented with 45 μg/mL kanamycin. These cultures were incubated on a shaker at 200 RPM at 37°C for 6 h, treated with 0.2 mM IPTG, and grown overnight.

5.7.2.3 Purification of Chimeric Polypeptides

Escherichia coli expression cultures were centrifuged in 1 L bottles at 4°C for 10 min and 3,000 g to concentrate the cells into a pellet. The supernatant was discarded and the cell pellets were resuspended in a total of 10 mL PBS. The cells were placed on ice and were lysed via 3 min of sonication (10 s on, 40 s off) (S-4000 Misonix Sonicator; Farmingdale, NY). Polyethyleneamine (PEI; final concentration of 1% w/v) was added to the lysate to precipitate nucleic acid contaminants, and the remaining cell debris was removed from the solution following centrifugation at 14,000 g for 10 min at 4°C. The ELP was then purified by two cycles of inverse transition cycling with minor modifications. The supernatant was heated to 60°C for 10 min, thereby inducing the CP phase transition and precipitation of contaminant proteins, then immediately placed on ice to redissolve the CP. Protein debris was removed by centrifugation (14,000 g, 10 min, 4°C). The supernatant (containing soluble CP) was heated to 37°C, and NaCl crystals were added to a final concentration of 1-3 M to induce the CP phase transition. CP aggregates were precipitated by centrifugation (14,000 g, 10 min, 25°C), and the supernatant was discarded. The CP was then resuspended in 20 mM Tris(2-carboxyethyl)phosphine hydrochloride (TCEP, pH 7.4), cooled, and centrifuged (14,000 g, 10 min, 4°C) to remove any remaining insoluble contaminants. This cycle (starting at the 60°C incubation) was repeated once more to yield the final product. The product was then dialyzed overnight in ddH_2O and lyophilized.

5.7.2.4 Analysis of Chimeric Polypeptides

The purity of the CPs was visually determined by SDS-PAGE, using 4-20% Tris-HCl Ready Gels (Bio-Rad, Hercules, CA) stained with $CuCl_2$ (0.5 M) (Appendix 8.3).

5.7.2.5 Conjugation of Molecules to Chimeric Polypeptides

15 mg of lyophilized CP was resuspended in 800 μL of 100 mM phosphate buffer, pH 7.4, and spiked with an additional 100 μL of 100 mM TCEP in water, pH 7.4. To generate the CP nanoparticles used to build the model, 100 μL of a 50 mM solution of n-benyzlmaleimide in DMSO was added to the CP solution dropwise, and allowed to mix for 3 h at room temperature. To generate fluorescent micelles, 0.2 mg of Rhodamine Red-X succinimidyl ester (Life Technologies; Carlsbad, CA) dissolved in 100 μL of DMSO was added to the CP solution dropwise, and allowed to mix for 3 h at room temperature. 3 mg of n-pyrenylmaleimide in 100 μL of DMSO was then added to the CP-Rhodamine solution dropwise, and allowed to mix for an additional 16 h at room temperature. Following conjugation, the CP conjugate was centrifuged at 13,000 g and 4°C for 10 min and purified by passage through a size exclusion column (PD10, GE Healthcare) and dialysis in ddH_2O overnight. The solution was then lyophilized and stored at 20°C for future use.

5.7.2.6 Thermal Turbidimetry

The optical density at 350 nm (OD_{350}) of each CP was measured as a function of temperature on a UV-vis spectrophotometer equipped with a multicell thermoelectric

temperature controller (Cary 300, Varian Instruments; Walnut Creek, CA). CP solutions in PBS ranging in concentration from 2 to 100 μM were heated at a rate of 1°C/min. The T_t was defined as the inflection point of the turbidity plot. To measure the transition in 90% fetal bovine serum (FBS), a 500 μM CP solution was diluted 10-fold into the FBS solution.

5.7.2.7 Conjugation of Doxorubicin

The conjugation of Dox to the CPs was performed as described elsewhere [88] with slight modifications. Dox was conjugated to the unique cysteine residues located on the C-terminus of the CP using the heterobifunctional linker n-β-maleimidopropionic acid hydrazide (BMPH; Pierce Biotechnology, Rockford, IL) in a two-step process. First, Dox (215 mg) and BMPH (100 mg) were codissolved in 100 mL of anhydrous methanol spiked with 100 μL of trifluoroacetic acid. This solution was stirred for 16 h at 20°C in the dark, dried using rotary evaporation, and then resuspended in 20 mL methanol. In the second step, this solution was immediately added dropwise to a solution containing the CP. Prior to this reaction, the CP was purified as described previously, incubated in a high capacity endotoxin removal resin (Thermo Scientific) for 2 h, and passed through a 0.2 μm filter. The CP solution was then incubated in 50 mM TCEP for 1 h at 20°C to eliminate disulfide crosslinking. Phase separation was triggered by the addition of crystallized NaCl to a final concentration of 1-3 M to remove excess TCEP and concentrate the CP solution. The pellet was then resuspended to a final concentration of

8.6 μmoles of CP in 10 mL of phosphate buffer (100 mM phosphate, 1 mM EDTA, pH 7.4). This solution was stirred for 3 h at 20°C in the dark, spiked with 1 mL of 100 mM TCEP (dissolved in water, pH 7), and then stirred for an additional 16 h. To purify the CP-Dox product, the methanol was first evaporated under a constant stream of N_2 to a total of 10 mL. A solution of 5 M NaCl was added to the CP-Dox solution to trigger phase separation (a 1:1 ratio was usually sufficient). This solution was centrifuged (5000 g, 10 min, 25°C), and the supernatant was discarded. The CP-Dox pellet was resuspended in PBS and centrifuged once more to remove any insoluble reactants (14000 g, 10 min, 25°C). Finally, the CP was purified from any remaining free drug reactants by passing the solution through a size exclusion column (PD10, GE Healthcare), dialyzing for 24-48 h (MWCO = 10-12 KDa) in 5 mM ammonium carbonate (pH 8.0), and lyophilizing for later use.

The degree of Dox conjugation to the CP was measured for each sample by resuspending 10-20 mg of lyophilized CP-Dox in 1 mL of PBS, and then dividing the concentration of Dox, determined via absorbance spectroscopy, by the concentration of CP. The CP concentration was determined gravimetrically on the lyophilized sample by adjusting for the added mass from the attached Dox-linker.

5.7.2.8 In Vitro Cytotoxicity

C26 murine colon carcinoma cells were maintained in complete media consisting of RPMI-1640 supplemented with 10% FBS, 4.5 g L^{-1} D-glucose, 10 mM HEPES, and 1

mM sodium pyruvate. Cells were maintained at 37°C and 5% CO_2 and passaged every 3 days. *In vitro* cytotoxicity was determined through the use of a colorimetric assay. $5x10^3$ C26 cells were seeded per 100 μL media on BD Falcon™ 96-well cell culture plates (BD; Franklin Lakes, NJ) and allowed to adhere for 24 h. The cell media was then removed and replaced with 120 μL complete media containing Dox or CP-Dox nanoparticles. The cells were incubated for 72 h at 37°C, after which 20 μL of CellTiter 96 AQueous™ (Promega; Madison, WI) 3-(4,5,-dimethyl2-yl)-5-(3-carboxymethoxyphenyl)-2-(4-sulfophenyl)-2H-tetrazolium (MTS) reagent was added to each well. The cells were incubated for an additional 30 min, and the absorbance of the solution was measured at 490 nm with a Victor³ microplate reader (Perkin Elmer; Waltham, MA). To calculate the IC_{50}, the data was fit to the equation: Viability = $1 / (1 + (C_{Dox}/IC_{50})^p)$, where C_{Dox} is the effective Dox concentration in the well, the IC_{50} measures the necessary dose to inhibit cell proliferation by 50%, and *p* represents the slope of the sigmoidal curve.

5.7.2.9 Pharmacokinetic Analysis

All animal experiments were done in accordance with Duke University's Institutional Animal Care and Use Committee. CP-Dox (15 mg Dox equivalents/kg body weight) was intravenously administered via tail vein into Balb/c mice. 10 μL blood was collected at select time points (40 s, 2 min, 5 min, 1 h, 2 h, 4 h, 8 h, 24 h) and diluted into 100 μL of heparin (1000 U/mL) in PBS. The samples were centrifuged (1000 g, 5 min, 4°C) to remove the red blood cells, and the Dox was released from the CP by incubating

10 μL of plasma in 490 μL of acidified isopropanol (75 mM HCl, 90% isopropanol) for 16 h at 4°C. The solution was loaded into a 96-well microplate in triplicate (125 μL per well), and Dox fluorescence was determined using a Victor^3 microplate reader (485 nm excitation, 590 nm emission). Plasma concentration was fit to a two compartment model to determine the pharmacokinetic parameters using SAAM II software (University of Washington, Seattle, WA).

5.7.2.10 Biodistribution Analysis

Balb/c mice were inoculated with C26 tumors on their right hind leg ($2.5x10^6$ cells in 30 μL). Once the tumors reached ~100 mm^3 (approximately 9 days following inoculation), the mice were anaesthetized with 50 mg/kg body weight of nembutol (*i.p.* administration), and administered CP-Dox (15 mg Dox equivalents/kg body weight) via tail vein injection. The mice were placed in a custom hyperthermia holder with a rectal temperature probe to monitor the core body temperature and a plastic shield to prevent direct skin contact with the heated water. The mice were placed in a water bath set to 43°C, such that the tumor bearing leg was submerged just far enough to completely cover the tumor mass. A fan was used to regulate the body temperature.

To determine whole body biodistribution (Figure 26), the mice were exposed to 1 h of continuous hyperthermia and were sacrificed 24 h following CP-Dox administration. To elucidate the effect of thermal cycling on tumor accumulation, mice were exposed to various hyperthermia schedules (Figure 29) and were sacrificed 2 h

following CP-Dox administration. Tissues were collected (heart, lungs, kidney, spleen, liver, muscle, and tumor), and 75-100 mg of tissue was weighed and suspended in 1 mL of acidified isopropanol (75 mM HCl, 90% isopropanol). The solution was homogenized using 2 mm Zirconia beads and a Beadbeater-16 (Biospec, Bartlesville, OK) for 120 secs. The samples were incubated at 4°C for 16 h in the dark to release conjugated Dox. The samples were then centrifuged (4°C, 10 min, 14000 g), and the supernatant was fluorescently assayed as described in the pharmacokinetic analysis. Untreated tissues were similarly extracted and used to create a background curve (fluorescent counts / mg tissue) to compensate for tissue autofluorescence.

5.7.2.11 Window Chamber and Microscopy

Nude mice were anaesthetized with a cocktail of ketamine and xylazine (100 mg/kg ketamine, 10 mg/kg xylazine, *i.p.*) and implanted with a dorsal skin fold window chamber. A titanium chamber was surgically implanted over a 1-cm circular incision in the dorsal skin fold. FaDu human squamous carcinoma cells at a concentration of $2x10^6$ cells in 30 μL of high glucose MEM was injected near the center of the window in the opposing layer of skin. The incision was then covered with a circular glass coverslip. All studies were performed 9-10 days following surgery, once the tumor reached a diameter of 2-3 mm.

To image the tumor vasculature, the mice were anaesthetized with 50 mg/kg body weight of nembutol and placed laterally recumbent upon a custom microscopy

stage that enabled heating of the window chamber. The tail vein was cannulated and 100 μL of 5 mg/mL 2 MDa dextran-fluorescein isothiocyanate (Invitrogen) was injected, followed by 200 μL of 425 μM CP nanoparticles (target plasma concentration of 50 μM) labeled with Rhodamine Red™-X Succinimidyl Ester (Invitrogen). The temperature of the stage was maintained at 37°C (physiological temperature) or 42°C (temperature achieved through mild hyperthermia). Images were taken with a Zeiss 780 upright confocal microscope. Data were obtained using two channels, in which dextran-fluorescein isothiocyanate was used to define the vasculature, and the rhodamine channel was used to view the distribution of CP nanoparticles. Upon injection of CPs at 37°C, fluorescent levels were adjusted to provide a yellow overlay.

5.7.2.12 Data Analysis

Non-linear regression analysis was performed with IBM SPSS Statistics 19.0 (SPSS, Chicago, IL). MATLAB (MathWorks; Natick, MA) was used to generate the 3-dimensional plot of the predicted T_t as a function of composition and chain length.

6. Highly Asymmetric Polypeptide Amphiphiles that Spontaneously Assemble into Unexpected Morphologies

6.1 Motivation

Self-assembly is a process by which amphiphilic components spontaneously interact in solution to form hierarchical structures, such as spherical and worm-like micelles, vesicles, disks, and sheets. Self-assembled systems have been studied extensively in recent decades due to their high degree of versatility; in particular, polymeric systems have been used in a variety of applications, including drug delivery [46, 75, 76, 88, 200], sensing [201], electronics [202, 203], and separation science [204]. The most common amphiphiles in these applications are block copolymers, in which two or more polymers with varying degrees of hydrophobicity are covalently linked. However, with the recent advances in controlled radical polymerization methods such as reversible addition-fragmentation chain transfer polymerization (RAFT), it is now possible to create highly asymmetric amphiphiles through end-functionalization of homopolymers with specifically tailored hydrophobic moieties, such as alkyl chains [205-207]. While these homopolymers are still able to self-assemble in aqueous solution, their geometries – and potentially the structural properties of their assemblies – may be quite distinct from those of classical block copolymers.

In this chapter, we investigate the structural properties of homo-biopolymer amphiphiles that have been end-functionalized using recombinant methods by

genetically fusing a variety of short hydrophobic peptides of precise sequence and length to the carboxy-terminus of an elastin-like polypeptide. Previous chapters describe a remarkably simple approach to building nanoscale thermoresponsive carriers out of these biopolymers for the targeted delivery of therapeutics by functionalizing the carboxy-terminus of a thermoresponsive elastin-like polypeptide with a short $(CGG)_8$ domain. The eight cysteine residues - unique to the polypeptide sequence - provide sites to which small molecule therapeutics can be covalently attached. We demonstrated that the fate of the polypeptide conjugate is inextricably tied to the hydrophobicity of the attached molecules; when the hydrophobicity is greater than a threshold value of LogD=1.5, the amphiphilic chimeric polypeptides assemble into sub-100 nm spherical micelles that retain the thermoresponsive behavior of the parent elastin-like polypeptide.

This simple assembly mechanism hints at a larger set of self-assembling polypeptides that may be able to access a range of morphological diversity unobtainable through stochastic chemical conjugation. The proposed structure of these highly asymmetric amphiphiles follows the motif: $(M)SKGPG - (VPG\alpha G)_n - (XG_y)_z$, where α represents the guest residue composition in the elastin-like polypeptide sequence, n is the number of pentameric repeats, X is the identity of the amino acid hydrophobe responsible for driving self-assembly, y is the number of glycine (G) spacers, and z is the number of repeats of the C-terminal assembly domain. We hoped that by sampling a

subset of this population, we would be able to better understand how the composition of the assembly domain influences the phase transition behavior and physicomechanical properties of the structure (*i.e.,* the size, stability, and morphology).

6.2 Physicochemical Characterization of Asymmetric Amphiphiles

Recombinant synthesis techniques were used to construct a series of asymmetric amphiphiles with a short assembly domain genetically fused to the carboxy-terminus of an elastin-like polypeptide (Figure 43, Appendix 8.2). The amphiphiles were transformed into *Escherichia coli*, purified using inverse transition cycling, lyophilized, and stored at -20°C for future use. Despite exploiting recombinant synthesis techniques, the compositional space necessary to screen all possible C-terminal peptide domains capable of driving assembly was immense; hence, we focused on a narrow but morphologically rich subset of the domains of the basic form $(XG_y)_z$, where X represents a number of hydrophobic amino acids selected from Urry's hydrophobicity index [180], y represents the number of glycine spacers and was varied between 0, 1, and 2, and z represents the number of assembly domain repeats, which was set at eight for all examined constructs (Table 7). All elastin-like polypeptide domains were comprised of the sequence $(VPGAG)_n$, where the number of pentapeptide repeats 'n' varied between 40, 80, and 160. A C-terminal tyrosine was included to facilitate absorbance based protein quantification (Figure 40, Appendix 8.1). Following purification, matrix-assisted

laser desorption/ionization mass spectrometry (MALDI-MS) was performed on each of the constructs to confirm their molecular weight (Appendix 8.4). In an attempt to understand the rules governing nanoparticle assembly, we then examined each construct with a variety of qualitative and quantitative techniques, including thermal turbidimetry, fluorescent spectroscopy, cryogenic transmission electron microscopy, static and dynamic light scattering, and single particle size analysis.

6.2.1 Thermal Behavior

We have previous shown that the thermal behavior of elastin-like polypeptides is exquisitely sensitive to its composition [182], attached proteins [84, 208] or compounds [77], as well as polymer concentration [158, 182], ionic strength [178], and the presence of solvents. In striking similarity to the thermal behavior of chimeric polypeptide conjugates seen in Figure 11A of Chapter 3, as the hydrophobicity of the fused assembly domain (Figure 30A) increases according to Urry's scale of hydrophobicity [180], the transition temperature of the construct decreases. In fact, thermal turbidimetry was sufficient to separate the constructs into two populations. The first population, comprised of the residues Leu, Ile, His, and Tyr, is primarily monomeric, and thus is characterized by transition temperatures that vary according to both hydrophobicity and the polymer concentration in solution (Figure 30B). As illustrated in Figure 31, however, the His and Leu constructs also contain a small fraction of assembled

nanoparticles. The absorbance increase, shown in Figure 31A, is indicative of the nanoparticle-to-globule phase transition, as it is both significantly lower than the unimer transition and does not show the same degree of concentration dependence (Figure 31B), whereas the second increase in absorbance represents the unimer-to-globule phase transition.

While many of the genetically encoded amphiphiles remained monomeric, the hydrophobic Trp and Phe domains spontaneously assembled into higher order structures whose transition behavior is approximated by the mathematical model developed for micelle formation in Chapter 5 (see the red dashed line in Figure 30B). Although this model was designed to predict the assembly of spherical micelles, we hypothesized that it could be applied to other higher order structures as they all exhibit a high local polypeptide concentration. This hypothesis was corroborated by the fact that the model also accurately predicts the transition temperature of constructs with lengths of 40 and 80 pentamers modified with the $(FGG)_8$ domain (see dashed lines in Figure 32A).

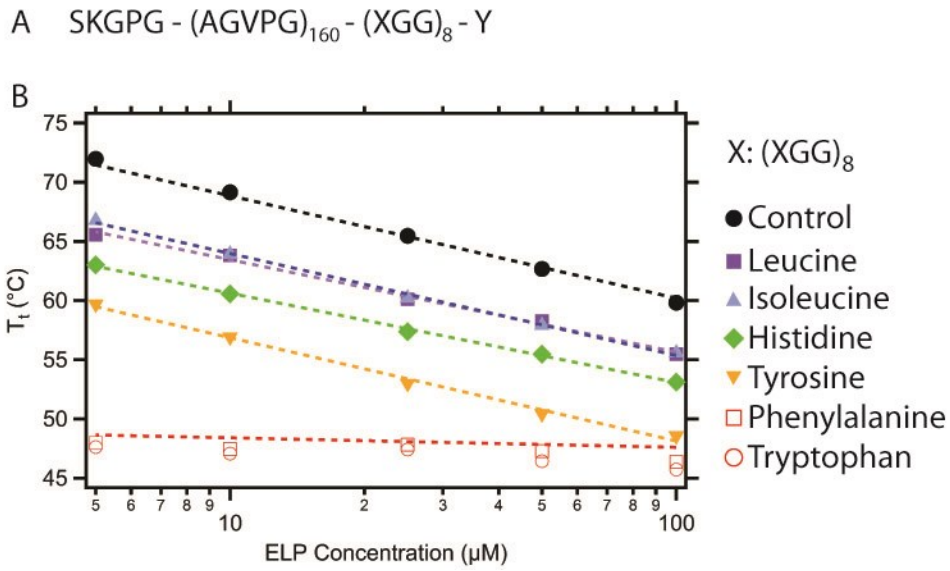

Figure 30: (A) Sequence and (B) transition behavior of ELPs that have been genetically fused to a C-terminal assembly domain. Black and red dashed lines represent the predicted transition temperature of the A[1]-160 construct as a unimer and micelle, respectively.

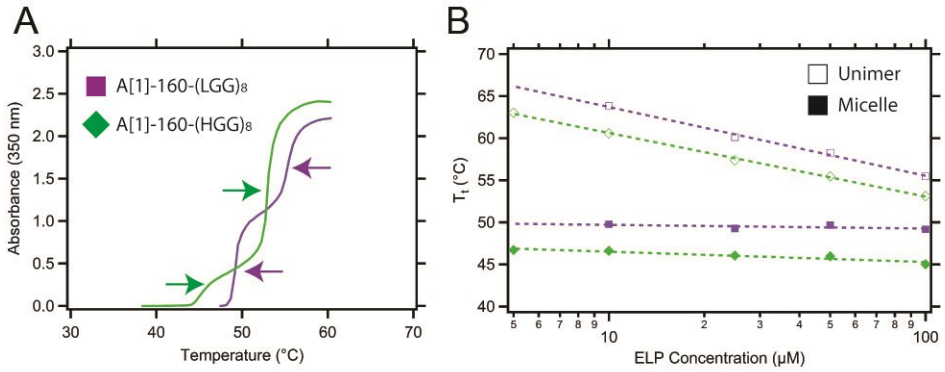

Figure 31: (A) Thermal turbidimetry profile at 100 μM amphiphile concentration. Arrows indicate discrete transition temperatures. (B) Transition behavior as a function of concentration for the genetically encoded amphiphiles containing an $(LGG)_8$ or $(HGG)_8$ domain.

Surprisingly, we observed that the number and distribution of glycine residues within the assembly domain can play a potent role in the assembly and transition temperatures of these asymmetric amphiphiles. For assembly domains comprised of tyrosine residues, for instance, incorporating 2 glycine spacers constrains the amphiphile to a monomeric form, thereby resulting in a high transition temperature that strongly depends on concentration (Figure 32B). Reducing the number of glycines between hydrophobic residues to a single residue or none at all results in the assembly of nanoparticles with low transition temperatures that are near-independent of concentration. This effect is most likely due to the hydrophilicity of the glycine residue: as the number of glycine residues decreases from 2 to 1, the overall hydrophobicity of the assembly domain surpasses the threshold necessary to induce nanoparticle assembly. It is also possible that the number of glycine residues controls the secondary structure of the assembly domain, which has demonstrated the ability to significantly enhance core interactions and stabilize structures. For instance, pH has been shown to trigger the transition of a poly(L-glutamic acid) block from a hydrophilic random coil to a hydrophobic alpha helix, thereby inducing the formation and stabilization of vesicles [209]. It is clear, however, that not all systems are affected by the presence or absence of glycine residues equally; assembly domains comprised of phenylalanine residues, for example, are sufficiently hydrophobic to assemble into structures with 0, 1, or 2 glycine spacers (Figure 32C).

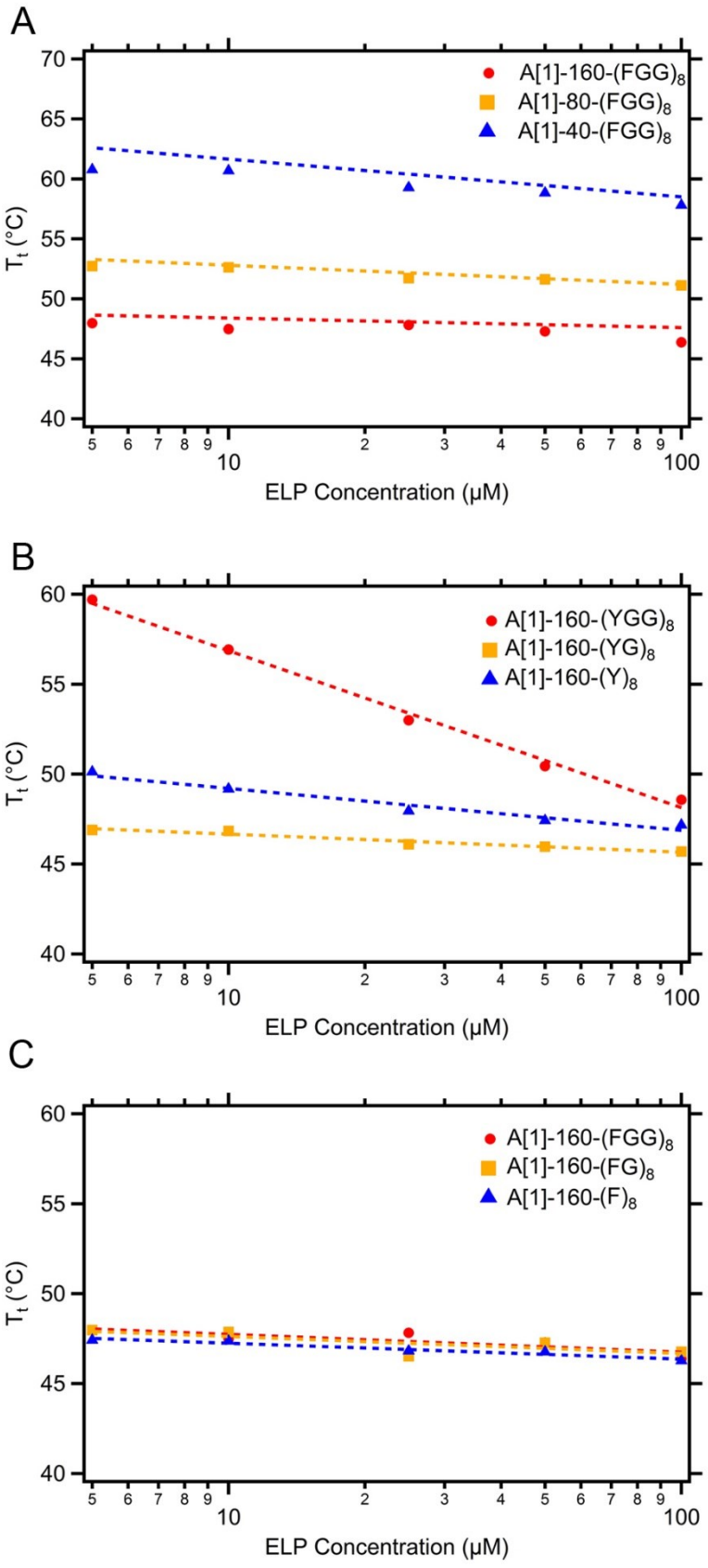
A
70
65
60
55
50
45
40
T_t (°C)
A[1]-160-(FGG)$_8$
A[1]-80-(FGG)$_8$
A[1]-40-(FGG)$_8$
5 6 7 8 9 10 2 3 4 5 6 7 8 9 100
ELP Concentration (μM)
B
60
55
50
45
40
T_t (°C)
A[1]-160-(YGG)$_8$
A[1]-160-(YG)$_8$
A[1]-160-(Y)$_8$
5 6 7 8 9 10 2 3 4 5 6 7 8 9 100
ELP Concentration (μM)
C
60
55
50
45
40
T_t (°C)
A[1]-160-(FGG)$_8$
A[1]-160-(FG)$_8$
A[1]-160-(F)$_8$
5 6 7 8 9 10 2 3 4 5 6 7 8 9 100
ELP Concentration (μM)

Figure 32: Thermal behavior of highly asymmetric polypeptides. (A) Transition temperatures of ELPs of varying size fused to C-terminal $(FGG)_8$ domains. Dashed lines represent the predicted transition behavior of assembled complexes according to Equation 5. (B) The number of glycine residues in the assembly domain can play a potent role in the transition behavior of asymmetric polypeptides with Tyr assembly domains but (C) plays almost no role in constructs with Phe assembly domains.

6.2.2 Nanoparticle Size Analysis

Dynamic light scattering was performed on each of the constructs to verify self-assembly. The unimeric domains comprised of Leu, Ile, His, and Tyr were comprised of random coils approximately 6 nm in radius (Figure 33A), with Leu and His displaying a second population (5-10% of total mass) at 39.4 ± 2.5 nm and 70.0 ± 8.3 nm, respectively (Table 7), in close agreement with thermal turbidimetry measurements (Figure 31). In contrast, the assembly-inducing domains generated nanoparticles whose hydrodynamic radii ranged from 30 to 90 nm (Figure 33B). As it is unlikely that spherical micelles can display diameters of ~180 nm, these values suggest that at least a few amphiphiles are assembling into more complex structures such as vesicles or worm-like micelles.

As the ionized form of tyrosine (Tyr_{pka} = 11.3) is 10 times more hydrophilic than neutral tyrosine, the A[1]-160-$(YG)_8$ construct offered a unique opportunity to affirm that assembly is primarily driven by the hydrophobicity of the assembly domain. Upon increasing the pH to 12, the vast majority of the A[1]-160-$(YG)_8$ constructs disassemble into unimers (Figure 33C) because the now charged tyrosinate residues could not

maintain a hydrophobic core, whereas the A[1]-160-$(FGG)_8$ constructs, which do not display a pKa within this range, remain unaffected by the increase in pH (Figure 33D).

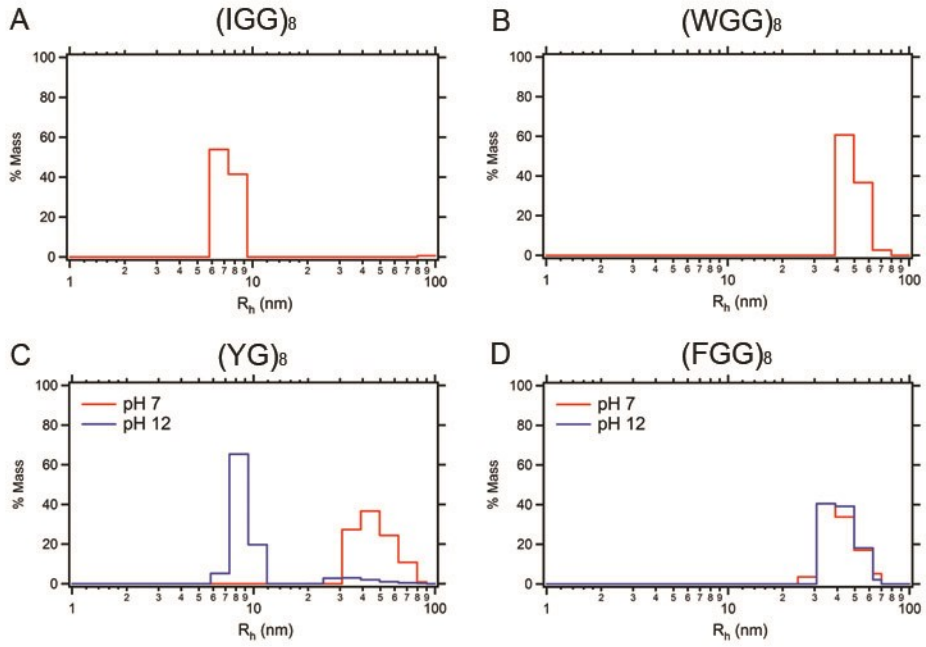

Figure 33: Dynamic light scattering of genetically encoded amphiphiles. (A) R_h distribution of A[1]-160-$(IGG)_8$ and (B) A[1]-160-$(WGG)_8$. (C) A[1]-160-$(YG)_8$ constructs dissociate at pH > pKa_{Tyr} because the pH-mediated conversion from tyrosine to tyrosinate vastly increases the hydrophilicity of the domain. (D) A[1]-160-$(FGG)_8$ constructs do not dissociate at high pH because phenylalanine residues do not become charged at high pH values.

Static light scattering was used to calculate the coordination number Z, or the number of amphiphiles per nanoparticle. The unimer domains measured between 1 and 13 amphiphiles/structure; as static light scattering is an ensemble technique, the coordination number reflects the weighted average between the assembled nanoparticles and the single chains (Table 7), thereby providing a coordination number

that neither reflects the unimeric state or nanoparticle state. This artifact explains the high coordination numbers for both the Leu and His domains, in accordance with the fact that thermal turbidimetry and dynamic light scattering indicated the coexistence of unimers and nanoparticles. The remaining nanoparticles displayed a wide range of Z, from weak aggregates (10 amphiphiles/NP) to nanoparticles (100-500 amphiphiles/NP) to what are likely large aggregates (1653 amphiphiles/NP).

Table 7: Results of size analyses on genetically encoded amphiphiles

Amphiphile	MW g·mol^{-1}	Z	R_h[a] (nm)	R[b] (nm)	Assembly
A[1]-160-$(IGG)_8$	1.35E+05	2	6.5 ± 0.8	n.d.	No
A[1]-160-$(LGG)_8$	3.93E+05	6	6.1 ± 0.7	n.d.	No[c]
A[1]-160-$(HGG)_8$	8.33E+05	13	6.7 ± 0.7	n.d.	No[c]
A[1]-160-$(YGG)_8$	5.99E+04	1	6.6 ± 0.8	n.d.	No
A[1]-160-$(FGG)_8$	6.89E+06	111	42.8 ± 9.9	53.5 ± 4.8	Yes
A[1]-160-$(WGG)_8$	2.64E+07	426	80.6 ± 35.6	76.0 ± 12.1	Yes
A[1]-160-$(YG)_8$	2.47E+07	399	72.7 ± 13.1	71.0 ± 8.9	Yes
A[1]-160-Y_8	6.40E+05	10	27.9 ± 3.0	n.d.	Yes
A[1]-160-$(FG)_8$	4.68E+06	76	33.0 ± 4.9	54.5 ± 5.5	Yes
A[1]-160-F_8	1.03E+08	1653	91.4 ± 9.7	73.0 ± 6.3	Yes
A[1]-80-$(FGG)_8$	9.00E+06	290	35.3 ± 4.3	55.5 ± 6.0	Yes
A[1]-40-$(FGG)_8$	8.62E+06	575	30.9 ± 2.6	54.5 ± 5.4	Yes

[a] R_h was determined with dynamic light scattering.
[b] R was determined using tunable resistance pulse sensing.
[c] Indicates partial assembly (~5% by mass).
Z Represents the coordination number, or the number of polypeptides per nanoparticle.
n.d. Indicates that the measurement was not performed.

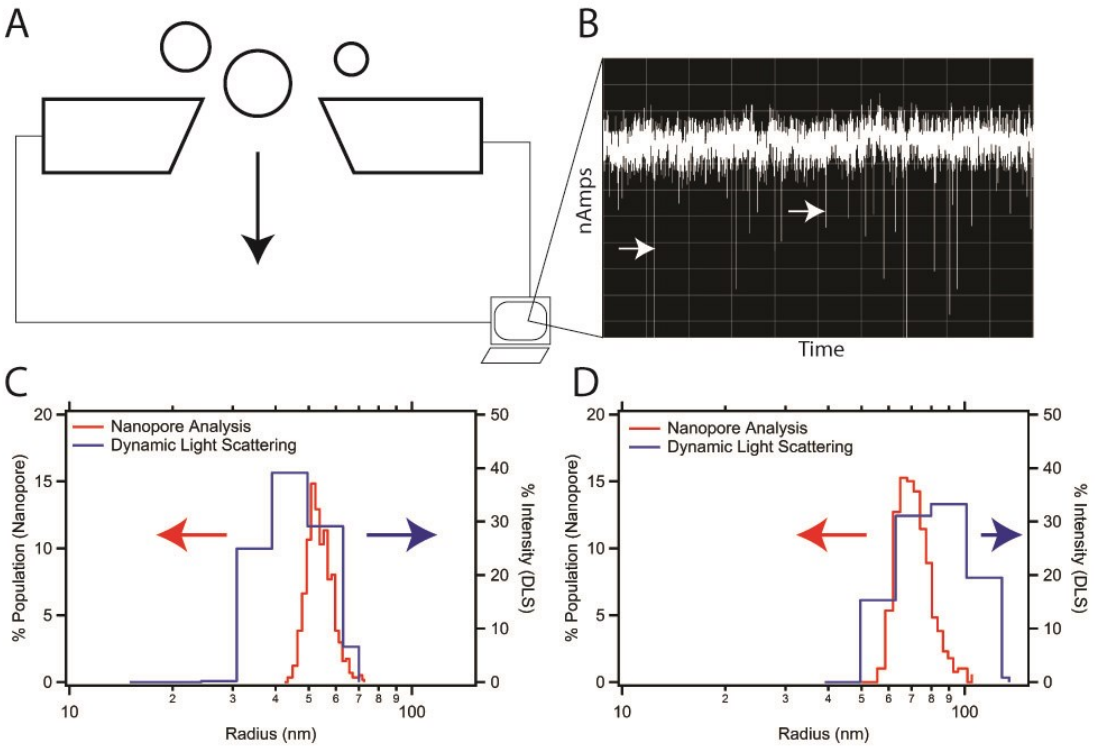

Figure 34: Nanoparticle size measured with tunable resistive pulse sensing (TRPS). (A-B) Pulsatile increases in measured resistance as nanoparticles flow through pores creates blockade events (white arrows) whose amplitude is proportional to the nanoparticle diameter. (C) A[1]-160-$(FGG)_8$ and (D) A[1]-160-$(YG)_8$ as measured with TRPS (red, left axis) and dynamic light scattering (blue, right axis).

As light scattering relies on ensemble analysis, the measured sizes are highly subject to contamination. In fact, as intensity is proportional to radius^6, small quantities of large aggregates can completely screen the presence of smaller structures, and sample polydispersity can greatly skew the measured size of the nanoparticle. To verify the sizes determined with dynamic light scattering, we used a particle-by-particle analysis technique that relies on tunable resistive pulse sensing (TRPS; Figure 34A). The

instrument is equipped with a sensors that measure the magnitude of transient changes in the ionic current flow caused by single nanoparticles traversing the pore (known as blockade events; Figure 34B). As the magnitude of the blockade event correlates to the size of the particle, the physical particle size can be measured following calibration against known standards. We found that the R_h and particle distribution determined with light scattering closely resembled the physical particle size measured using tunable resistive pulse sensing (Table 7). TRPS is, however, constrained by the quality and pore sizes of the available sieves. As the smallest pore size available measured diameters between 70 and 200 nm, there were five constructs whose sizes could not be determined (n.d.). The radial distribution of two representative constructs determined by both DLS and TRPS are shown in Figure 34C-D.

6.2.3 Fluorescence Spectrophotometry

Fluorescence spectrophotometry using pyrene as a probe was used to sample the hydrophobicity of the inner core of the self-assembled structures. As described in detail in Chapter 3, plotting the ratio of the pyrene fluorescence at 370-373 nm to the fluorescence at 381-384 nm against the concentration of the amphiphile yields a two-state curve that quantitatively describes the thermodynamic stability of the nanoparticles, termed the critical aggregation concentration (CAC). Herein we define the inflection point of the two state curve as the CAC, which is listed for each of the

constructs in Table 8. Constructs that do not provide a lipophilic environment into which pyrene can partition exhibit a fluorescent pattern independent from amphiphile concentration as the fluorescence spectrum of pyrene in water does not change with the concentration of the amphiphile.

Figure 35A indicates that of the three most hydrophobic assembly domains, the $(YGG)_8$ domain was unable to induce assembly, whereas the $(WGG)_8$ and $(FGG)_8$ domains were sufficiently hydrophobic to self-assemble into structures. Surprisingly, the $(FGG)_8$ domain formed a more hydrophobic core than $(WGG)_8$ – seen by the lower I_1/I_3 ratio at high concentrations – despite the fact that tryptophan is more hydrophobic than phenylalanine. While this anomaly is not fully understood, it is possible that the smaller phenylalanine side chain allows higher packing densities or facilitates more π-π stacking interactions. We also observed that decreasing the molecular weight of the ELP domain from 60 to 30 to 15 kDa only slightly increased the hydrophobicity and stability of the $(FGG)_8$ core (Figure 35B, Table 8).

Although we anticipated that greater numbers of hydrophilic glycine residues in the core would decrease core hydrophobicity and stability, this interaction turned out to be more complex. For instance, the presence or absence of glycines did not significantly affect the hydrophobicity or stability of the phenylalanine domains. However, it did play a pivotal role within the tyrosine domains. In agreement with thermal turbidimetry and light scattering analysis, the $(YGG)_8$ domain was unable to induce structure

formation, as observed by the absence of a concentration dependence in the I_1/I_3 ratio. However, by halving the core glycine content to $(YG)_8$, the domain was able to drive the assembly of nanoparticles with a clearly defined hydrophobic core. Upon total elimination of the assembly domain glycine residues (Y_8), the pyrene assay indicates the complete absence of a hydrophobic core, although thermal turbidimetry, light scattering, and tunable resistive pulse sensing indicate that nanoparticles remain the predominant species. It is possible that this particular domain drives the formation of aggregates that lack a defined core rather than the core-shell structures observed for the other domains, although the structure cannot be fully elucidated without a discriminating technique such as small angle x-ray scattering or small angle neutron scattering. These studies are currently ongoing.

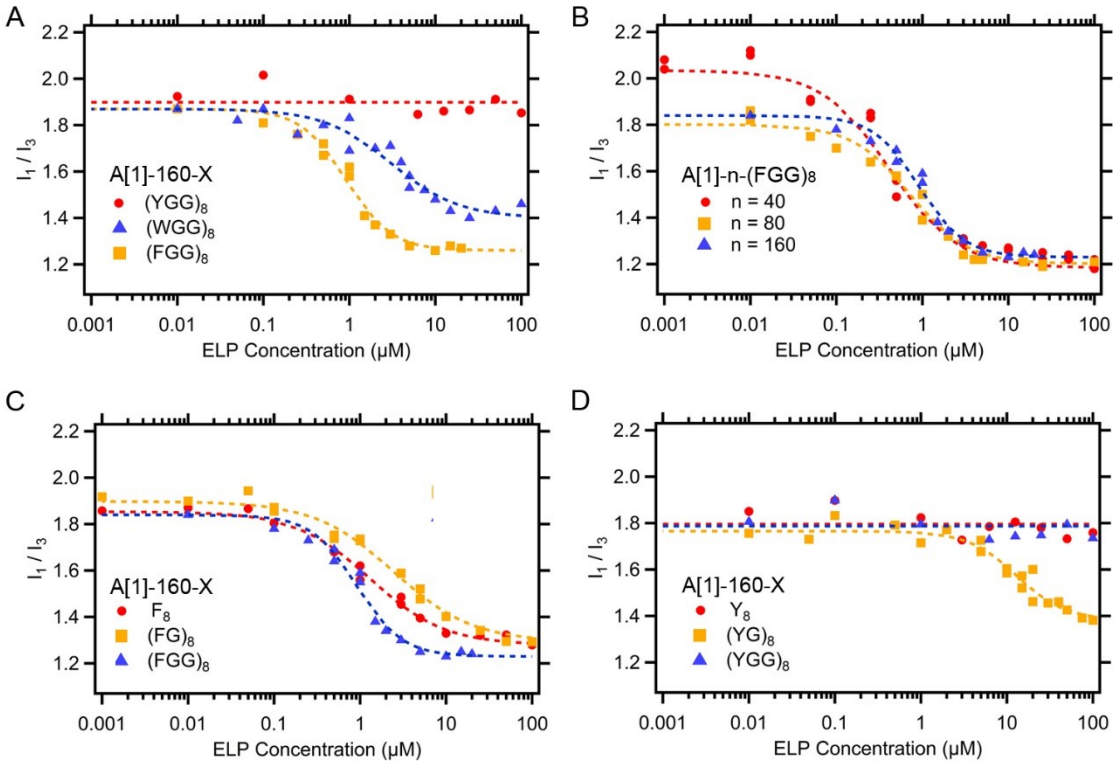

Figure 35: Fluorescence spectrophotometry of genetically encoded amphiphiles. Pyrene analysis of (A) ELPs fused to a series of $(XGG)_8$ domains, (B) a series of ELPs of various molecular weights fused to an $(FGG)_8$ domain, (C-D) Pyrene curves of a series of (C) phenylalanine-based and (D) tyrosine-based assembly domains fused to an ELP.

Table 8: Critical Aggregation Concentration and Core Hydrophobicity of Genetically Encoded Amphiphiles determined via fluorescence spectrophotometry

Amphiphile	CAC (μM)	Minimum I_1/I_3
A[1]-160-$(IGG)_8$	n.d.	n.d.
A[1]-160-$(LGG)_8$	n.d.	n.d.
A[1]-160-$(HGG)_8$	n.d.	n.d.
A[1]-160-$(YGG)_8$	n.d.	n.d.
A[1]-160-$(FGG)_8$	0.9 ± 0.1	1.26
A[1]-160-$(WGG)_8$	3.1 ± 0.4	1.41
A[1]-160-$(YG)_8$	13.0 ± 1.3	1.40
A[1]-160-Y_8	n.d.	1.73
A[1]-160-$(FG)_8$	2.5 ± 0.2	1.31
A[1]-160-F_8	1.3 ± 0.1	1.28
A[1]-80-$(FGG)_8$	0.7 ± 0.1	1.20
A[1]-40-$(FGG)_8$	0.4 ± 0.0	1.19

n.d. not determined

6.2.4 Cryogenic Transmission Electron Microscopy

To determine the morphologies of the different assemblies, it was necessary to perform cryogenic transmission electron microscopy (cryo-TEM). The samples were imaged at a high concentration (200 μM amphiphile) and a low voltage (80 keV) to increase contrast between the buffer and the highly hydrated polypeptide chains. We observed that many of these highly asymmetric amphiphiles formed unexpected morphologies (Figure 36). In contrast to conjugation-driven assembly, which yielded spherical micelles, genetically encoded amphiphiles spontaneously assembled into spherical micelles, worm-like micelles, and even vesicles. Most of the samples were

dominated by spherical and worm-like micelles (Figure 36A-D), where the lengths of the worms ranged from an average 57 nm to 170 nm and the thickness of the inner core averaged 8 nm (Table 9). Two of the constructs (A[1]-160-$(FGG)_8$ and A[1]-160-$(WGG)_8$) also displayed significant quantities of vesicles (Figure 36E-F) with average radii of 45.4 and 31.3 nm, respectively, and a shell thickness of approximately 7.5 nm. It is not surprising to observe an equilibrium between various morphologies, as it has been shown to exist in a variety of polymersome systems [210, 211]. However, we still do not fully understand why some constructs only seem to form worm-like micelles (e.g., A[1]-40-$(FGG)_8$) and why others seem to only form vesicles (e.g., A[1]-160-$(WGG)_8$). These studies are currently ongoing.

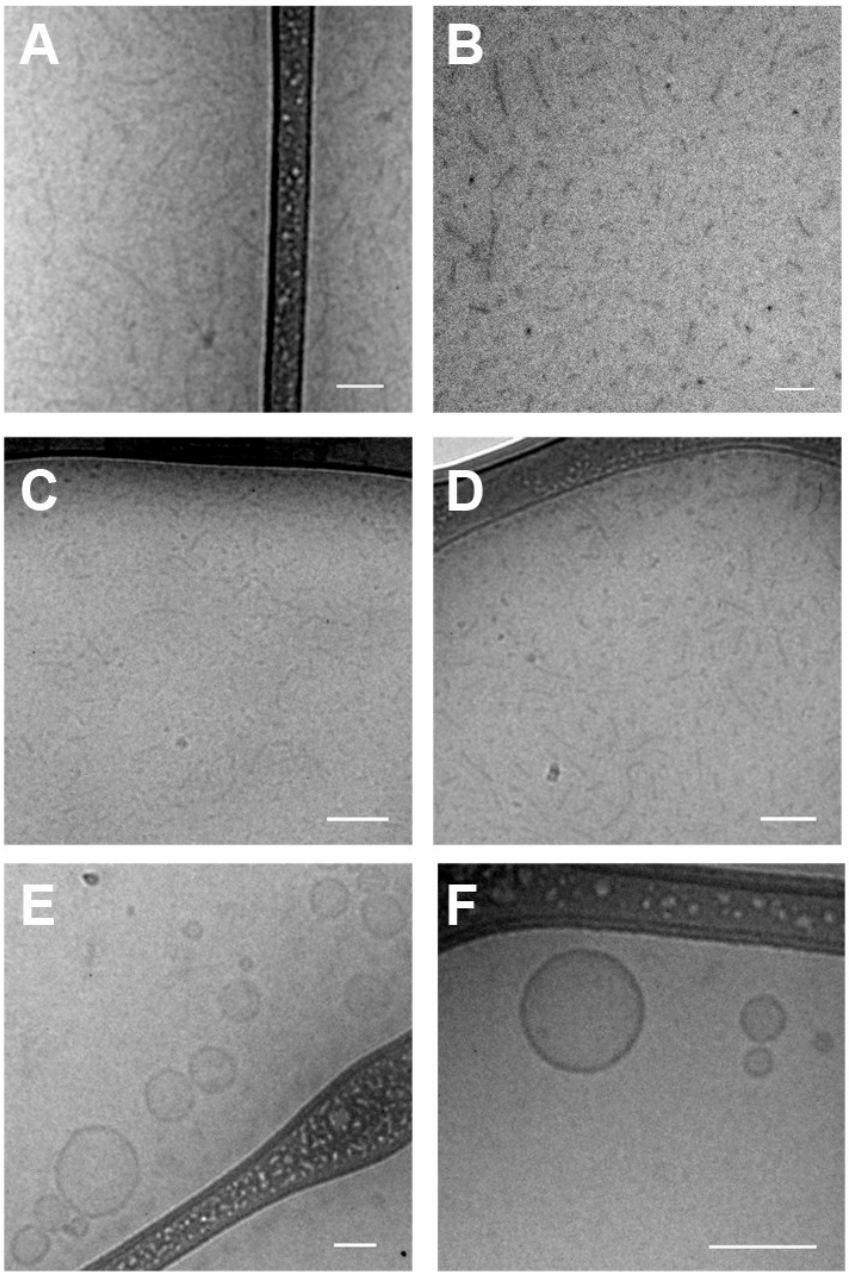

Figure 36: Cryogenic transmission electron microscopy of genetically encoded amphiphiles. Many of the genetically encoded amphiphiles were predominantly comprised of spherical and worm-like micelles, including: the (A) A[1]-160-$(YG)_8$, (B) A[1]-160-$(FGG)_8$, (C) A[1]-80-$(FGG)_8$, and (D) A[1]-40-$(FGG)_8$ constructs. (E) A[1]-160-$(FGG)_8$ and (F) A[1]-160-$(WGG)_8$ were the only samples to also contain spherical vesicles. All samples were imaged at 200 μM. Scale bars represent 100 nm.

Table 9: Physical characteristics of self-assembled structures via cryogenic-transmission electron microscopy.

	Worm-like Micelles		Vesicles	
Construct	**Length (nm)**	**Membrane (nm)**	**Radius (nm)**	**Membrane (nm)**
A[1]-40-$(FGG)_8$	56.6 ± 26.0	6.5 ± 1.5	n.d.	n.d.
A[1]-80-$(FGG)_8$	63.5 ± 25.4	6.5 ± 1.5	n.d.	n.d.
A[1]-160-$(FGG)_8$	110.2 ± 34.0	10.0 ± 1.7	45.4 ± 16.9	7.9 ± 1.3
A[1]-160-$(WGG)_8$	n.d.	n.d.	31.3 ± 11.7	7.0 ± 1.2
A[1]-160-$(YG)_8$	169.0 ± 39.9	9.9 ± 1.8	n.d.	n.d.

n.d. : not determined because these structures were not observed
Data reported as mean ± standard deviation, with a minimum of 25 measurements.

6.2.5 Pharmacokinetics of Genetically Encoded Amphiphiles

To determine whether the *in vivo* properties of these homo-biopolymers benefit from spontaneous self-assembly, two genetically encoded amphiphiles and a single chain ELP were injected into the mouse tail vein, and the plasma concentration was tracked longitudinally over 24 hours via an N-terminal conjugated fluorophore. The two selected amphiphiles, A[1]-160-$(FGG)_8$ and A[1]-160-$(YG)_8$, were similar in both molecular weight and nanoparticle size (Table 7). However, the A[1]-160-$(FGG)_8$ construct displayed a critical aggregation concentration of approximately 0.9 μM (56 times lower than the initial concentration of 50 μM), whereas the A[1]-160-$(YG)_8$ construct displayed a CAC of 13.0 μM, only ~4 times lower than the initial concentration. The plasma concentration of each construct was fit to a two-compartment model (Figure 37), and their pharmacokinetic parameters were calculated (Table 17,

Appendix 8.8). Within the first 2 hours, the injected amphiphiles partitioned out of the plasma in an effort to establish a dynamic equilibrium between the plasma and tissue compartments, resulting in the rapid decline of the plasma concentration. As the plasma concentration approached the CAC of the A[1]-160-$(YG)_8$ construct, the nanoparticles began to dissociate into unimers. Thus, while this construct exhibited all of the characteristics of nanoparticles *ex vivo*, it displayed an elimination half-life and an area under the curve (AUC) that was indistinguishable from that of a single chain control *in vivo* (Table 10). In contrast, the A[1]-160-$(FGG)_8$ construct, which remained assembled into stable nanoparticles to concentrations below 1 μM, did not dissociate upon *in vivo* administration and thus displayed an elimination half-life of 16 hours (75% longer than the control) and an AUC of 628 μM·h (90% higher than the control). This suggests that the phenylalanine-based constructs may provide a distinct biological advantage when delivering therapeutics as they will remain circulating longer and provide a higher exposure levels than the tyrosine-based constructs.

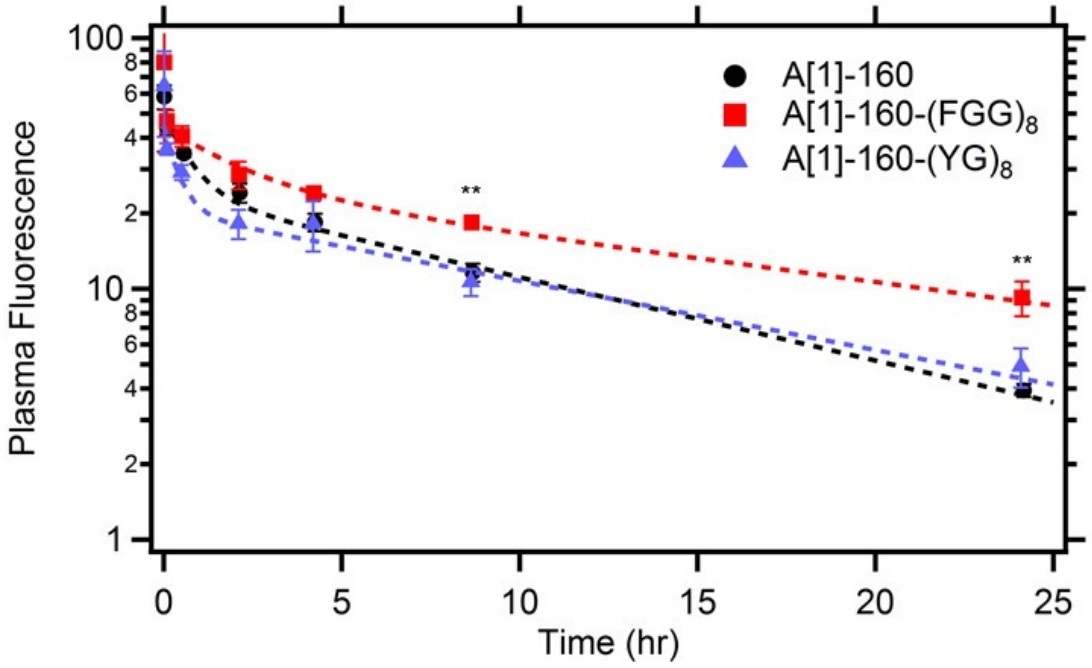

Figure 37: Plasma concentration of two genetically encoded amphiphile assemblies compared to a single chain ELP as a function of time. The data points represent mean ± SD (n=3) and the dashed lines represent the curves of best fit to the two compartment model by SAAM II. Significance (one-way ANOVA, Tukey post-hoc test) was calculated for A[1]-160-$(FGG)_8$ and A[1]-160-$(YG)_8$ against the A[1]-160 control for all time points. **p<0.005

Table 10: Pharmacokinetic parameters of two genetically encoded amphiphiles following plasma injection

Parameter		A[1]-160	A[1]-160-$(FGG)_8$	A[1]-160-$(YG)_8$
elimination half-life	[hr]	9.1 (0.5)	16.0 (2.6)	10.9 (1.0)
area under the curve	[μM hr]	332.1 (9.9)	628.0 (40.1)	329.7 (19.1)

[a]Data represent the mean (SD) of the best fit parameters determined by SAAM II.

6.3 Conclusions

This chapter illustrates a very simple approach to build morphologically rich structures by genetically end-functionalizing a water soluble homopolypeptide with a short hydrophobic domain of precise length and composition. We observed that the assembled structures were highly sensitive to the composition of the assembly domain. Typically, the morphology of self-assembled systems are a composite of multiple factors, including the composition of the polymers, the concentration in solution, polymer-solvent interactions, and most importantly, the size ratio of the hydrophilic to the hydrophobic block, known as the hydrophilic fraction [210]. As a general rule, when this fraction exceeds 60%, polymer diblocks tend to form spherical micelles. Polymers favor worm-like micelles between 45% and 55%, and vesicles are constrained to the narrow region between 25% and 45% [212]. The unexpected finding with this system is that worm-like micelles and vesicles form when the hydrophilic fraction is as high as 97%, a regime that would classically only allow a spherical micellar structure. Surprisingly, many of these systems were also extremely stable despite their degree of asymmetry. In fact, we were able to show that one of the constructs demonstrated a significant increase in both the plasma half-life and systemic exposure *in vivo* compared to a single chain control.

We have found that many of the assembly domains utilizing the aromatic amino acids – tyrosine, phenylalanine, and tryptophan – assemble into structures that are

sensitive to the number of glycine residues between the hydrophobes. The $(YGG)_8$ domain, for instance, remains monomeric, while the $(YG)_8$ domain drives worm-like micelle formation and the Y_8 domain induces the formation of nanoscale aggregates. The hydrophilic fraction does not seem to play a significant role in the $(FGG)_8$ domain morphologies in the hydrophilic fraction regime of 97% (chain length n=160) down to 94% (n=80) or 88% (n=40), although only the longest chain length (n=160) was observed to induce the formation of vesicles in equilibrium with the worm-like and spherical micelles observed within the n=40 and 80 samples.

We elected to use elastin-like polypeptides as the principal component of these structures for several reasons: (1) they undergo a soluble-to-insoluble phase above a specific temperature that can be specifically tuned to occur within a narrow (2°C) temperature window that has prompted their use in a variety of biomedical applications including the delivery of protein [84, 208] and chemical therapeutics [76, 77, 88]; (2) they are designed on the genetic level, providing precise control over their molecular weight as well as the number and distribution of reactive sites along the polymer chain; (3) they are biodegradable [81] and non-toxic [80]; and (4) they can be expressed at high yield from *Escherichia coli* and rapidly purified by exploiting their phase transition behavior [84, 85].

ELPs also retain their unique thermal behavior upon fusion to proteins and peptides, and thus provide a useful platform to construct environmentally responsive

polypeptide amphiphiles. The fusion of a hydrophobic peptide to one end of the soluble polypeptide generates amphiphilic molecules with the capacity to assemble into complex structures that can then collapse into a hydrophobic aggregate in response to subtle temperature triggers.

Although many of the rules dictating the physicomechanical characteristics of structures assembled with these hydrophobic domains remain unknown, it is our hope that this work provides a starting point to exploit the versatility of these genetically encoded domains for a diverse range of drug delivery and biomedical applications.

6.4 Materials and Methods

6.4.1 Materials

Restriction enzymes and T4 DNA ligase were purchased from New England Biolabs (Ipswich, MA). All custom oligonucleotides were synthesized by Integrated DNA Technologies Inc. (Coralville, IA). The DNA miniprep and gel purification kits were purchased from Qiagen Inc. (Germantown, MD). EB5α™ and BL21™ *Escherichia coli* cells were purchased from Edge BioSystems (Gaithersburg, MD). All *Escherichia coli* cultures were grown in TBDry™ media purchased from MO BIO Laboratories, Inc (Carlsbad, CA). Kanamycin was purchased from CalBioChem (San Diego, CA).

6.4.2 Methods

6.4.2.1 Synthesis of asymmetric polypeptides

The highly asymmetric amphiphiles were synthesized from purchased oligomers using plasmid reconstruction recursive directional ligation (Figure 43, Appendix 8.2) [213]. The asymmetric amphiphiles described in this chapter are of the form: SKGPG-$(AGVPG)_n$-$(XG_z)_8$-Y, where the polypeptide length n (40, 80, or 160), the number of glycine spacers y (0, 1, or 2) , and the identity of the hydrophobic residue X are systematically varied (Figure 40, Appendix 8.1).

6.4.2.2 Expression and purification of asymmetric amphiphiles

Each construct was expressed using a previously published hyperexpression protocol, which relies on the leakiness of the T7 promoter [161]. 50 mL cultures were grown overnight and used to inoculate 1 L flasks of TBDry supplemented with 45 μg/mL kanamycin. The flasks were then incubated at 37°C for 24 h and 190 rpm. Each construct was purified using a modified Inverse Transition Cycling protocol [84], where the solution was never heated above room temperature due to the irreversible thermal nature of a few of the constructs. Briefly, the cell suspension was centrifuged at 3,000 rpm for 10 min at 4°C, the cell pellet resuspended in PBS and then lysed via sonication on ice for 3 min (10 s on, 40 s off) (Masonix S-4000; Farmingdale, NY). Polyethyleneimine (PEI) 0.7% w/v was added to the lysate to precipitate nucleic acid contaminants. The

supernatant was then subjected to multiple rounds of ITC as follows. The solution was transitioned on ice through the addition of 3 M NaCl. The coacervate was then centrifuged for 10 min at 14,000 g and 20°C, the supernatant decanted, and the pellet resuspended in phosphate buffer. This suspension was cooled to 4°C, and then centrifuged for 10 min at 14,000 and 4°C to remove any insoluble contaminants. Typically, 3-5 rounds of ITC generated a sufficiently pure product (>95% by SDS-PAGE).

6.4.2.3 Thermal Characterization.

Turbidity profiles were obtained for each of the constructs by recording the optical density as a function of temperature (1°C/min ramp) on a temperature controlled UV-Vis spectrophotometer (Cary 300 Bio; Varian Instruments; Palo Alto, CA). The T_t was defined as the inflection point of the turbidity profile. Samples were measured in phosphate buffered saline solution at five different solution concentrations between 1 - 100 μM.

6.4.2.4 Light Scattering Analysis

Dynamic light scattering was used to determine the hydrodynamic radius (R_h) of the various constructs at 25°C and 25 μM amphiphile concentration using a Dynapro plate reader (Wyatt Technology; Santa Barbara, CA), following filtration through 0.22 μm Millex-GV filters (Millipore; Billerica, MA). The data was analyzed with a regularization fit for Raleigh spheres. Static light scattering measurements were performed using the ALV/CGS-3 goniometer system (Germany). Samples for the

ALV/CGS-3 goniometer system were prepared in PBS at 25 μM and filtered through 0.22 μm Millex-GV filters into a 10 mm disposable borosilicate glass tube (Fischer). Measurements were obtained at 25°C for angles between 30°-150° at 5° increments, with each angle consisting of 3 runs for 10 seconds. Results were analyzed by partial Zimm plot analysis using ALV/Dynamic and Static FIT and PLOT software.

6.4.2.5 Tunable Resistive Pulse Sensing

Lyophilized samples were resuspended in phosphate buffered saline to a concentration of 50 μM and filtered through 0.22 μm Millex-GV filters. 40 μL of the sample was loaded onto a qNano (Izon; Christchurch, New Zealand) instrument equipped with 50 – 150 nm pores (A[1]-160-$(FGG)_8$, A[1]-160-$(FG)_8$, A[1]-80-$(FGG)_8$, and A[1]-40-$(FGG)_8$) or 100-300 nm pores (A[1]-160-$(YG)_8$, A[1]-160-F_8, and A[1]-160-$(WGG)_8$). Samples were measured for at least 30 seconds and a minimum of 500 blockade events were recorded per sample. Samples were calibrated against known standards (Izon) for the same stretch and voltage.

6.4.2.5 Fluorescence Spectroscopy

An assay to determine the critical aggregation concentration (CAC) using pyrene as a probe was performed using a Cary Eclipse spectrophotometer equipped with a Xenon flash lamp (Varian Instruments; Palo Alto, CA). 1 μL of a stock solution of 12 mM pyrene (Fluka/Sigma-Aldrich; St. Louis, MO) in ethanol was diluted into 20 mL of PBS. Both the stock solution and the PBS mixture were sonicated for 10 minutes prior to use.

This solution was used to resuspend 1-5 mg of lyophilized sample, which was then used to create a dilution series. Each sample was placed in a reduced volume cuvette, and scanned (Ex: 334; Em: 360-380, Ex slit 10 nm; Em slit 2.5 nm). Pyrene fluorescence displays four peaks; the intensity at the first (I_1; 370-373 nm) and third peak (I_3; 381-384 nm) were recorded. The ratio I_1/I_3 was plotted as a function of CP concentration. The CAC was defined as the inflection point of the sigmoid of best fit.

6.4.2.6 Cryogenic Transmission Electron Microscopy

Cryogenic Transmission Electron Microscopy was performed at the University of Pennsylvania in the Penn Regional Nanotechnology Facility (Philadelphia, PA). Lacey formvar/carbon grids (Ted Pella) were washed in chloroform to remove the formvar template and carbon coated with a Quorum Q150T ES carbon coater (Quorum Technologies, United Kingdom). Grids were cleaned with hydrogen/oxygen plasma for 15 s using the Solarus Advanced Plasma System 950 (Gatan, Pleasanton, CA). A 200 μM sample in the form of a 2 μl drop was deposited onto the grid and added to a Gatan Cp3 cryoplunger (Gatan, Pleasanton, CA). The samples were blotted by hand and plunged into liquid ethane. Grids were transferred to a Gatan CT3500TR cryoholder (Gatan, Pleasanton, CA) and immediately inserted into a JEOL 2010 TEM (JEOL, Tokyo, Japan) operating at 80 keV. Micrographs were imaged with an Orius SC200 digital camera.

6.4.2.7 Pharmacokinetic Analysis

All animal experiments were done in accordance with Duke University's Institutional Animal Care and Use Committee. Genetically encoded amphiphiles labeled with an N-terminal Alexa Fluor® 488 sulfodicholorphenol ester (Invitrogen; Carlsbad, CA) were intravenously administered via tail vein into Balb/c mice (400 μg/g body weight). 10 μL blood was collected at select time points (40 s, 5 min, 30 min, 2 h, 4 h, 8 h, 24 h) and diluted into 100 μL of heparin (1000 U/mL) in PBS. The samples were centrifuged (1000 g, 5 min, 4°C) to remove the red blood cells. The solution was loaded into a 96-well microplate in triplicate (25 μL per well), and the fluorescence was determined using a Victor^3 microplate reader (485 nm excitation, 535 nm emission). Plasma concentration was fit to a two compartment model to determine the pharmacokinetic parameters using SAAM II software (University of Washington, Seattle, WA).

7. Conclusions and Future Directions

The polypeptide platform described in this thesis represents a modular and robust drug delivery vehicle. Its size and stability in serum enable it to accumulate in solid tumors by the enhanced permeability and retention effect, and its unique thermal behavior allows the carrier to exhibit a rapid and reversible phase transition from nanoparticle to insoluble aggregate in serum. While the studies presented herein demonstrate a significant increase in tumor drug accumulation in response to cyclic heating, there are a variety of different paths future researchers may explore to improve the efficacy and versatility of this system.

7.1 Designing Novel Sequences Based on Elastin-like Polypeptides

This thesis demonstrates that the transition temperature of elastin-like polypeptide drug carriers (unimers and nanoparticles) can be precisely determined through the composition, chain length, and concentration of the polypeptide [182]. While the combination of valines and alanines in the guest residue position was carefully selected to provide nanoparticles that transition between 37 and 42°C for the chain lengths of 40, 80, and 160 pentapeptides, it is possible that others will (1) require smaller or larger ELPs or CPs to display a unimeric or micellar transition temperature outside of the range provided by these two residues, (2) require constructs that display pH and thermal sensitivity, or (3) want to predict the transition temperature of

zwitterionic sequences. In the first case, the selection of aliphatic binary residue combinations such as glycine and leucine would provide a large transition temperature range while avoiding complicating effects such as charge, π-π stacking, and pH. Recent works by MacKay show that single chain ELPs comprised of serine residues exhibit very peculiar thermal behaviors that would not be conducive to modeling by any of these equations, as the intermolecular hydrogen bonding seems to eliminate both length and concentration dependence of the transition temperature of unimeric ELPs [214]. For this reason, glycine was selected as it is likely hydrophilic enough for most purposes and should not alter the innate tendencies of most ELP chains. If pH sensitivity is desired, a combination of histidines and glycines may provide ELPs that both transition in a wide range of physiological temperatures as well as exhibit a pH dependence that is appropriate for physiological triggers. In this case, it would be possible to combine Equation 3 with the MacKay model [91] in an effort to incorporate the Henderson-Hasselbalch relationship such that the predicted transition temperature would depend on sequence, chain length, concentration, and solution pH. In the final case, combinations of lysines and glutamates or arginines and glutamates would yield zwitterionic ELPs, though the transition temperatures would likely be quite high due to the presence of charged residues.

When it is necessary to design constructs that exhibit a phase transition within a narrow temperature or pH range, constructing a predictive model similar to Equation 4

and 5 can eliminate much of the guesswork. While Chapters 4 and 5 show models constructed from 8 independent libraries (24 constructs total), many of these libraries did not influence the outcome of the model. In fact, we observed that the Ala-Val system only required three ELP libraries (3 different molecular weights per library, 9 constructs total) to fully predict the transition temperatures of the ELP superlibrary: 100% guest residue A, 100% guest residue B, and the 50:50 mixture of the two guest residues (45 measurements, r^2=0.992). When designing future sequence combinations, it would be logical to first generate these three foundational libraries with which to build the model, then only build the libraries with the desired properties.

7.2 Improving the Pharmacokinetic Profile of Chimeric Polypeptide Nanoparticles

One of the more interesting and unanticipated behaviors *in vivo* was that the pharmacokinetics of chimeric polypeptides was primarily determined by the chain length of the monomeric polymer rather than the size of the nanoparticle. CP nanoparticles with chain lengths measuring between 15 and 30 kDa, for instance, were rapidly cleared by the kidneys, whereas CP nanoparticles formed with 60 kDa chains exhibited a much longer plasma half-life and little to no kidney uptake. Despite forming large (30-60 nm diameter) micelles, *in vivo*, the fate of these CPs were tied to the fate of the polymer molecular weight. To be clear, that does not mean that the micelle and the single chain polymer show the same half-life, rather that micelles with shorter chains

experience drastically shorter half-lives than nanoparticles with longer chains. This was a peculiar finding because the *in vivo* thermal behavior of the nanoparticles clearly indicates that a significant portion of these structures remained fully formed even hours after injection. We hypothesized that this effect may be due to the equilibrium that self-assembled structures maintain with their unimeric counterparts; when the unimeric structures display a molecular weight below the renal filtration cutoff, the kidneys are able to continuously clear the unimers from circulation. To circumvent this effect, it may be possible to increase the stability of the circulating micelles through internal core crosslinking by incorporation of lysines [215], lysines and glutamines [216], cysteines to exploit disulfide crosslinking [200], or noncanonical amino acids using residue specific incorporation technologies [217].

Crosslinking and stabilizing the nanoparticle may enable a higher degree of control over the size of the micelles by permitting the use of even smaller chain CPs without the associated poor pharmacokinetic profile. CP-Dox micelles comprised of 15 kDa, 30 kDa, and 60 kDa chains exhibited increasing diameters of 30, 38, and 54 nm, respectively. Although it is possible that the 30 nm micelles improved the penetration depth of the drug into the tumor, their biodistribution profile (high kidney accumulation) precluded their use in mice. As we hypothesized that this trait may be due to the continuous, renal-induced clearance of single chain polymers from the serum, crosslinking may prevent this poor pharmacokinetic profile. Finally, it is unlikely that

core crosslinking will significant reduce the amount of released drug within the tumor. CP nanoparticles remain highly solvated in the core; once a drug is released due to changes in pH or hydrolysis, it is unlikely that a soluble CP carrier will be able to inhibit the diffusion of the free drug.

Others have also shown that diblock micelles tend to display pharmacokinetic profiles that are tied to the molecular weight of the polymer [198]. It may be possible to extend the plasma half-life of these diblocks by designing the hydrophobic core with an ELP composed primarily or partially of hydrophobic amino acids such as phenylalanines, tyrosines, or tryptophans. Chapter 6 demonstrates that only a few of these amino acids are necessary to direct assembly of stable nanoparticles; a core that is rich in these amino acids may be much more stable than a core rich in valines [208] or isoleucines [198], and thus be able to withstand the mechanical stress of circulation.

7.3 Strategies to Improve Treatment Efficacy

A simple strategy to enhance the antitumor effect of CP-drug conjugates would be combination therapy. There are a large number of chemotherapeutic drug combinations (a few of which are mentioned in Chapter 1) that synergistically enhance tumor toxicity. As the degree of synergy is typically tied to the molar ratio of the two (or more) chemotherapeutics, it is important to precisely control this ratio to limit the number of experimental variables. For instance, a logical next step would be to examine

the efficacy of CP-Doxorubicin and CP-Paclitaxel in combination, two constructs that have been extensively characterized. The two primary delivery routes are to (1) co-inject CP-Dox and CP-PTX at a predetermined ratio, and (2) inject a single CP conjugated to two drugs simultaneously. While the first strategy enables the ratio of the two drugs to be held constant across experiments by simply adjusting the injection ratio of the two conjugates, the second strategy requires precision control over the conjugation ratio of both drugs across multiple batches, and thus will likely confound the outcome of repeated *in vivo* studies.

All of the CP-drug conjugates that our group has developed to this point exploit unique cysteine residues as drug attachment sites. However, there are a number of situations in which an orthogonal chemistry may be required for site-specific conjugation. For instance, using cysteines for drug attachment sites would not be advisable if the CP chain or an attached peptide ligand contained cysteine residues, or if two different drugs were being conjugated to the same CP chain. In either case, it would be worth exploring the incorporation of noncanonical amino acids as they can provide completely orthogonal click chemistries such as azides and aldehydes [218]. Carboxyl and amine chemistry, while available through natural amino acids such as glutamates and lysines, are not preferred because the polypeptide would require site-specific protection and deprotection of the carboxy- and amino-terminus to prevent polypeptide polymerization.

7.4 Asymmetric Polypeptide Amphiphiles

Finally, the chapter discussing genetically encoded amphiphiles opens many possibilities to explore the rules governing how these short peptides induce extreme morphological variability once appended to their respective biopolymer and how they can be harnessed to provide useful drug carriers. One possibility would be to utilize these hydrophobic domains in combination with drug attachment domains to induce the formation of thermally responsive spherical micelles, worm-like micelles, or vesicles despite carrying a hydrophilic drug that would not normally drive assembly. Although hydrophilic drugs do not suffer from insolubility *in vivo*, they still display poor pharmacokinetics that could be greatly improved through chemical conjugation to nanoparticles or thermally targeted nanoparticles. Preliminary data does indicate that this new class of nanoparticle is feasible, as we have shown that the hydrophilic chemotherapeutic gemcitabine does not drive assembly when conjugated to a $(CGG)_8$ domain, but does not interfere with the assembly of a $(YG)_6$-$(CGG)_8$ domain upon conjugation. While the attachment of gemcitabine is not the driving force for assembly, the drug still reaps the same benefits from an improved pharmacokinetic and biodistribution profile as hydrophobic drugs (Chapters 3 and 5). It may also be fascinating to explore whether other morphologies (toroids, for instance) can be constructed through the use of noncanonical amino acids or if the conjugation and

assembly domains can be merged into the same residues, such as p-propargyloxyphenylalanine (tyrosine + alkyne) or p-acetylphenylalanine (phenylalanine + aldehyde) [218].

A number of questions remain concerning the morphology of these genetically encoded amphiphiles. While we have characterized many of the amphiphiles with a variety of techniques, they have not shed any light on whether secondary structure formation within the assembly domains plays a role in morphological variety. Future studies could include circular dichroism (CD) and fourier transform infrared spectroscopy (FTIR) to directly measure secondary structure interactions, and electron paramagnetic resonance (EPR) to determine the degree of solvation of the ELP chain.

It would also be interesting to explore the *in vitro* and *in vivo* differences induced by simply changing the morphology from spheres to worms to vesicles. For example, various systems have shown significant differences between micelles and worms in the pharmacokinetic profile [219, 220] and in the primary organs targeted [221-223], as well as differences in the quantities and mechanisms of cellular uptake [224, 225], although in many of these experiments it can be difficult to tease out whether the changes are due to differences in morphology or absolute size. Branching from this work, one could compare the pharmacokinetic and biodistribution profiles of spherical micelles assembled via conjugation of hydrophobic molecules such as pyrenylmaleimide and the worm-like micelles observed in the $(YG)_8$ genetically encoded amphiphile system by

appending a small fraction of hydrophilic fluorophores on the N-terminus of the ELP chains. It would also be feasible to instead use the attachment of doxorubicin to A[1]-160-$(CGG)_8$ to induce the formation of spherical micelles and compare the pharmacokinetic and biodistribution profiles of the drug directly against A[1]-160-$(YG)_8$-$(CGG)_8$-doxorubicin, although it is unknown whether the attachment of doxorubicin will perturb the assembly of worm-like micelles.

In summary, this thesis describes a novel method for the construction of highly repetitive polypeptides and a model to predict their phase transition behavior based on their composition, chain length, and concentration. These constructed polypeptides were assembled into thermoresponsive micelles through the attachment of drugs that display a minimum threshold hydrophobicity, and were shown to display an *in vivo* transition temperature within the narrow range of 37-42°C. Finally, we demonstrated that these thermally responsive micelles induced a 2.6 fold increase in tumor drug accumulation by thermal cycling. It is our hope that this work will serve as a foundation for others to develop new thermally responsive sequences and find new uses for these versatile polypeptides.

8. Appendices

8.1 Gene sequences

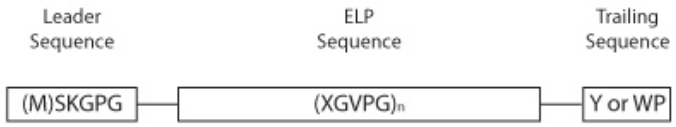

Leader Sequence

ATG AGC AAA GGG CCG GGC
(M) S K G P G

ƒ Alanine = 1

(GCC GGA GTG CCT GGT GCA GGT GTG CCA GGC GCG GGT GTT CCA GGA GCA GGC GTT CCA GGT GCG GGT GTT CCT GGC
A G V P G A G V P G A G V P G A G V P G A G V P G

GCC GGA GTG CCT GGT GCA GGT GTG CCA GGC GCG GGT GTT CCA GGA GCA GGC GTT CCA GGT GCG GGT GTT CCT GGC)$_n$
A G V P G A G V P G A G V P G A G V P G A G V P G

TAC TGA TAA TGA
Y . . .

ƒ Alanine = 0.9

(GCC GGA GTG CCT GGT GCA GGT GTG CCA GGC GTG GGT GTT CCA GGA GCA GGC GTT CCA GGT GCG GGT GTT CCT GGC
A G V P G A G V P G V G V P G A G V P G A G V P G

GCG GGT GTT CCG GGC GCC GGT GTC CCA GGT GCG GGC GTA CCG GGC GCC GGT GTT CCT GGT GCG GGC GTG CCG GGC)$_n$
A G V P G A G V P G A G V P G A G V P G A G V P G

TGG CCG TGA TAA
W P . .

ƒ Alanine = 0.8

(GCC GGA GTG CCT GGT GCA GGT GTG CCA GGC GTG GGT GTT CCA GGA GCA GGC GTT CCA GGT GCG GGT GTT CCT GGC
A G V P G A G V P G V G V P G A G V P G A G V P G

GCC GGA GTG CCT GGT GCA GGT GTG CCA GGC GTG GGT GTT CCA GGA GCA GGC GTT CCA GGT GCG GGT GTT CCT GGC)$_n$
A G V P G A G V P G V G V P G A G V P G A G V P G

TAC TGA TAA TGA
Y . . .

ƒ Alanine = 0.7

(GCC GGA GTG CCT GGT GCA GGT GTG CCA GGC GTG GGT GTT CCA GGA GCA GGC GTT CCA GGT GTG GGT GTT CCT GGC
A G V P G A G V P G V G V P G A G V P G V G V P G

GCC GGA GTG CCT GGT GCA GGT GTG CCA GGC GTG GGT GTT CCA GGA GCA GGC GTT CCA GGT GCG GGT GTT CCT GGC)$_n$
A G V P G A G V P G V G V P G A G V P G A G V P G

TGG CCG TGA TAA
W P . .

Figure 38: Gene sequence of ELP unimers. The ELP constructs consist of a leader sequence (MSKGP) followed by the ELP sequence. The methionine is cleaved during expression. A short trailer was included (Y… or WP..) to permit $A_{280\,nm}$ protein quantification. The repeat unit n=4, 8, and 16 represent the 40, 80, and 160 pentamer sequences, respectively [182].

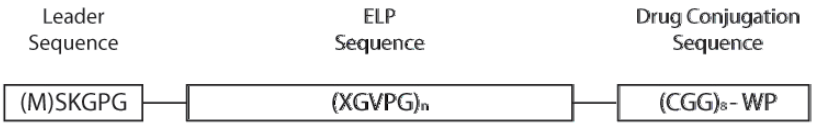

Leader Sequence

ATG AGC AAA GGG CCG GGC
(M) S K G P G

Drug Conjugation Sequence

TGC GGT GGT TGC GGC GGT TGC GGT GGC TGC GGC GGC TGC GGT GGC TGC GGC GGT TGC GGT GGC TGC
C G G C G G C G G C G G C G G C G G C G G C
GGC TGG CCG TGA TAA
G W P . .

ƒ Alanine = 1

(GCC GGA GTG CCT GGT GCA GGT GTG CCA GGC GCG GGT GTT CCA GGA GCA GGC GTT CCA GGT GCG GGT GTT CCT GGC
A G V P G A G V P G A G V P G A G V P G A G V P G
GCC GGA GTG CCT GGT GCA GGT GTG CCA GGC GCG GGT GTT CCA GGA GCA GGC GTT CCA GGT GCG GGT GTT CCT GGC)$_n$
A G V P G A G V P G A G V P G A G V P G A G V P G

ƒ Alanine = 0.9

(GCC GGA GTG CCT GGT GCA GGT GTG CCA GGC GTG GGT GTT CCA GGA GCA GGC GTT CCA GGT GCG GGT GTT CCT GGC
A G V P G A G V P G V G V P G A G V P G A G V P G
GCG GGT GTT CCG GGC GCC GGT GTC CCA GGT GCG GGC GTA CCG GGC GCC GGT GTT CCT GGT GCG GGC GTG CCG GGC)$_n$
A G V P G A G V P G A G V P G A G V P G A G V P G

ƒ Alanine = 0.8

(GCC GGA GTG CCT GGT GCA GGT GTG CCA GGC GTG GGT GTT CCA GGA GCA GGC GTT CCA GGT GCG GGT GTT CCT GGC
A G V P G A G V P G V G V P G A G V P G A G V P G
GCC GGA GTG CCT GGT GCA GGT GTG CCA GGC GTG GGT GTT CCA GGA GCA GGC GTT CCA GGT GCG GGT GTT CCT GGC)$_n$
A G V P G A G V P G V G V P G A G V P G A G V P G

ƒ Alanine = 0.7

(GCC GGA GTG CCT GGT GCA GGT GTG CCA GGC GTG GGT GTT CCA GGA GCA GGC GTT CCA GGT GTG GGT GTT CCT GGC
A G V P G A G V P G V G V P G A G V P G V G V P G
GCC GGA GTG CCT GGT GCA GGT GTG CCA GGC GTG GGT GTT CCA GGA GCA GGC GTT CCA GGT GCG GGT GTT CCT GGC)$_n$
A G V P G A G V P G V G V P G A G V P G A G V P G

Figure 39: Gene sequence of ELP micelles that assemble through drug conjugation. The ELP constructs consist of a leader sequence (MSKGP) followed by the ELP sequence. The methionine is cleaved during expression. A short cysteine-rich trailer was appended to the C-terminus $(CGG)_8WP$ to both allow site specific drug conjugation to the unique cysteine residues and permit $A_{280\ nm}$ protein quantification via the tryptophan reside ($\varepsilon = 5630\ mol^{-1}cm^{-1}$). The repeat unit n=4, 8, and 16 represent the 40, 80, and 160 pentamer sequences, respectively.

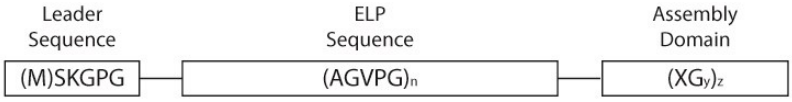

Leader Sequence

ATG AGC AAA GGG CCG GGC
(M) S K G P G

ELP Sequence

(GCC GGA GTG CCT GGT GCA GGT GTG CCA GGC GCG GGT GTT CCA GGA GCA GGC GTT CCA GGT GCG GGT GTT CCT GGC
A G V P G A G V P G A G V P G A G V P G A G V P G

GCC GGA GTG CCT GGT GCA GGT GTG CCA GGC GCG GGT GTT CCA GGA GCA GGC GTT CCA GGT GCG GGT GTT CCT GGC)$_n$
A G V P G A G V P G A G V P G A G V P G A G V P G

$(LGG)_8$

CTG GGC GGT CTG GGT GGC CTG GGT GGT CTG GGT GGC CTG GGC GGT CTG GGT GGT CTG GGC GGC TTG GGT GGC
L G G L G G L G G L G G L G G L G G L G G L G G L G G
TAC TGA TAA ACT
Y . . .

$(IGG)_8$

ATC GGC GGT ATT GGT GGC ATT GGT GGT ATC GGT GGC ATC GGC GGT ATC GGT GGT ATT GGC GGC ATC GGT GGC
I G G I G G I G G I G G I G G I G G I G G I G G I G G
TAC TGA TAA ACT
Y . . .

$(HGG)_8$

CAT GGC GGT CAC GGC GGC CAC GGT GGT CAC GGT GGC CAT GGC GGT CAT GGT GGT CAC GGC GGT CAT GGT GGC
H G G H G G H G G H G G H G G H G G H G G H G G H G G
TAC TGA TAA ACT
Y . . .

$(WGG)_8$

TGG GGC GGT TGG GGC GGC TGG GGT GGT TGG GGT GGC TGG GGC GGT TGG GGT GGT TGG GGC GGC TGG GGT GGC
W G G W G G W G G W G G W G G W G G W G G W G G W G G
TAC TGA TAA ACT
Y . . .

$(FG)_8$

TTC GGC TTT GGC TTC GGT TTC GGT TTT GGT TTC GGT TTC GGC TTT GGC TAC TGA TAA ACT
F G F G F G F G F G F G F G F G Y . . .

F_8

TTC TTT TTC TTC TTT TTC TTC TTT TAC TGA TAA
F F F F F F F F Y . .

$(YGG)_8$

TAT GGC GGT TAC GGC GGC TAC GGT GGT TAT GGT GGC TAT GGC GGT TAC GGT GGT TAT GGC GGC TAC GGT GGC
Y G G Y G G Y G G Y G G Y G G Y G G Y G G Y G G Y G G
TAC TGA TAA ACT
Y . . .

$(YG)_8$

TAT GGC TAC GGC TAC GGT TAT GGT TAT GGT TAC GGT TAT GGC TAC GGC TAC TGA TAA ACT
Y G Y G Y G Y G Y G Y G Y G Y G Y G Y . . .

Y_8

TAT TAC TAT TAT TAT TAC TAC TAT TAC TGA TAA
Y Y Y Y Y Y Y Y Y . .

Figure 40: Gene sequence of genetically encoded amphiphiles. The ELP constructs consist of a leader sequence (MSKGP) followed by the ELP sequence. The methionine is cleaved during expression. The repeat unit n=4, 8, and 16 represent the 40, 80, and 160 pentamer sequences, respectively. Each assembly domain is shown with both the shorthand notation and the actual sequence, followed by a single tyrosine that allows $A_{280\ nm}$ protein quantification ($\varepsilon = 1290\ mol^{-1}cm^{-1}$).

8.2 Gene Libraries

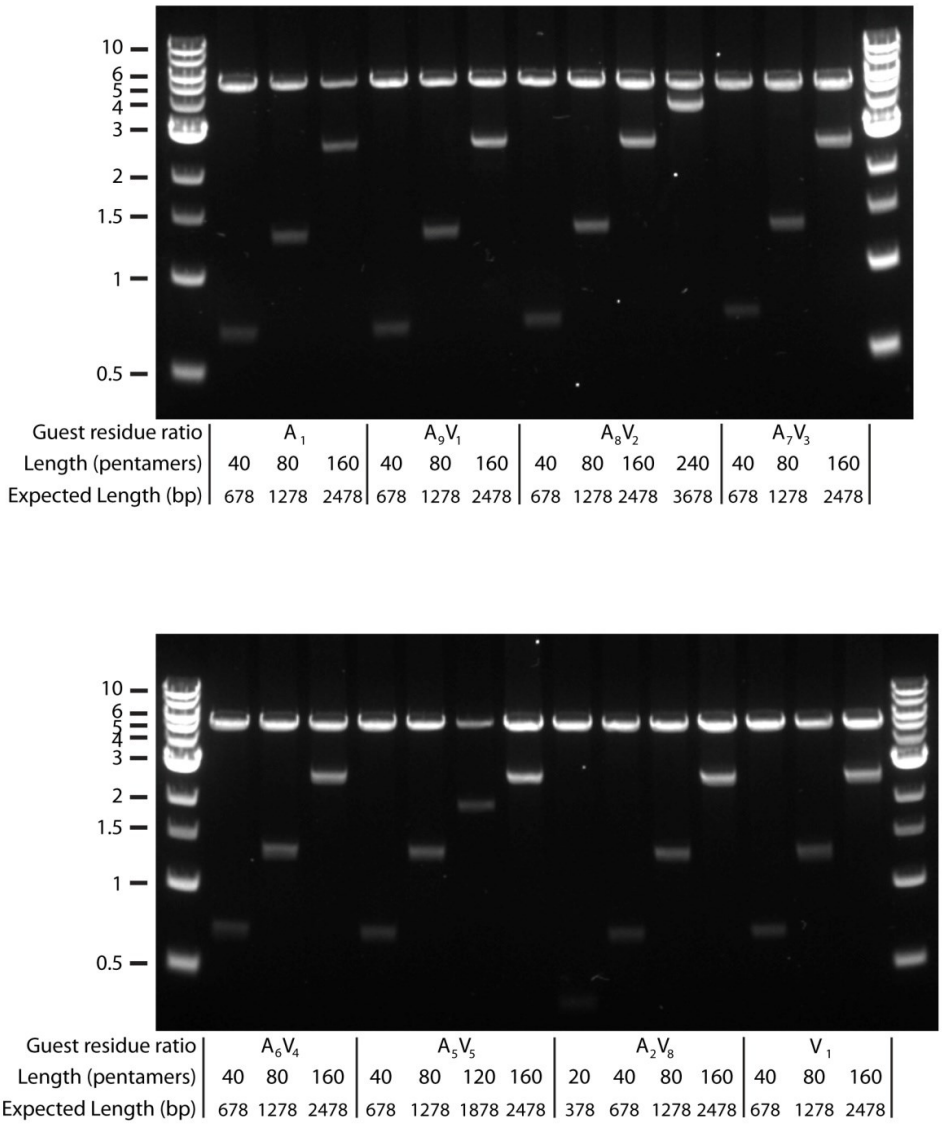

Figure 41: ELP unimer gene libraries. ELP genes were run on a 1% agarose gel and stained with Sybr Safe (Invitrogen). The left and right lanes represent a size standard ladder (1 KB DNA Ladder, New England Biolabs) with the length (kb) shown on the left. The remaining lanes represent diagnostic digests of the constructs restricted with BamHI-HF and XbaI (hence appending 66 bp of flanking sequences to each band). The composition of the guest residue ratio and the expected length of the ELP constructs (shown in pentamers and basepairs) are displayed on the bottom [182].

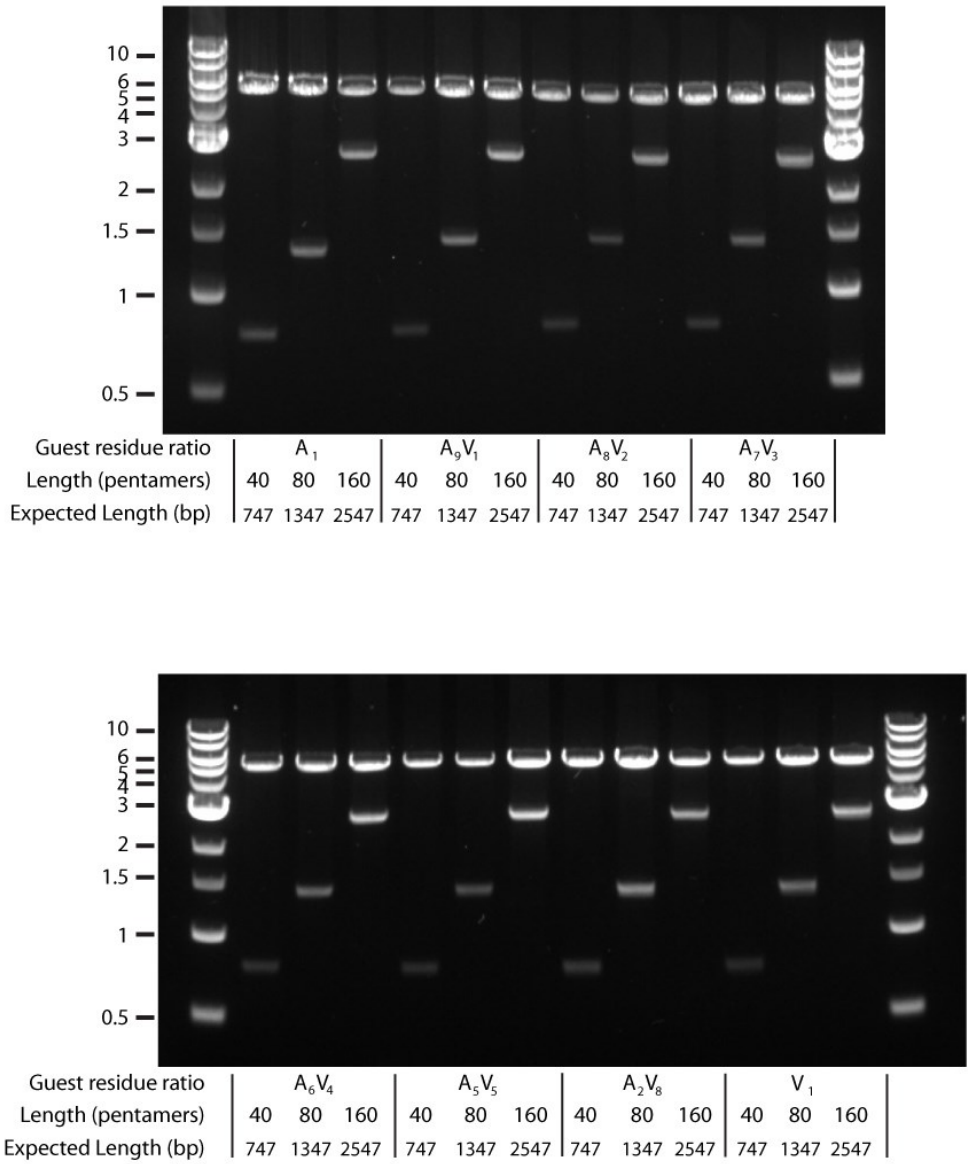

Figure 42: CP gene libraries. CP genes were run on a 1% agarose gel and stained with Sybr Safe. The left and right lanes represent a size standard ladder with the length (kb) shown on the left. The remaining lanes represent diagnostic digests of the constructs restricted with BamHI-HF and XbaI (hence appending 66 bp of flanking sequences to each band). The composition of the guest residue ratio and the expected length of the ELP constructs (shown in pentamers and basepairs) are displayed on the bottom.

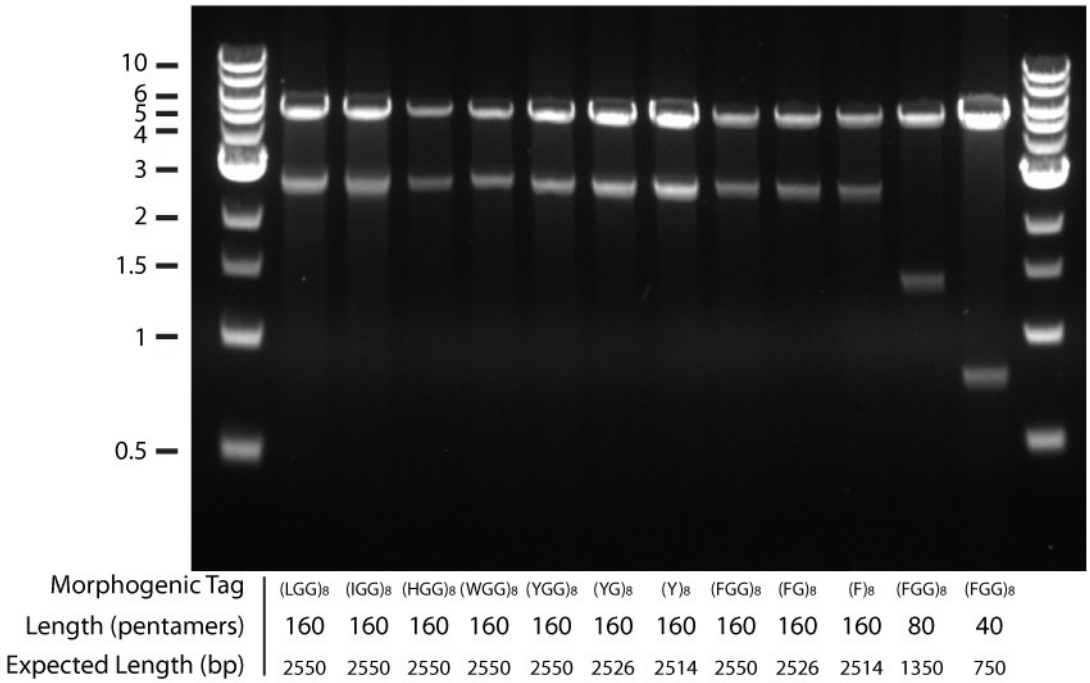

Morphogenic Tag	$(LGG)_8$	$(IGG)_8$	$(HGG)_8$	$(WGG)_8$	$(YGG)_8$	$(YG)_8$	$(Y)_8$	$(FGG)_8$	$(FG)_8$	$(F)_8$	$(FGG)_8$	$(FGG)_8$
Length (pentamers)	160	160	160	160	160	160	160	160	160	160	80	40
Expected Length (bp)	2550	2550	2550	2550	2550	2526	2514	2550	2526	2514	1350	750

Figure 43: Genetically encoded amphiphile gene libraries. The amphiphile genes were run on a 1% agarose gel and stained with Sybr Safe. The left and right lanes represent a size standard ladder with the length (kb) shown on the left. The remaining lanes represent diagnostic digests of the constructs restricted with BamHI-HF and XbaI (hence appending 66 bp of flanking sequences to each band). The composition of the morphogenic domain and the expected length of the amphiphiles (shown in basepairs and elastin-like polypeptide pentamers) are displayed on the bottom.

8.3 Protein Expression Libraries

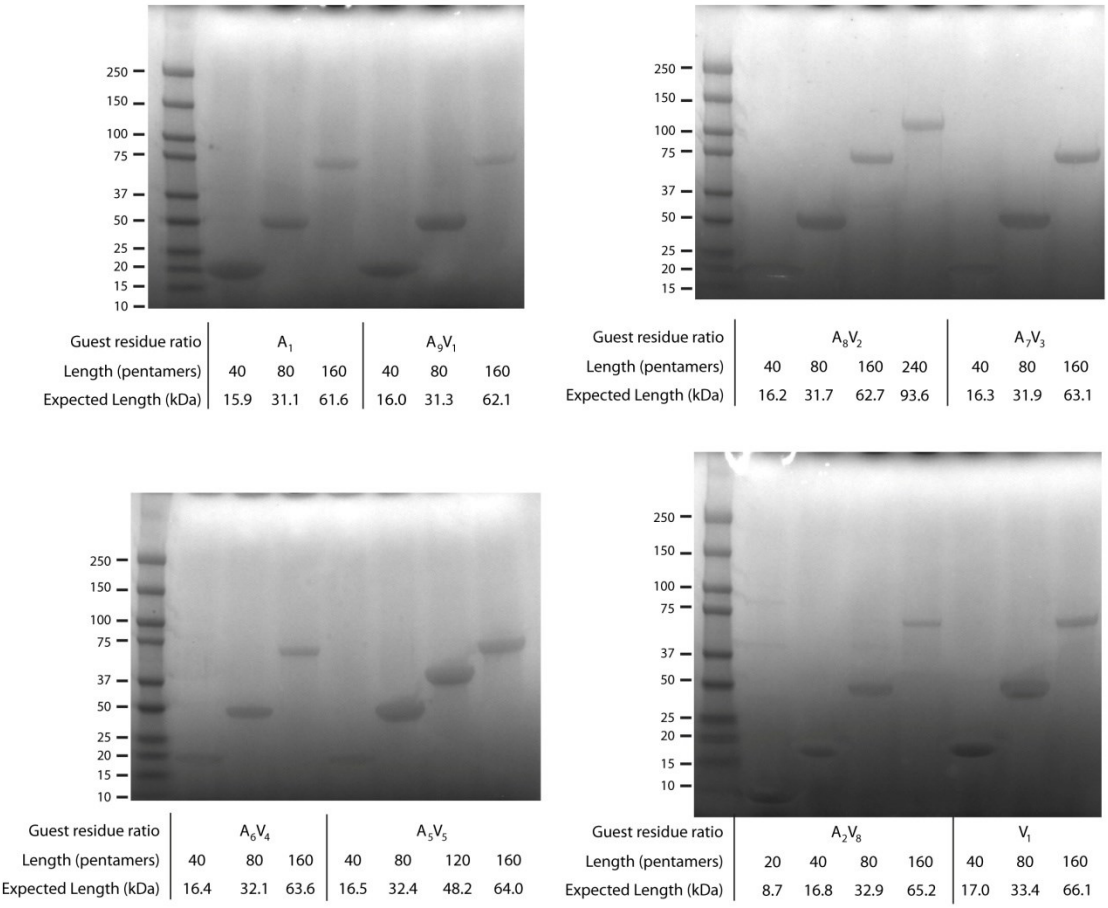

Figure 44: ELP unimer expression libraries. Proteins purified by 2-3 cycles of inverse transition cycling were run on an SDS-PAGE gel and stained with $CuCl_2$. The left lane is the Bio-Rad Kaleidoscope Protein Ladder, with the molecular weights (in kDa) shown on the left. The remaining lanes represent the purified proteins with the guest residue ratio (composition), and length (pentamers and kDa) shown beneath their respective lanes [182].

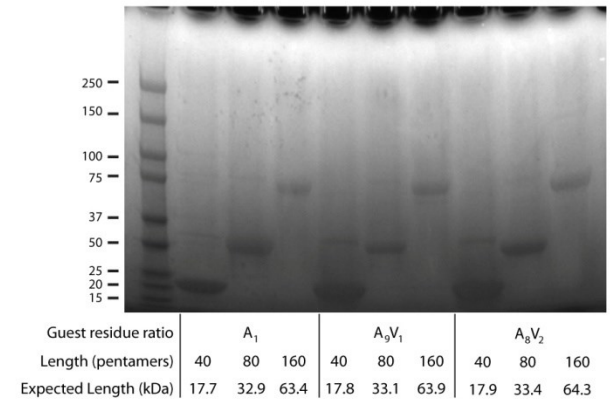

Guest residue ratio	A_1			A_9V_1			A_8V_2		
Length (pentamers)	40	80	160	40	80	160	40	80	160
Expected Length (kDa)	17.7	32.9	63.4	17.8	33.1	63.9	17.9	33.4	64.3

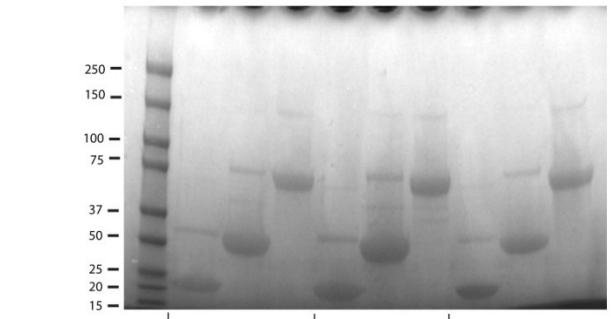

Guest residue ratio	A_7V_3			A_6V_4			A_5V_5		
Length (pentamers)	40	80	160	40	80	160	40	80	160
Expected Length (kDa)	18.0	33.6	64.8	18.1	33.8	65.2	18.2	34.0	65.7

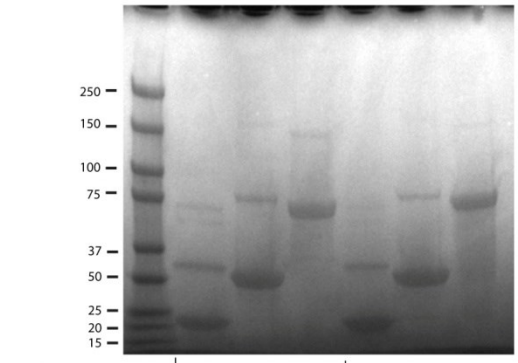

Guest residue ratio	A_2V_8			V_1		
Length (pentamers)	40	80	160	40	80	160
Expected Length (kDa)	18.6	34.7	67.0	18.8	35.2	67.9

Figure 45: ELP micelle expression libraries. Proteins purified by 2-3 cycles of inverse transition cycling were run on an SDS-PAGE gel and stained with $CuCl_2$. The left lane is the Bio-Rad Kaleidoscope Protein Ladder, with the molecular weights (in kDa) shown on the left. The remaining lanes represent the purified proteins with the guest

residue ratio (composition), and length (pentamers and kDa) shown beneath their respective lanes. The dimer and trimer bands that appear above the primary band are indicative of the formation of cysteine-cysteine disulfide bonds between the drug conjugation domains of different ELP chains.

8.4 MALDI-MS

Table 11: MALDI-MS results for ELP_1 and ELP_2 libraries constructed with PEe-RDL. Molecular weights could not be accurately determined (n.d.) for species larger than 160 pentapeptides. Theoretical masses were determined by inputting the theoretical amino acid composition of the peptide into the exPASy Proteomics Server [226], which then outputs the sum of the isotopically averaged mass of each individual amino acid [153].

	Length (Pentamer)	Expected (g/mol)	Measured (g/mol)	Error (%)
ELP_4	30	12465.7	12476.2	0.1
	60	24750.3	23524.9	-5.0
	60 L_1T_1	26914.7	26965	0.2
	120	49319.4	49309.3	0.0
	240	98457.7	n.d.	n.d.
ELP_2	80 L_1	30561.1	30502.7	-0.2
	160 L_1	60514.6	59539.6	-1.6
	240 L_1	90468	n.d.	n.d.
	320 L_1	120421.5	n.d.	n.d.

Table 12: MALDI-MS results for ELP unimers. Theoretical masses were determined by inputting the theoretical amino acid composition of the peptide into the exPASy Proteomics Server [226], which then outputs the sum of the isotopically averaged mass of each individual amino acid [182].

fAlanine	Length (pentamer)	Expected (g/mol)	Measured (g/mol)	Error (%)
1	40	15864.9	15833.4	-0.20
1	80	31122.2	31034.5	-0.28
1	160	61636.7	61425.2	-0.34
0.9	40	15977.1	15966.7	-0.07
0.9	80	31346.6	31265.1	-0.26
0.9	160	62085.6	61916.6	-0.27
0.9	240*	93618.0	93486.7	-0.14
0.8	40	16209.5	16169.7	-0.25
0.8	80	31691.2	31604.0	-0.28
0.8	160	62654.6	62467.7	-0.30
0.7	40	16321.7	16273.2	-0.30
0.7	80	31915.6	31855.2	-0.19
0.7	160	63103.5	62908.3	-0.31
0.6	40	16433.9	16384.5	-0.30
0.6	80	32140	32049.6	-0.28
0.6	160	63552.3	63405.1	-0.23
0.5	40	16546.1	16513.4	-0.20
0.5	80	32364.5	32269.0	-0.30
0.5	120*	48182.8	48140.9	-0.09
0.5	160	64001.2	63799.0	-0.32
0.2	20*	8685.1	8713.0	0.32
0.2	40	16762.6	16728.7	-0.20
0.2	80	32917.6	32861.4	-0.17
0.2	160	65227.6	65148.3	-0.12
0	40	16987	16924.5	-0.37
0	80	33366.5	33265.9	-0.30
0	160	66125.3	65983.2	-0.21

*Lengths followed by an asterisk were not used in the construction of the model

Table 13: MALDI-MS results for genetically encoded amphiphiles. Theoretical masses were determined by inputting the theoretical amino acid composition of the peptide into the exPASy Proteomics Server [226], which then outputs the sum of the isotopically averaged mass of each individual amino acid.

Trailer	Length	Expected	Measured	Error (%)
Control	160	61636.7	61425.2	-0.34
$(IGG)_8$	160	63454.8	63495.7	0.06
$(LGG)_8$	160	63454.8	63434.1	-0.03
$(HGG)_8$	160	63646.7	64147.3	0.79
$(WGG)_8$	160	64039.3	n.d.	n.d.
$(YGG)_8$	160	63855	63852.6	0.00
$(YG)_8$	160	63398.5	63463.5	0.10
Y_8	160	62942.1	63027.8	0.14
$(FGG)_8$	160	63727	63760.9	0.05
$(FG)_8$	160	63270.6	63319.6	0.08
F_8	160	62814.1	n.d.	n.d.
$(FGG)_8$	80	33212.4	33233.3	0.06
$(FGG)_8$	40	17955.1	17959.9	0.03

n.d.: not determined

8.5 Thermal Profiles

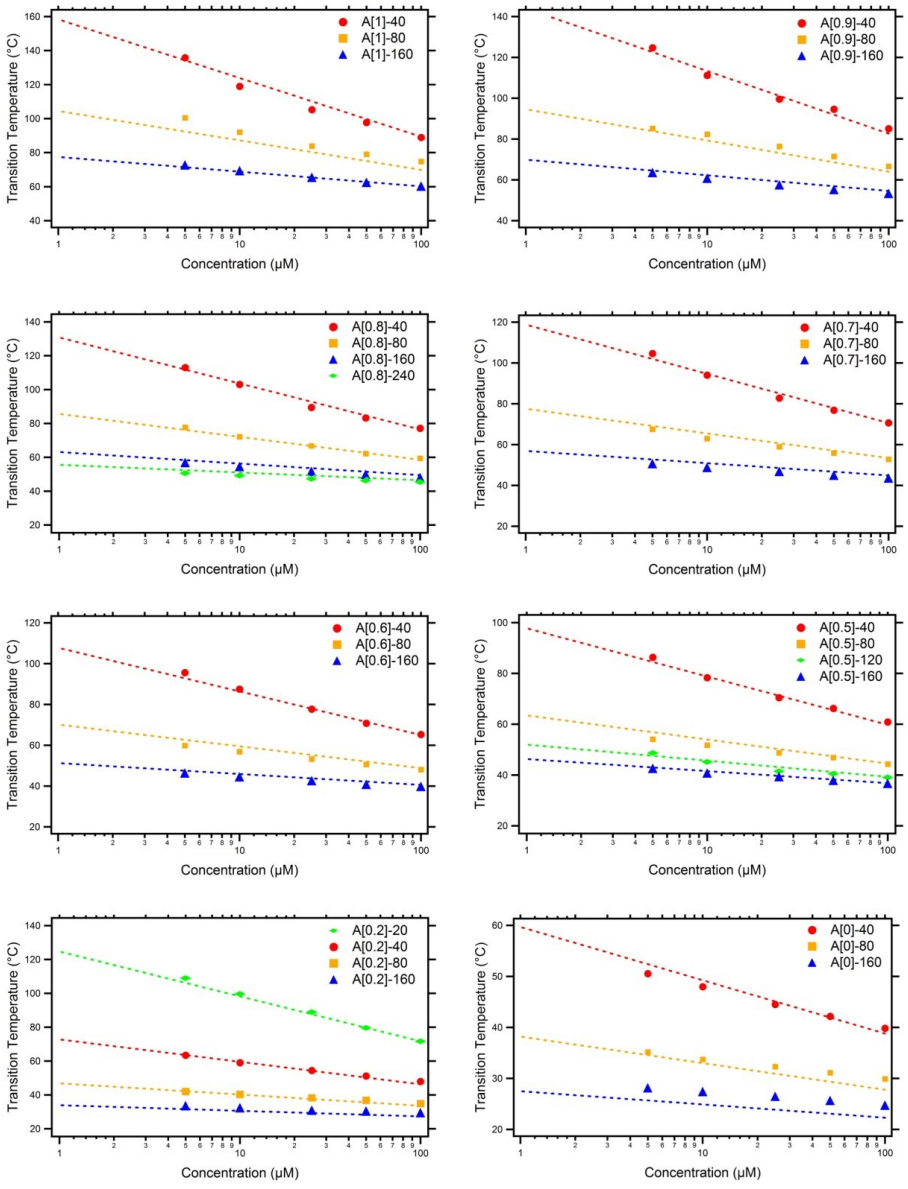

Figure 46: Thermal properties for ELP unimer libraries. The measured transition temperatures for each of the three molecular weights synthesized (40, 80, and 160 pentamers) as a function of ELP concentration for each ELP library. The three data sets shown in green represent the three ELP constructs designed to test the fidelity of the model at molecular weights other than 40, 80, and 160 pentamers. The dashed lines represent the predicted transition temperatures derived from the ELP unimer model (Equation 4) [182].

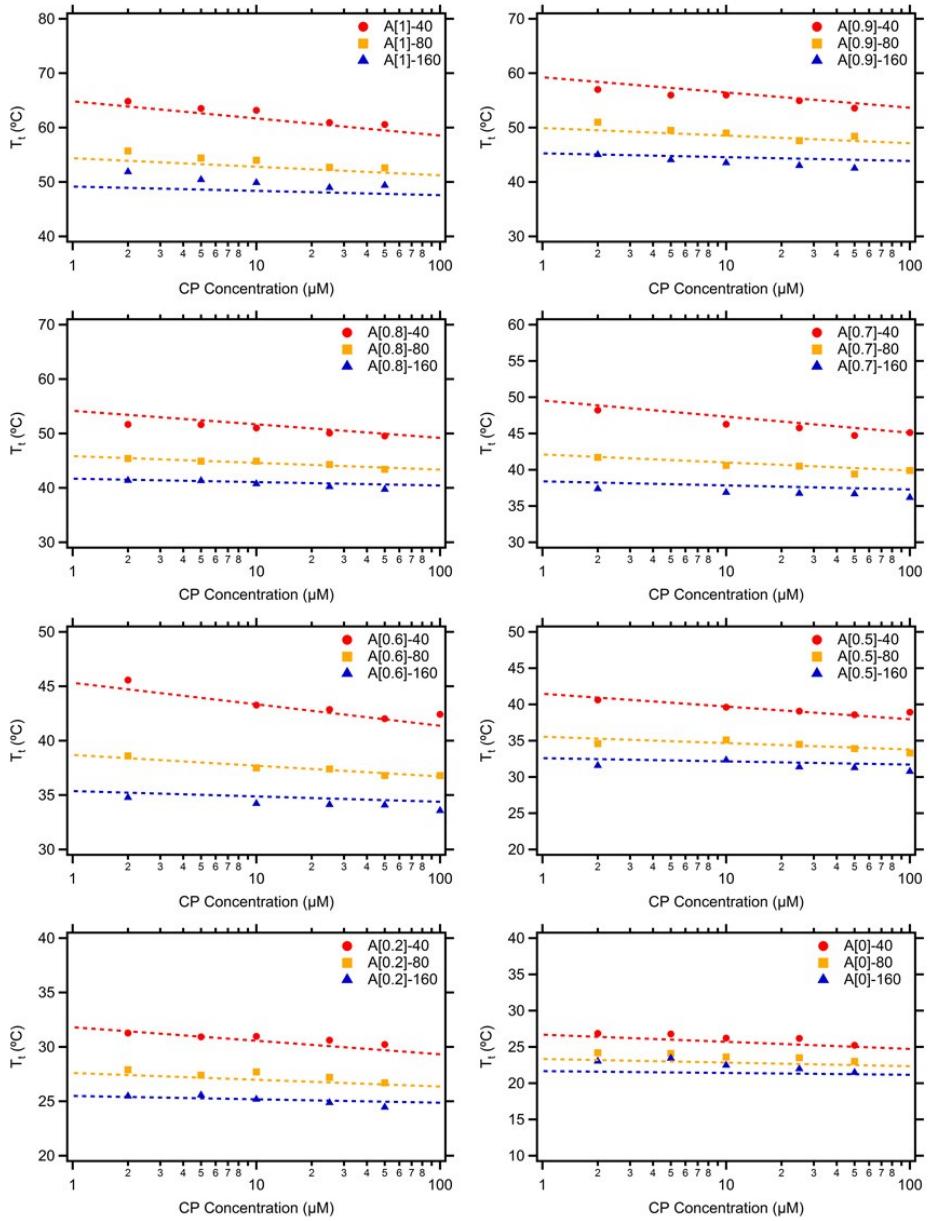

Figure 47: Thermal properties for ELP micelle libraries. Each ELP construct was conjugated to n-benzylmaleimide and purified, at which point the transition temperature was measured as a function of ELP concentration. The dashed lines represent the predicted transition temperatures derived from the ELP micelle model (Equation 5).

8.6 Transition Temperatures of ELP Unimers

Table 14: ELP compositions and lengths necessary for designing ELP unimers with a specific transition temperature (rounded to the nearest 1°C) at select concentrations in PBS. The ELP nomenclature is A[X]-Y, where X represents the fraction of alanine (A) in the guest residue composition (rest, valine (V)), and Y represents the length of the ELP in pentamers [182].

T_t	1 uM	5 uM	10 uM	25 uM	50 uM	100 uM	250 uM	500 uM	1000 uM
19									A[0]-180 A[0]-200
20							A[0]-200	A[0]-160 A[0]-180 A[0]-200	A[0]-140 A[0]-160
21						A[0]-200	A[0]-160 A[0]-180	A[0]-140	A[0]-100 A[0]-120 A[0.1]-180 A[0.1]-200
22				A[0]-200	A[0]-180 A[0]-200	A[0]-160 A[0]-180	A[0]-140	A[0]-120 A[0.1]-180 A[0.1]-200	A[0.1]-140 A[0.1]-160
23			A[0]-200	A[0]-180	A[0]-160	A[0]-140 A[0.1]-200	A[0]-120 A[0.1]-160 A[0.1]-180 A[0.1]-200	A[0]-100 A[0.1]-140 A[0.1]-160	A[0]-80 A[0.1]-100 A[0.1]-120 A[0.2]-200
24		A[0]-200	A[0]-180	A[0]-160	A[0]-140 A[0.1]-200	A[0]-120 A[0.1]-180	A[0]-100 A[0.1]-140	A[0]-80 A[0.1]-120 A[0.2]-180 A[0.2]-200	A[0]-60 A[0.2]-140 A[0.2]-160 A[0.2]-180
25	A[0]-200	A[0]-180	A[0]-160	A[0]-140 A[0.1]-200	A[0]-120 A[0.1]-180	A[0.1]-140 A[0.1]-160	A[0.1]-120 A[0.2]-180 A[0.2]-200	A[0.1]-100 A[0.2]-160	A[0.1]-80 A[0.2]-120
26	A[0]-180	A[0]-160	A[0]-140 A[0.1]-200	A[0]-120 A[0.1]-160 A[0.1]-180	A[0.1]-160	A[0]-100 A[0.2]-200	A[0]-80 A[0.1]-100 A[0.2]-160	A[0.1]-80 A[0.2]-120 A[0.2]-140	A[0.2]-100 A[0.3]-160 A[0.3]-180 A[0.3]-200
27		A[0]-140 A[0.1]-180 A[0.1]-200	A[0.1]-180		A[0]-100 A[0.1]-140 A[0.2]-180 A[0.2]-200	A[0.1]-120 A[0.2]-160 A[0.2]-180	A[0.2]-140	A[0]-60 A[0.2]-100 A[0.3]-180 A[0.3]-200	A[0.1]-60 A[0.2]-80 A[0.3]-120 A[0.3]-140
28	A[0]-160 A[0.1]-200	A[0.1]-160	A[0]-120 A[0.1]-160	A[0]-100 A[0.1]-140 A[0.2]-180 A[0.2]-200	A[0.1]-120 A[0.2]-160	A[0]-80 A[0.1]-100 A[0.2]-140	A[0.1]-80 A[0.2]-120 A[0.3]-180 A[0.3]-200	A[0.3]-140 A[0.3]-160	A[0]-40 A[0.3]-100 A[0.4]-200

T_t	1 uM	5 uM	10 uM	25 uM	50 uM	100 uM	250 uM	500 uM	1000 uM
29	A[0]-140 A[0.1]-180	A[0]-120 A[0.2]-200	A[0.1]-140 A[0.2]-180 A[0.2]-200	A[0.1]-120 A[0.2]-160	A[0]-80 A[0.2]-140	A[0.2]-120 A[0.3]-180 A[0.3]-200	A[0]-60 A[0.2]-100 A[0.3]-140 A[0.3]-160	A[0.1]-60 A[0.2]-80 A[0.3]-120 A[0.4]-200	A[0.2]-60 A[0.3]-80 A[0.4]-160 A[0.4]-180
30		A[0.1]-140 A[0.2]-180	A[0]-100	A[0.2]-140	A[0.1]-100 A[0.3]-180 A[0.3]-200	A[0.3]-160	A[0.3]-120	A[0.3]-100 A[0.4]-160 A[0.4]-180	A[0.4]-120 A[0.4]-140
31	A[0]-120 A[0.1]-160 A[0.2]-200	A[0]-100	A[0.1]-120 A[0.2]-160	A[0]-80 A[0.1]-100 A[0.3]-180 A[0.3]-200	A[0.2]-120 A[0.3]-160	A[0]-60 A[0.1]-80 A[0.2]-100 A[0.3]-140	A[0.1]-60 A[0.2]-80 A[0.4]-180 A[0.4]-200	A[0.4]-140	A[0.1]-40 A[0.3]-60 A[0.4]-100 A[0.5]-200
32	A[0.1]-140 A[0.2]-180	A[0.1]-120 A[0.2]-160	A[0.2]-140 A[0.3]-200	A[0.2]-120 A[0.3]-160	A[0.1]-80 A[0.3]-140	A[0.3]-120 A[0.4]-180 A[0.4]-200	A[0.3]-100 A[0.4]-140 A[0.4]-160	A[0]-40 A[0.2]-60 A[0.3]-80 A[0.4]-120	A[0.4]-80 A[0.5]-140 A[0.5]-160 A[0.5]-180
33		A[0.2]-140 A[0.3]-200	A[0]-80 A[0.1]-100 A[0.3]-180		A[0.2]-100 A[0.4]-200	A[0.4]-160	A[0.4]-120	A[0.4]-100 A[0.5]-160 A[0.5]-180 A[0.5]-200	A[0.2]-40 A[0.5]-120
34	A[0]-100 A[0.1]-120 A[0.2]-160	A[0.1]-100 A[0.3]-180	A[0.2]-120 A[0.3]-160	A[0.1]-80 A[0.2]-100 A[0.3]-140 A[0.4]-200	A[0]-60 A[0.3]-120 A[0.4]-180	A[0.2]-80 A[0.3]-100 A[0.4]-140	A[0.2]-60 A[0.3]-80 A[0.5]-180 A[0.5]-200	A[0.1]-40 A[0.3]-60 A[0.5]-140	A[0.4]-60 A[0.5]-100
35	A[0.3]-200	A[0]-80 A[0.2]-120 A[0.3]-160	A[0.3]-140 A[0.4]-200	A[0.3]-120 A[0.4]-180	A[0.4]-160	A[0.1]-60 A[0.5]-200	A[0]-40 A[0.4]-100 A[0.5]-160	A[0.4]-80 A[0.5]-120	A[0.5]-80 A[0.6]-160 A[0.6]-180 A[0.6]-200
36	A[0.2]-140 A[0.3]-180	A[0.4]-200	A[0.1]-80 A[0.2]-100 A[0.4]-180	A[0]-60 A[0.4]-160	A[0.2]-80 A[0.3]-100 A[0.4]-140 A[0.5]-200	A[0.4]-120 A[0.5]-180	A[0.5]-140	A[0.5]-100 A[0.6]-180 A[0.6]-200	A[0.3]-40 A[0.6]-120 A[0.6]-140
37		A[0.3]-140 A[0.4]-180	A[0.3]-120	A[0.4]-140	A[0.1]-60 A[0.4]-120 A[0.5]-180	A[0.3]-80 A[0.5]-160	A[0.3]-60 A[0.4]-80 A[0.5]-120 A[0.6]-200	A[0.2]-40 A[0.4]-60 A[0.6]-160	A[0.5]-60 A[0.6]-100
38	A[0]-80 A[0.1]-100 A[0.2]-120 A[0.3]-160	A[0.1]-80 A[0.2]-100	A[0]-60 A[0.4]-160	A[0.2]-80 A[0.3]-100 A[0.5]-180 A[0.5]-200	A[0.5]-160	A[0.2]-60 A[0.4]-100 A[0.5]-140	A[0.1]-40 A[0.5]-100 A[0.6]-160 A[0.6]-180	A[0.5]-80 A[0.6]-120 A[0.6]-140	A[0.4]-40 A[0.6]-80 A[0.7]-200

T_t	1 uM	5 uM	10 uM	25 uM	50 uM	100 uM	250 uM	500 uM	1000 uM
39	A[0.4]-200	A[0.3]-120 A[0.4]-160	A[0.4]-140 A[0.5]-200	A[0.1]-60 A[0.4]-120	A[0.3]-80	A[0]-40 A[0.5]-120 A[0.6]-200	A[0.6]-140		A[0.7]-140 A[0.7]-160 A[0.7]-180
40	A[0.3]-140 A[0.4]-180	A[0.5]-200	A[0.2]-80 A[0.3]-100 A[0.5]-180	A[0.5]-160	A[0.2]-60 A[0.4]-100 A[0.5]-140 A[0.6]-200	A[0.6]-180	A[0.6]-120	A[0.3]-40 A[0.6]-100 A[0.7]-180 A[0.7]-200	A[0]-20 A[0.6]-60 A[0.7]-100 A[0.7]-120
41		A[0]-60 A[0.4]-140 A[0.5]-180	A[0.4]-120	A[0.3]-80 A[0.5]-140	A[0.5]-120 A[0.6]-180	A[0.3]-60 A[0.4]-80 A[0.5]-100 A[0.6]-160	A[0.2]-40 A[0.4]-60 A[0.5]-80 A[0.7]-200	A[0.5]-60 A[0.6]-80 A[0.7]-140 A[0.7]-160	A[0.5]-40 A[0.7]-80
42	A[0.1]-80 A[0.2]-100 A[0.3]-120 A[0.4]-160	A[0.2]-80 A[0.3]-100	A[0.1]-60 A[0.5]-160	A[0.4]-100 A[0.6]-200	A[0]-40 A[0.6]-160	A[0.1]-40 A[0.6]-140	A[0.6]-100 A[0.7]-160 A[0.7]-180	A[0.7]-120	A[0.8]-180 A[0.8]-200
43	A[0.5]-200	A[0.4]-120 A[0.5]-160	A[0.5]-140 A[0.6]-200	A[0.2]-60 A[0.5]-120 A[0.6]-180	A[0.4]-80	A[0.6]-120 A[0.7]-200	A[0.7]-140	A[0.4]-40 A[0.7]-100	A[0.1]-20 A[0.7]-60 A[0.8]-120 A[0.8]-140 A[0.8]-160
44	A[0.4]-140 A[0.5]-180		A[0.3]-80 A[0.4]-100 A[0.6]-180	A[0.6]-160	A[0.3]-60 A[0.5]-100 A[0.6]-140	A[0.5]-80 A[0.7]-180	A[0.6]-80	A[0.6]-60 A[0.8]-180 A[0.8]-200	A[0.6]-40 A[0.8]-100
45	A[0]-60	A[0.1]-60 A[0.5]-140 A[0.6]-200		A[0]-40 A[0.6]-140	A[0.6]-120 A[0.7]-200	A[0.4]-60 A[0.7]-160	A[0.3]-40 A[0.5]-60 A[0.7]-120	A[0.7]-80 A[0.8]-140 A[0.8]-160	A[0.2]-20 A[0.8]-80
46	A[0.3]-100 A[0.5]-160	A[0.4]-100 A[0.6]-180	A[0.5]-120 A[0.6]-160	A[0.4]-80 A[0.5]-100 A[0.7]-200	A[0.1]-40 A[0.7]-180	A[0.2]-40 A[0.6]-100 A[0.7]-140	A[0.7]-100 A[0.8]-180 A[0.8]-200	A[0]-20 A[0.8]-120	A[0.7]-40 A[0.8]-60
47	A[0.2]-80 A[0.4]-120	A[0.3]-80	A[0.2]-60	A[0.3]-60 A[0.7]-180	A[0.5]-80 A[0.7]-160		A[0.8]-160	A[0.5]-40 A[0.8]-100	A[0.9]-140 A[0.9]-160 A[0.9]-180 A[0.9]-200
48	A[0.6]-200	A[0.5]-120 A[0.6]-160	A[0.6]-140 A[0.7]-200	A[0.6]-120 A[0.7]-160	A[0.6]-100 A[0.7]-140	A[0.7]-120 A[0.8]-200	A[0.4]-40 A[0.6]-60 A[0.8]-140	A[0.7]-60 A[0.9]-200	A[0.3]-20 A[0.9]-100 A[0.9]-120
49	A[0.5]-140 A[0.6]-180	A[0.2]-60 A[0.7]-200	A[0]-40 A[0.4]-80 A[0.5]-100 A[0.7]-180	A[0.1]-40	A[0.4]-60 A[0.8]-200	A[0.6]-80 A[0.8]-180	A[0.7]-80 A[0.8]-120	A[0.8]-80 A[0.9]-160 A[0.9]-180	A[0.8]-40 A[0.9]-80

T_t	1 uM	5 uM	10 uM	25 uM	50 uM	100 uM	250 uM	500 uM	1000 uM
50	A[0.1]-60	A[0.6]-140	A[0.6]-120	A[0.5]-80 A[0.7]-140	A[0.2]-40 A[0.7]-120 A[0.8]-180	A[0.3]-40 A[0.5]-60 A[0.7]-100 A[0.8]-160	A[0.9]-200	A[0.1]-20 A[0.6]-40 A[0.9]-140	A[0.4]-20 A[0.9]-60
51	A[0.4]-100 A[0.6]-160	A[0.4]-80 A[0.5]-100 A[0.7]-180	A[0.3]-60 A[0.7]-160	A[0.6]-100 A[0.8]-200		A[0.8]-140	A[0.8]-100 A[0.9]-180	A[0.9]-120	A[1]-180 A[1]-200
52	A[0.3]-80 A[0.5]-120	A[0]-40		A[0.4]-60 A[0.8]-180	A[0.6]-80 A[0.8]-160		A[0.5]-40 A[0.9]-140 A[0.9]-160	A[0.8]-60 A[0.9]-100	A[0.9]-40 A[1]-100 A[1]-120 A[1]-140 A[1]-160
53	A[0.7]-200	A[0.6]-120 A[0.7]-160	A[0.7]-140 A[0.8]-200	A[0.7]-120	A[0.5]-60 A[0.7]-100 A[0.8]-140	A[0.7]-80 A[0.8]-120 A[0.9]-200	A[0]-20 A[0.7]-60 A[0.8]-80	A[0.2]-20 A[0.9]-80 A[1]-200	A[0.5]-20 A[1]-60 A[1]-80
54	A[0.6]-140	A[0.3]-60	A[0.1]-40 A[0.5]-80 A[0.6]-100	A[0.2]-40 A[0.8]-160		A[0.6]-60 A[0.9]-180	A[0.9]-120	A[0.7]-40 A[1]-160 A[1]-180	
55	A[0.7]-180	A[0.7]-140 A[0.8]-200	A[0.8]-180	A[0.6]-80 A[0.8]-140	A[0.3]-40 A[0.8]-120 A[0.9]-200	A[0.4]-40 A[0.8]-100 A[0.9]-160	A[0.9]-100	A[1]-120 A[1]-140	A[0.6]-20 A[1]-40
56	A[0.2]-60	A[0.8]-180	A[0.7]-120 A[0.8]-160	A[0.7]-100 A[0.9]-200	A[0.9]-180	A[0.9]-140	A[0.6]-40 A[1]-180 A[1]-200	A[0.9]-60 A[1]-100	
57	A[0.4]-80 A[0.5]-100 A[0.7]-160	A[0.5]-80 A[0.6]-100	A[0.4]-60	A[0.5]-60	A[0.7]-80 A[0.9]-160		A[0.1]-20 A[0.8]-60 A[1]-160	A[0.3]-20 A[0.8]-40	A[0.7]-20
58	A[0.6]-120	A[0.1]-40 A[0.7]-120 A[0.8]-160		A[0.8]-120 A[0.9]-180	A[0.6]-60 A[0.8]-100	A[0.8]-80 A[0.9]-120 A[1]-200	A[0.9]-80 A[1]-140	A[1]-80	A[0.8]-20
59	A[0.8]-200		A[0.6]-80 A[0.8]-140 A[0.9]-200	A[0.3]-40 A[0.9]-160	A[0.9]-140	A[0.7]-60 A[1]-180	A[1]-120		A[0.9]-20 A[1]-20
60	A[0]-40 A[0.7]-140	A[0.4]-60	A[0.2]-40 A[0.7]-100 A[0.9]-180		A[0.4]-40 A[1]-200	A[0.5]-40 A[0.9]-100 A[1]-160		A[0.4]-20 A[1]-60	
61	A[0.3]-60 A[0.8]-180	A[0.8]-140 A[0.9]-200		A[0.7]-80 A[0.8]-100 A[0.9]-140	A[0.9]-120 A[1]-180	A[0]-20	A[0.2]-20 A[0.7]-40 A[1]-100	A[0.9]-40	

T_t	1 uM	5 uM	10 uM	25 uM	50 uM	100 uM	250 uM	500 uM	1000 uM
62		A[0.9]-180	A[0.5]-60 A[0.8]-120 A[0.9]-160	A[1]-200		A[1]-140	A[0.9]-60		
63	A[0.5]-80 A[0.6]-100 A[0.8]-160	A[0.6]-80 A[0.7]-100		A[0.6]-60	A[0.8]-80 A[1]-160	A[1]-120	A[1]-80		
64	A[0.7]-120	A[0.2]-40 A[0.8]-120		A[0.9]-120 A[1]-180	A[0.7]-60 A[0.9]-100	A[0.8]-60 A[0.9]-80		A[0.5]-20	
65	A[0.9]-200	A[0.9]-160	A[0.3]-40 A[0.7]-80 A[0.9]-140 A[1]-200	A[0.4]-40 A[1]-160	A[1]-140	A[0.6]-40		A[1]-40	
66	A[0.1]-40 A[0.8]-140	A[0.5]-60	A[0.8]-100		A[0.5]-40	A[0.1]-20 A[1]-100	A[0.3]-20 A[0.8]-40		
67	A[0.9]-180	A[0.9]-140 A[1]-200	A[1]-180	A[0.8]-80	A[0]-20 A[1]-120		A[1]-60		
68	A[0.4]-60		A[0.6]-60 A[0.9]-120	A[0.9]-100 A[1]-140				A[0.6]-20	
69	A[0.7]-100	A[0.7]-80 A[0.8]-100 A[1]-180	A[1]-160	A[0.7]-60	A[0.9]-80				
70	A[0.6]-80 A[0.9]-160	A[0.3]-40		A[1]-120	A[0.8]-60 A[1]-100	A[0.9]-60 A[1]-80	A[0.4]-20		
71	A[0.8]-120	A[0.9]-120 A[1]-160	A[1]-140	A[0.5]-40	A[0.6]-40	A[0.7]-40	A[0.9]-40	A[0.7]-20	
72	A[1]-200		A[0.4]-40 A[0.8]-80			A[0.2]-20			
73	A[0.2]-40 A[0.9]-140	A[0.6]-60	A[0.9]-100	A[0]-20 A[0.9]-80	A[0.1]-20				
74		A[1]-140		A[1]-100				A[0.8]-20	
75	A[0.5]-60 A[1]-180		A[0.7]-60 A[1]-120	A[0.8]-60	A[1]-80		A[0.5]-20		
76		A[0.8]-80 A[0.9]-100			A[0.9]-60	A[0.8]-40 A[1]-60	A[1]-40		
77	A[0.8]-100	A[0.4]-40						A[0.9]-20	
78	A[0.7]-80 A[0.9]-120 A[1]-160	A[1]-120		A[0.6]-40	A[0.7]-40	A[0.3]-20			
79			A[0.5]-40 A[0.9]-80						

T_t	1 uM	5 uM	10 uM	25 uM	50 uM	100 uM	250 uM	500 uM	1000 uM
80	A[0.3]-40	A[0.7]-60	A[1]-100	A[0.1]-20 A[1]-80	A[0.2]-20		A[0.6]-20	A[1]-20	
81	A[1]-140								
82			A[0]-20						
83	A[0.6]-60		A[0.8]-60	A[0.9]-60	A[1]-60	A[0.9]-40			
84		A[0.9]-80 A[1]-100				A[0.4]-20			
85	A[0.9]-100	A[0.5]-40		A[0.7]-40	A[0.8]-40				
86	A[0.8]-80 A[1]-120		A[0.6]-40				A[0.7]-20		
87			A[1]-80		A[0.3]-20				
88		A[0]-20 A[0.8]-60		A[0.2]-20					
89	A[0.4]-40					A[1]-40			
90			A[0.1]-20	A[1]-60					
91	A[0.7]-60		A[0.9]-60			A[0.5]-20	A[0.8]-20		
92		A[1]-80			A[0.9]-40				
93		A[0.6]-40		A[0.8]-40					
94	A[1]-100				A[0.4]-20				
95	A[0.9]-80		A[0.7]-40						
96				A[0.3]-20			A[0.9]-20		
97		A[0.1]-20 A[0.9]-60							
98	A[0.5]-40		A[0.2]-20			A[0.6]-20			
99			A[1]-60						
100					A[1]-40				
101	A[0.8]-60			A[0.9]-40			A[1]-20		
102		A[0.7]-40			A[0.5]-20				
103	A[0]-20								
104	A[1]-80		A[0.8]-40	A[0.4]-20					
105						A[0.7]-20			
106		A[0.2]-20 A[1]-60							
107									
108	A[0.6]-40		A[0.3]-20						
109									
110				A[1]-40	A[0.6]-20				
111	A[0.9]-60								
112		A[0.8]-40				A[0.8]-20			
113	A[0.1]-20		A[0.9]-40	A[0.5]-20					
114									
115									
116									
117		A[0.3]-20							
118			A[0.4]-20						
119	A[0.7]-40				A[0.7]-20				
120						A[0.9]-20			
121									
122	A[1]-60								
123		A[0.9]-40		A[0.6]-20					
124			A[1]-40						
125	A[0.2]-20								

8.7 Physical properties of CP conjugates

Table 15: Physical characteristics of CP conjugates

	Attached Molecule	Log(D)	Molecules/ELP	Rh (nm)	Rg (nm)	ρ	CN	Tt slope	Assembly
--	Unconjugated Control	--	0	5.7				-5.78	No
1	N-Methoxycarbonylmaleimide	-0.87	6.4	6.3				-5.84	No
2	N-Ethylmaleimide	0.68	6.4	5.7				-5.79	No
3	N-Phenylmaleimide	1.09	3.6	5.5				-6.43	No
4	N-Propylmaleimide	1.22	3.3	5.8				-4.96	No
5	N-tert-Butylmaleimide	1.38	5.9	6.1				-4.82	No
6	N-(Para-tolyl)-maleimide	1.55	3.8	33.5	34	1.01	9.1	-1	Yes
7	N-Benzylmaleimide	1.78	3.9	40.2	30.6	0.76	18.3	-0.71	Yes
8	N-(4-ethylphenyl)-maleimide	2.08	5.3	33.4	23	0.69	27.1	-0.68	Yes
9	N-[4-(2-Benzimidazolyl)phenyl]maleimide	2.12	5.5	30.5	26.4	0.87	15.8	-0.74	Yes
10	N-(9-Acridinyl)maleimide	2.27	5	27.3	28.3	1.04	11.7	-0.85	Yes
11	N-(1-naphthyl)-maleimide	2.32	5.6	58.3	47.3	0.81	22.5	--	Yes
12	2-maleimidofluorene	3.04	5.3	47.5	45.2	0.95	63.4	--	Yes
13	N-(3-Fluoranthyl)maleimide	4.04	4.1	55.7	47.1	0.85	43.8	--	Yes
14	N-(1-Pyrenyl)maleimide	4.04	4.3	39.1	33.6	0.86	40.5	-0.79	Yes
Gem	Gemcitabine	-2.2	5	5.7	37.8	6.59	0.93		No
Oxy	Oxycodone	1.2	4	9.7	17.6	1.81	1.3		No
PTX	Paclitaxel	4	2	53.3	57.7	1.08	72		Yes

8.8 In Vivo Pharmacokinetic Parameters

Table 16: Pharmacokinetic parameters for CP-Dox micelles of various chain lengths

		Chain Length (Pentamers)		
Parameter	Symbol	40	80	160
initial concentration	Co [μM]	229.1 (13.9)	224.8 (12.4)	293.1 (12.6)
distribution half-life	α $t_{1/2}$ [58]	33.6 (9.0)	126.7 (67.2)	71.9 (22.2)
elimination half-life	β $t_{1/2}$ [hr]	9.6 (0.4)	12.1 (1.0)	15.5 (0.9)
area under the curve	AUC [μM hr]	1202.9 (42.8)	2690.5 (119.6)	3734.6 (112.3)
plasma clearance	CL [μL hr^{-1} g^{-1}]	0.15 (.01)	0.07 (0.00)	0.05 (0.00)
initial volume of distribution	Vo [μL g^{-1}]	0.77 (0.05)	0.78 (0.04)	0.60 (0.03)
tissue to plasma rate constant	k_{tp} [hr^{-1}]	0.47 (0.12)	0.23 (0.13)	0.33 (0.11)
plasma to tissue rate constant	k_{pt} [hr^{-1}]	0.65 (0.21)	0.08 (0.05)	0.21 (0.07)
elimination rate constant	k_e [hr^{-1}]	0.19 (0.01)	0.08 (0.01)	0.08 (0.00)

Table 17: Pharmacokinetic parameters for asymmetric amphiphiles with various assembly domains

		A[1]-160-X		
Parameter	Symbol	X = None	X = $(FGG)_8$	X = $(YG)_8$
initial concentration	Co [μM]	50.4 (2.4)	44.6 (1.7)	44.7 (3.8)
distribution half-life	α $t_{1/2}$ [58]	30.7 (7.9)	94.4 (35.9)	17.1 (6.6)
elimination half-life	β $t_{1/2}$ [hr]	9.1 (0.5)	16.0 (2.6)	10.9 (1.0)
area under the curve	AUC [μM hr]	332.1 (9.9)	628.0 (40.1)	329.7 (19.1)
plasma clearance	CL [μL hr^{-1} g^{-1}]	0.53 (.02)	0.28 (0.02)	0.53 (0.03)
initial volume of distribution	Vo [μL g^{-1}]	3.5 (0.17)	3.94 (0.15)	3.94 (0.33)
tissue to plasma rate constant	k_{tp} [hr^{-1}]	0.68 (0.18)	0.27 (0.12)	1.14 (0.42)
plasma to tissue rate constant	k_{pt} [hr^{-1}]	0.59 (0.17)	0.14 (0.05)	1.22 (0.53)
elimination rate constant	k_e [hr^{-1}]	0.15 (0.01)	0.07 (0.01)	0.14 (0.01)

8.9 Detailed Procedures

8.9.1 PRe-RDL

8.9.1.1 Concatemerization

This is the first step when inserting many oligos into a vector at once. This can also be modified to insert a single oligo into a vector, if you are designing complementary leader or trailer vectors, for instance. All references to DNA quantities are based on a normal miniprep eluted into 50 μL of ddH_2O.

Vector Prep

15 μL DNA

2 μL BseRI

9 μL NEB 2, NEB 4, or CutSmart Buffer

64 μL H_2O

Incubate at 37°C for 3 h (can leave overnight)

Add 1 μL CIP, incubate at 37°C for 15 min

PCR Purification

Add 500 μL PBI solution to the entire vector prep

Follow the directions from the PCR Purification Kit (Qiagen)

Elute in 30 μL H_2O

Concatemerization Ligation (1 h)

3 μL Vector Prep

1 μL Oligo (if only want 1 insert, use 0.1 μL)

2 μL 10x Ligase Buffer

1 μL Ligase

13 μL H_2O

Incubate at Room Temp for 1 h

*If none of the colonies have a high insert to vector ratio, simultaneously try a vector:insert ratio of 1:1, 1:3, and 1:5. Miniprep or colony PCR all colonies from the 1:3 and the 1:5 plates.

Transformation and Plating (~1.5 hrs)

3 μL of Ligation mixture

25 μL of EB5α cells, unthawed on ice

Incubate mixture on ice for ~5 minutes

Place on 42°C hot plate for 45 sec

Incubate on ice for 2 min

Add 50 μL Luria Broth

Incubate at 37°C for 1 h (recovery period)

Plate on prewarmed agarose plates

Incubate plates at 37°C overnight

8.9.1.2 PRe-RDL Day 1:

prRDL A Reaction (3 h)

40uL DNA

2uL AcuI

4uL BglI

9uL NEB4

35uL H_2O

prRDL B Reaction (3 h)

40uL DNA

2uL BseRI

4uL BglI

9uL NEB4

35uL H_2O

Incubate both preps for ~3 h at 37°C.

Gel Purification (1 h)

Make a 1% low melting point gel (0.75 g agarose, 75 mL TAE buffer, 7.5 μL SybrSafe)

Let cool in 4°C fridge for ~1 hour before use

Use large 4 well comb

Add 18 μL loading dye to each prep

Load all 106 μL of prep into a single well on the gel

Run gel at 130mV (takes ~30 min)

When gel purifying, always cut out the top band (whole procedure ~30 min)

Expect:

PRe-RDL A: 1586 bp, 1821 bp, 1891 + ELP

PRe-RDL B: 1891 bp, 3407 + ELP

*If you have more than 3 bands for an 'A' cut or 2 bands for a 'B' cut, prepare new DNA and start over. The most common cause is incomplete DNA digestion due to poor mixing of the enzymes and DNA or suboptimal cutting conditions (time period is too short, temperature is not 37°C, etc).

Mix the band of agarose that was cut from the gel with:

400 μL Buffer QG

80 μL Isopropanol

Follow the directions from the Gel Purification Kit (Qiagen)

Elute in 30 μL H_2O

Ligation (~ 1 h)

3 μL PRe-RDL A

3 μL PRe-RDL B

2 μL 10x Ligase Buffer

1 μL Ligase

11 μL H_2O

Incubate at room temperature for 1 h

8.9.1.3 PRe-RDL Day 2:

Colony PCR (3 h)

Use cPCR to rapidly screen for fragments <2 Kb

12.5 μL Master Mix

1 μL Forward Primer

1 μL Reverse Primer

10.5 μL H_2O

Pick colony with a pipette tip and pipette up and down until tip is clean

Remember to number colonies on the plates

Place plates back in the incubator

Run PCR program A-29 (Jon)

Make sure to change extension time (1 min per kb)

Make a 1% agarose gel (0.50 g agarose in 50 mL TAE)

Let solidify at room temperature for 15-30 minutes before use

Run 9 μL of PCR solution on gel (no dye is needed)

Remember to include a ladder – either *BstEIII* for large ELPs (>1500 bp) or *100bp* for smaller ELPs

Run at 130mV for ~30 minutes

Runtime depends on gene size. Longer genes require longer runtimes.

Observe gel, pick colonies to grow (15 min)

4 mL TBDry Media

4 μL kanamycin

Colony

Incubate overnight at 37°C.

8.9.1.4 PRe-RDL Day 3:

Miniprep all samples

Use 750 μL to make a DMSO stock for each sample

Use 3 mL to miniprep

Follow directions included with the Miniprep Kit (Qiagen)

Elute minipreps in 50 μL ddH_2O

Diagnostic Digest

10 μL DNA

0.5 μL BamHI

0.5 μL XbaI

2 μL CutSmart Buffer

7 μL H_2O

Incubate 1 hr at 37°C.

Make a 1% agarose gel right after starting incubation.

Run Diagnostic Digest at 130mV for ~20-30 minutes.

Sequence

Check the DNA concentration (should be ~80-100 ng/μL)

If sequencing with Eton, submit 10-15 μL DNA in H_2O

On the following morning, check the sequences in SeqBuilder. If the forward and reverse sequencing are appropriate, start the process again at Day 1 using the selecting sequences.

8.9.2 Drug Conjugations

8.9.2.1 Synthesis of CP-Gemcitabine Conjugate

Synthesis of 3′, 5′-O-Bis (tert-Butoxycarbonyl)gemcitabine (1):

Selective protection of 3′-OH and 5′-OH of gemcitabine was performed as described previously [227]. Briefly, to a stirred solution of gemcitabine hydrochloride (240 mg, 0.8 mmol) in 16 mL of 1M aqueous KOH, di-*tert*-butyl dicarbonate (DBDC) (1.75 g, 8 mmol) in 16 mL of dioxane was added drop wise. The reaction mixture was then stirred at 25°C for an additional 40 min and extracted with ethyl acetate, washed with brine, dried over Na_2SO_4 and concentrated to dryness under reduced pressure.

At 25°C, additional DBDC (1.74 g) in 16 mL of dioxane was added to a stirred clear solution of the above residue, followed by the addition of 40 mL of 1 M aqueous KOH. The reaction mixture was stirred at 25°C for another 40 min and subsequently extracted by a similar procedure as described before. The product was purified by

column chromatography, and synthesis was confirmed via TLC (chloroform-acetone-EtOH 5:4:1) and LC/MS (Agilent Series 1100 LC/MSD Trap; Agilent Technologies). R_f: 0.6 in CH_2Cl_2-acetone-EtOH 5:4:1. ESI/MS: 464 [M+H].

Synthesis of 3′,5′-O-Bis(tert-butoxycarbonyl)-4-N-(ß-maleimidopropiocarbonyl) gemcitabine (2):

To a stirred solution of BMPA (0.036 g, 0.2 mmol) and EDCI (0.041 g, 0.2 mmol) in anhydrous DCM at 0°C, 1 (0.05 g, 0.1 mmol) was added, along with a catalytic amount of triethylamine. The reaction mixture was stirred for an additional 16 h at room temperature and subsequently extracted with ethyl acetate, washed with brine, dried over Na_2SO_4 and concentrated to dryness under reduced pressure. The product was purified by column chromatography, and synthesis of 2 was confirmed via TLC (chloroform-acetone-EtOH 5:4:1) and LC/MS. R_f: 0.8 in CH_2Cl_2-acetone-EtOH 5:4:1. ESI/MS: 615 [M+H].

Synthesis of activated gemcitabine and conjugation of activated gemcitabine and CP:

Prior to conjugation to CP, gemcitabine-BMPA was activated via removal of *t*-BOC groups. Trifluoroacetic acid (500 μL) was added to a stirred solution of 2 (0.05 g, 0.1 mmol) in anhydrous DCM (500 μL) at 0°C, and the reaction mixture was stirred at 0°C for 3 h. TFA was subsequently removed under reduced pressure and the mixture was triturated with ether to yield the desired product 3. Activated gemcitabine 3 was immediately used for the next step.

Prior to reaction, purified CP was suspended in reaction buffer (0.1 M NaPO4, 1 mM EDTA, pH 7.0) and reduced with 1 mL of TCEP at neutral pH (100 mM, pH 7.0) at ~5x excess to thiol. Excess TCEP was removed from the solution by initiating the phase transition with sodium chloride (2.5 M) and centrifugation at 4,000 rpm at 25°C for 10 min. The CP pellet obtained by centrifugation was re-suspended in 5 mL of reaction buffer. Activated gemcitabine (0.03 g, 0.07 mmol) was re-suspended in 2 mL of methanol and slowly transferred to the stirring CP solution. After mixing, 1 mL of pH neutral TCEP (100 mM) was added and the reactants were stirred for 16 hours at 20°C in the dark. After reaction, the methanol was evaporated under a nitrogen stream, and unreacted gemcitabine precipitates were removed via centrifugation at 13,000 rpm at 4°C for 10 minutes. The supernatant contained CP-gemcitabine conjugate, which was further purified by initiating the CP phase transition with sodium chloride (2.5 M) to aggregate the CP-Gem conjugate followed by centrifugation at 4,000 rpm at 25°C for 10 min. The CP-gemcitabine conjugate pellet obtained by centrifugation was re-suspended in phosphate buffered saline (PBS) (pH 7.4) at a concentration of 10 mg / mL and purified using size exclusion PD-10 chromatography (GE Healthcare Life Sciences).

Determination of gemcitabine conjugation ratio:

The conjugation ratio of gemcitabine to CP was determined by matrix-assisted laser desorption/ionization time-of-flight mass spectrometry (MALDI-TOF-MS) of the CP-gemcitabine conjugates and free CP using a Voyager DE-Pro Maldi-MS (Applied

Biosystems) instrument equipped with a nitrogen laser (337 nm). The MALDI-TOF-MS samples were prepared in an aqueous 50% acetonitrile solution containing 0.1% TFA, using a sinapinic acid matrix. The conjugation ratio was determined by examining the increase in mass of the conjugate relative to free CP.

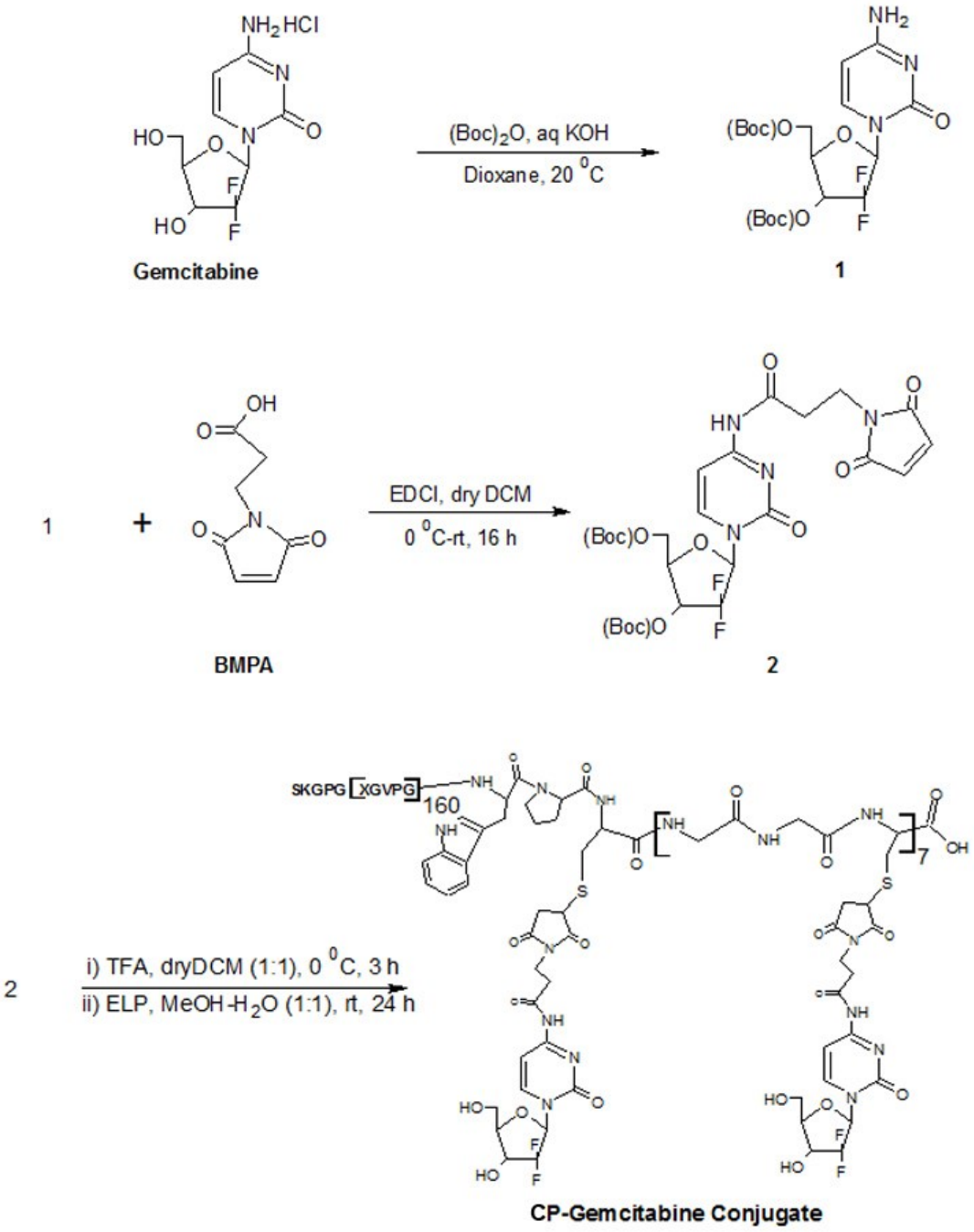

Figure 48: Synthesis scheme for CP-Gemcitabine conjugate.

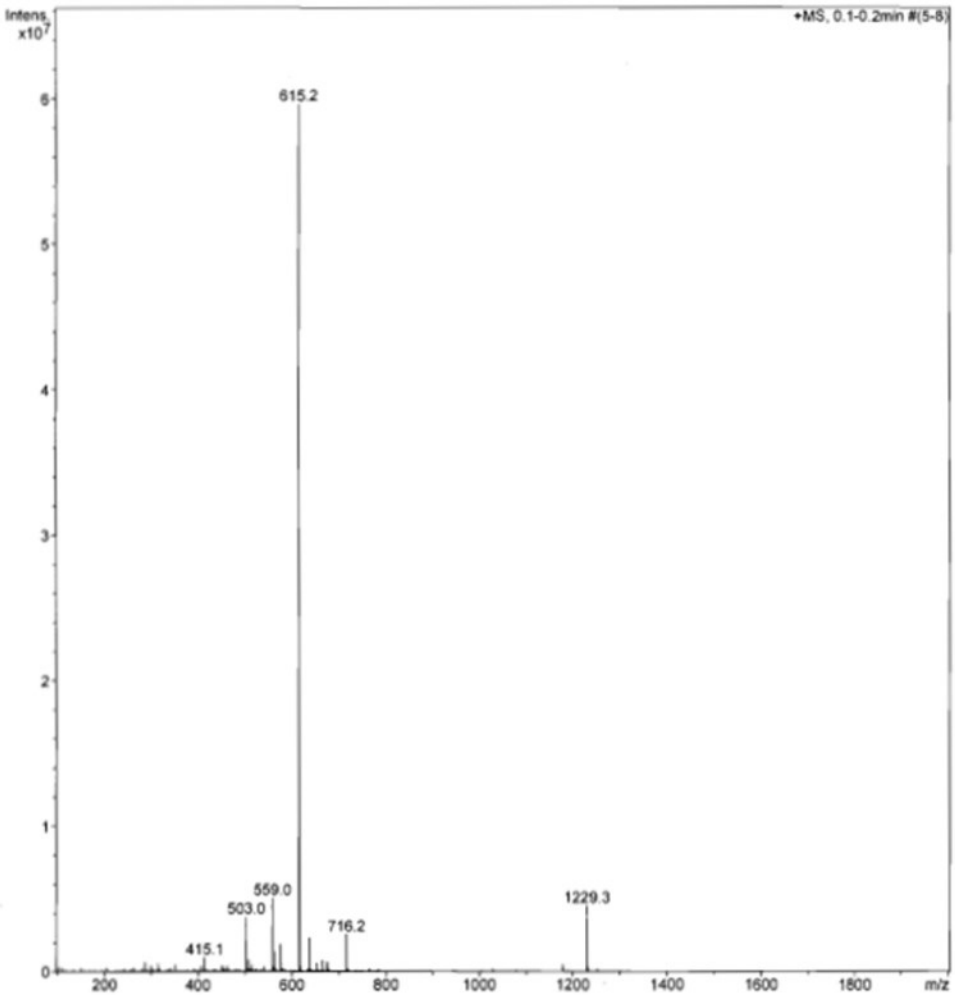

Figure 49: ESI-MS of 3′,5′-O-Bis(tert-butoxycarbonyl)-4-N-(ß-maleimidopropiocarbonyl) gemcitabine (2)

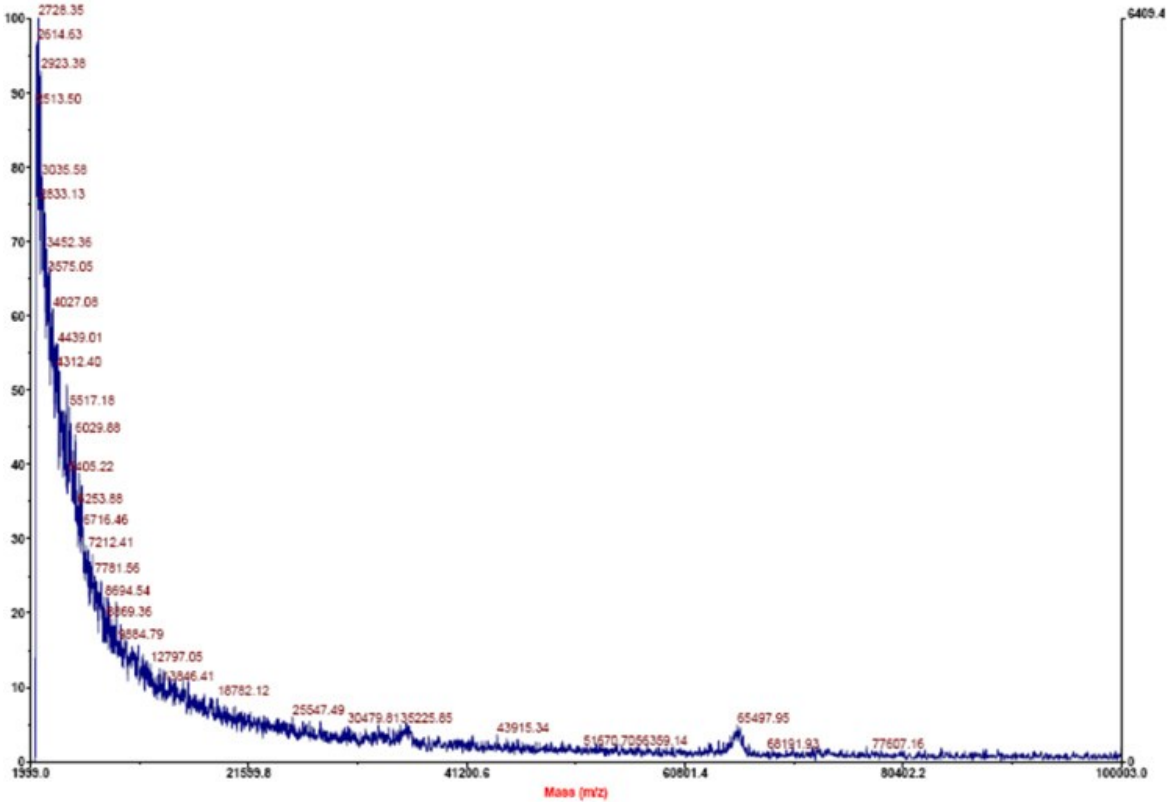

Figure 50: MALDI-MS of CP-Gemcitabine conjugate

8.9.2.2 Synthesis of CP-Oxycodon Conjugate

Synthesis of Oxycodone-BMPH (I) conjugate:

Oxycodone-BMPH was prepared as described previously [2]. Briefly, oxycodone (25 mg, 79.2 μmoles) and BMPH (28 mg, 95 μmoles) were co-dissolved in 1 mL anhydrous methanol with 2 μL of tri-fluoroacetic acid. The reactants were stirred for 16 h at 20°C in the dark. The white precipitate was isolated by centrifugation and washed with MeOH. Drying under vacuum produced the white purified product (I). Activated

BMPH was immediately used in a second reaction with the ELP. ESI-MS: 481 [M+H], 503 [M+Na].

Conjugation of oxycodone with CP:

Prior to conjugation with activated oxycodone, purified CP was suspended in reaction buffer (0.1 M NaPO4, 1 mM EDTA, pH 7.0) and reduced with 1 mL of TCEP at neutral pH (100 mM, pH 7.0) at ~5x excess to thiol. Excess TCEP was removed from the solution by initiating the phase transition with sodium chloride (2.5 M) and centrifugation at 4,000 rpm at 25 °C for 10 minutes. The CP pellet obtained by centrifugation was re-suspended in ~1 mL of reaction buffer. Compound I was re-suspended in ~1 mL of methanol-H_2O (1:1) and slowly transferred to the stirring CP solution. 1 mL of pH neutral TCEP (100 mM) was added and the reactants were stirred for 16 hr at 20°C in the dark. After reaction, the methanol was evaporated under a nitrogen stream to a volume ~1 mL. Unreacted oxycodone precipitates were removed via centrifugation at 13,000 rpm at 10°C for 10 min. The supernatant was further purified by initiating the CP phase transition with sodium chloride (2.5 M) to aggregate the CP-oxycodone conjugate followed by centrifugation at 4,000 rpm at 25°C for 10 min. The CP-oxycodone pellet obtained by centrifugation was re-suspended in phosphate buffered saline (PBS) (pH 7.4) at a concentration of ~10 mg mL^{-1} and dialyzed using Spectra/Por 2 membrane (Spectrum labs, MWCO 12-14 kD) in 20 % acetonitrile-water, followed by 100% DI water.

Determination of the oxycodon conjugation ratio:

The conjugation ratio of oxycodon to CP was determined by matrix-assisted laser desorption/ionization time-of-flight mass spectrometry (MALDI-TOF-MS) of the CP-oxycodone conjugates and free CP using a Voyager DE-Pro Maldi-MS (Applied Biosystems) instrument equipped with a nitrogen laser (337 nm). The MALDI-TOF-MS samples were prepared in an aqueous 50% acetonitrile solution containing 0.1% TFA, using a sinapinic acid matrix. The conjugation ratio was determined by examining the increase in mass of the conjugate relative to free CP.

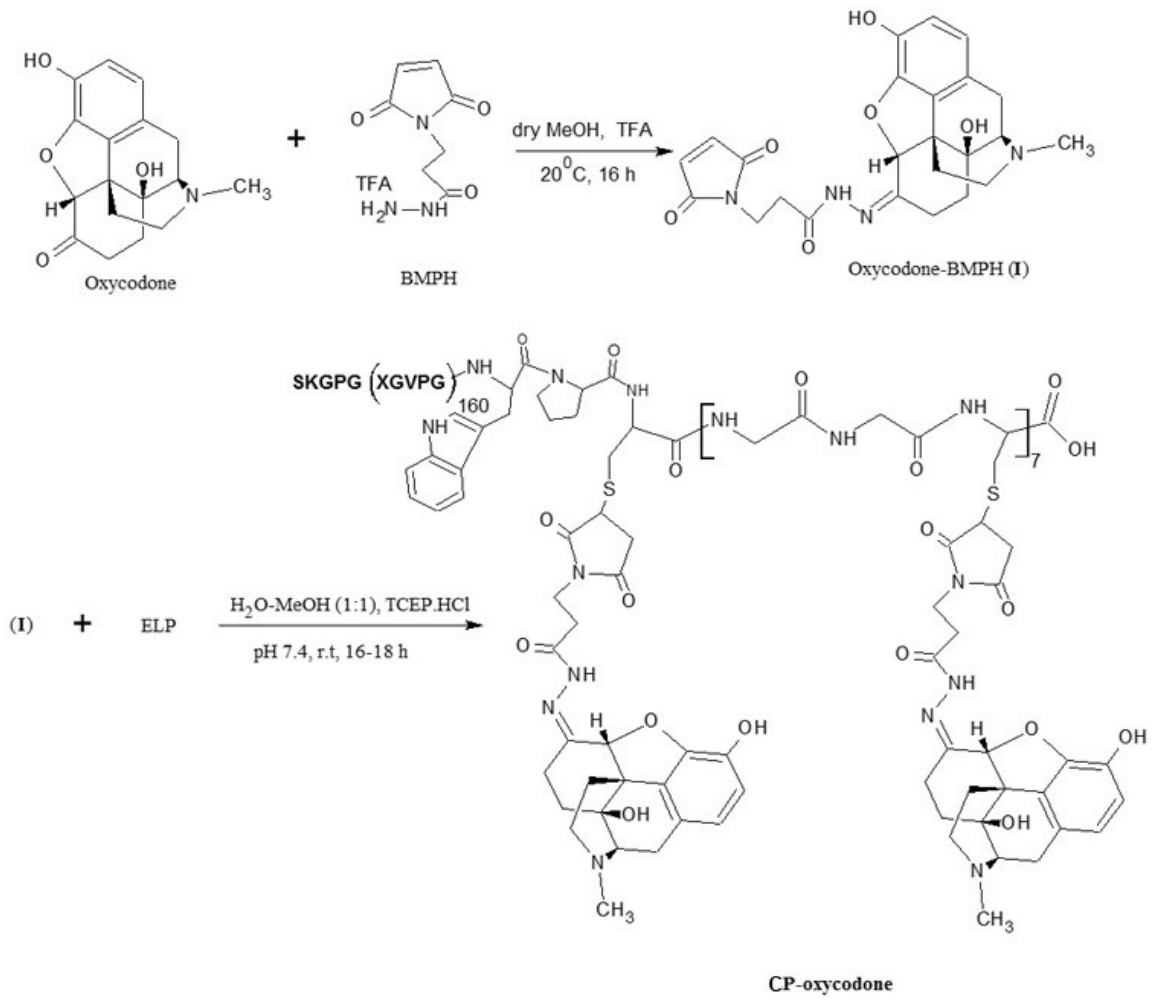

Figure 51: Synthesis scheme for CP-Oxycodon conjugate

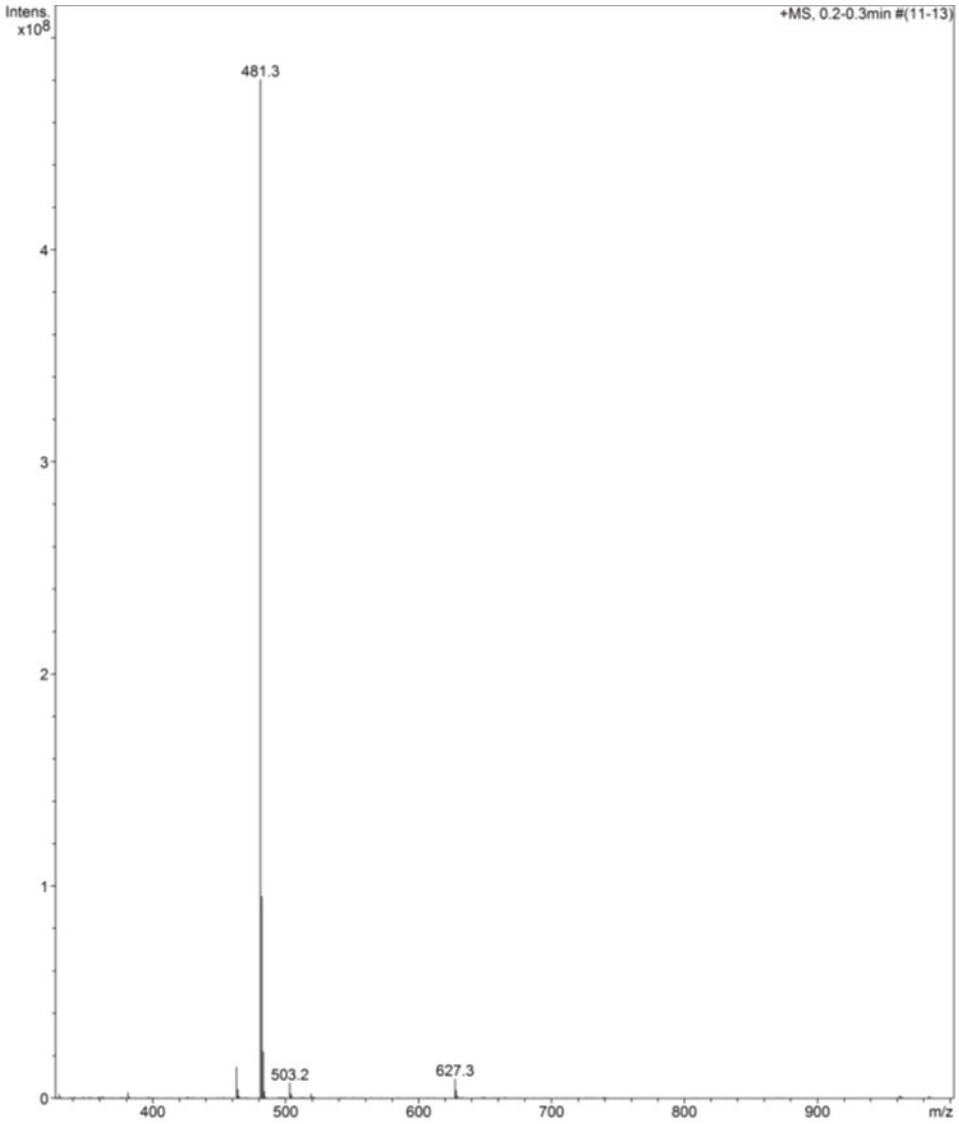

Figure 52: ESI-MS of Oxycodone-BMPH (I).

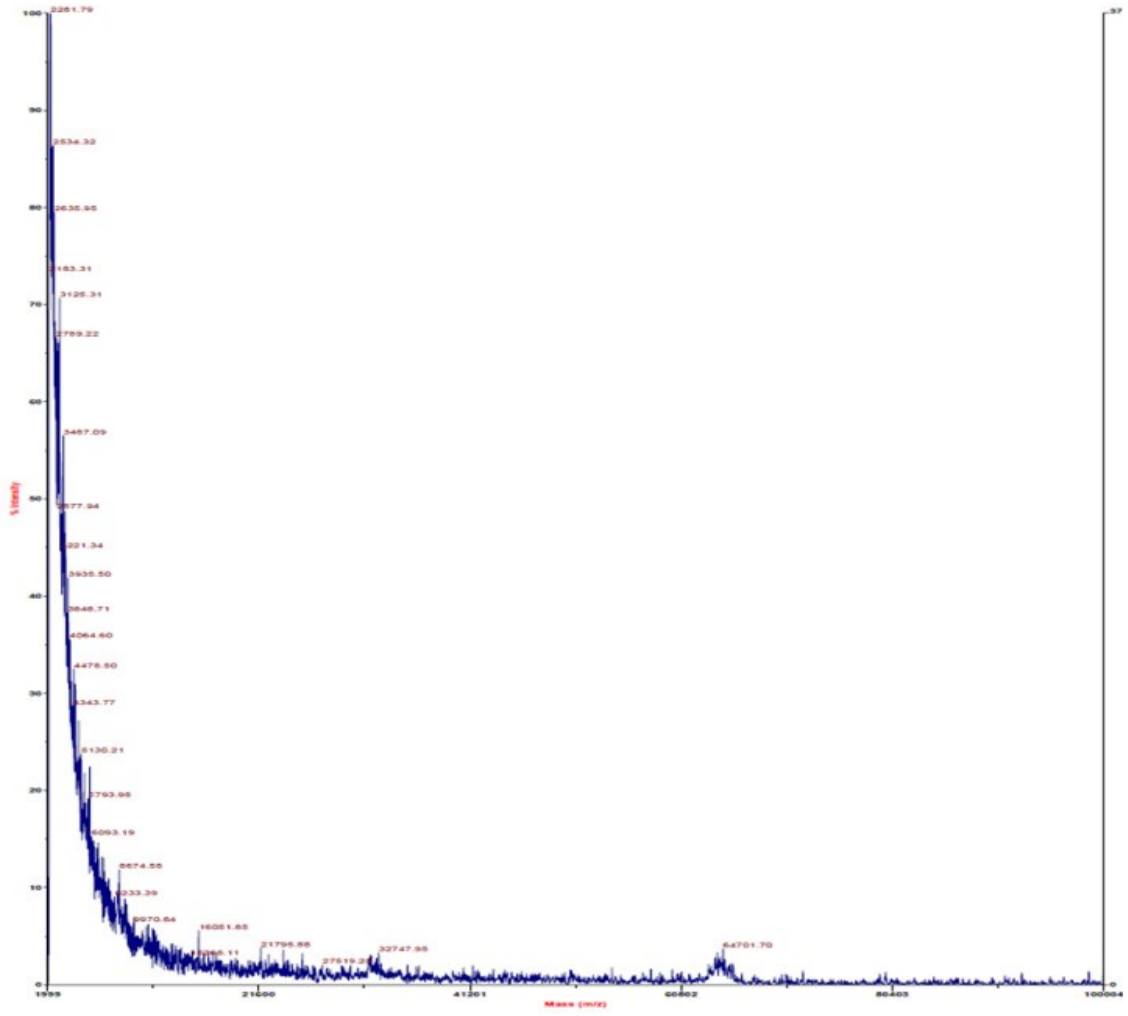

Figure 53: MALDI-MS of CP-Oxycodone conjugate

8.9.2.3 Synthesis of CP-Paclitaxel Conjugate

Synthesis of paclitaxel-levulinic acid (I) conjugate:

Paclitaxel-levulinic acid was prepared as described previously [228]. Briefly, levulinic acid (0.08 g, 0.7 mmol) and DCC (0.145 g, 0.7 mmol) were codissolved in dry DMF and stirred for 30 min at -20°C. Paclitaxel (0.5 g, 0.58 mmol) and DMAP (0.5 g, 0.58

mmol) were dissolved in dry DMF and were added to the above mixture. The reaction mixture left stirred for 24 h at 4°C. The reaction mixture was filtered and the DMF was evaporated to dryness. Compound I was purified with column chromatography with silica gel and 1.5% MeOH in chloroform as eluent. R_f: 0.48 in EtOAc/Hexane=2:1.

Synthesis of activated paclitaxel (II) and conjugation of paclitaxel with CP:

Compound I (0.05 g, 0.05 mmol) and BMPH (0.018 g, 0.06 mmol) were dissolved in dry MeOH and stirred in the dark for 48 h at 45°C. After the MeOH was evaporated to dryness, compound II was purified with column chromatography with silica gel and 2-2.5 % MeOH in chloroform as eluent. Compound II was immediately used in the next step. R_f: 0.6 in 10 % MeOH in $CHCl_3$. ESI-MS: 1117 [M+H], 1139 [M+Na].

Prior to conjugation with activated paclitaxel, purified CP was suspended in reaction buffer (0.1 M NaPO4, 1 mM EDTA, pH 7.0) and reduced with 1 mL of TCEP at neutral pH (100 mM, pH 7.0) at ~5x excess to thiol. Excess TCEP was removed from the solution by initiating the phase transition with sodium chloride (2.5 M) and centrifugation at 4,000 rpm at 25°C for 10 min. The CP pellet obtained by centrifugation was resuspended in ~2 mL of reaction buffer. Compound IV was resuspended in ~2 mL of methanol and slowly transferred to the stirring CP solution. 1 mL of pH neutral TCEP (100 mM) was added and the reactants were stirred for 16 h at 20°C in the dark. After reaction, the methanol was evaporated under a nitrogen stream to a volume ~20 mL. Unreacted paclitaxel (PTX) precipitates were removed via centrifugation at 13,000 rpm

at 10°C for 10 min. The supernatant was further purified by initiating the CP phase transition with sodium chloride (2.5 M) to aggregate the CP-PTX conjugate followed by centrifugation at 4,000 rpm at 25°C for 10 min. The CP-PTX pellet obtained by centrifugation was resuspended in phosphate buffered saline (PBS) (pH 7.4) at a concentration of ~10 mg mL^{-1} and dialyzed using Spectra/Por 2 membrane (Spectrum labs, MWCO 12-14 kD) in 20 % acetonitrile-water, followed by 100% DI water.

Determination of the paclitaxel conjugation ratio:

The conjugation ratio of paclitaxel to CP was determined by matrix-assisted laser desorption/ionization time-of-flight mass spectrometry (MALDI-TOF-MS) of the CP-Paclitaxel conjugate and free CP using a Voyager DE-Pro Maldi-MS (Applied Biosystems) instrument equipped with a nitrogen laser (337 nm). The MALDI-TOF-MS samples were prepared in an aqueous 50% acetonitrile solution containing 0.1% TFA, using a sinapinic acid matrix. The conjugation ratio was determined by examining the increase in mass of the conjugate relative to free CP.

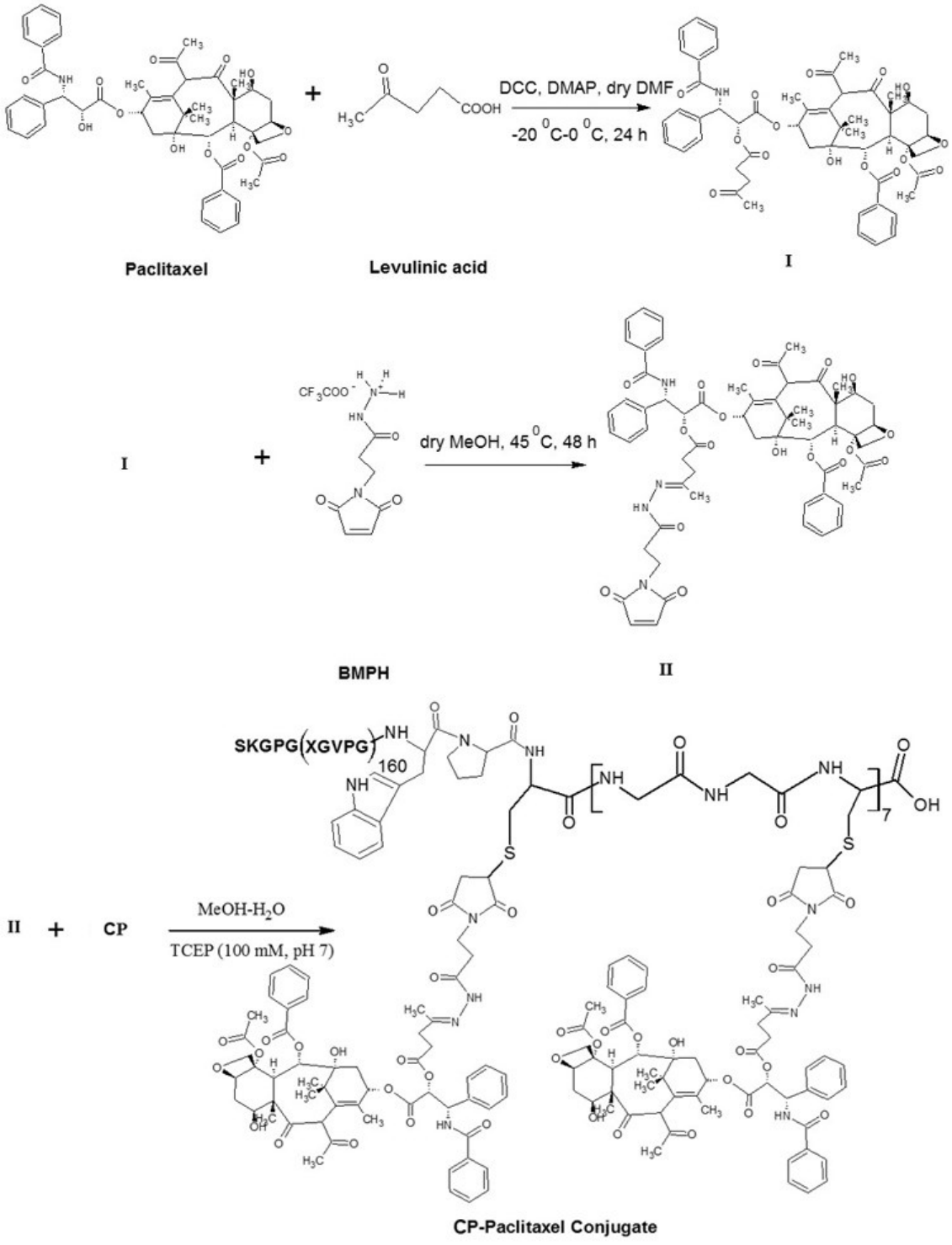

Figure 54: Synthesis scheme for CP-Paclitaxel conjugate

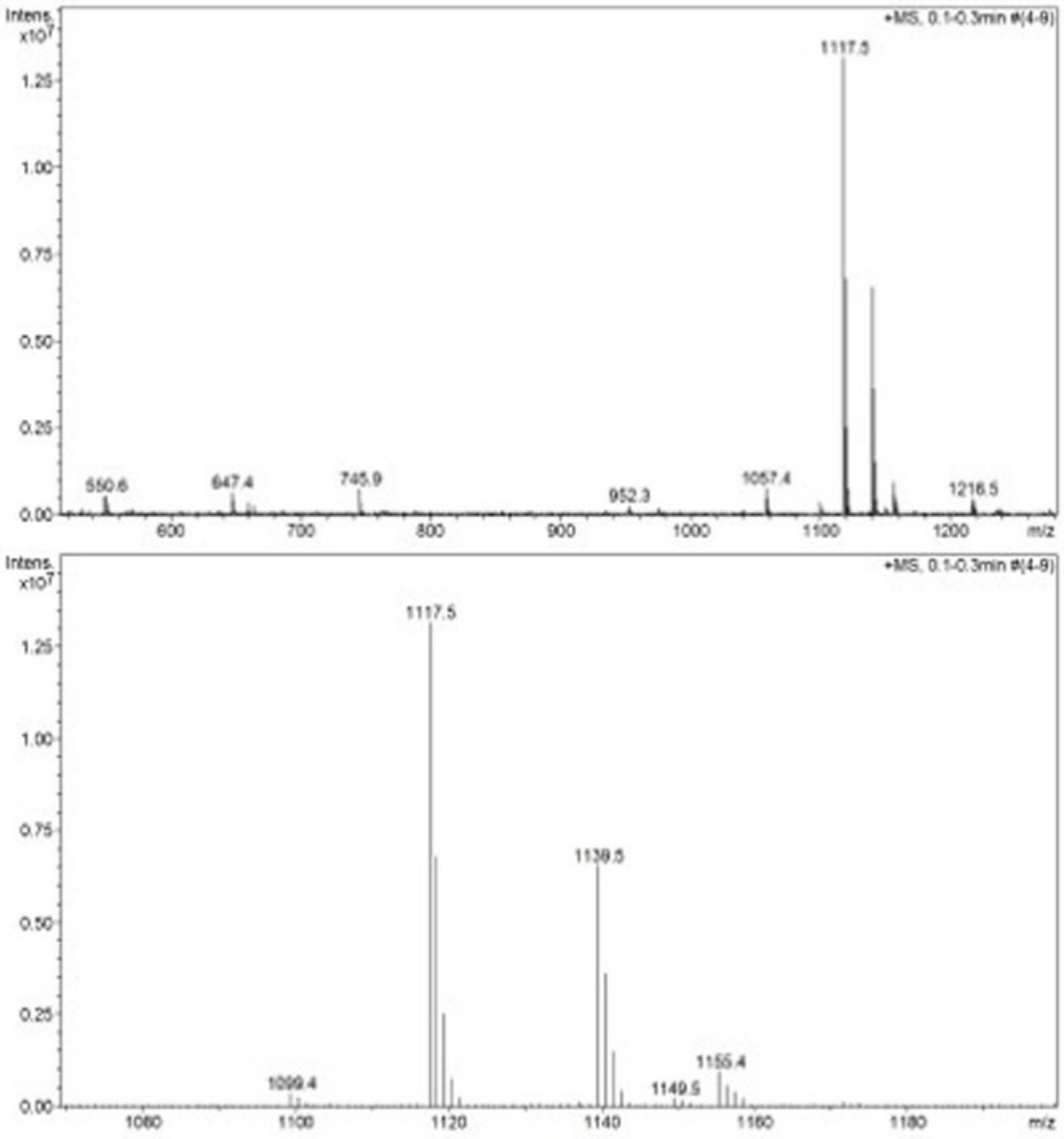

Figure 55: ESI-MS of activated Paclitaxel (II)

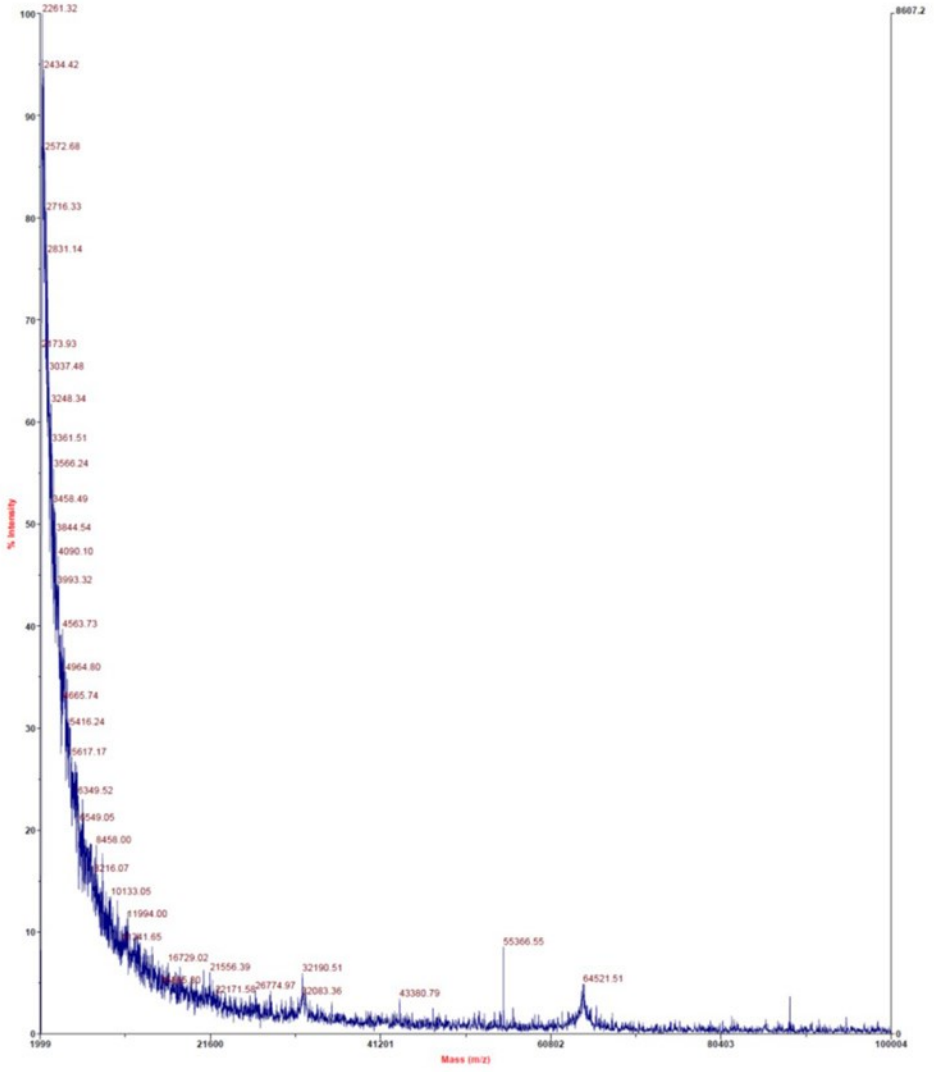

Figure 56: MALDI-MS of CP-Paclitaxel conjugate

References

1. Lakdawalla, D.N., E.C. Sun, A.B. Jena, C.M. Reyes, D.P. Goldman, and T.J. Philipson, An economic evaluation of the war on cancer. *Journal of Health Economics* **29**, 333-346 (2010).

2. Cancer facts and figures. (2013).

3. Tannock, I.F., R. Hill, R. Bristow, and L. Harrington, *Basic science of oncology*. 5 ed. 2013: McGraw-Hill Professional.

4. Fink-Retter, A., D. Gschwantler-Kaulich, G. Hudelist, R. Mueller, E. Kubista, K. Czerwenka, et al., Differential spatial expression and activation pattern of egfr and her2 in human breast cancer. *Oncology Reports* **18**, 299-304 (2007).

5. Taniguchi, K., J. Okami, K. Kodama, M. Higashiyama, and K. Kato, Intratumor heterogeneity of epidermal growth factor receptor mutations in lung cancer and its correlation to the response to gefitinib. *Cancer Science* **99**, 929-935 (2008).

6. Hanahan, D. and R.A. Weinberg, Hallmarks of cancer: The next generation. *Cell* **144**, 646-674 (2011).

7. Vokes, E.E. and H.M. Golomb, *Oncologic therapies*. 2002, Springer.

8. Borek, C., Antioxidants and radiation therapy. *Journal of Nutrition* **134**, 3207s-3209s (2004).

9. Willers, H. and K.D. Held, Introduction to clinical radiation biology. *Hematology-Oncology Clinics of North America* **20**. (2006).

10. Yoshioka, Y., Current status and perspectives of brachytherapy for prostate cancer. *International Journal of Clinical Oncology* **14**, 31-36 (2009).

11. Eifel, P.J., Concurrent chemotherapy and radiation therapy as the standard of care for cervical cancer. *Nature Clinical Practice Oncology* **3**, 248-255 (2006).

12. Tannock, I.F., Treatment of cancer with radiation and drugs. *Journal of Clinical Oncology* **14**, 3156-3174 (1996).

13. de Gramont, A., A. Figer, M. Seymour, M. Homerin, A. Hmissi, J. Cassidy, et al., Leucovorin and fluorouracil with or without oxaliplatin as first-line treatment in advanced colorectal cancer. *Journal of Clinical Oncology* **18**, 2938-2947 (2000).

14. Schiller, J.H., D. Harrington, C.P. Belani, C. Langer, A. Sandler, J. Krook, et al., Comparison of four chemotherapy regimens for advanced non-small-cell lung cancer. *New England Journal of Medicine* **346**, 92-98 (2002).

15. Gewirtz, D.A., A critical evaluation of the mechanisms of action proposed for the antitumor effects of the anthracycline antibiotics adriamycin and daunorubicin. *Biochemical Pharmacology* **57**, 727-741 (1999).

16. Ganguly, A., H.L. Yang, and F. Cabral, Paclitaxel-dependent cell lines reveal a novel drug activity. *Molecular Cancer Therapeutics* **9**, 2914-2923 (2010).

17. Muller, H.J. and J. Boos, Use of l-asparaginase in childhood all. *Critical Reviews in Oncology Hematology* **28**, 97-113 (1998).

18. Pieters, R., S.P. Hunger, J. Boos, C. Rizzari, L. Silverman, A. Baruchel, et al., L-asparaginase treatment in acute lymphoblastic leukemia. *Cancer* **117**, 238-249 (2011).

19. Cliby, W.A., K.A. Lewis, K.K. Lilly, and S.H. Kaufmann, S phase and g(2) arrests induced by topoisomerase i poisons are dependent on atr kinase function. *Journal of Biological Chemistry* **277**, 1599-1606 (2002).

20. Hecht, S.M., Bleomycin: New perspectives on the mechanism of action. *Journal of Natural Products* **63**, 158-168 (2000).

21. Falk, M.H. and R.D. Issels, Hyperthermia in oncology. *Int J Hyperthermia* **17**, 1-18 (2001).

22. Overgaard, J., D. Gonzalez Gonzalez, M.C. Hulshof, G. Arcangeli, O. Dahl, O. Mella, et al., Hyperthermia as an adjuvant to radiation therapy of recurrent or metastatic malignant melanoma. A multicentre randomized trial by the european society for hyperthermic oncology. 1996. *Int J Hyperthermia* **25**, 323-34 (2009).

23. van der Zee, J., D. Gonzalez Gonzalez, G.C. van Rhoon, J.D. van Dijk, W.L. van Putten, and A.A. Hart, Comparison of radiotherapy alone with radiotherapy plus hyperthermia in locally advanced pelvic tumours: A prospective, randomised, multicentre trial. Dutch deep hyperthermia group. *Lancet* **355**, 1119-25 (2000).

24. Vernon, C.C., J.W. Hand, S.B. Field, D. Machin, J.B. Whaley, J. van der Zee, et al., Radiotherapy with or without hyperthermia in the treatment of superficial localized breast cancer: Results from five randomized controlled trials. International collaborative hyperthermia group. *Int J Radiat Oncol Biol Phys* **35**, 731-44 (1996).

25. Dewhirst, M.W., E. Jones, T. Samulski, Z. Vujaskovic, C. Li, and L. Prosnitz, eds. *Hyperthermia*. Cancer 6, ed. D.W. Kufe, et al. 2003, BC Decker: Hamilton. 623-636.

26. Dewhirst, M.W., B.L. Viglianti, M. Lora-Michiels, M. Hanson, and P.J. Hoopes, Basic principles of thermal dosimetry and thermal thresholds for tissue damage from hyperthermia. *Int J Hyperthermia* **19**, 267-94 (2003).

27. Song, C.W., Effect of local hyperthermia on blood flow and microenvironment: A review. *Cancer Res* **44**, 4721s-4730s (1984).

28. Hauck, M.L., M.W. Dewhirst, D.D. Bigner, and M.R. Zalutsky, Local hyperthermia improves uptake of a chimeric monoclonal antibody in a subcutaneous xenograft model. *Clinical Cancer Research* **3**, 63-70 (1997).

29. Kong, G., R.D. Braun, and M.W. Dewhirst, Characterization of the effect of hyperthermia on nanoparticle extravasation from tumor vasculature. *Cancer Research* **61**, 3027-3032 (2001).

30. Viglianti, B.L., P. Stuaffer, E. Repasky, E. Jones, Z. Vujaskovic, and M. Dewhirst, eds. *Hyperthermia*. Cancer medicine 8, ed. K. Hong, et al. 2010, People's Medical Publishing House: Shelton. 528-540.

31. Genet, S.C., Y. Fujii, J. Maeda, M. Kaneko, M.D. Genet, K. Miyagawa, et al., Hyperthermia inhibits homologous recombination repair and sensitizes cells to ionizing radiation in a time- and temperature-dependent manner. *Journal of Cellular Physiology* **228**, 1473-1481 (2013).

32. Raaphorst, G.P., C.E. Ng, and D.P. Yang, Thermal radiosensitization and repair inhibition in human melanoma cells: A comparison of survival and DNA double strand breaks. *International Journal of Hyperthermia* **15**, 17-27 (1999).

33. Brizel, D.M., S.P. Scully, J.M. Harrelson, L.J. Layfield, R.K. Dodge, H.C. Charles, et al., Radiation therapy and hyperthermia improve the oxygenation of human soft tissue sarcomas. *Cancer Research* **56**, 5347-5350 (1996).

34. Jones, E.L., L.R. Prosnitz, M.W. Dewhirst, P.K. Marcom, P.H. Hardenbergh, L.B. Marks, et al., Thermochemoradiotherapy improves oxygenation in locally advanced breast cancer. *Clinical Cancer Research* **10**, 4287-4293 (2004).

35. Vujaskovic, Z., J.M. Poulson, A.A. Gaskin, D.E. Thrall, R.L. Page, H.C. Charles, et al., Temperature-dependent changes in physiologic parameters of spontaneous canine soft tissue sarcomas after combined radiotherapy and hyperthermia treatment. *International Journal of Radiation Oncology Biology Physics* **46**, 179-185 (2000).

36. Roti, J.L.R., Heat-induced alterations of nuclear protein associations and their effects on DNA repair and replication. *International Journal of Hyperthermia* **23**, 3-15 (2007).

37. Westra, A. and W.C. Dewey, Variation in sensitivity to heat shock during cell-cycle of chinese hamster cells in-vitro. *International Journal of Radiation Biology and Related Studies in Physics Chemistry and Medicine* **19**, 467-& (1971).

38. Feyerabend, T., R. Steeves, G.J. Wiedemann, E. Richter, and H.I. Robins, Rationale and clinical status of local hyperthermia, radiation, and chemotherapy in locally advanced malignancies. *Anticancer Research* **17**, 2895-2897 (1997).

39. Marmor, J.B., Interactions of hyperthermia and chemotherapy in animals. *Cancer Research* **39**, 2269-2276 (1979).

40. Minchinton, A.I. and I.F. Tannock, Drug penetration in solid tumours. *Nature Reviews Cancer* **6**, 583-592 (2006).

41. Duncan, R., Polymer conjugates as anticancer nanomedicines. *Nature Reviews Cancer* **6**, 688-701 (2006).

42. Vasey, P.A., S.B. Kaye, R. Morrison, C. Twelves, P. Wilson, R. Duncan, et al., Phase i clinical and pharmacokinetic study of pk1 n-(2-hydroxypropyl)methacrylamide copolymer doxorubicin : First member of a new class of chemotherapeutic agents - drug-polymer conjugates. *Clinical Cancer Research* **5**, 83-94 (1999).

43. Chuang, V.T.G., U. Kragh-Hansen, and M. Otagiri, Pharmaceutical strategies utilizing recombinant human serum albumin. *Pharmaceutical Research* **19**, 569-577 (2002).

44. Vandamme, T.F., A. Lenourry, C. Charrueau, and J. Chaumeil, The use of polysaccharides to target drugs to the colon. *Carbohydrate Polymers* **48**, 219-231 (2002).

45. Allen, T.M., Liposomes - opportunities in drug delivery. *Drugs* **54**, 8-14 (1997).

46. Kataoka, K., A. Harada, and Y. Nagasaki, Block copolymer micelles for drug delivery: Design, characterization and biological significance. *Adv Drug Deliv Rev* **47**, 113-31 (2001).

47. Odonnell, P.B. and J.W. McGinity, Preparation of microspheres by the solvent evaporation technique. *Advanced Drug Delivery Reviews* **28**, 25-42 (1997).

48. Yasuhiro Matsumura, H.M., A new concept for macromolecular therapeutics in cancer chemotherapy: Mechanism of tumoritropic accumulation of proteins and the antitumor agent smancs. *Cancer Research* **46**, 6387-6392 (1986).

49. Maeda, H., G.Y. Bharate, and I. Daruwalla, Polymeric drugs for efficient tumor-targeted drug delivery based on epr-effect. *European Journal of Pharmaceutics and Biopharmaceutics* **71**, 409-419 (2009).

50. Yuan, F., M. Dellian, D. Fukumura, M. Leunig, D.A. Berk, V.P. Torchilin, et al., Vascular permeability in a human tumor xenograft: Molecular size dependence and cutoff size. *Cancer Research* **55**, 3752-3756 (1995).

51. Yuan, F., Transvascular drug delivery in solid tumors. *Seminars in Radiation Oncology* **8**, 164-175 (1998).

52. Seymour, L.W., Y. Miyamoto, H. Maeda, M. Brereton, J. Strohalm, K. Ulbrich, et al., Influence of molecular-weight on passive tumor accumulation of a soluble macromolecular drug carrier. *European Journal of Cancer* **31A**, 766-770 (1995).

53. Gabizon, A., R. Catane, B. Uziely, B. Kaufman, T. Safra, R. Cohen, et al., Prolonged circulation time and enhanced accumulation in malignant exudates of doxorubicin encapsulated in polyethylene-glycol coated liposomes. *Cancer Research* **54**, 987-992 (1994).

54. Matsumura, Y. and H. Maeda, A new concept for macromolecular therapeutics in cancer-chemotherapy - mechanism of tumoritropic accumulation of proteins and the antitumor agent smancs. *Cancer Research* **46**, 6387-6392 (1986).

55. Allen, T.M., Ligand-targeted therapeutics in anticancer therapy. *Nature Reviews Cancer* **2**, 750-763 (2002).

56. Chilkoti, A., M.R. Dreher, D.E. Meyer, and D. Raucher, Targeted drug delivery by thermally responsive polymers. *Advanced Drug Delivery Reviews* **54**, 613-630 (2002).

57. Bidwell, G.L., A.N. Davis, I. Fokt, W. Priebe, and D. Raucher, A thermally targeted elastin-like polypeptide-doxorubicin conjugate overcomes drug resistance. *Investigational New Drugs* **25**, 313-326 (2007).

58. Minko, T., P. Kopeckova, V. Pozharov, and J. Kopecek, Hpma copolymer bound adriamycin overcomes mdr1 gene encoded resistance in a human ovarian carcinoma cell line. *Journal of Controlled Release* **54**, 223-233 (1998).

59. Ryser, H.J.P. and W.C. Shen, Conjugation of methotrexate to poly(l-lysine) increases drug transport and overcomes drug-resistance in cultured-cells. *Proceedings of the National Academy of Sciences of the United States of America* **75**, 3867-3870 (1978).

60. Maeda, H., J. Wu, T. Sawa, Y. Matsumura, and K. Hori, Tumor vascular permeability and the epr effect in macromolecular therapeutics: A review. *Journal of Controlled Release* **65**, 271-284 (2000).

61. Jain, R.K., Delivery of novel therapeutic agents in tumors - physiological barriers and strategies. *Journal of the National Cancer Institute* **81**, 570-576 (1989).

62. Heldin, C.H., K. Rubin, K. Pietras, and A. Ostman, High interstitial fluid pressure - an obstacle in cancer therapy. *Nature Reviews Cancer* **4**, 806-813 (2004).

63. Dreher, M.R., W.G. Liu, C.R. Michelich, M.W. Dewhirst, and A. Chilkoti, Thermal cycling enhances the accumulation of a temperature-sensitive biopolymer in solid tumors. *Cancer Res* **67**, 4418-24 (2007).

64. Needham, D., G. Anyarambhatla, G. Kong, and M.W. Dewhirst, A new temperature-sensitive liposome for use with mild hyperthermia: Characterization and testing in a human tumor xenograft model. *Cancer Res* **60**, 1197-201 (2000).

65. Needham, D. and M.W. Dewhirst, The development and testing of a new temperature-sensitive drug delivery system for the treatment of solid tumors. *Adv Drug Deliv Rev* **53**, 285-305 (2001).

66. Brannon-Peppas, L. and J.O. Blanchette, Nanoparticle and targeted systems for cancer therapy. *Advanced Drug Delivery Reviews* **56**, 1649-1659 (2004).

67. Gu, F., L. Zhang, B.A. Teply, N. Mann, A. Wang, A.F. Radovic-Moreno, et al., Precise engineering of targeted nanoparticles by using self-assembled biointegrated block copolymers. *Proceedings of the National Academy of Sciences of the United States of America* **105**, 2586-2591 (2008).

68. Parker, N., M.J. Turk, E. Westrick, J.D. Lewis, P.S. Low, and C.P. Leamon, Folate receptor expression in carcinomas and normal tissues determined by a quantitative radioligand binding assay. *Analytical Biochemistry* **338**, 284-293 (2005).

69. Muss, H.B., A.D. Thor, D.A. Berry, T. Kute, E.T. Liu, F. Koerner, et al., C-erbb-2 expression and response to adjuvant therapy in women with node-positive early breast-cancer. *New England Journal of Medicine* **330**, 1260-1266 (1994).

70. Gasselhuber, A., M.R. Dreher, A. Partanen, P.S. Yarmolenko, D. Woods, B.J. Wood, et al., Targeted drug delivery by high intensity focused ultrasound mediated hyperthermia combined with temperature-sensitive liposomes: Computational modelling and preliminary in vivo validation. *International Journal of Hyperthermia* **28**, 337-348 (2012).

71. Gasselhuber, A., M.R. Dreher, F. Rattay, B.J. Wood, and D. Haemmerich, Comparison of conventional chemotherapy, stealth liposomes and temperature-sensitive liposomes in a mathematical model. *Plos One* **7**, (2012).

72. Liu, B.R., M. Yang, X.L. Li, X.P. Qian, Z.T. Shen, Y.T. Ding, et al., Enhanced efficiency of thermally targeted taxanes delivery in a human xenograft model of gastric cancer. *Journal of Pharmaceutical Sciences* **97**, 3170-3181 (2008).

73. Peng, C.L., H.M. Tsai, S.J. Yang, T.Y. Luo, C.F. Lin, W.J. Lin, et al., Development of thermosensitive poly(n-isopropylacrylamide-co-((2-dimethylamino) ethyl methacrylate))-based nanoparticles for controlled drug release. *Nanotechnology* **22**, 265608 (2011).

74. Zhang, J., Z. Qian, and Y. Gu, In vivo anti-tumor efficacy of docetaxel-loaded thermally responsive nanohydrogel. *Nanotechnology* **20**, 325102 (2009).

75. MacEwan, S.R. and A. Chilkoti, Digital switching of local arginine density in a genetically encoded self-assembled polypeptide nanoparticle controls cellular uptake. *Nano Letters* **12**, 3322-3328 (2012).

76. McDaniel, J.R., S.R. MacEwan, M. Dewhirst, and A. Chilkoti, Doxorubicin-conjugated chimeric polypeptide nanoparticles that respond to mild hyperthermia. *Journal of Controlled Release* **159**, 362-367 (2012).

77. McDaniel, J.R., J. Bhattacharyya, K.B. Vargo, W. Hassouneh, D.A. Hammer, and A. Chilkoti, Self-assembly of thermally responsive nanoparticles of a genetically encoded peptide polymer by drug conjugation. *Angewandte Chemie. International Edition in English* **52**, 1683-1687 (2013).

78. Gray, W.R., L.B. Sandberg, and J.A. Foster, Molecular model for elastin structure and function. *Nature* **246**, 461-6 (1973).

79. Tatham, A.S. and P.R. Shewry, Elastomeric proteins: Biological roles, structures and mechanisms. *Trends Biochem Sci* **25**, 567-71 (2000).

80. Urry, D.W., T.M. Parker, M.C. Reid, and D.C. Gowda, Biocompatibility of the bioelastic materials, poly(gvgvp) and its gamma-irradiation cross-linked matrix - summary of generic biological test-results. *Journal of Bioactive and Compatible Polymers* **6**, 263-282 (1991).

81. Shamji, M.F., H. Betre, V.B. Kraus, J. Chen, A. Chilkoti, R. Pichika, et al., Development and characterization of a fusion protein between thermally responsive elastin-like polypeptide and interleukin-1 receptor antagonist: Sustained release of a local antiinflammatory therapeutic. *Arthritis Rheum* **56**, 3650-61 (2007).

82. Liu, W.E., M.R. Dreher, D.Y. Furgeson, K.V. Peixoto, H. Yuan, M.R. Zalutsky, et al., Tumor accumulation, degradation and pharmacokinetics of elastin-like polypeptides in nude mice. *Journal of Controlled Release* **116**, 170-178 (2006).

83. Meyer, D.E. and A. Chilkoti, Genetically encoded synthesis of protein-based polymers with precisely specified molecular weight and sequence by recursive directional ligation: Examples from the elastin-like polypeptide system. *Biomacromolecules* **3**, 357-367 (2002).

84. Meyer, D.E. and A. Chilkoti, Purification of recombinant proteins by fusion with thermally-responsive polypeptides. *Nat Biotechnol* **17**, 1112-5 (1999).

85. Trabbic-Carlson, K., L. Liu, B. Kim, and A. Chilkoti, Expression and purification of recombinant proteins from escherichia coli: Comparison of an elastin-like polypeptide fusion with an oligohistidine fusion. *Protein Sci* **13**, 3274-84 (2004).

86. Raucher, D. and A. Chilkoti, Enhanced uptake of a thermally responsive polypeptide by tumor cells in response to its hyperthermia-mediated phase transition. *Cancer Res* **61**, 7163-70 (2001).

87. Meyer, D.E., G.A. Kong, M.W. Dewhirst, M.R. Zalutsky, and A. Chilkoti, Targeting a genetically engineered elastin-like polypeptide to solid tumors by local hyperthermia. *Cancer Res* **61**, 1548-54 (2001).

88. MacKay, J.A., M.N. Chen, J.R. McDaniel, W.G. Liu, A.J. Simnick, and A. Chilkoti, Self-assembling chimeric polypeptide-doxorubicin conjugate nanoparticles that abolish tumours after a single injection. *Nat Mater* **8**, 993-9 (2009).

89. Dreher, M.R., D. Raucher, N. Balu, O.M. Colvin, S.M. Ludeman, and A. Chilkoti, Evaluation of an elastin-like polypeptide-doxorubicin conjugate for cancer therapy. *Journal of Controlled Release* **91**, 31-43 (2003).

90. Walker, L., E. Perkins, F. Kratz, and D. Raucher, Cell penetrating peptides fused to a thermally targeted biopolymer drug carrier improve the delivery and antitumor efficacy of an acid-sensitive doxorubicin derivative. *Int J Pharm* **436**, 825-32 (2012).

91. MacKay, J.A., D.J. Callahan, K.N. FitzGerald, and A. Chilkoti, Quantitative model of the phase behavior of recombinant ph-responsive elastin-like polypeptides. *Biomacromolecules* **11**, 2873-2879 (2010).

92. Kim, B. and A. Chilkoti, Allosteric actuation of inverse phase transition of a stimulus-responsive fusion polypeptide by ligand binding. *Journal of the American Chemical Society* **130**, 17867-17873 (2008).

93. Callahan, D.J., W.E. Liu, X.H. Li, M.R. Dreher, W. Hassouneh, M. Kim, et al., Triple stimulus-responsive polypeptide nanoparticles that enhance intratumoral spatial distribution. *Nano Letters* **12**, 2165-2170 (2012).

94. Strzegowski, L.A., M.B. Martinez, D.C. Gowda, D.W. Urry, and D.A. Tirrell, Photomodulation of the inverse temperature transition of a modified elastin poly(pentapeptide). *Journal of the American Chemical Society* **116**, 813-814 (1994).

95. Yokoyama, M., M. Miyauchi, N. Yamada, T. Okano, Y. Sakurai, K. Kataoka, et al., Characterization and anticancer activity of the micelle-forming polymeric anticancer drug adriamycin-conjugated poly(ethylene glycol)-poly(aspartic acid) block copolymer. *Cancer Research* **50**, 1693-1700 (1990).

96. Kataoka, K., A. Harada, and Y. Nagasaki, Block copolymer micelles for drug delivery: Design, characterization and biological significance. *Advanced Drug Delivery Reviews* **47**, 113-131 (2001).

97. Kuckling, D., H.J.P. Adler, K.F. Arndt, L. Ling, and W.D. Habicher, Temperature and ph dependent solubility of novel poly(n-isopropylacrylamide) copolymers. *Macromolecular Chemistry and Physics* **201**, 273-280 (2000).

98. Yang, M., Y.T. Ding, L.Y. Zhang, X.P. Qian, X.Q. Jiang, and B.R. Liu, Novel thermosensitive polymeric micelles for docetaxel delivery. *Journal of Biomedical Materials Research. Part A* **81A**, 847-857 (2007).

99. Liu, B.R., M. Yang, R.T. Li, Y.T. Ding, X.P. Qian, L.X. Yu, et al., The antitumor effect of novel docetaxel-loaded thermosensitive micelles. *European Journal of Pharmaceutics and Biopharmaceutics* **69**, 527-534 (2008).

100. Kohori, F., K. Sakai, T. Aoyagi, M. Yokoyama, M. Yamato, Y. Sakurai, et al., Control of adriamycin cytotoxic activity using thermally responsive polymeric micelles composed of poly(n-isopropylacrylamide-co-n,n-dimethylacrylamide)-b-poly(d,l-lactide). *Colloids and Surfaces. B, Biointerfaces* **16**, 195-205 (1999).

101. Li, W., J.F. Li, J. Gao, B.H. Li, Y. Xia, Y.C. Meng, et al., The fine-tuning of thermosensitive and degradable polymer micelles for enhancing intracellular uptake and drug release in tumors. *Biomaterials* **32**, 3832-3844 (2011).

102. Liu, S.Q., Y.W. Tong, and Y.Y. Yang, Incorporation and in vitro release of doxorubicin in thermally sensitive micelles made from poly(n-isopropylacrylamide-co-n,n-dimethylacrylamide)-b-poly(d,l-lactide-co-glycolide) with varying compositions. *Biomaterials* **26**, 5064-5074 (2005).

103. Akimoto, J., M. Nakayama, K. Sakai, and T. Okano, Temperature-induced intracellular uptake of thermoresponsive polymeric micelles. *Biomacromolecules* **10**, 1331-1336 (2009).

104. Akimoto, J., M. Nakayama, K. Sakai, and T. Okano, Thermally controlled intracellular uptake system of polymeric micelles possessing poly(n-isopropylacrylamide)-based outer coronas. *Molecular Pharmaceutics* **7**, 926-935 (2010).

105. McDaniel, J.R., M.W. Dewhirst, and A. Chilkoti, Actively targeting solid tumours with thermoresponsive drug delivery systems that respond to mild hyperthermia. *Int J Hyperthermia* **29**, 501-10 (2013).

106. Simnick, A.J., M. Amiram, W.G. Liu, G. Hanna, M.W. Dewhirst, C.D. Kontos, et al., In vivo tumor targeting by a ngr-decorated micelle of a recombinant diblock copolypeptide. *Journal of Controlled Release* **155**, 144-151 (2011).

107. Simnick, A.J., C.A. Valencia, R.H. Liu, and A. Chilkoti, Morphing low-affinity ligands into high-avidity nanoparticles by thermally triggered self-assembly of a genetically encoded polymer. *Acs Nano* **4**, 2217-2227 (2010).

108. Wender, P.A., D.J. Mitchell, K. Pattabiraman, E.T. Pelkey, L. Steinman, and J.B. Rothbard, The design, synthesis, and evaluation of molecules that enable or enhance cellular uptake: Peptoid molecular transporters. *Proc Natl Acad Sci U S A* **97**, 13003-8 (2000).

109. Bangham, A.D., M.M. Standish, and J.C. Watkins, Diffusion of univalent ions across the lamellae of swollen phospholipids. *J Mol Biol* **13**, 238-52 (1965).

110. Allen, T.M., C. Hansen, F. Martin, C. Redemann, and A. Yau-Young, Liposomes containing synthetic lipid derivatives of poly(ethylene glycol) show prolonged circulation half-lives in vivo. *Biochim Biophys Acta* **1066**, 29-36 (1991).

111. Huang, S.K., K.D. Lee, K. Hong, D.S. Friend, and D. Papahadjopoulos, Microscopic localization of sterically stabilized liposomes in colon carcinoma-bearing mice. *Cancer Res* **52**, 5135-43 (1992).

112. Huang, S.K., F.J. Martin, G. Jay, J. Vogel, D. Papahadjopoulos, and D.S. Friend, Extravasation and transcytosis of liposomes in kaposi's sarcoma-like dermal lesions of transgenic mice bearing the hiv tat gene. *Am J Pathol* **143**, 10-4 (1993).

113. Immordino, M.L., P. Brusa, F. Rocco, S. Arpicco, M. Ceruti, and L. Cattel, Preparation, characterization, cytotoxicity and pharmacokinetics of liposomes containing lipophilic gemcitabine prodrugs. *J Control Release* **100**, 331-46 (2004).

114. Gabizon, A.A., Liposomal anthracyclines. *Hematol Oncol Clin North Am* **8**, 431-50 (1994).

115. Lorusso, D., A. Di Stefano, V. Carone, A. Fagotti, S. Pisconti, and G. Scambia, Pegylated liposomal doxorubicin-related palmar-plantar erythrodysesthesia ('hand-foot' syndrome). *Ann Oncol* **18**, 1159-64 (2007).

116. Yatvin, M.B., J.N. Weinstein, W.H. Dennis, and R. Blumenthal, Design of liposomes for enhanced local release of drugs by hyperthermia. *Science* **202**, 1290-3 (1978).

117. Papahadjopoulos, D., T.M. Allen, A. Gabizon, E. Mayhew, K. Matthay, S.K. Huang, et al., Sterically stabilized liposomes: Improvements in pharmacokinetics and antitumor therapeutic efficacy. *Proc Natl Acad Sci U S A* **88**, 11460-4 (1991).

118. Li, L., T.L. ten Hagen, D. Schipper, T.M. Wijnberg, G.C. van Rhoon, A.M. Eggermont, et al., Triggered content release from optimized stealth thermosensitive liposomes using mild hyperthermia. *J Control Release* **143**, 274-9 (2010).

119. Lindner, L.H., M.E. Eichhorn, H. Eibl, N. Teichert, M. Schmitt-Sody, R.D. Issels, et al., Novel temperature-sensitive liposomes with prolonged circulation time. *Clin Cancer Res* **10**, 2168-78 (2004).

120. Kong, G., G. Anyarambhatla, W.P. Petros, R.D. Braun, O.M. Colvin, D. Needham, et al., Efficacy of liposomes and hyperthermia in a human tumor xenograft model: Importance of triggered drug release. *Cancer Res* **60**, 6950-7 (2000).

121. Manzoor, A.A., L.H. Lindner, C.D. Landon, J.Y. Park, A.J. Simnick, M.R. Dreher, et al., Overcoming limitations in nanoparticle drug delivery: Triggered, intravascular release to improve drug penetration into tumors. *Cancer Res* **72**, 5566-5575 (2012).

122. Ponce, A.M., Z. Vujaskovic, F. Yuan, D. Needham, and M.W. Dewhirst, Hyperthermia mediated liposomal drug delivery. *Int J Hyperthermia* **22**, 205-13 (2006).

123. Yarmolenko, P.S., Y. Zhao, C. Landon, I. Spasojevic, F. Yuan, D. Needham, et al., Comparative effects of thermosensitive doxorubicin-containing liposomes and hyperthermia in human and murine tumours. *Int J Hyperthermia* **26**, 485-98 (2010).

124. Chen, Q., S. Tong, M.W. Dewhirst, and F. Yuan, Targeting tumor microvessels using doxorubicin encapsulated in a novel thermosensitive liposome. *Mol Cancer Ther* **3**, 1311-7 (2004).

125. Amiji, M.M., ed. *Nanotechnology in cancer therapy*. 2007, Taylor & Francis Group: Boca Raton, FL. 677-721.

126. Hayashi, H., K. Kono, and T. Takagishi, Temperature-controlled release property of phospholipid vesicles bearing a thermo-sensitive polymer. *Biochim Biophys Acta* **1280**, 127-34 (1996).

127. Kono, K., R. Nakai, K. Morimoto, and T. Takagishi, Thermosensitive polymer-modified liposomes that release contents around physiological temperature. *Biochim Biophys Acta* **1416**, 239-50 (1999).

128. Newkome, G.R., C.N. Moorefield, G.R. Baker, M.J. Saunders, and S.H. Grossman, Chemistry of micelles .13. Unimolecular micelles. *Angewandte Chemie. International Edition in English* **30**, 1178-1180 (1991).

129. Jansen, J.F.G.A., E.M.M. Debrabandervandenberg, and E.W. Meijer, Encapsulation of guest molecules into a dendritic box. *Science* **266**, 1226-1229 (1994).

130. Kimura, M., M. Kato, T. Muto, K. Hanabusa, and H. Shirai, Temperature-sensitive dendritic hosts: Synthesis, characterization, and control of catalytic activity. *Macromolecules* **33**, 1117-1119 (2000).

131. Zhao, Y.J., X.P. Fan, D. Liu, and Z. Wang, Pegylated thermo-sensitive poly(amidoamine) dendritic drug delivery systems. *International Journal of Pharmaceutics* **409**, 229-236 (2011).

132. Rezaei, S.J.T., M.R. Nabid, H. Niknejad, and A.A. Entezami, Multifunctional and thermoresponsive unimolecular micelles for tumor-targeted delivery and site-specifically release of anticancer drugs. *Polymer* **53**, 3485-3497 (2012).

133. Chandra, S., S. Dietrich, H. Lang, and D. Bahadur, Dendrimer-doxorubicin conjugate for enhanced therapeutic effects for cancer. *Journal of Materials Chemistry* **21**, 5729-5737 (2011).

134. Qian, Z.Y., S.Z. Fu, and S.S. Feng, Nanohydrogels as a prospective member of the nanomedicine family. *Nanomedicine (Lond)* **8**, 161-4 (2013).

135. Zhang, J., H. Chen, L. Xu, and Y. Gu, The targeted behavior of thermally responsive nanohydrogel evaluated by nir system in mouse model. *J Control Release* **131**, 34-40 (2008).

136. Matyjaszewski, K. and J. Xia, Atom transfer radical polymerization. *Chem Rev* **101**, 2921-90 (2001).

137. Siegwart, D.J., J.K. Oh, and K. Matyjaszewski, Atrp in the design of functional materials for biomedical applications. *Progress in Polymer Science* **37**, 18-37 (2012).

138. Chiefari, J., Y.K. Chong, F. Ercole, J. Krstina, J. Jeffery, T.P.T. Le, et al., Living free-radical polymerization by reversible addition-fragmentation chain transfer: The raft process. *Macromolecules* **31**, 5559-5562 (1998).

139. Moad, G., E. Rizzardo, and S.H. Thang, Living radical polymerization by the raft process. *Australian Journal of Chemistry* **58**, 379-410 (2005).

140. Lazaris, A., S. Arcidiacono, Y. Huang, J.F. Zhou, F. Duguay, N. Chretien, et al., Spider silk fibers spun from soluble recombinant silk produced in mammalian cells. *Science* **295**, 472-476 (2002).

141. Zhou, C.C., B.X. Leng, J.R. Yao, J. Qian, X. Chen, P. Zhou, et al., Synthesis and characterization of multiblock copolymers based on spider dragline silk proteins. *Biomacromolecules* **7**, 2415-2419 (2006).

142. Nettles, D.L., S.H. Elder, and J.A. Gilbert, Potential use of chitosan as a cell scaffold material for cartilage tissue engineering. *Tissue Engineering* **8**, 1009-1016 (2002).

143. Panitch, A., T. Yamaoka, M.J. Fournier, T.L. Mason, and D.A. Tirrell, Design and biosynthesis of elastin-like artificial extracellular matrix proteins containing periodically spaced fibronectin cs5 domains. *Macromolecules* **32**, 1701-1703 (1999).

144. Nath, N. and A. Chilkoti, Creating "smart" surfaces using stimuli responsive polymers. *Advanced Materials* **14**, 1243-7 (2002).

145. Kopecek, J., Smart and genetically engineered biomaterials and drug delivery systems. *European Journal of Pharmaceutical Sciences* **20**, 1-16 (2003).

146. Kurihara, H., T. Morita, M. Shinkai, and T. Nagamune, Recombinant extracellular matrix-like proteins with repetitive elastin or collagen-like functional motifs. *Biotechnology Letters* **27**, 665-670 (2005).

147. Mi, L.X., Molecular cloning of protein-based polymers. *Biomacromolecules* **7**, 2099-2107 (2006).

148. Lee, J.H., P.M. Skowron, S.M. Rutkowska, S.S. Hong, and S.C. Kim, Sequential amplification of cloned DNA as tandem multimers using class-iis restriction enzymes. *Genetic Analysis-Biomolecular Engineering* **13**, 139-145 (1996).

149. Amiram, M., F.G. Quiroz, D.J. Callahan, and A. Chilkoti, A highly parallel method for synthesizing DNA repeats enables the discovery of 'smart' protein polymers. *Nature Materials* **10**, 141-148 (2011).

150. Stahl, S., A. Sjolander, M. Hansson, P.A. Nygren, and M. Uhlen, A general strategy for polymerization, assembly and expression of epitope-carrying peptides applied to the plasmodium falciparum antigen pf155/resa. *Gene* **89**, 187-93 (1990).

151. McMillan, R.A., T.A.T. Lee, and V.P. Conticello, Rapid assembly of synthetic genes encoding protein polymers. *Macromolecules* **32**, 3643-3648 (1999).

152. Padgett, K.A. and J.A. Sorge, Creating seamless junctions independent of restriction sites in pcr cloning. *Gene* **168**, 31-35 (1996).

153. McDaniel, J.R., J.A. MacKay, F.G. Quiroz, and A. Chilkoti, Recursive directional ligation by plasmid reconstruction allows rapid and seamless cloning of oligomeric genes. *Biomacromolecules* **11**, 944-952 (2010).

154. Bickle, T.A. and D.H. Kruger, Biology of DNA restriction. *Microbiological Reviews* **57**, 434-450 (1993).

155. Szybalski, W., S.C. Kim, N. Hasan, and A.J. Podhajska, Class-iis restriction enzymes - a review. *Gene* **100**, 13-26 (1991).

156. Chow, D.C., M.R. Dreher, K. Trabbic-Carlson, and A. Chilkoti, Ultra-high expression of a thermally responsive recombinant fusion protein in e. Coli. *Biotechnol Prog* **22**, 638-46 (2006).

157. McPherson, D.T., J. Xu, and D.W. Urry, Product purification by reversible phase transition following escherichia coli expression of genes encoding up to 251 repeats of the elastomeric pentapeptide gvgvp. *Protein Expr Purif* **7**, 51-7 (1996).

158. Meyer, D.E. and A. Chilkoti, Quantification of the effects of chain length and concentration on the thermal behavior of elastin-like polypeptides. *Biomacromolecules* **5**, 846-851 (2004).

159. Kempe, T., S.B.H. Kent, F. Chow, S.M. Peterson, W.I. Sundquist, J.J. Litalien, et al., Multiple-copy genes - production and modification of monomeric peptides from large multimeric fusion proteins. *Gene* **39**, 239-245 (1985).

160. Lewis, R.V., M. Hinman, S. Kothakota, and M.J. Fournier, Expression and purification of a spider silk protein: A new strategy for producing repetitive proteins. *Protein Expression and Purification* **7**, 400-406 (1996).

161. Guda, C., X. Zhang, D.T. McPherson, J. Xu, J.H. Cherry, D.W. Urry, et al., Hyper expression of an environmentally friendly synthetic-polymer gene. *Biotechnology Letters* **17**, 745-750 (1995).

162. Maeda, H., L.W. Seymour, and Y. Miyamoto, Conjugates of anticancer agents and polymers - advantages of macromolecular therapeutics invivo. *Bioconjugate Chemistry* **3**, 351-362 (1992).

163. Veronese, F.M. and C. Monfardini, Stabilization of substances in circulation. *Bioconjugate Chemistry* **9**, 418-450 (1998).

164. Livingstone, D.J., Theoretical property predictions. *Current Topics in Medicinal Chemistry* **3**, 1171-1192 (2003).

165. Petrauskas, A.A. and E.A. Kolovanov, Acd/log p method description. *Perspectives in Drug Discovery and Design* **19**, 99-116 (2000).

166. Manners, I., J. Massey, K.N. Power, and M.A. Winnik, Self-assembly of a novel organometallic-inorganic block copolymer in solution and the solid state: Nonintrusive observation of novel wormlike poly(ferrocenyldimethylsilane)-b-poly(dimethylsiloxane) micelles. *Journal of the American Chemical Society* **120**, 9533-9540 (1998).

167. Zhao, C.L., M.A. Winnik, G. Riess, and M.D. Croucher, Fluorescence probe techniques used to study micelle formation in water-soluble block copolymers. *Langmuir* **6**, 514-516 (1990).

168. Urry, D.W., Physical chemistry of biological free energy transduction as demonstrated by elastic protein-based polymers. *Journal of Physical Chemistry B* **101**, 11007-11028 (1997).

169. Koizumi, F., M. Kitagawa, T. Negishi, T. Onda, S. Matsumoto, T. Hamaguchi, et al., Novel sn-38-incorporating polymeric micelles, nk012, eradicate vascular endothelial growth factor-secreting bulky tumors. *Cancer Research* **66**, 10048-10056 (2006).

170. Hamaguchi, T., Y. Matsumura, M. Suzuki, K. Shimizu, R. Goda, I. Nakamura, et al., Nk105, a paclitaxel-incorporating micellar nanoparticle formulation, can extend in vivo antitumour activity and reduce the neurotoxicity of paclitaxel. *British Journal of Cancer* **92**, 1240-1246 (2005).

171. Kataoka, K., Y. Bae, S. Fukushima, and A. Harada, Design of environment-sensitive supramolecular assemblies for intracellular drug delivery: Polymeric micelles that are responsive to intracellular ph change. *Angewandte Chemie International Edition* **42**, 4640-4643 (2003).

172. Kataoka, K., N. Nishiyama, S. Okazaki, H. Cabral, M. Miyamoto, Y. Kato, et al., Novel cisplatin-incorporated polymeric micelles can eradicate solid tumors in mice. *Cancer Research* **63**, 8977-8983 (2003).

173. Kwon, G., M. Naito, M. Yokoyama, T. Okano, Y. Sakurai, and K. Kataoka, Micelles based on ab block copolymers of poly(ethylene oxide) and poly(beta-benzyl l-aspartate). *Langmuir* **9**, 945-949 (1993).

174. Hyun, J., W.K. Lee, N. Nath, A. Chilkoti, and S. Zauscher, Capture and release of proteins on the nanoscale by stimuli-responsive elastin-like polypeptide "switches". *Journal of the American Chemical Society* **126**, 7330-7335 (2004).

175. Liu, W.G., J.A. MacKay, M.R. Dreher, M.N. Chen, J.R. McDaniel, A.J. Simnick, et al., Injectable intratumoral depot of thermally responsive polypeptide-radionuclide conjugates delays tumor progression in a mouse model. *Journal of Controlled Release* **144**, 2-9 (2010).

176. Megeed, Z., R.M. Winters, and M.L. Yarmush, Modulation of single-chain antibody affinity with temperature-responsive elastin-like polypeptide linkers. *Biomacromolecules* **7**, 999-1004 (2006).

177. Shamji, M.F., J. Chen, A.H. Friedman, W.J. Richardson, A. Chilkoti, and L.A. Setton, Synthesis and characterization of a thermally-responsive tumor necrosis factor antagonist. *Journal of Controlled Release* **129**, 179-186 (2008).

178. Cho, Y.H., Y.J. Zhang, T. Christensen, L.B. Sagle, A. Chilkoti, and P.S. Cremer, Effects of hofmeister anions on the phase transition temperature of elastin-like polypeptides. *Journal of Physical Chemistry B* **112**, 13765-13771 (2008).

179. Urry, D.W., Free-energy transduction in polypeptides and proteins based on inverse temperature transitions. *Progress in Biophysics & Molecular Biology* **57**, 23-57 (1992).

180. Urry, D.W., The change in gibbs free energy for hydrophobic association - derivation and evaluation by means of inverse temperature transitions. *Chemical Physics Letters* **399**, 177-183 (2004).

181. Urry, D.W., C.H. Luan, T.M. Parker, D.C. Gowda, K.U. Prasad, M.C. Reid, et al., Temperature of polypeptide inverse temperature transition depends on mean residue hydrophobicity. *Journal of the American Chemical Society* **113**, 4346-4348 (1991).

182. McDaniel, J.R., D.C. Radford, and A. Chilkoti, A unified model for de novo design of elastin-like polypeptides with tunable inverse transition temperatures. *Biomacromolecules* **14**, 2866-72 (2013).

183. Ribeiro, A., F.J. Arias, J. Reguera, M. Alonso, and J.C. Rodriguez-Cabello, Influence of the amino-acid sequence on the inverse temperature transition of elastin-like polymers. *Biophysical Journal* **97**, 312-320 (2009).

184. Nuhn, H. and H.A. Klok, Secondary structure formation and lcst behavior of short elastin-like peptides. *Biomacromolecules* **9**, 2755-2763 (2008).

185. Zhang, Y.J. and P.S. Cremer, Interactions between macromolecules and ions: The hofmeister series. *Current Opinion in Chemical Biology* **10**, 658-663 (2006).

186. Dewhirst, M.W., Z. Vujaskovic, E. Jones, and D. Thrall, Re-setting the biologic rationale for thermal therapy. *International Journal of Hyperthermia* **21**, 779-790 (2005).

187. Meyer, D.E., G.A. Kong, M.W. Dewhirst, M.R. Zalutsky, and A. Chilkoti, Targeting a genetically engineered elastin-like polypeptide to solid tumors by local hyperthermia. *Cancer Research* **61**, 1548-1554 (2001).

188. Dreher, M.R., W.G. Liu, C.R. Michelich, M.W. Dewhirst, and A. Chilkoti, Thermal cycling enhances the accumulation of a temperature-sensitive biopolymer in solid tumors. *Cancer Research* **67**, 4418-4424 (2007).

189. Raucher, D. and A. Chilkoti, Enhanced uptake of a thermally responsive polypeptide by tumor cells in response to its hyperthermia-mediated phase transition. *Cancer Research* **61**, 7163-7170 (2001).

190. Bidwell, G.L., I. Fokt, W. Priebe, and D. Raucher, Development of elastin-like polypeptide for thermally targeted delivery of doxorubicin. *Biochemical Pharmacology* **73**, 620-631 (2007).

191. MacKay, J.A., M.N. Chen, J.R. McDaniel, W.G. Liu, A.J. Simnick, and A. Chilkoti, Self-assembling chimeric polypeptide-doxorubicin conjugate nanoparticles that abolish tumours after a single injection. *Nature Materials* **8**, 993-999 (2009).

192. Fox, M.E., F.C. Szoka, and J.M.J. Frechet, Soluble polymer carriers for the treatment of cancer: The importance of molecular architecture. *Accounts of Chemical Research* **42**, 1141-1151 (2009).

193. Ruggiero, A., C.H. Villa, E. Bander, D.A. Rey, M. Bergkvist, C.A. Batt, et al., Paradoxical glomerular filtration of carbon nanotubes. *Proceedings of the National Academy of Sciences of the United States of America* **107**, 12369-12374 (2010).

194. Lu, J.M., C.M. Peterson, J. Guo-Shiah, Z.W. Gu, C.A. Peterson, R.C. Straight, et al., Cooperativity between free and n-(2-hydroxypropyl) methacrylamide copolymer bound adriamycin and meso-chlorin e(6) monoethylene diamine induced photodynamic therapy in human epithelial ovarian carcinoma in vitro. *International Journal of Oncology* **15**, 5-16 (1999).

195. Mahmud, A., X.B. Xiong, and A. Lavasanifar, Development of novel polymeric micellar drug conjugates and nano-containers with hydrolyzable core structure for doxorubicin delivery. *European Journal of Pharmaceutics and Biopharmaceutics* **69**, 923-934 (2008).

196. L, S., Y. A, and W.-P. S, *Applied biopharmaceutics & pharmacokinetics*. 6 ed. 2012: McGraw-Hill Medical. 811.

197. To, H., S. Ohdo, M. Shin, H. Uchimaru, E. Yukawa, S. Higuchi, et al., Dosing time dependency of doxorubicin-induced cardiotoxicity and bone marrow toxicity in rats. *Journal of Pharmacy and Pharmacology* **55**, 803-810 (2003).

198. Janib, S.M., S. Liu, R. Park, M.K. Pastuszka, P. Shi, A.S. Moses, et al., Kinetic quantification of protein polymer nanoparticles using non-invasive imaging. *Integrative Biology* **5**, 183-194 (2013).

199. Stone, E., L. Chantranupong, C. Gonzalez, J. O'Neal, M. Rani, C. VanDenBerg, et al., Strategies for optimizing the serum persistence of engineered human arginase i for cancer therapy. *Journal of Controlled Release* **158**, 171-179 (2012).

200. Kakizawa, Y., A. Harada, and K. Kataoka, Glutathione-sensitive stabilization of block copolymer micelles composed of antisense DNA and thiolated poly(ethylene glycol)-block-poly(l-lysine): A potential carrier for systemic delivery of antisense DNA. *Biomacromolecules* **2**, 491-7 (2001).

201. Senaratne, W., L. Andruzzi, and C.K. Ober, Self-assembled monolayers and polymer brushes in biotechnology: Current applications and future perspectives. *Biomacromolecules* **6**, 2427-2448 (2005).

202. Herr, D.J.C., Directed block copolymer self-assembly for nanoelectronics fabrication. *Journal of Materials Research* **26**, 122-139 (2011).

203. Biswas, A., I.S. Bayer, A.S. Biris, T. Wang, E. Dervishi, and F. Faupel, Advances in top-down and bottom-up surface nanofabrication: Techniques, applications & future prospects. *Advances in Colloid and Interface Science* **170**, 2-27 (2012).

204. Najer, A., D.L. Wu, D. Vasquez, C.G. Palivan, and W. Meier, Polymer nanocompartments in broad-spectrum medical applications. *Nanomedicine* **8**, 425-447 (2013).

205. Du, J.Z., H. Willcock, J.P. Patterson, I. Portman, and R.K. O'Reilly, Self-assembly of hydrophilic homopolymers: A matter of raft end groups. *Small* **7**, 2070-2080 (2011).

206. Kujawa, P., F. Segui, S. Shaban, C. Diab, Y. Okada, F. Tanaka, et al., Impact of end-group association and main-chain hydration on the thermosensitive properties of hydrophobically modified telechelic poly(n-isopropylacrylamides) in water. *Macromolecules* **39**, 341-348 (2006).

207. Patterson, J.P., E.G. Kelley, R.P. Murphy, A.O. Moughton, M.P. Robin, A. Lu, et al., Structural characterization of amphiphilic homopolymer micelles using light scattering, sans, and cryo-tem. *Macromolecules* **46**, 6319-6325 (2013).

208. Hassouneh, W., K. Fischer, S.R. MacEwan, R. Branscheid, C.L. Fu, R. Liu, et al., Unexpected multivalent display of proteins by temperature triggered self-assembly of elastin-like polypeptide block copolymers. *Biomacromolecules* **13**, 1598-605 (2012).

209. Rodriguez-Hernandez, J. and S. Lecommandoux, Reversible inside-out micellization of ph-responsive and water-soluble vesicles based on polypeptide diblock copolymers. *J Am Chem Soc* **127**, 2026-7 (2005).

210. Discher, B.M., Y.Y. Won, D.S. Ege, J.C. Lee, F.S. Bates, D.E. Discher, et al., Polymersomes: Tough vesicles made from diblock copolymers. *Science* **284**, 1143-6 (1999).

211. Vargo, K.B., R. Parthasarathy, and D.A. Hammer, Self-assembly of tunable protein suprastructures from recombinant oleosin. *Proc Natl Acad Sci U S A* **109**, 11657-62 (2012).

212. Srinivas, G., D.E. Discher, and M.L. Klein, Self-assembly and properties of diblock copolymers by coarse-grain molecular dynamics. *Nat Mater* **3**, 638-44 (2004).

213. McDaniel, J.R., J.A. Mackay, F.G. Quiroz, and A. Chilkoti, Recursive directional ligation by plasmid reconstruction allows rapid and seamless cloning of oligomeric genes. *Biomacromolecules* **11**, 944-52 (2010).

214. Janib, S.M., M.F. Pastuszka, S. Aluri, Z. Folchman-Wagner, P.Y. Hsueh, P. Shi, et al., A quantitative recipe for engineering protein polymer nanoparticles. *The Royal Society of Chemistry* (2013).

215. O'Reilly, R.K., C.J. Hawker, and K.L. Wooley, Cross-linked block copolymer micelles: Functional nanostructures of great potential and versatility. *Chem Soc Rev* **35**, 1068-83 (2006).

216. Fuchs, S., M. Kutscher, T. Hertel, G. Winter, M. Pietzsch, and C. Coester, Transglutaminase: New insights into gelatin nanoparticle cross-linking. *J Microencapsul* **27**, 747-54 (2010).

217. Young, T.S. and P.G. Schultz, Beyond the canonical 20 amino acids: Expanding the genetic lexicon. *J Biol Chem* **285**, 11039-44 (2010).

218. Liu, W.S., A. Brock, S. Chen, S.B. Chen, and P.G. Schultz, Genetic incorporation of unnatural amino acids into proteins in mammalian cells. *Nature Methods* **4**, 239-244 (2007).

219. Geng, Y., P. Dalhaimer, S.S. Cai, R. Tsai, M. Tewari, T. Minko, et al., Shape effects of filaments versus spherical particles in flow and drug delivery. *Nature Nanotechnology* **2**, 249-255 (2007).

220. Muro, S., C. Garnacho, J.A. Champion, J. Leferovich, C. Gajewski, E.H. Schuchman, et al., Control of endothelial targeting and intracellular delivery of therapeutic enzymes by modulating the size and shape of icam-1-targeted carriers. *Molecular Therapy* **16**, 1450-1458 (2008).

221. Decuzzi, P., B. Godin, T. Tanaka, S.Y. Lee, C. Chiappini, X. Liu, et al., Size and shape effects in the biodistribution of intravascularly injected particles. *Journal of Controlled Release* **141**, 320-327 (2010).

222. Devarajan, P.V., A.B. Jindal, R.R. Patil, F. Mulla, R.V. Gaikwad, and A. Samad, Particle shape: A new design parameter for passive targeting in splenotropic drug delivery. *Journal of Pharmaceutical Sciences* **99**, 2576-2581 (2010).

223. Park, J.H., G. von Maltzahn, L.L. Zhang, A.M. Derfus, D. Simberg, T.J. Harris, et al., Systematic surface engineering of magnetic nanoworms for in vivo tumor targeting. *Small* **5**, 694-700 (2009).

224. Zhang, K., H.F. Fang, Z.Y. Chen, J.S.A. Taylor, and K.L. Wooley, Shape effects of nanoparticles conjugated with cell-penetrating peptides (hiv tat ptd) on cho cell uptake. *Bioconjugate Chemistry* **19**, 1880-1887 (2008).

225. Champion, J.A. and S. Mitragotri, Role of target geometry in phagocytosis. *Proceedings of the National Academy of Sciences of the United States of America* **103**, 4930-4934 (2006).

226. Gasteiger E., H.C., Gattiker A., Duvaud S., Wilkins M.R., Appel R.D., Bairoch A., Protein identification and analysis tools on the expasy server, in *The proteomics protocols handbook*, J.M. Walker, Editor. 2005, Humana Press. p. 571-607.

227. Gallo, J.M. and Z.W. Guo, Selective protection of 2 ',2 '-difluorodeoxycytidine (gemcitabine). *Journal of Organic Chemistry* **64**, 8319-8322 (1999).

228. Etrych, T., M. Sirova, L. Starovoytova, B. Rihova, and K. Ulbrich, Hpma copolymer conjugates of paclitaxel and docetaxel with ph-controlled drug release. *Molecular Pharmaceutics* **7**, 1015-1026 (2010).

Biography

Jonathan R. McDaniel was born on October 27, 1984 in Raleigh, North Carolina. He graduated summa cum laude from the University of Illinois at Urbana-Champaign in May of 2007 with a B.S. in Materials Science and Engineering and a B.A. in Molecular and Cellular Biology. He pursued a Ph.D in the Department of Biomedical Engineering at Duke University, where he was presented with the Outstanding Graduate Teaching Assistant award in 2009 and the Kewaunee Student Achievement award in 2013. His work has helped produce the following publications:

(1) McDaniel JR, Dewhirst MW, and Chilkoti A, Actively targeting solid tumors by thermoresponsive drug delivery systems that respond to mild hyperthermia, *International Journal of Hyperthermia*, 2013. 29, 501-510. [23924317]

(2) McDaniel JR, Radford DC, and Chilkoti A, A unified model for de novo design of elastin-like polypeptides with tunable inverse transition temperatures, *Biomacromolecules*, 2013. 14, 2866-2872. [23808597]

(3) McDaniel JR, Bhattacharyya J, Vargo KB, Hassouneh W, Hammer DA, and Chilkoti A, Self-assembly of thermally responsive nanoparticles of a genetically encoded peptide polymer by drug conjugation, *Angewandte Chemie International Edition*, 2013. 52, 1683-1687. [23280697]

(4) Weller D, McDaniel JR, Fischer K, Chilkoti A, and Schmidt M. Stimuli-responsive cylindrical polymer brushes with elastin-like polypeptide side chains. *Macromolecules*, 2013. 46, 4966-4971.

(5) Kurzbach D, Hassouneh W, McDaniel JR, Jaumann E, Chilkoti A, and Hinderberger D, Hydration layer coupling and cooperativity in phase behavior of stimulus responsive peptide polymers, *Journal of the American Chemical Society*, 2013. 135, 11299-11308. [23822733]

(6) Sinclair SM, Bhattacharyya J, McDaniel JR, Gooden DM, Gopalaswamy R, Chilkoti A, and Setton LA, A genetically engineered thermally responsive sustained release curcumin depot to treat neuroinflammation, *Journal of Controlled Release*, 2013. 171, 38-47. [23830979]

(7) McDaniel JR, MacEwan SR, Dewhirst M, and Chilkoti A, Doxorubicin-conjugated chimeric polypeptide nanoparticles that respond to mild hyperthermia, *Journal of Controlled Release,* 2012. 159, 362-367. [22421424]

(8) Liu W, McDaniel JR, Li X, Asai D, Quiroz FG, Schaal J, Park J, Zalutsky M, and Chilkoti A, Brachytherapy using injectable seeds that are self assembled from genetically encoded polypeptides in situ, *Cancer Research*, 2012. 72, 5956-65. [23155121]

(9) Chen M, McDaniel JR, MacKay JA, and Chilkoti A, Nanoscale Self-Assembly for Delivery of Therapeutics and Imaging Agents. *Technology and Innovation,* 2011. 13, 5-25.

(10) Fluegel S, Buehler J, Fischer K, McDaniel JR, Chilkoti A, and Schmidt M, Self-assembly of monodisperse oligonucleotide-elastin block copolymers into stars and compound micelles. *Chemistry (Weinheim an der Bergstrasse, Germany)*, 2011. 17, 5503-5506. [21469235]

(11) McDaniel JR, MacKay JA, Quiroz FG, and Chilkoti A, Recursive directional ligation by plasmid reconstruction allows rapid and seamless cloning of oligomeric genes. *Biomacromolecules*, 2010. 11(4): p. 944-952. [20184309]

(12) McDaniel JR, Callahan DJ, and Chilkoti A, Drug delivery to solid tumors by elastin-like polypeptides. *Advanced drug delivery reviews*, 2010. 62: 1456-1467.[20546809]

(13) Liu WG, MacKay JA, Dreher MR, Chen MN, McDaniel JR, Simnick AJ, Callahan DJ, Zalutsky MR, and Chilkoti A, Injectable intratumoral depot of thermally responsive polypeptide-radionuclide conjugates delays tumor progression in a mouse model. *Journal of Controlled Release*, 2010. 144(1): p. 2-9.[20117167]

(14) Fluegel S, Fischer K, McDaniel JR, Chilkoti A, and Schmidt M, Chain stiffness of elastin-like polypeptides. *Biomacromolecules*. 2010. 11, 3216-3218. [20961120]

(15) MacKay JA, Chen MN, McDaniel JR, Liu WG, Simnick AJ, and Chilkoti A, Self-assembling chimeric polypeptide-doxorubicin conjugate nanoparticles that abolish tumours after a single injection. *Nature Materials*, 2009. 8(12): p. 993-999. [19898461]

(16) Wu YQ, MacKay JA, McDaniel JR, Chilkoti A, and Clark RL, Fabrication of elastin-like polypeptide nanoparticles for drug delivery by electrospraying. *Biomacromolecules*, 2009. 10(1): p. 19-24.[19072041]

(17) Grego S, McDaniel JR, and Stoner BR, Wavelength interrogation of grating-based optical biosensors in the input coupler configuration. *Sensors and Actuators B-Chemical*, 2008. 131(2): p. 347-355.